UNIVERSITY OF OKLAHOMA

GRADUATE COLLEGE

THE IMPACTS CLIMATE VARIABILITY AND ANTHROPOGENIC ACTIVITY ON TERRESTRIAL ECOSYSTEM CARBON CYCLING

A DISSERTATION

SUBMITTED TO THE GRADUATE FACULTY

in partial fulfillment of the requirements for the

Degree of

DOCTOR OF PHILOSOPHY

By

RUSSELL BACKWOODS BOOMTREE DOUGHTY
Norman, Oklahoma
2019

THE IMPACTS OF CLIMATE VARIABILITY AND ANTHROPOGENIC ACTIVITY ON TERRESTRIAL ECOSYSTEM CARBON CYCLING

A THESIS APPROVED FOR THE

DEPARTMENT OF MICROBIOLOGY AND PLANT BIOLOGY

BY THE COMMITTEE CONSISTING OF

Dr. Xiangming Xiao, Chair

Dr. Heather McCarthy

Dr. Jennifer Koch

Dr. Lara Souza

Dr. Jeff Basara

This dissertation, and all my work, is dedicated to my late grandfather,

Lester Monroe Doughty, Jr.

Acknowledgements

This work would not be possible without the considerate and patient contributions of my lab mates, advisor Dr. Xiangming Xiao, committee members, and family. Dr. Yao Zhang was instrumental in teaching me about solar-induced chlorophyll fluorescence, and Xiaocui Wu took the time to teach me how to run the Vegetation Photosynthesis Model. Dr. Rajen Bajgain has taught me everything I ever wanted to know about eddy covariance systems in the field and how to process and utilize eddy tower data in my research. Dr. Yuanwei Qin always has helpful comments on how to address the scientific questions we seek to answer. Dr. Jie Wang and Dr. Yuting Zhou provided me valuable feedback and background information for Chapter 2, and their collaboration on work in Oklahoma has inspired and humbled me as an Oklahoman. Dr. Zhenhua Zhou was helpful by providing healthy skepticism and constructive criticism that helped resolve issues that may have arisen during the review process.

Dr. Heather McCarthy joyfully provided me the background I needed in plant physiology to be a successful student. Dr. Jeff Basara has molded how I approach the interactions between plants and climate variability. Dr. Jennifer Koch has been vital to my progress as a computer scientist by showing me additional and more appropriate coding methods. Dr. Lara Souza has helped me think of bigger-picture ideas and how my work fits into the broader context. Dr. Xiangming Xiao has not only always made himself available when I have questions and seek feedback but has been patient and thorough in his explanations. His guidance in academia and in personal life decisions have helped me be successful in school and in life. I will always be indebted to Dr. Xiao and his wife Bo for their generosity.

Brad and Charlette Hearne have been supportive of my journey at the University of Oklahoma and have always given me and my wife a place to unwind and put things into

perspective on the beautiful Glover River in McCurtain County. Charlette has provided me ample opportunities to contribute to the protection of Oklahoma's water resources for future generations, something for which we have a shared love. Her passion is infectious.

Shuang Ma, my wife, has been not only been encouraging and a complete joy, but has further honed my knowledge of ecosystem processes and climate feedbacks by discussing and involving me in her own doctoral research for which I will be forever grateful. Shuntao Ma, my father-in-law, has been has provided us with endless love and inspiration.

Table of Contents

List of Tables

List of Figures

Abstract

There is a near consensus among climate scientists that global temperatures are rising, climate variability will increase, and climate extremes will become more extreme. What is debated, however, is how terrestrial ecosystems and croplands will respond to these predicted changes in climate. The global carbon flux budget is largely driven by terrestrial photosynthesis and croplands are the foundation of global food security. Thus, the impact of changes in climate on terrestrial ecosystems and croplands has received considerable attention in recent decades. My overall objective was to identify how drought and pluvial events affect croplands in Oklahoma and the Amazon rainforest so that these responses can be incorporated into earth system models that simulate the impact on and feedbacks between climate and vegetation.

In this study, I hypothesized that the responses of grassland, winter wheat (*Triticum aestivum* L.), other C3 cropland, and C4 cropland to drought and pluvial events are largely determined by their respective photosynthetic pathway and landowners' ability or inability to irrigate. The specific objective was to analyze the response of gross primary production (GPP) for irrigated and non-irrigated grasslands, winter wheat, other C3 croplands, and C4 croplands in Caddo County, Oklahoma to the 2011 drought and pluvial 2015. For this analysis, we used four datasets each year from 2010 to 2016: (1) satellite-based GPP data from the Vegetation Photosynthesis Model (GPP_{VPM}) (Jin et al. 2015; Zhang et al. 2017a); (2) the MODIS GPP product (GPP_{MOD17}) (Running and Zhao 2015); (3) the Cropland Data Layer (CDL); and (4) irrigation permit data from the Oklahoma Water Resources Board (OWRB). Our analysis included three main steps: (1) compare GPP estimates at three eddy flux towers (GPP_{EC}) placed in sites with native grassland, old world bluestem pasture (*Bothriochloa caucasica* C.E. Hubb.), and winter wheat in El Reno, Oklahoma, with GPP_{VPM} and GPP_{MOD17}; (2) compare 8-day, intra-

annual GPP_{VPM} estimates in 2011, 2013, and 2015 for eight 500 m pixels, one each for irrigation-permitted and non-permitted grasslands, winter wheat, other C3 croplands, and C4 croplands in Caddo County; and (3) analyze the responses of each land cover type at the county scale to the 2011 drought and pluvial 2015.

I also sought to advance our scientific knowledge on how the Amazon rainforest responded to extreme climate events. I used monthly SIF data from GOME-2 and OCO-2, gross primary production estimates from the Vegetation Photosynthesis Model (GPP_{VPM}), and MODIS-based vegetation indices for 2007-2017 to investigate 1) to what degree were the seasonality of SIF, photosynthesis, and greenness of moist tropical forests consistent with each other, and 2) how did dry-season SIF, photosynthesis, and greenness change during the strong El Niño (2010 and 2016) and La Niña years (2008 and 2011). I hypothesized that the forested Amazonian sites have increased SIF, photosynthesis, and greenness during the dry-season, and that dry-season SIF, productivity, and greenness are enhanced during the two El Niño years but reduced during the two La Niña years. The rationale is that leaf flush and phenology drive the dry-season greening of the moist tropical Amazon forest and that productivity will be enhanced in drier dry seasons due to increased sunlight and a lack of water limitation. To further investigate the seasonality of SIF in the Amazon, I also analyzed SIF data from the TROPOspheric Monitoring Instrument (TROPOMI), which launched in October 2017. The data from the satellite, also called the Sentinel-5 Precursor, has a spatio-temporal resolution of 3.5 km by 7 km with near-daily global coverage. I also conducted a global comparison of SIF with GPP and vegetation indices to investigate if SIF better captures vegetation dynamics in some regions on Earth, and to determine which vegetation index best agrees with SIF in space and time.

Chapter 1: Introduction

1.1 Background

At the state level, the spatial impact of drought and pluvial events on croplands in Oklahoma is largely unknown because agricultural statistics are country-level at best. Moreover, the impact of climate extremes on Oklahoma's irrigated croplands has not been studied. Thus, to address this lack of knowledge I aimed to address these state-level issues by determine the impact of drought, pluvial, and irrigation on the gross primary production of grasslands and croplands in Oklahoma.

Globally, the Amazon rainforest is the largest contributor to global gross primary production (GPP), and the biomass of the high-latitude forests are the largest stores of terrestrial carbon. The impact of drought on the productivity of the Amazon and rising global temperatures on high-latitude forests are hotly debated topics. I contributed to these debates by 1) evaluating the seasonality of and determining the impact of La Niña and El Niño on dry-season solar-induced chlorophyll fluorescence (SIF), photosynthesis, and greenness for moist tropical Amazon forests.

1.2 Objectives

Terrestrial ecosystems are the largest portion of the global carbon flux budget and are the largest contributor to terrestrial precipitation. However, ***what is not known*** is how terrestrial ecosystems will respond to future expected changes in climate. My ***long-term goal*** is to improve knowledge of how terrestrial ecosystems respond to extreme climate events. The ***overall objective*** of my research is to identify the roles of specific terrestrial ecosystems in biogeochemical cycling and the factors that drive and affect those roles, so that we can better understand how perturbations in one ecosystem may affect the global biogeochemical cycle.

My ***central hypothesis*** is that the impacts of drought, pluvial, and land-cover and land-use change on terrestrial ecosystems are highly variable and heterogenous across space and time. The ***rationale*** for my research is that a better understanding of how terrestrial ecosystems respond to perturbations in climate and how changes in land-cover affect the biogeochemical cycle is critical to forecasting the effect of climate change on these systems and to making informed decisions aimed at mitigating those effects.

My specific objectives were to:

1. Determine the impact of drought, pluvial, and irrigation on the gross primary production of grasslands and croplands in Oklahoma.
2. Evaluate the seasonality of and determine the impact of La Niña and El Niño on dry-season solar-induced chlorophyll fluorescence (SIF), photosynthesis, and greenness for moist tropical Amazon forests.
3. Assess the seasonality of TROPOMI SIF during the dry season in the Amazon.
4. Determine where TROPOMI SIF is inconsistent with GPP and vegetation indices.

1.3 Organization of the dissertation

This dissertation consists of one introductory chapter, four main chapters, and one summary chapter. Chapters 2 and 4 have been published in peer-reviewed journals. Chapter 3 has been reviewed by two different journals and I am revising it for resubmission. Chapter 5 remains in preparation, but it will soon be submitted to a high impact journal.

Chapter 2: Responses of gross primary production of grasslands and croplands under drought, pluvial, and irrigation conditions during 2010-2016, Oklahoma, USA

For this study, I used irrigation data from the Oklahoma Water Resources Board (OWRB), eddy covariance towers El Reno, Oklahoma, Cropland Data Layer (CDL), Vegetation Photosynthesis

Model (VPM), and MODIS. I hypothesized that the responses of grassland, winter wheat, other C3 cropland, and C4 cropland to drought and pluvial events are largely determined by their respective photosynthetic pathway and landowners' ability or inability to irrigate.

Chapter 3: Dry-season greenness, fluorescence, and photosynthesis of moist tropical forests in the Amazon

I used SIF data from GOME-2 and OCO-2, the Vegetation Photosynthesis Model, vegetation indices derived from MODIS, and climate data from National Centers for Environmental Prediction (NCEP) Reanalysis 2 and the Tropical Rainfall Measuring Mission. I hypothesized that 1) SIF, photosynthesis, and greenness increases during the dry season for moist tropical Amazon forests; 2) El Niño enhances dry-season SIF, photosynthesis, and greenness; and 3) La Niña suppresses dry-season SIF, photosynthesis, and greenness.

Chapter 4: TROPOMI reveals dry-season increase of solar-induced chlorophyll fluorescence in the Amazon forest

For this study, I collaborated with colleagues at NASA's Jet Propulsion Lab and CalTech in Pasadena, California to evaluate data from a newly launched spaceborne platform, TROPOspheric Monitoring Instrument (TROPOMI), to investigate if there was a seasonality of TROPOMI SIF that matched previously published EVI and GPP data. I hypothesized that the seasonality of TROPOMI SIF would match GPP as estimated using eddy covariance flux data and spaceborne vegetation indices.

Chapter 5: Inconsistencies between TROPOMI solar-induced chlorophyll fluorescence, gross primary production, and vegetation indices

Using TROPOMI SIF data, I conducted global spatial and temporal comparisons of TROPOMI SIF with GPP from VPM, GPP as estimated by the Moderate Resolution Imaging Spectroradiometer

(MODIS) product, and three vegetation indices, near infrared reflectance of vegetation (NIRv), the enhanced vegetation index (EVI), and the normalized difference vegetation index (NDVI), to determine where GPP and VIs disagreed with TROPOMI SIF. I hypothesized that 1) TROPOMI SIF could better track the dynamics of vegetation function, especially in sparsely vegetated, wet, inundated, and/or cloudy regions; 2) NIRv is more consistent with SIF and GPP than EVI; and 3) bidirectional reflectance distribution function adjusted and non-adjusted surface reflectance have similar consistencies with SIF.

1.4 List of publications from the dissertation

Doughty, R., Xiao, X., Wu, X., Zhang, Y., Bajgain, R., Zhou, Y., Qin, Y., Zou, Z., McCarthy, H., Friedman, J. and Wagle, P., 2018. Responses of gross primary production of grasslands and croplands under drought, pluvial, and irrigation conditions during 2010–2016, Oklahoma, USA. *Agricultural Water Management*, 204, pp.47-59.

Doughty, R., Xiao, X., Wu, X., Qin, Y., Zhang, Y., Parazoo, N., and Moore III, B., 2019. Fluorescence, photosynthesis, and greenness of Amazon forests in dry season and El Niño years. *In prep*.

Doughty, R., Köhler, P., Frankenberg, C., Magney, T.S., Xiao, X., Qin, Y., Wu, X. and Moore, B., 2019. TROPOMI reveals dry-season increase of solar-induced chlorophyll fluorescence in the Amazon forest. *Proceedings of the National Academy of Sciences*, p.201908157.

Doughty, R., Köhler, P., Frankenberg, C., Xiao, X., Qin, Y., Wu., Ma, S., and Moore, B. 2019. Inconsistencies between TROPOMI solar-induced chlorophyll fluorescence, gross primary production, and vegetation indices. *In prep*.

Chapter 2: Responses of gross primary production of grasslands and croplands under drought, pluvial, and irrigation conditions during 2010-2016, Oklahoma, USA

Abstract

To accurately estimate the terrestrial carbon cycle and food production, it is essential to understand how gross primary production (GPP) of irrigated and non-irrigated grasslands and croplands respond to drought and pluvial events. This study analyzed annual GPP of irrigation-permitted and non-permitted grasslands, winter wheat (*Triticum aestivum* L.), other C3 croplands, and C4 croplands in Caddo County of western Oklahoma from 2010 through 2016, a period which consisted of extreme drought (2011) and pluvial events (2015). First, we compared GPP from the Vegetation Photosynthesis Model (GPP_{VPM}) and GPP data from the Moderate Resolution Imaging Spectroradiometer (GPP_{MOD17}) with GPP estimates from three eddy covariance towers (GPP_{EC}) in Oklahoma. GPP_{VPM} more accurately estimated mean daily GPP_{EC} at each of the three sites than GPP_{MOD17}. Second, we analyzed the seasonal and interannual dynamics of GPP_{VPM} for eight pixels, one each for the four irrigation-permitted and non-permitted land types. The interannual variation of GPP_{VPM} was due to the complexity of decision making and practice for irrigation, cropping intensity, and crop types. Finally, at the county scale, annual GPP_{VPM} from the 2011 drought and pluvial 2015 were compared with mean annual GPP_{VPM} from the other 5 years of the study period. The results show that for the 2011 drought: 1) non-permitted C4 croplands had the largest percentage decrease in GPP, but permitted C4 croplands had the smallest decrease; 2) regardless of water rights, GPP was significantly lower than the 5-year reference mean for grasslands, winter wheat, and other C3 crops; and 3) non-permitted lands were more affected by drought than irrigation-permitted lands, except for grasslands, which had similar percentage reductions in GPP. Results for the pluvial year 2015 show that: 1) GPP was significantly higher for grasslands, winter

wheat, and non-permitted C3 croplands than the 5-year reference mean, but there was no significant difference in GPP for irrigation-permitted C3 croplands or non-permitted C4 croplands; and 2) GPP for C4 irrigation-permitted croplands was lower than the 5-year reference mean. Crop-specific responses to drought and pluvial events largely depend on a landowner's ability to irrigate, and caution should be used when assessing or generalizing how crops respond to climate variability, drought, and pluvial conditions in the absence of irrigation-related data.

2.1 Introduction

Drought can severely reduce forage, hay, crop, and livestock production, resulting in economic losses, reduced employment, and increased commodity prices that have spillover effects into other non-agricultural markets (Ziolkowska 2016). Similarly, flooding and heavy precipitation events can cause crop damage and reduce yields (Rosenzweig et al. 2002). However, sustainable food production needs more knowledge about landscape-scale, crop-specific responses to drought and pluvial events and the role of irrigation in those responses to changes in climate. Recent studies have used MODIS and Landsat data products to estimate crop yield at large spatial scales (Doraiswamy et al. 2004; Xin et al. 2013), but they did not consider a water management component because it is largely unknown how crops respond to irrigation at the landscape scale (Yuan et al. 2015). More specifically, He et al. (2018) expected that more specific model calibrations for irrigated and non-irrigated crops would increase the precision of their crop yield estimates.

Although national agricultural survey and economic data can give us insight into how extreme weather events and changes in climate have affected crop-specific yields and market prices, such data does not provide wisdom on the physiological responses of vegetation to drought and pluvial events at high temporal or spatial resolution. Similarly, meteorological drought indices,

such as the Palmer Drought Severity Index (PDSI) (Palmer 1965) and the Standardized Precipitation Index (SPI) (McKee et al. 1993), are widely used as indicators of drought, but they do not measure plant productivity. Agricultural drought indices, such as the Crop Moisture Index (CMI) (Palmer 1968), often use soil moisture to indicate drought, but they are not an explicit indicator of vegetation stress and fail to capture variances in soil moisture due to irrigation at the field scale. Satellite-based remote sensing vegetation indices (VIs), such as the greenness-related Enhanced Vegetation Index (EVI) (Huete et al. 2002; Huete et al. 1997a; Justice et al. 1998), and water-related VIs such as Normalized Difference Water Index (NDWI) (Gao 1996b) and Land Surface Water Index (LSWI) (Xiao et al. 2004; Zhou et al. 2017b), have been used as proxies for several biophysical and biochemical variables such as plant response to drought (Bajgain et al. 2016; Bajgain et al. 2015; Wagle et al. 2014) and rainfall (Chandrasekar et al. 2010), leaf area index (Boegh et al. 2002), canopy chlorophyll content (Blackburn 1998; Gitelson et al. 2005), and gross primary production (the total amount of carbon fixed by plants) (Wagle et al. 2015). However, satellite-based remote sensing techniques have not yet been developed to capture landscape-scale irrigation activities with high accuracy at interannual timescales (Masoner et al. 2003; Ozdogan et al. 2010). Thus, irrigated and non-irrigated crop-specific responses to drought and pluvial events remain unknown at large spatial scales.

The response of vegetation to drought and pluvial events are not only determined by external factors such as temperature, precipitation, and sunlight, but also by the species' photosynthetic pathways. Generally, plants with the C3 photosynthetic pathway are less drought-resistant than plants that perform C4 photosynthesis (Nayyar and Gupta 2006; Tilman and Downing 1994). Previous studies have shown that C4 plants (1) have a higher quantum yield (Ehleringer et al. 1997), or light use efficiency (LUE) (Chen et al. 2011; Haxeltine and Prentice

1996; Xiao 2006), in that they can fix more CO_2 per photon absorbed by chlorophyll than C3 plants; and (2) have a higher water use efficiency (WUE) (Hsiao and Acevedo 1974; O'Leary 1988), in that they can fix more CO_2 per molecule of water than C3 plants. Thus, the response of a monoculture to drought and pluvial events are expected to differ for C3 or C4 crop species (Chaves et al. 2003), and the response of grasslands depends upon the ratio of C3 to C4 species in the grassland community (Tilman and Downing 1994).

In this study, we hypothesized that the responses of grassland, winter wheat (*Triticum aestivum* L.), other C3 cropland, and C4 cropland to drought and pluvial events are largely determined by their respective photosynthetic pathway and landowners' ability or inability to irrigate. The specific objective of this study was to analyze the response of gross primary production (GPP) for irrigated and non-irrigated grasslands, winter wheat, other C3 croplands, and C4 croplands in Caddo County, Oklahoma (Fig. 2.1) to the 2011 drought and pluvial 2015.

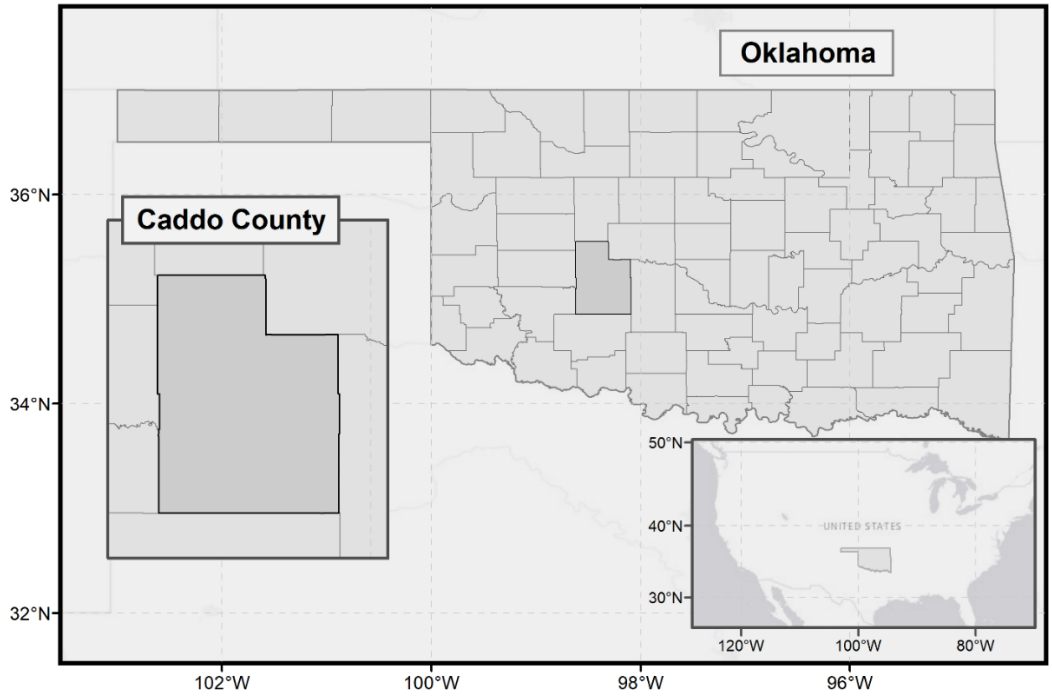

Figure 2.1| Location of Caddo County, Oklahoma, United States.

2.2 Materials and Methods

For our analysis, we used four datasets each year from 2010 to 2016: (1) satellite-based GPP data from the Vegetation Photosynthesis Model (GPP_{VPM}) (Jin et al. 2015; Zhang et al. 2017a); (2) the MODIS GPP product (GPP_{MOD17}) (Running and Zhao 2015); (3) the Cropland Data Layer (CDL); and (4) irrigation permit data from the Oklahoma Water Resources Board (OWRB). Our analysis included three main steps: (1) we compared GPP estimates at three eddy flux towers (GPP_{EC}) placed in sites with native grassland, old world bluestem pasture (*Bothriochloa caucasica* C.E. Hubb.), and winter wheat in El Reno, Oklahoma, with GPP_{VPM} and GPP_{MOD17}; (2) we compared 8-day, intra-annual GPP_{VPM} estimates in 2011, 2013, and 2015 for eight 500 m pixels, one each for irrigation-permitted and non-permitted grasslands, winter wheat, other C3 croplands, and C4 croplands in Caddo County; and (3) we analyzed the responses of each land cover type at the county scale to the 2011 drought and pluvial 2015. For steps 2 and 3, we determined which 500 m GPP_{VPM} pixels were suitable for study in each year 2010-2016 using the workflow illustrated in Fig. 2.

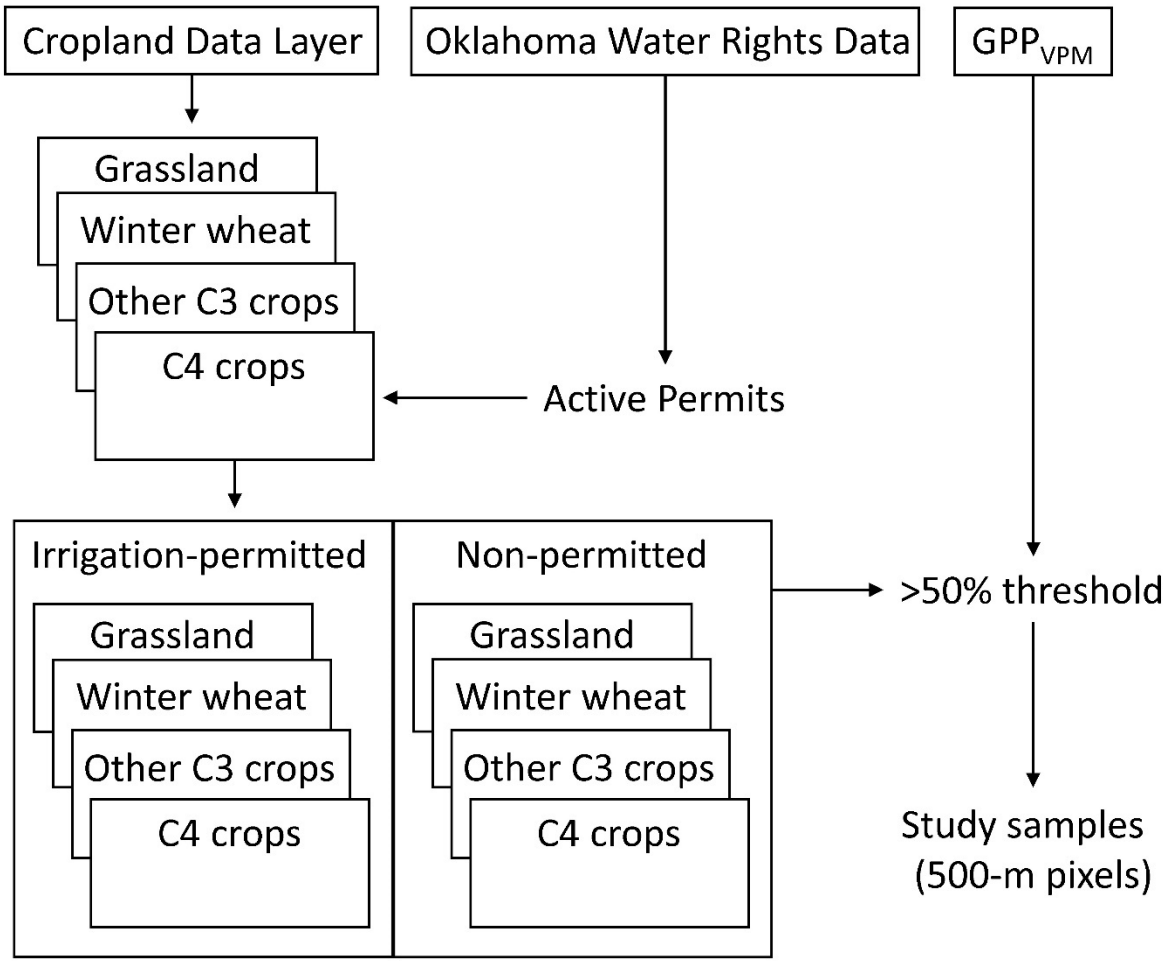

Figure 2.2 | The workflow used to determine which 500 m pixels were a majority irrigation-permitted and non-permitted grasslands or croplands for each year 2010-2016.

2.2.1 Study area

The state of Oklahoma, located in the Southern Great Plains of the United States (US), has been characterized as being in a region with reoccurring periods of drought (Basara et al. 2013; Christian et al. 2015), heavy rainfall events (McCorkle et al. 2016), high variability in precipitation (Weaver et al. 2016), and increased climate variability (Flanagan et al. 2017b). For Oklahoma, a period of prolonged drought began in 2011 (Fernando et al. 2016; Flanagan et al. 2017a) and persisted for most of the state until May 2015 when it was broken by record amounts of

precipitation (Oklahoma Climatological Survey 2015). Thus, these dipolar climate events in Oklahoma provided a suitable region in which we were able to conduct our study.

We selected a Caddo County, Oklahoma as our pilot study area because it has a high concentration of both irrigation-permitted and non-permitted land (Fig. 2.3(a)) and the county experienced the extreme climate events of 2011 and 2015. Apart from a brief break in the drought in the spring of 2012, no less than 60% of Caddo County was in climatological drought for 4.5 years, from January 2011 to May 2015 (Fig. 2.4). Entering 2015, 100% of the county was in drought. However, 2015 became the wettest year on record for Caddo County with precipitation of 1285 mm as recorded by the Fort Cobb Mesonet station in Caddo County, beating the old record set in 1923 by 61 mm (Oklahoma Climatological Survey 2017a).

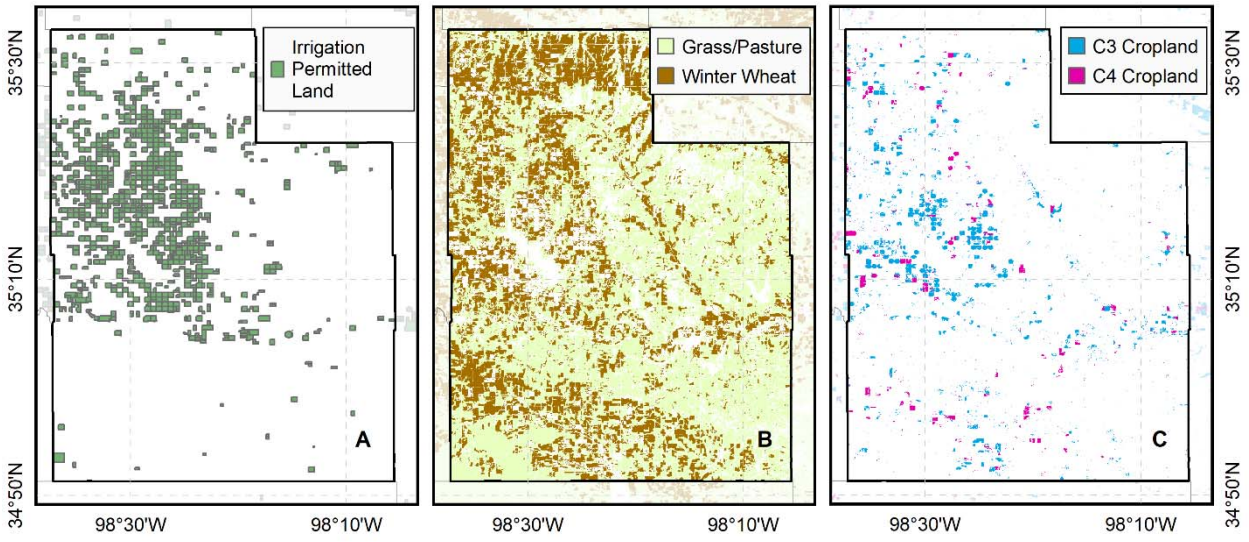

Figure 2.3 | Spatial distribution of (a) irrigation-permitted land, (b) grass/pasture and winter wheat, and (c) C3 and C4 croplands in Caddo County.

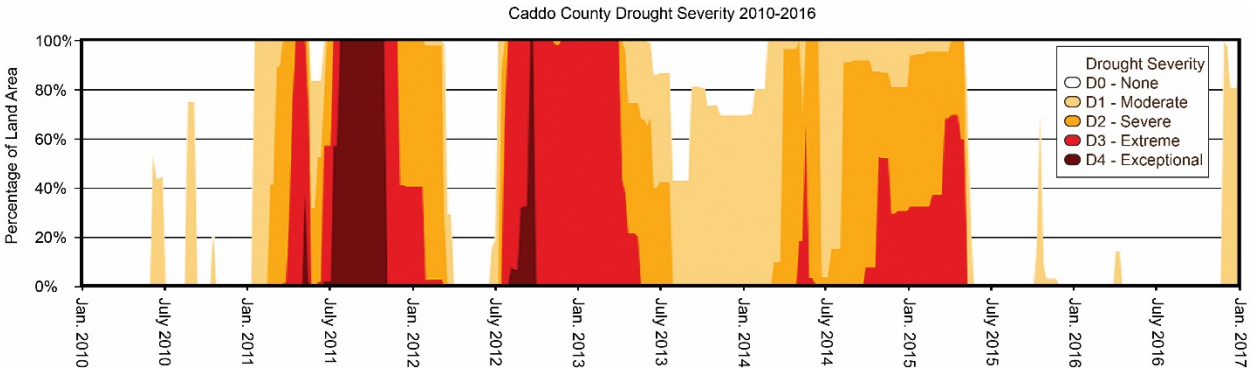

Figure 2.4 | Drought severity for Caddo County and the Upper Washita River Watershed 2010-2016. Adapted from United States Drought Monitor (2017).

The predominant geologic formation in the study area is the Permian-age Rush Springs formation, which is composed of cross-bedded, fine-grained sandstone with some dolomite and gypsum beds ranging from 57 to 91 meters in thickness (Becker and Runkle 1998). Soils in Caddo County are characterized as dark and loamy with clayey to loamy subsoils developed on Permian shales, mudstones, sandstones and/or alluvial deposits under tall grasses (Carter and Gregory 2008).

Caddo County largely overlies the Rush Springs Aquifer, a bedrock aquifer that has provided adequate flow for irrigation in the northern portion of the county. The Rush Springs Aquifer is the second most developed aquifer in the state after the Ogallala Aquifer (Oklahoma Water Resources Board 2012). Some irrigation wells have been reported to produce over 3,785 liters of water a minute, and daily crop irrigation water use (159 million liters) accounts for 77.8% of daily water withdrawals on average (Becker and Runkle 1998). Due to the accessibility of groundwater from the Rush Springs Aquifer and the high density of irrigation-permitted lands, Caddo County ranked third in the state of Oklahoma for area of land permitted for irrigation (438 km^2) as a proportion of the county's total land area (13.1%) in 2016. There were 1062 active permits in the county for irrigation during the 2016 planting season. The total area of land in the

county dedicated to active irrigation permits was 43.5% of the county's total cropland area (1006 km^2) (Oklahoma Water Resources Board 2017).

Natural vegetation types in Caddo County are primarily tallgrass prairie dominated by little bluestem (*Schizachyrium scoparium*) and post oak-blackjack forest (Hoagland 2000; Johnson and Luza 2008). The grasslands classification used in our study includes native prairies, improved pastures, hay fields, and open herbaceous spaces as classified by the Cropland Data Layer (CDL). Average annual temperature and precipitation for Caddo County are 16 ℃ and 816 mm, respectively (Oklahoma Climatological Survey 2017a). Most of the precipitation falls in late spring and early summer, with May and June being the wettest months, and the average growing season is 208 days in length (Oklahoma Climatological Survey 2017b).

Caddo County has been an important contributor to Oklahoma's agricultural industry. In 2016, Caddo County ranked second among all counties in sheep inventory (2,000 head) and third in beef cattle (49,000 head) and hog inventories (60,000 head). The county ranked sixth in acres of cotton (12,600) and sorghum (9,900) planted, eighth in acres of alfalfa harvested (4,300), twelfth in acres of other harvested hay (50,000), and thirteenth in the number of acres planted for wheat (173,500) (United States Department of Agriculture National Agricultural Statistics Service Oklahoma Field Office 2017).

2.2.2 Data and preprocessing methods

2.2.2.1 Cropland Data Layer (CDL) 2010-2016

The Cropland Data Layer (CDL) is produced annually by the United States Department of Agriculture (USDA) to provide acreage estimates to the Agricultural Statistics Board for the state's major commodities. The first CDL dataset became available for Oklahoma in 2007. The spatial resolution of the data layer was 56 m from 2007 to 2009, but beginning in 2010 the resolution was

30 m. Thus, this study uses CDL data from 2010 to 2016 so that interannual comparisons can be made at the same spatial resolution. The overall accuracy of the CDL dataset for Oklahoma ranges from 80.3% in 2014 to 92.2% in 2012, and annual crop-specific accuracies are reported for the dominant crops in Caddo County in Table 2.1 as published in the CDL metadata (https://www.nass.usda.gov/Research_and_Science/Cropland/metadata/meta.php). For a complete list of crop type classifications, see Table S2.1.

Table 2.1. Overall and crop-specific accuracies of the Oklahoma Cropland Data Layer (CDL) 2010-2016 as reported in the CDL metadata. PA is producer's accuracy, and UA is user's accuracy rounded to the nearest 1 percent.

	C3 Crops										C4 Croplands				
Year	Winter Wheat		Cotton		Canola		Alfalfa		Rye		Corn		Sorghum		Overall
	PA	UA	PA	UA	PA	UA	PA	UA	PA	UA	PA	UA	PA	UA	
2010	92	95	89	85	71	96	78	84	67	59	89	90	68	73	84
2011	92	93	79	78	68	91	68	83	57	64	89	90	51	64	83
2012	95	97	92	90	97	94	92	94	80	77	93	97	82	86	92
2013	94	93	80	78	71	84	83	85	64	65	90	85	72	71	83
2014	90	93	93	78	80	71	79	76	69	54	89	89	75	71	80
2015	96	92	86	81	71	92	80	87	48	73	89	91	82	82	86
2016	96	90	87	82	77	98	82	88	54	76	93	92	79	81	85

The CDL dataset incorporates non-agricultural land cover types (e.g., grasslands) from the National Land Cover Database (NLCD), which is updated every 5 years. In 2014, all CDL datasets were recoded by combining Pasture/Grass, Grassland Herbaceous, and Pasture/Hay categories into a single category named Grass/Pasture (United States Department of Agriculture National Agricultural Statistics Service 2017) due to inconsistencies and large margins in error when attempting to break grasslands into different categories (Wickham et al. 2017; Wickham et al. 2013). The CDL Grass/Pasture category for 2010-2013 was derived from the 2006 NLCD, and the Grass/Pasture category for 2014-2016 was derived from the 2011 NLCD (United States Department of Agriculture National Agricultural Statistics Service 2017).

For this study, we grouped the multitude of vegetative land cover types (Table S2.1) into four categories: grasslands, winter wheat, other C3 croplands, and C4 croplands. Pixels in which double-cropping occurred in a year were excluded from the study. Winter wheat was considered separately from the other C3 crops because winter wheat is the dominant cropland type in the region and the crop has a different growing season and irrigation regime relative to other C3 crops. More specifically, winter wheat was expected to respond differently to drought than crops planted in the spring and summer months, which are characterized by high temperatures and low amounts of precipitation. Crops with the C3 photosynthetic pathway were expected to respond differently to water and temperature stress than C4 crops given the greater LUE and WUE of C4 plants (Ehleringer et al. 1997; Epstein et al. 1997).

The spatial distribution of grasslands, winter wheat, other C3 croplands, and C4 croplands for 2016 in Caddo County are illustrated in Fig. 2.3(b,c). According to the 2016 CDL, Caddo County was approximately 49% grassland, 31% cropland, 11% forest and shrubland, 6% developed, 2% fallow and barren, 1% open water, and 0.02% wetland. The county's croplands were dominated by winter wheat, which constituted 85% of the total single-cropland area, with other C3 and C4 crops comprising 11% and 3.5% of the cropland area, respectively. Double-crop systems were 3.4% of the total cropland area. The predominant C3 crops among those classified by the CDL were cotton, canola, alfalfa, and rye. Corn and sorghum were the only C4 crops.

2.2.2.2 Water rights data during 2010-2016

The Oklahoma Water Resource Board (OWRB) provided a geospatial vector dataset that is updated monthly and documents all statewide groundwater and surface water rights permits. Applicants for any type of water right must declare whether water will be used for public water supply, recreation, livestock, irrigation, or some other use. Groundwater right applicants must

dedicate one acre to their water rights permit for each two acre-feet they wish to utilize each year but are not required to report where the water will be used. For groundwater irrigation permits issued after 1973, the well supplying the groundwater must be located on the dedicated land. Thus, it is generally assumed that the water will be used on the land dedicated to the water rights permit due to the added cost of transporting water from its source.

Applicants seeking surface water rights for irrigation, on the other hand, must report the land boundaries in which the water will be used, and they cannot apply for more than 2 acre-feet/year (0.25 hectare-meters/year) of water for each acre they intend to irrigate. Given these rules, we assume that the lands dedicated to a groundwater permit or lands reported as the area of use on a surface water permit accurately reflect the boundary in which irrigation is expected to occur. The OWRB does not actively monitor each permit in the field to assess whether a permit holder is exercising their right to withdraw water, nor do they meter water use due to the extensive cost of obtaining such data. Thus, there is no comprehensive information on who used water or how much water they used in a year.

The OWRB's geospatial vector (polygon) dataset was used to create annual datasets of all active irrigation permits for 2010-2016. For a permit to be listed in an annual dataset, it must meet the following conditions: 1) for new permits, the permit must be granted by the end of the planting season for all non-winter wheat crops (August 1st each year); 2) for existing permits, the permit must not have become inactive or have an expiration date prior to the end of the planting season for all non-winter wheat crops; 3) permits must have a valid issue date (not null); 4) inactive or expired permits must have a valid date of deactivation or expiration (not null); and 5) permits must not be temporary or special. Temporary permits are only valid for 90 days, and special permits are valid for 6 months and cannot be renewed for the same water-use purpose. Thus, these two permit

types were not considered to be reliable, consistent sources of irrigation at large spatial scales and were excluded from the study.

After preprocessing, the annual active irrigation permit database was used to select 500 m pixels that were a majority (>50%) irrigation-permitted grassland, winter wheat, other C3 cropland, or C4 cropland. Pixels representing non-permitted lands were defined as pixels that did not contain any irrigation-permitted land but were a majority (>50%) of one of the four land cover types. These two thresholds ensured that the 500 m pixels were mutually exclusive, and that the same pixel wasn't representative of both irrigation-permitted and non-permitted land. The total number of pixels for each irrigation-permitted and non-permitted land cover type 2010-2016 used in our analyses is reported in Table 2.2.

Table 2.2. The total number of 500 m pixels (samples) used in our study for each irrigation-permitted and non-permitted land cover type 2010-2016.

	2010		2011		2012		2013		2014		2015		2016		Total
Cover Type	Perm.	Non.	Perm.	Non.	Perm.	Non.	Perm.	Non.	Perm.	Non.	Perm.	Non.	Perm.	Non.	Obs.
Grassland	396	6,862	359	6,516	350	6,663	359	6,762	356	6,862	298	6,428	292	6,399	48,902
Winter Wheat	471	1,840	504	2,148	417	2,277	528	2,269	509	1,908	585	2,302	570	2,261	18,589
C3 Cropland	124	154	167	123	196	158	126	115	133	134	135	91	138	89	1,883
C4 Cropland	4	18	12	29	5	32	54	90	15	56	16	48	18	50	447
Total	995	8,874	1,042	8,816	968	9,130	1,067	9,236	1,013	8,960	1,034	8,869	1,018	8,799	69,821

2.2.2.3 Climate data during 2010-2016

The climate data used in this study originated from the Oklahoma Mesonet (https://www.mesonet.org), which is a world-class network of 121 automated environmental monitoring stations. There is at least one Mesonet observation tower in each of Oklahoma's 77 counties, three of which are in Caddo County. We calculated the aridity index (AI) for each year from 1979-2016 using data gathered at the Fort Cobb Mesonet station (Brock et al. 1995; McPherson et al. 2007), which is near the geographic center of Caddo County, using the equation:

$$AI = \frac{P}{PET} \quad (1)$$

where AI is aridity index, P is annual total precipitation, and PET is mean annual potential evapotranspiration (Middleton and Thomas 1992). Annual departures from mean annual precipitation and aridity index for 1979-2016 (Fig. 2.5), as recorded by the Ft. Cobb Mesonet station, illustrate the high variability in climate that is characteristic of our study area.

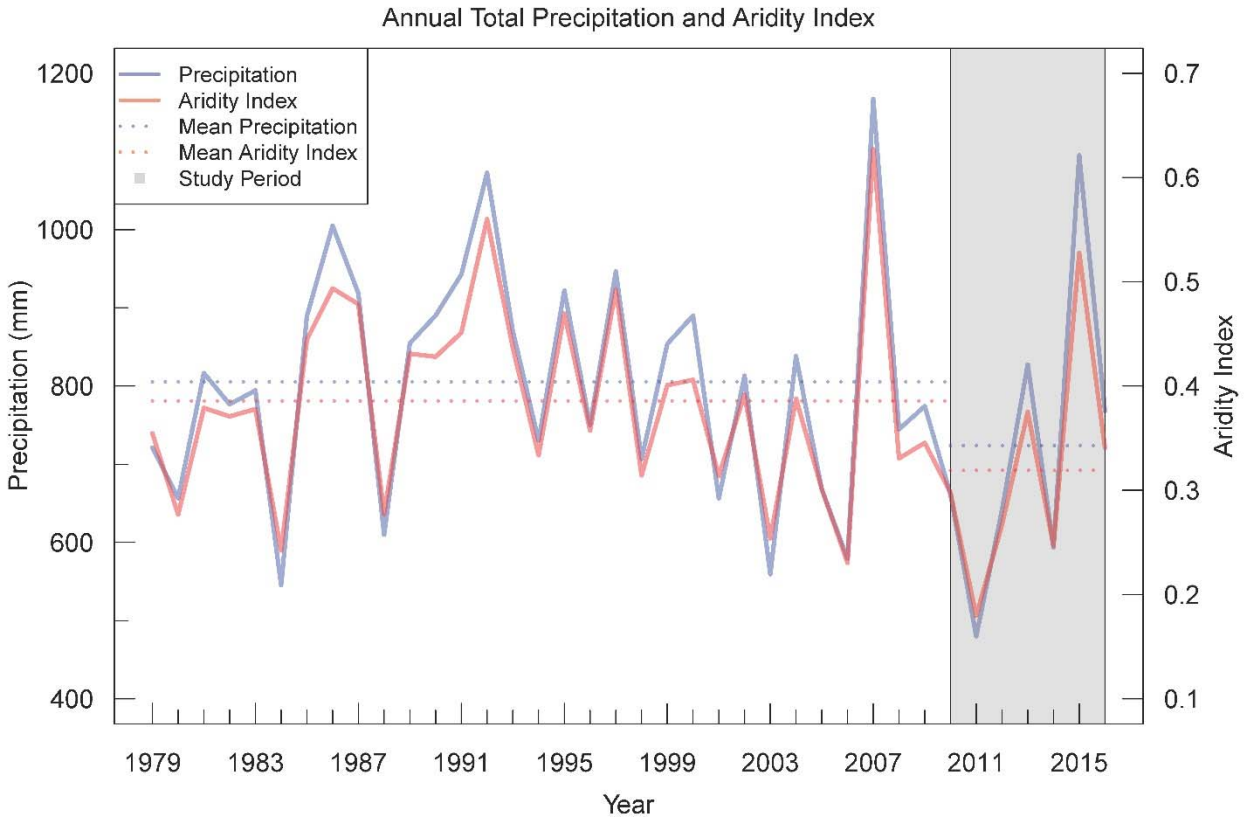

Figure 2.5 | Annual precipitation and aridity index recorded at the Fort Cobb Mesonet station in Caddo County 1979-2016. The shaded area represents the study period 2010-2016 and the dashed lines are the means for their respective period.

For our study period 2010-2016, we identified 2011 as the most arid year, 2015 as the most humid year, and 2013 as a relatively normal year. Thus, for our site level analyses, we defined 2011 as the drought year, 2015 as the pluvial year, and 2013 as a normal year. For our county-

level analyses, we considered the combination of 2010, 2012, 2013, 2014, and 2016 as a baseline to which the 2011 drought and pluvial 2015 could be compared.

2.2.2.4 GPP simulations from the Vegetation Photosynthesis Model during 2010-2016

The Vegetation Photosynthesis Model (Xiao et al. 2004) was used to estimate annual total gross primary production (GPP_{VPM}) for 2010-2016 at 500 m spatial resolution. The model partitions the fraction of absorbed photosynthetically active radiation (*f*PAR) by vegetation into PAR absorbed by chlorophyll ($fPAR_{chl}$) and non-photosynthetic vegetation ($fPAR_{NPV}$) to estimate GPP of vegetation over the growing season. Thus, GPP_{VPM} is a product of $fPAR_{chl}$, PAR, and light-use efficiency (ε_g):

$$GPP_{VPM} = fPAR_{chl} \times PAR \times \varepsilon_g \quad (2)$$

where $fPAR_{chl}$ value is estimated as a function of the Enhanced Vegetation Index (EVI), calculated from spectral data obtained from the space-borne Moderate Resolution Imaging Spectroradiometer (MODIS) platform (Zhang et al. 2016; Zhang et al. 2017a).

The ratio of C3 to C4 plants affects primary production at any given location (Ehleringer et al. 1997; Epstein et al. 1997). Thus, this study calculated average GPP_{VPM} at 8-day intervals for each 500 m MODIS pixel using the ratio of C3/C4 vegetation using the CDL and in-situ derived maximum light-use efficiencies of C3 (0.035 mol CO_2 mol^{-1} PAR) and C4 (0.0525 mol CO_2 mol^{-1} PAR) plants as detailed by Zhang et al. (2017a). Thus, GPP_{VPM} for each pixel was calculated as:

$$GPP_{VPM} = \sum_i f_i \times \varepsilon_i \times fPAR_{chl} \times PAR \quad (3)$$

where f_i and ε_i are the area fraction and light-use efficiency, respectively, for C3 and C4 croplands. Annual GPP_{VPM} was calculated from the 8-day dataset by multiplying each year's multi-day average observation by the number of days observed and summing the totals.

2.2.2.5 MOD17 GPP dataset during 2010-2016

The 8-day, 500 m GPP_{MOD17} data used in this study was from the MOD17A2H version 6 product (Running et al. 2004). The version 6 product has been improved by using updated Biome Property Look Up Tables (BPLUT) and an updated version of the daily Global Modeling and Assimilation Office (GMAO) meteorological data (Running and Zhao 2015). The GPP_{MOD17} product also uses a LUE model to estimate GPP. The primary difference between GPP_{MOD17} and GPP_{VPM} is that GPP_{MOD17} uses $FPAR_{canopy}$, which is calculated as the fraction of photosynthetically active radiation absorbed by the canopy (Running et al. 2004), whereas GPP_{VPM} uses $FPAR_{chl}$, which is the fraction of photosynthetically active radiation absorbed by chlorophyll (Xiao et al. 2004). GPP_{MOD17} uses the $FPAR_{canopy}$ data product (MOD15A2H) and GPP_{VPM} uses $FPAR_{chl}$ estimated from the enhanced vegetation index (EVI).

2.2.2.6 *In-situ* GPP data from eddy covariance towers

GPP data from two Integrated Grassland Observation Sites (iGOS), iGOS-East (35.54865° N, 98.03759° W) and iGOS-West (35.54679° N, 98.04529° W), and data from the Integrated Cropland Observation System (iCOS) (35.56850° N, 98.05580° W) were used to evaluate GPP_{VPM} and GPP_{MOD17}. These three flux towers are located at the United States Department of Agriculture's Agricultural Research Service (USDA-ARS) Grazinglands Research Laboratory (GRL) in El Reno, Oklahoma. iGOS-East is a native tallgrass prairie, iGOS-West is an old world bluestem (*Bothriochloa caucasica* C. E. Hubb.) pasture that is bailed and grazed by cattle throughout the year (Zhou et al. 2017a), and iCOS is a single-crop winter wheat site.

These three sites use Li-COR 7500 open path gas analyzer and a CSAT3 sonic-anemometer to measure the net ecosystem exchange of CO_2 between land and the atmosphere (NEE). The measured NEE was first gap-filled and then partitioned into GPP and ecosystem respiration (ER)

based on the short-term temperature sensitivity of ER (Lloyd and Taylor 1994; Reichstein et al. 2005). The partitioned half-hourly GPP data was summed to get daily GPP, which was converted into 8-day means to match the temporal resolution of GPP_{VPM} and GPP_{MOD17} data. Our study utilized all years for which GPP data was available from the three towers (GPP_{EC}). The GPP_{EC} data were available for the entire years of 2015 and 2016 for iGOS-East; 05/08/2014 – 12/31/2014, 01/08/2015 – 10/25/2015, and the entire year 2016 for iGOS-West; and the entire year 2015 and 01/01/2016 – 9/30/2016 for iCOS. Simple linear regression analyses were conducted between GPP_{VPM} and GPP_{EC}, and between GPP_{MOD17} and $GPP_{EC,}$ for each tower site in each year to assess the accuracy of GPP_{VPM} and GPP_{MOD17}.

2.2.3 Statistical Data Analyses

Eight 500 m pixels from the GPP_{VPM} dataset were chosen from within the study area to illustrate field-scale seasonal dynamics and interannual variation of GPP during the 2011 drought, normal 2013, and pluvial 2015. One pixel was chosen for each of the irrigation-permitted and non-permitted land cover types (grassland, winter wheat, other C3 croplands, and C4 croplands). We made these choices by first filtering potential sites by determining which lands had the same vegetative cover in each of the three years by using the CDL datasets for 2011, 2013, and 2015. Next, we calculated the percentage cover of each land type using a fishnet of 500 m pixels and selected those pixels that had the highest amount of cover. The irrigation-permitted C3 crop pixel was a cotton field, and the non-permitted C3 crop pixel was alfalfa. Both C4 pixels were corn fields.

For each permitted and non-permitted land cover type, we computed the percentage departure of GPP during the 2011 drought and pluvial 2015 from the 5-year reference mean using the following steps. First, we calculated mean GPP for the reference years by averaging annual

GPP from 2010, 2012, 2013, 2014, and 2016. Second, annual GPP for the 2011 drought and pluvial 2015 was calculated. Third, the 5-year reference mean was subtracted from mean annual GPP in 2011 and 2015 to calculate the deviation from the mean. Finally, the resultant differences between annual GPP in 2011 and 2015 and the mean annual GPP during the reference years were divided by the 5-year reference mean to compute the percentage departure from the 5-year reference mean.

Permitted and non-permitted sample sizes for each plant type in each year were independent, unequal, and assumed to have unequal variances. Thus, to determine whether the departure from the 5-year reference mean in 2011 or 2015 was statistically significant, a Welch's two-sample t-test (Delacre et al. 2017; Ruxton 2006) was performed for each irrigation-permitted and non-permitted land cover type (Table S2.2). Welch's two-sample t-tests were also conducted to explore whether there was a significant difference between GPP in the 2011 drought or pluvial 2015 for irrigation-permitted and non-permitted lands of each land cover type (Tables S2.3, S2.4).

2.3 Results

2.3.1 A comparison of GPP_{VPM}, GPP_{MOD17}, and GPP_{EC} at the three eddy flux tower sites during 2014-2016

GPP_{VPM} more accurately estimated mean daily GPP_{EC} at each of the three GRL sites than GPP_{MOD17}. More specifically, GPP_{VPM} had less underestimation and greater R^2 values than GPP_{MOD17} (Fig. 2.6). The VPM model performed best at the native prairie site (iGOS-East), where GPP_{VPM} slightly underestimated GPP_{EC} in 2015 and 2016. Performance at the winter wheat site (iCOS) was similar with slight under estimations of GPP_{EC} in both 2015 and 2016. GPP_{VPM} had larger underestimations of GPP_{EC} at the old world bluestem site (iGOS West) relative to the other two sites, but GPP_{VPM} had a greater ability to predict GPP_{EC} than GPP_{MOD17} at each site. The close

correlation between GPP_{VPM} to GPP_{EC} at eddy tower sites near our study area indicated that GPP_{VPM} was suitable for use at larger spatial scales.

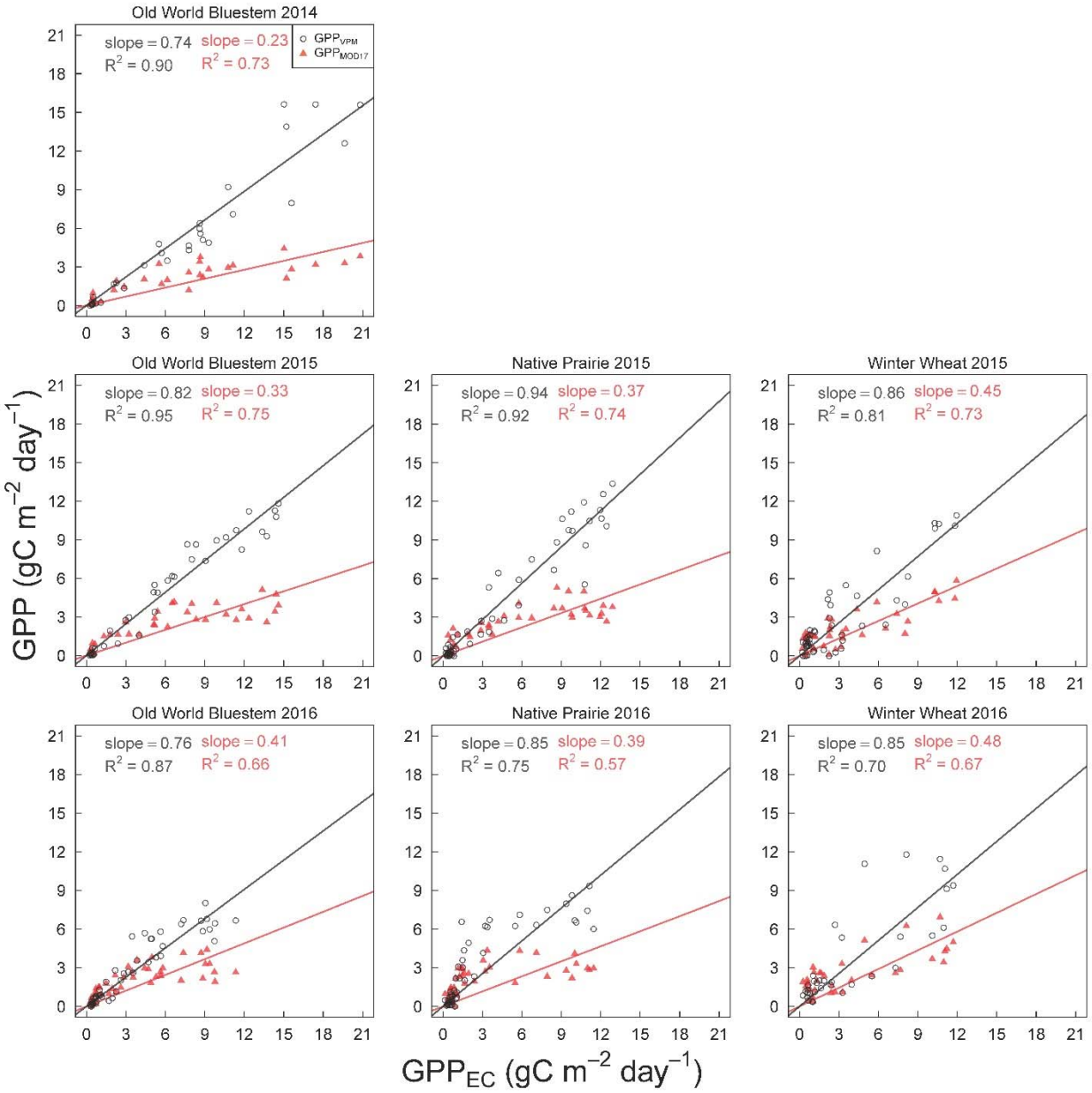

Figure 2.6 | Simple linear regression of GPPEC/GPPVPM and GPPEC/GPPMOD17 at the old world bluestem (iGOS-West), native prairie (iGOS-East), and winter wheat (iCOS) sites in Oklahoma.

The seasonal dynamics and interannual variations of GPP_{EC}, GPP_{VPM}, and GPP_{MOD17} were illustrated in Fig. 2.7. At the old world bluestem site, GPP_{VPM} underestimated GPP_{EC} throughout

most of the 2014, 2015, and 2016 growing seasons. GPP_{VPM} underestimated GPP_{EC} during the early growing season in 2015 at the native prairie site, but overestimated GPP_{EC} during the early growing season in 2016. In both years, GPP_{VPM} tended to overestimate GPP_{EC} near the end of the growing season. At the winter wheat site, GPP_{VPM} tracked GPP_{EC} well in both years, but GPP_{VPM} was phase shifted, which indicated that there might be some type of lag effect. This lag effect is evident to a greater degree for GPP_{MOD17}, especially in 2016 when the peaks for both GPP_{MOD17} and GPP_{VPM} occurred well after the peak in GPP_{EC}.

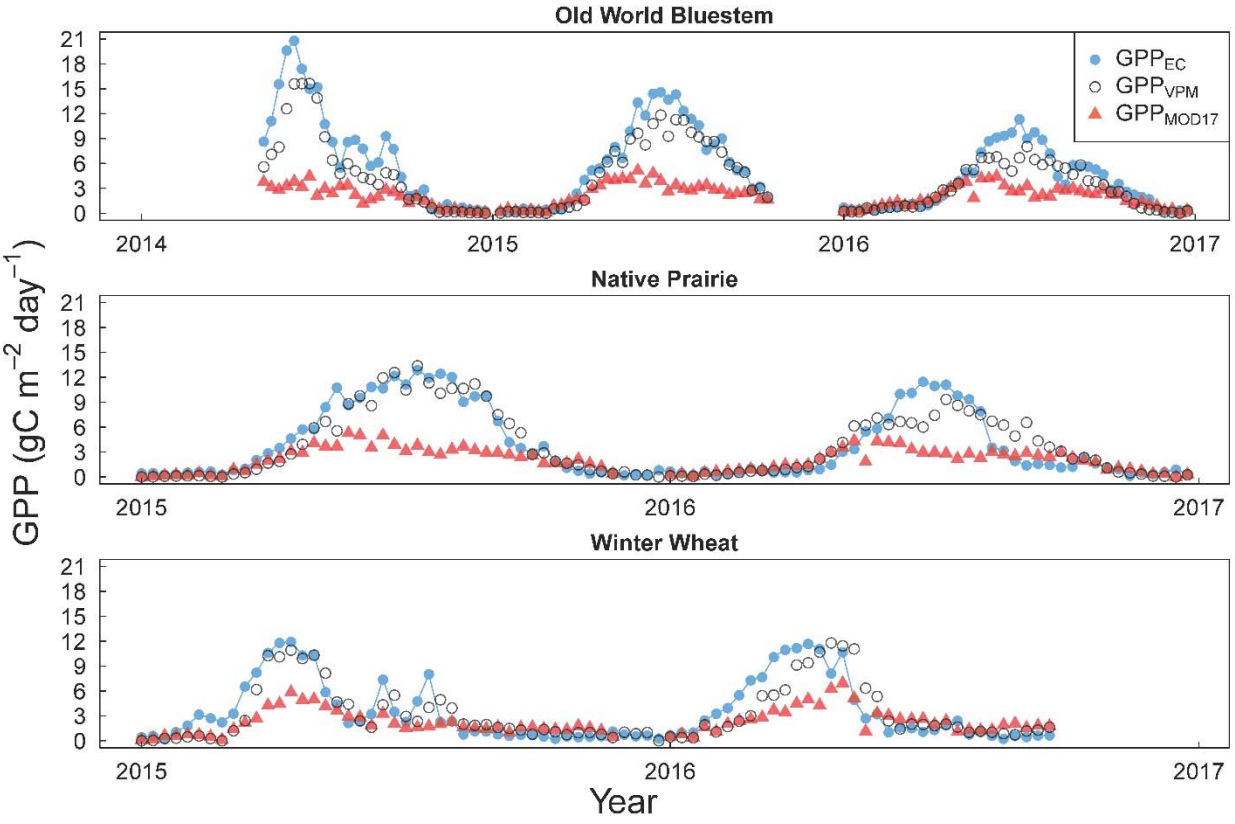

Figure 2.7 | Eight-day seasonal dynamics and interannual variations of tower-based (GPPEC), VPM-modeled (GPPVPM), and MODIS-modeled (GPPMOD17) gross primary production at the old world bluestem (iGOS-West), native prairie (iGOS-East), and winter wheat (iCOS) sites

2.3.2. Seasonal dynamics and interannual variation of GPP at selected irrigation-permitted and non-permitted sites during 2011 drought, normal 2013, and pluvial 2015

The seasonal dynamics and interannual variation of 8-day mean GPP_{VPM} for eight selected pixels in pair-wise comparison (with irrigation permit, without irrigation permit) are illustrated in Fig. 2.8. For all eight pixels, regardless of water rights, the 2011 drought caused a shortened growing season with lower mean GPP relative to 2013. Conversely, the growing season of all the sites was prolonged in pluvial 2015 and had higher mean GPP than normal.

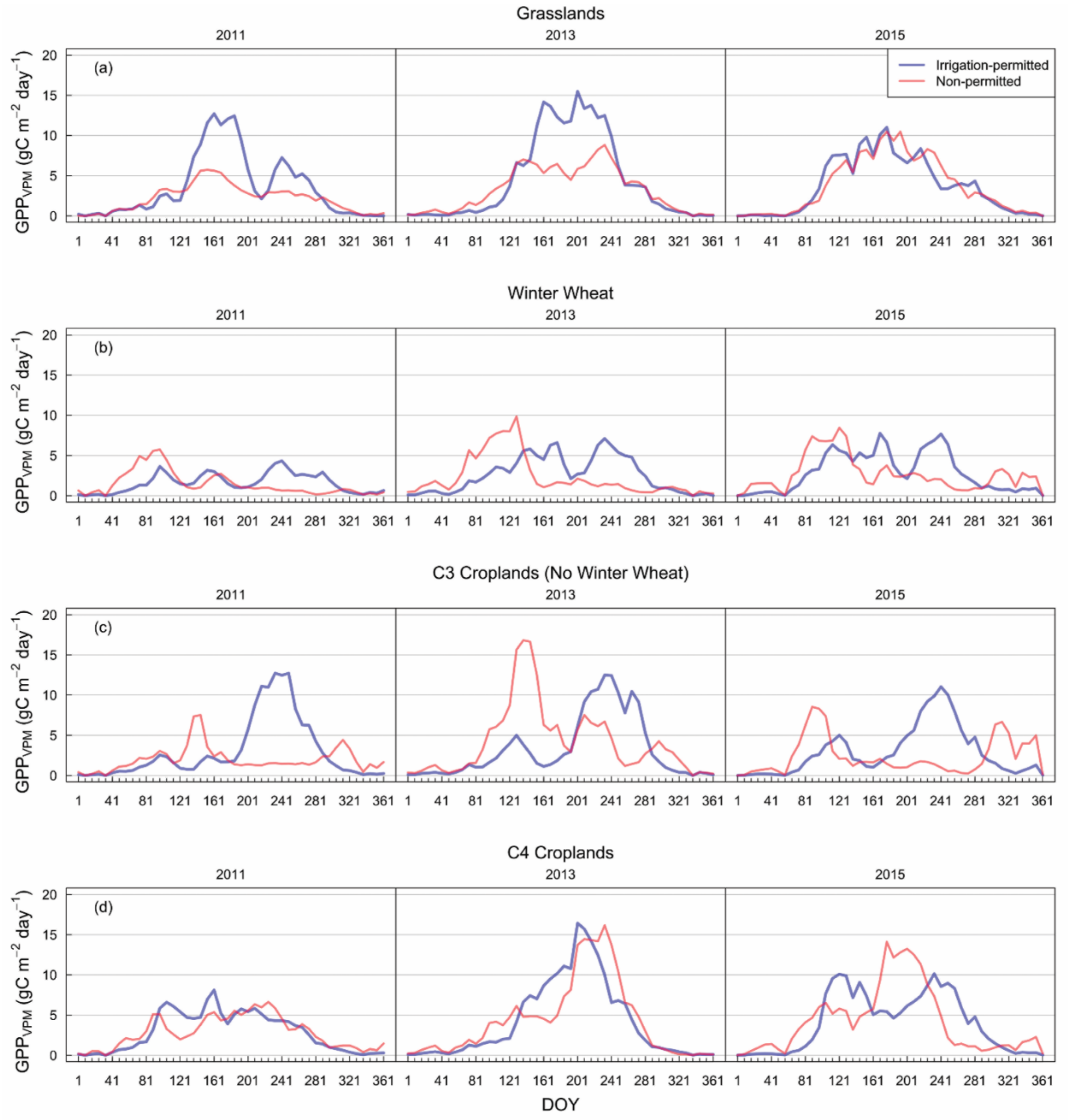

Figure 2.8 | Pixel-level, 8-day GPPVPM for irrigation-permitted and non-permitted (a) grasslands, (b) winter wheat, (c) other C3 croplands, and (d) C4 croplands in 2011 drought, normal 2013, and pluvial 2015.

The irrigation-permitted grassland field had substantially higher mean GPP_{VPM} during the growing season in 2011 and 2013 than the non-permitted grassland field, but the trends in GPP_{VPM} for these two fields are extremely similar in pluvial 2015 (Fig. 2.8(a)). Irrigation clearly affects the

cropping intensity in the winter wheat pixels (Fig. 2.8(b)). For the pixel without an irrigation permit, only winter wheat crop was cultivated during the year, with a peak in GPP_{VPM} in mid-April and a harvest in June. For the winter wheat pixel with an irrigation permit, a summer crop rotation was implemented. The seasonal dynamics of GPP also suggested that winter wheat was grown for grain production in 2013 and 2015 but might be grazed in 2011. As for other C3 cropland pixels, the irrigation-permitted cotton site had peak GPP_{VPM} in mid-September with a growing season between mid-July and late October (Fig. 2.8(c)). GPP_{VPM} in the non-permitted alfalfa field peaked in the spring. We expected a greater difference in the magnitude of GPP_{VPM} for the two C4 cropland pixels in 2011 and 2013 (Fig. 2.8(d)). The similarity in the trend and magnitude of GPP_{VPM} at these two sites during the drought and normal year suggested that the farmer with an irrigation permit might not have irrigated in these years. In 2015, the irrigation-permitted C4 site had peaks in the spring and again in the fall, which suggested that the site was double cropped, whereas GPP for the non-permitted C4 site had a peak in mid-summer signaling a single crop. The interannual variation of GPP_{VPM} over these eight pixels was clearly due to the complexity of decision making and practice for irrigation, cropping intensity, and crop types.

2.3.3. County-scale responses of GPP_{VPM} in drought and pluvial years during 2010-2016

GPP_{VPM} for all land cover types were significantly reduced by the 2011 drought, except for irrigation-permitted C4 croplands (Fig. 2.9). As for pluvial 2015, grasslands, winter wheat, and non-permitted C3 croplands experienced significant gains in GPP_{VPM} relative to the 5-year reference mean, but the response of GPP_{VPM} for permitted C3 croplands and non-permitted C4 croplands was insignificant. Irrigation-permitted C4 crops were the only land cover type to have a significant reduction in GPP during pluvial 2015. Irrigation-permitted croplands (winter wheat, other C3 croplands, and C4 croplands) had significantly higher mean annual GPP than non-

permitted croplands in the 2011 drought, pluvial 2015, and across all years in the study period (Fig. 2.10).

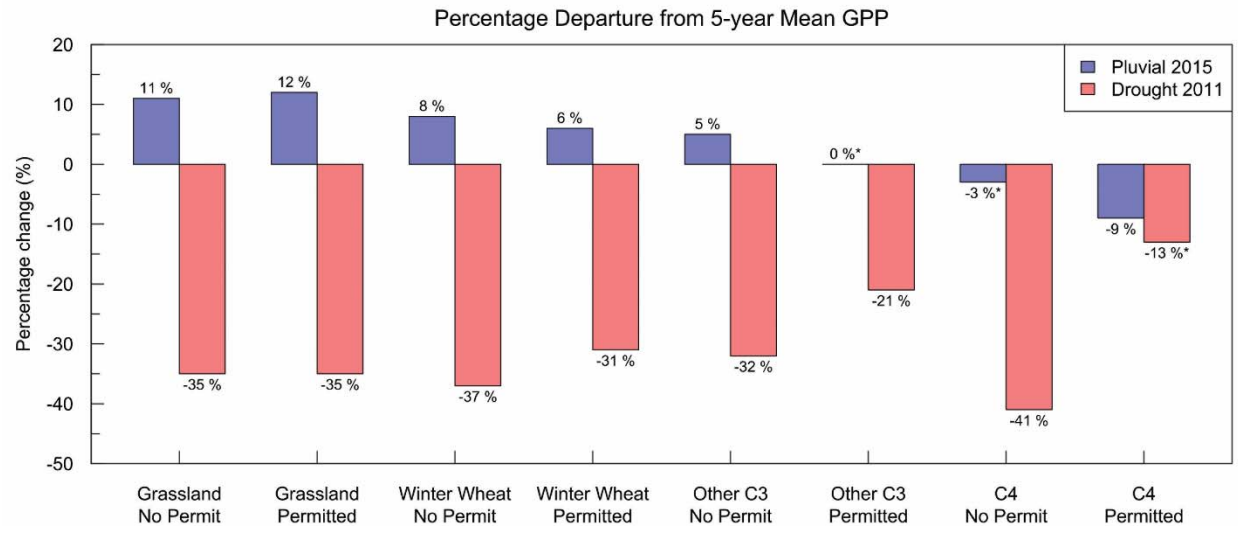

Figure 2.9 | Percentage departure of GPPVPM from the 5-year reference mean for irrigation-permitted and non-permitted grasslands and croplands during the 2011 drought and pluvial 2015 in Caddo County. The percentage departure calculations and p-values for the 2011 drought and pluvial 2015 were reported in Table S2.3 and Table S2.4, respectively. *Not significant.

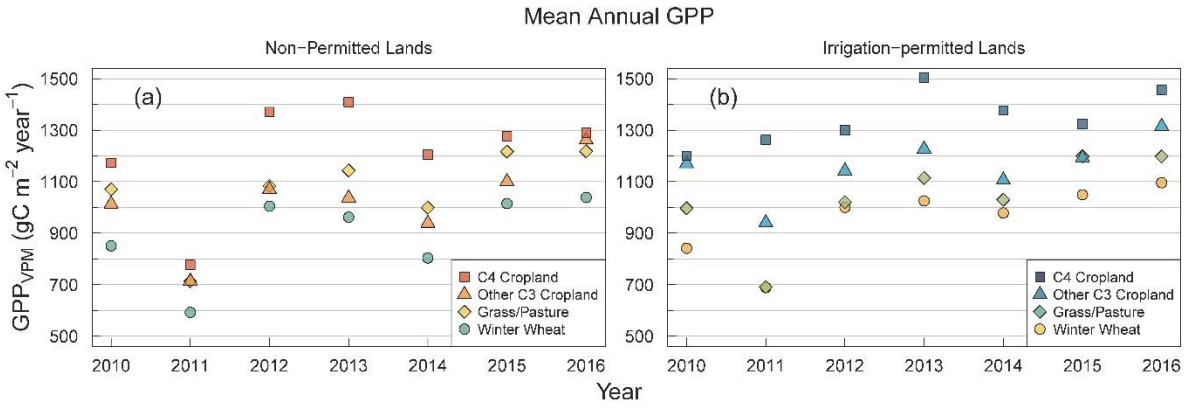

Figure 2.10 | Mean annual GPP for (a) non-permitted and (b) irrigation-permitted grasslands and croplands in Caddo County 2010-2016.

For the 2011 drought, irrigation-permitted and non-permitted grasslands had similar significant negative departures from the 5-year reference mean (Fig. 2.11(a)). Likewise, irrigation-permitted and non-permitted grasslands had similar gains in mean GPP for pluvial 2015 relative to the 5-year reference mean. These percentage gains in GPP for pluvial 2015 were the highest

among all land cover classes. Interestingly, non-permitted grasslands had slightly higher mean GPP in the 2011 drought (22 gC m^{-2} $year^{-1}$), in pluvial 2015 (18 gC m^{-2} $year^{-1}$), and for the entire study period (36 gC m^{-2} $year^{-1}$) than grasslands permitted for irrigation ($p < 0.05$). Fig. 2.11(a) also illustrates that GPP for non-permitted lands are relatively normally distributed, whereas GPP for irrigation-permitted grasslands tend to be right-skewed during the 2011 drought.

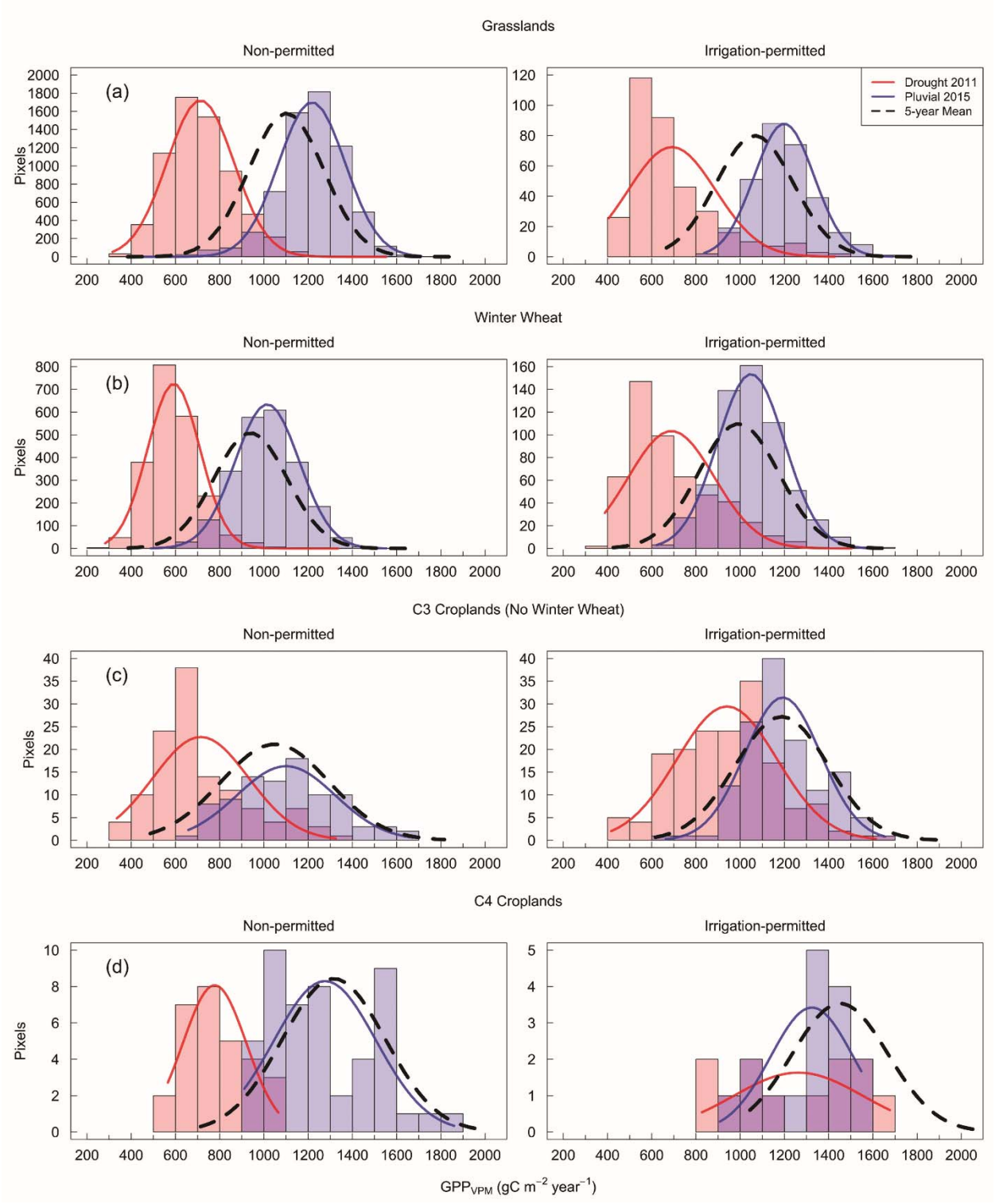

Figure 2.11 | Responses of GPP to the 2011 drought and pluvial 2015 in Caddo County for irrigation-permitted and non-permitted (a) grasslands, (b) winter wheat, (c) other C3 croplands, and (d) C4 croplands. All responses are significantly different ($p < 0.05$) from the 5-year reference

mean, except for C3 irrigation-permitted croplands in 2015, C4 non-permitted croplands in 2015, and C4 irrigation-permitted croplands in 2011 (Table S2.3, S2.4).

Reductions in mean annual GPP during the 2011 drought for irrigation-permitted winter wheat were significantly less than that of non-permitted winter wheat (Fig. 2.11(b)). For pluvial 2015, non-permitted winter wheat had larger increases in GPP relative to the 5-year reference mean (8%) than irrigation-permitted winter wheat (6%). Like grasslands, Fig. 2.11(b) reflects a normal distribution of GPP for winter wheat, except for the 2011 drought when GPP is right-skewed for lands permitted for irrigation.

The 2011 drought had a significant impact on GPP for irrigation-permitted and non-permitted C3 croplands relative to the 5-year reference mean (Fig. 2.11(c)), but the response of GPP for irrigation-permitted C3 croplands in pluvial 2015 was not significant and for non-permitted the response was a marginal increase (5%). The distribution of GPP for irrigation-permitted and non-permitted C3 croplands are relatively normal, except for non-permitted C3 croplands during the 2011 drought which is right-skewed. This abnormal distribution could be caused by differences in how various C3 crop types, such as cotton and alfalfa, respond to drought and/or differences in their growing seasons.

GPP of irrigation-permitted and non-permitted C4 croplands responded very differently to the 2011 drought (Fig. 2.11(d)). Of all land cover types, non-permitted C4 croplands had the highest percentage drop in GPP from the 5-year reference mean during the 2011 drought, whereas irrigation-permitted C4 croplands had no statistically significant change in mean GPP. There was no significant difference between mean GPP in pluvial 2015 and the 5-year reference mean for non-permitted C4 croplands, but C4 irrigation-permitted croplands experienced a decrease in GPP.

2.4 Discussion

2.4.1 Impacts of the 2011 drought on GPP for irrigation-permitted and non-permitted lands

A majority of the irrigation permits in the study area were for groundwater, a water source that is buffered from the effects of drought relative to surface water resources. If our study areas had been in areas irrigated mostly or solely by surface water, then the buffering effect of irrigation during drought may have been muted. For Caddo County, all lands dedicated to irrigation permits tended to have higher productivity than non-irrigated lands during the 2011 drought, except for grasslands.

Responses of GPP for irrigation-permitted and non-permitted grasslands to drought and pluvial conditions were extremely similar at the county scale (Fig 11(a)). These grasslands could be former croplands on which irrigation occurred in the past, or perhaps some landowners have incorporated pasture and/or grazing into their rotation. The similarity in mean annual GPP for irrigation-permitted and non-permitted grasslands, and the similar response to drought and pluvial conditions, could occur if many of the land owners did not exercise their right to irrigate. This hypothesis appears plausible, given that our site-level analysis demonstrated that GPP_{VPM} captured increased GPP for the irrigation-permitted site during the 2011 drought and normal 2013, and that irrigation was unnecessary in 2015 given the record rainfall totals (Fig. 2.8(a)).

There are a couple of possible explanations as to why landowners would not exercise their water right on grass or pasture lands. First, market prices could discourage irrigation in that it may not be profitable to irrigate grasslands because the cost of irrigation is not offset by added profits gained from enhanced grass (hay) production. Second, many of the landowners with irrigation permits for grasslands might be raising cattle on that land, which is an agricultural system that may

not benefit from irrigation. For instance, studies have shown that grazing cattle on irrigated lands necessitates intensive management (Volesky and Clark 2003), and that calf gain-weight is higher per acre for dry lot grazing than irrigated pasture grazing (Dunn and Olson 2009).

As for winter wheat, some studies have shown that irrigation can boost winter wheat harvests, but only when applied in certain amounts shortly before or after planting and/or before harvest if the soil is dry (Eck 1988; Musick and Lamm 1990; Peck 1979). In fact, irrigation can be a risk to winter wheat productivity, especially in the winter months when the crop is dormant (Yonts et al. 2009). Over-irrigation can cause lodging, leaf rust, or mildew (Al-Kaisi and Shanahan 1999; Bennett 1984; Roelfs 1992). Thus, it is possible that winter wheat croplands dedicated to irrigation permits are not necessarily irrigated every year. Rather, access to irrigation for these landowners may afford them an opportunity to double-crop in certain years when weather and commodity prices create favorable conditions (MacKown et al. 2007; Shapiro et al. 1992), or to boost winter wheat yields in years when soil moisture is low.

Expectedly, irrigation-permitted C3 and C4 croplands had smaller reductions in mean annual GPP during the 2011 drought than their non-permitted counterparts. However, our results indicate that the percentage reduction in GPP in 2011 from the 5-year mean was greater for non-permitted C4 croplands than non-permitted grassland, winter wheat, and other C3 croplands. This result was unexpected given, as previously discussed, that C4 plants have a higher light use efficiency, greater water use efficiency, and are more drought-resistant than C3 plants. However, although maize is a C4 plant, it has been shown to be sensitive to high temperature, particularly during tassel, pollination, and grain fill (Kim et al. 2007; Muchow 1990; Muchow et al. 1990). C4 croplands may have suffered a greater reduction in mean GPP due to stressors in addition to the

drought. For example, management practices such as fertilization, planting date, or tilling may have exacerbated the impact of the drought for these non-permitted C4 croplands.

As previously mentioned, the Oklahoma Water Resources Board (OWRB) does not require water meters for groundwater or surface water use. Thus, water managers don't know exactly who has used water or how much water was used. However, future studies may be able to determine which lands were irrigated by monitoring intra-annual and interannual changes in GPP. We demonstrated in our study that the interannual changes in GPP were significantly different for irrigation-permitted and non-permitted croplands, especially during drought (Table S2.2). Thus, the irrigation-permitted pixels with substantially less annual total GPP than the mean might be considered as non-irrigated lands and those pixels with substantially more GPP than the mean might signal that a landowner was fully utilizing their water permit. Likewise, if the GPP of a pixel during drought is marginally or not significantly different than the GPP of that pixel during non-drought years, then the marginal change in GPP could signal irrigation.

2.4.2 Impacts of pluvial 2015 on GPP for irrigated and non-irrigated lands

It is not known why mean GPP for non-permitted grassland was slightly higher than irrigation-permitted grassland in 2011, 2015, and the entire study period ($p < .05$) (Table S2.2). Land management practices, such as grazing, bailing, fertilization, and burning can not only influence GPP directly (Fischer et al. 2012; Zhou et al. 2017a), but alter community species composition (Ewing and Engle 1988; Kelting 1954; Mitchell et al. 1996; Niu et al. 2013). As previously discussed, it is likely that non-permitted lands are more often grazed by livestock than those lands that are permitted for irrigation. However, it does not seem likely that grazing promoted GPP for these land types as several studies have shown grazing can inhibit overall GPP (Oates and Jackson 2014; Rogiers et al. 2005), that the effect of grazing on GPP is negligible (Senapati et al.

2014), or that increases in GPP are temporary (Zhang et al. 2015). Nevertheless, grasslands experienced the largest percentage gains in mean annual GPP than the other land cover types, which reflected the year-long growing season of grassland systems.

Irrigation-permitted C4 croplands were the only land cover type to exhibit a significant decrease in GPP during pluvial 2015. The decrease might be attributed to a saturation of soil water content above what is beneficial to the growth of C4 crops due to excessive rainfall, leaching of nitrates beyond the root zone, or the timing of rainfall. For example, a study of drip-irrigated corn (*Zea mays* L.) by Payero et al. (2008) found that over-irrigated treatments could dramatically reduce water use efficiency (WUE), aboveground dry biomass, and grain yield. Irrigation and fertilization techniques can minimize leaching of nitrates out of the root zone (Gheysari et al. 2009; Sexton et al. 1996), but with record-breaking rainfall in 2015 such techniques might not have been possible to implement. Also, persistent cloud cover may have reduced photosynthetically active radiation in the month of May, which would have interfered with the early growth of corn and sorghum.

2.4.3 Implications of irrigation for carbon budgets and food security

This study indicates that irrigation may buffer reductions in terrestrial carbon uptake due to drought and increased asynchronousity between precipitation and temperature. Results also indicate, at the landscape scale, that C4 croplands can respond differently to drought than grasslands, winter wheat, and other C3 croplands. Such drought responses could provide additional insight into why Wolf et al. (2016) found little annual change in the terrestrial uptake of carbon during the 2012 North American drought. In consideration of overall greenhouse gas (GHG) emissions, however, irrigation also plays a role in soil organic carbon fluxes, and the emission of methane (CH_4) and nitrous oxide (N_2O) (Lal 2004; Snyder et al. 2009; Trost et al. 2013).

Clearly, plants are more productive in arid conditions when they are irrigated. Although groundwater is often considered a renewable resource, Earth's groundwater resources are being depleted faster than they are being recharged (Wada et al. 2010). For example, between 2001-2016 the groundwater levels of the Rush Springs Aquifer and the Ogallala Aquifer (an important groundwater resource for 8 midwestern states) declined by 3 m and 5.8 m, respectively (Khand et al. 2017). Our analysis provides insight into how the productivity of irrigated grasslands and croplands, and how their responses to drought and pluvial events, may change in the future if groundwater resources were to become inaccessible due to depletion, pollution, or technological limitations.

2.4.4 Socioecological insights

Some farmers in the United States are uncertain about Earth's changing climate. For instance, Arbuckle et al. (2013) reported that out of a survey of almost 5,000 corn farmers, 31% of respondents were uncertain if climate change is occurring. Using the same survey data, Mase et al. (2017) noted that only 16% of corn farmers report that changing weather patterns are hurting their farm operation. However, our results indicate that farmers' experiences in a changing climate might be influenced by the type of crop they plant and their water rights. Farmers with groundwater irrigation rights may not be experiencing drought, pluvial conditions, increased climate variability, and a changing climate like those with no groundwater access.

For instance, our study indicates that non-permitted C4 croplands experienced the largest percentage decrease in GPP during the 2011 drought compared to grasslands and other cropland types, but irrigation-permitted C4 crops did not experience a significant decline in GPP. Thus, generalizations about farmers that plant the same crop type, such as corn, or pooled responses from a diverse group of crop producers (Rejesus et al. 2013), might be an oversimplification. Ongoing

and future surveys of farmers would be more useful if land management practices, such as water use, grazing, fertilization, rotations, harvest, and burning, were paired with geospatial information like precipitation, temperature, and water availability. For example, such information may allow us to further understand why some farmers don't 'believe' in climate change, although there is little disagreement on what science knows about climate change (Kahan 2015; Kahan et al. 2012). This additional survey data information can shed new insight into what has shaped farmers' cultural identity in regards to climate change (Kahan 2016; VanWinkle and Friedman 2017).

2.5 Conclusion

Gross primary production of grasslands and croplands respond differently to drought and pluvial conditions. How a certain crop type responds to drought depends on whether the land owner has access to irrigation. This study found that vegetation on irrigation-permitted lands in Caddo County had higher mean GPP during the drought and less variable, more stable GPP during the study period 2010-2016. Responses of GPP for irrigation-permitted and non-permitted grasslands to drought and pluvial conditions were extremely similar, indicating that landowners were likely not exercising their right to irrigate grasslands. Caution should be used when assessing or generalizing how a specific crop species responds to climate variability, drought, and pluvial conditions in the absence of irrigation-related data. Future research into the effect of a changing climate on terrestrial vegetation should not only consider the ratio of C3 and C4 species in grasslands or whether a crop species is C3 or C4, but also consider whether the vegetation is irrigated or not. Thus, it is important to gather geospatial information on irrigation permits, irrigation practices, and the amount of irrigation water used.

2.6 Supplementary materials

Table S2.1. Cropland Data Layer (CDL) crop type classifications for Oklahoma 2010-2016. The inclusion of a crop type classification on this list doesn't necessarily indicate that the crop type

was detected. ‘Yes’ indicates that the crop type classification was included in the CDL that year, and ‘No’ indicates that the crop type classification was not included.

Crop Type	Photosynthetic Pathway	2010	2011	2012	2013	2014	2015	2016
Corn	C4	Yes	Yes	Yes	Yes	Yes	Yes	Yes
Cotton	C3	Yes	Yes	Yes	Yes	Yes	Yes	Yes
Sorghum	C4	Yes	Yes	Yes	Yes	Yes	Yes	Yes
Soybeans	C3	Yes	Yes	Yes	Yes	Yes	Yes	Yes
Sunflower	C3	Yes	Yes	Yes	Yes	Yes	Yes	Yes
Peanuts	C3	Yes	Yes	Yes	Yes	Yes	Yes	Yes
Sweet Corn	C4	Yes	Yes	Yes	Yes	Yes	Yes	Yes
Barley	C3	Yes	Yes	Yes	Yes	Yes	Yes	Yes
Durum Wheat	C3	No	Yes	No	Yes	No	Yes	No
Spring Wheat	C3	No	Yes	Yes	Yes	Yes	Yes	Yes
Winter Wheat	C3	Yes	Yes	Yes	Yes	Yes	Yes	Yes
Rye	C3	Yes	Yes	Yes	Yes	Yes	Yes	Yes
Oats	C3	Yes	Yes	Yes	Yes	Yes	Yes	Yes
Millet	C3	Yes	Yes	Yes	Yes	Yes	Yes	Yes
Speltz	C3	No	No	No	No	No	No	Yes
Canola	C3	Yes	Yes	Yes	Yes	Yes	Yes	Yes
Safflower	C3	Yes	Yes	Yes	Yes	No	No	Yes
Alfalfa	C3	Yes	Yes	Yes	Yes	Yes	Yes	Yes
Non-alfalfa Hay	C3	No	No	No	Yes	Yes	Yes	Yes
Dry Beans	C3	Yes	Yes	Yes	Yes	No	Yes	Yes
Potatoes	C3	No	No	No	Yes	Yes	No	Yes
Other Crops	C3	Yes	Yes	Yes	Yes	Yes	Yes	Yes
Watermelons	C3	Yes	Yes	Yes	Yes	Yes	Yes	Yes
Peas	C3	Yes	Yes	Yes	Yes	Yes	Yes	Yes
Herbs	C3	Yes	Yes	Yes	Yes	Yes	Yes	Yes
Clover/Wildflowers	C3	Yes	Yes	Yes	Yes	Yes	Yes	Yes
Sod/Grass Seed	C3	No	No	No	Yes	Yes	Yes	Yes
Switchgrass	C4	Yes	Yes	Yes	Yes	No	No	No
Fallow/Idle Cropland	C3	Yes	Yes	Yes	Yes	Yes	Yes	Yes
Peaches	C3	Yes	Yes	Yes	Yes	Yes	Yes	Yes
Christmas Trees	C3	No	No	No	No	No	No	Yes
Grapes	C3	No	No	No	Yes	No	No	No
Pecans	C3	Yes	Yes	Yes	Yes	Yes	Yes	Yes
Triticale	C3	Yes	Yes	Yes	Yes	Yes	Yes	Yes
Peppers	C3	No	No	No	No	No	No	Yes

Cantaloupes	C3	No	No	No	No	Yes	No	No
Greens	C3	Yes	Yes	Yes	No	Yes	Yes	No
Vetch	C3	Yes	Yes	Yes	Yes	No	No	No
Turnips	C3	No	Yes	No	No	No	No	No
Radishes	C3	No	No	Yes	No	No	No	No
Pumpkins	C3	No	No	No	No	No	Yes	Yes
Blueberries	C3	No	No	No	No	No	Yes	No

Table S2.2. Differences in GPP for irrigation-permitted and non-permitted lands during 2011 drought, 2013 normal year, pluvial 2015, and all years 2010-2016 using Welch's t-test.

Grass/Pasture	Mean GPP (g C/m^2/year)			
	Permitted	Non-permitted	Difference	p-value
Drought (2011)	691	713	-22	0.04
Normal (2013)	1114	1143	-29	<.01
Pluvial (2015)	1199	1217	-18	0.03
All years (2010-2016)	1026	1063	-36	<.01
Winter Wheat	Mean GPP (g C/m^2/year)			
	Permitted	Non-permitted	Difference	p-value
Drought (2011)	689	593	96	<.01
Normal (2013)	1025	962	63	<.01
Pluvial (2015)	1049	1015	34	<.01
All years (2010-2016)	959	902	58	<.01
C3 Cropland	Mean GPP (g C/m^2/year)			
	Permitted	Non-permitted	Difference	p-value
Drought (2011)	940	715	226	<.01
Normal (2013)	1227	1037	190	<.01
Pluvial (2015)	1193	1100	92	<.01
All years (2010-2016)	1148	1007	141	<.01
C4 Cropland	Mean GPP (g C/m^2/year)			
	Permitted	Non-permitted	Difference	p-value
Drought (2011)	1263	777	486	<.01
Normal (2013)	1504	1409	95	<.01
Pluvial (2015)	1324	1276	48	<.01
All years (2010-2016)	1417	1262	155	<.01

Table S2.3. Percentage departure calculations for the 2011 drought and p-values for irrigation-permitted and non-permitted lands using Welch's t-test.

	GPP (g C yr^{-1} m^{-2})				
Land Cover	Drought (2011)	5-year Mean	Difference	Change %	p-value
C4 Non-perm	777	1316	-539	-41%	<.01
WW Non-perm	593	940	-347	-37%	<.01
GP Non-perm	713	1101	-388	-35%	<.01
GP Permitted	691	1066	-375	-35%	<.01
C3 Non-perm	715	1050	-335	-32%	<.01
WW Permitted	689	993	-304	-31%	<.01
C3 Permitted	940	1188	-248	-21%	<.01
C4 Permitted	1263	1452	-189	-13%	0.05079

Table S2.4. Percentage departure calculations for pluvial 2015 and p-values for irrigation-permitted and non-permitted lands using Welch's t-test.

	GPP (g C yr^{-1} m^{-2})				
Land Cover	Pluvial (2015)	5-year Mean	Difference	Change %	p-value
GP Permitted	1199	1066	133	12%	<.01
GP Non-perm	1217	1101	116	11%	<.01
WW Non-perm	1015	940	75	8%	<.01
WW Permitted	1049	993	56	6%	<.01
C3 Non-perm	1100	1050	50	5%	0.048
C3 Permitted	1193	1188	4	0%	0.8
C4 Non-perm	1276	1316	-40	-3%	0.28
C4 Permitted	1324	1451.69	-127	-9%	0.02

Chapter 3: Dry-season greenness, fluorescence, and photosynthesis of moist tropical forests in the Amazon

Abstract

Photosynthesis of the Amazon Basin affects the global carbon cycle and climate. However, it has been intensely debated if the moist forest greens-up in the dry season and if El Niño drought decreases photosynthesis. For the first time, we analyze 11 years (2007-2017) of satellite-retrieved vegetation remote sensing data including greenness, solar-induced chlorophyll fluorescence (SIF), and gross primary production (GPP) for ten eddy flux tower sites, moist forest regions, and the entire Amazon Basin to investigate the seasonality of greenness, SIF, and GPP and the effect of El Niño and La Niña events on them. Our analysis included vegetation indices derived from MODIS surface reflectance data and bidirectional reflectance distribution function (BRDF) corrected MODIS data, which accounts for the effect of sun-sensor geometry on satellite-observed reflectance. We examine two hypotheses that address whether there is a dry-season green-up and the effect of ENSO events on photosynthesis: (1) greenness, SIF, and GPP show consistent temporal dynamics and (2) these data are anomalously low during El Niño dry seasons, but anomalously high during preceding La Niñas dry seasons. Our results accepted the first hypothesis as there is a consistent increase in greenness, SIF, and GPP during the dry season (June-October) for moist forests. Our results rejected the second hypothesis and indicated the contrary, with dry-season greenness, SIF, and GPP lower than normal during the 2007-2008 La Niña and higher than normal during the 2009-2010 El Niño. For the 2010-2011 La Niña and 2015-2016 El Niño, our results were inconclusive but didn't support our second hypothesis. We conclude that the dry-season resistance of greenness, SIF, and GPP of the moist Amazonian forests to climate variability

should be considered in earth system models that estimate the impacts of climate variability on moist Amazon forests and/or its role in the variability of atmospheric CO_2.

3.1 Introduction

The seasonal dynamics of forest canopy structure and function in the Amazon are critically important to the regional and global carbon cycles, but these dynamics have been the subject of intense debates over the last two decades (Galvão et al. 2011; Huete et al. 2006; Lee et al. 2013; Morton et al. 2014; Saleska et al. 2007; Saleska et al. 2016; Samanta et al. 2010; Xiao et al. 2006; Xiao et al. 2005). A limited number of field studies at the leaf (Albert et al. 2018; Wu et al. 2018) and stand (Restrepo-Coupe et al. 2013; Saleska et al. 2003) levels have assessed the seasonal dynamics of the tropical Amazon's forest canopy structure and function, and have concluded that photosynthetic capacity increased in the dry season. Three studies analyzed reflectance-based vegetation indices from the Moderate Resolution Imaging Spectroradiometer (MODIS) and in-situ leaf litterfall data, and suggested that leaf flush, queued by increases of sunlight after the wet season, drives dry-season green-up in the Amazonian forests (Huete et al. 2006; Xiao et al. 2006; Xiao et al. 2005). Conversely, two studies argued that sun-sensor geometry created artifacts in the MODIS surface reflectance data, which caused greenness to artificially increase during the dry season (Galvão et al. 2011; Morton et al. 2014). However, more recent studies have concluded that dry-season increases in greenness remained after correcting the MODIS data (Guan et al. 2015; Maeda et al. 2014; Saleska et al. 2016).

It has also been debated whether drought years further increase dry-season photosynthesis in the Amazon or suppress it (Asner and Alencar 2010; Brando et al. 2010; Gatti et al. 2014; Huete et al. 2006; Khand et al. 2017; Liu et al. 2017; Samanta et al. 2010; Xu et al. 2011). Some field studies that have found decreased gross primary production (GPP) in moist Amazonian forest (>

2000 mm mean annual precipitation) during drought (Doughty et al. 2015; Gatti et al. 2014; Nepstad et al. 2004). More recent studies have analyzed spaceborne solar-induced chlorophyll fluorescence (SIF), which is a small amount of energy emitted by plants after its chlorophyll absorbs photosynthetically active radiation (PAR), from platforms such as the Greenhouse Gases Observing Satellite (GOSAT), the Global Ozone Monitoring Experiment-2 (GOME-2), and the Orbiting Carbon Observatory (OCO-2). Several such studies have contributed an increase in atmospheric CO_2 to a large reduction in Amazonian SIF or GPP (Lee et al. 2013; Liu et al. 2017; Parazoo et al. 2013). Another study reported seemingly conflicting results in that GOME-2 SIF decreased but greenness increased during the 2015-2016 El Niño (Yang et al. 2018a), and another study found that the 2015-2016 El Niño suppressed SIF after a multi-step correction of the GOME-2A data (Koren et al. 2018), which suffers from sensor degradation (Zhang et al. 2018a).

The response of moist Amazon forests to drought is a debate because forests that are not water limited may have increased photosynthesis during a meteorological drought due to less cloud cover and increased sunlight (Bonal et al. 2008; Brando et al. 2010; Condit et al. 2004; Graham et al. 2003), and it is difficult to disentangle processes in the Amazon at the regional scale because frequent cloud cover obscures spaceborne measurements and installing a network of eddy covariance towers in the moist Amazonian interior is not feasible. Furthermore, it is challenging to generalize about how drought affects the Amazon, because meteorological drought severity is temporally and spatially heterogenous within and across drought events, which further complicates assessments of the impact of drought on Amazonian forests at both site and regional scales (Lewis et al. 2011; Marengo et al. 2008). For instance, the 2010 drought event mostly affected the western and southern Amazon Basin and was driven by an El Niño and North Atlantic warming (Marengo

et al. 2011), whereas the 2015-2016 ENSO-driven drought was unprecedented and largely affected the northern and southeastern regions (Jiménez-Muñoz et al. 2016).

Furthermore, the legacy effects of drought on tree mortality (Doughty et al. 2015; Nepstad et al. 2007; Phillips et al. 2009), fire frequency and severity (Aragao et al. 2008; Aragao et al. 2007), and canopy structure (Saatchi et al. 2013) may linger long after drought and can have positive feedbacks (Laurance and Williamson 2001). Thus, the impacts of drought at the landscape scale is a mosaic of localized responses driven by site-specific characteristics, history, and climate than a homogenous response. Nevertheless, it is vital to characterize how drought and pluvial events affect the productivity of the forest so that we can better understand and more accurately predict the effects of earth's climate variability and human land management on atmospheric CO2 concentrations.

Here, we used monthly SIF data from GOME-2 and OCO-2, GPP estimates from the Vegetation Photosynthesis Model (GPP_{VPM}), and MODIS-based vegetation indices for 2007-2017 to investigate (1) to what degree the seasonality of greenness, SIF, and GPP of moist tropical forests were consistent with each other, and (2) how did dry-season greenness, SIF, and GPP change during the strong El Niño (2009-2010 and 2015-2016) and La Niña years (2007-2008 and 2010-2011). We hypothesized that (1) the moist forests exhibit an increase in dry-season productivity through greenness, SIF, and GPP indicators, and (2) that September and dry-season greenness, SIF, and GPP is lower than normal during the two El Niño years and higher than normal during the two La Niña years.

Our study was novel in two ways. First, we analyzed changes in greenness, SIF, and GPP at monthly (September) and the dry-season (June-October) scales, whereas previous studies have conducted analyses at annual, or drought- and El Niño-year, time scales. Second, we include two

La Niña events in our analyses, whereas previous studies have focused nearly exclusively on drought or El Niño events. The results from our study have significant implications for dynamic global vegetation models (DGVMs) as generally they have poorly represented the seasonal dynamics of photosynthesis in the Amazon (Restrepo‐Coupe et al. 2017), which has created large uncertainties in predicting how seasonally moist tropical Amazonian forests respond to climate variability and change. Furthermore, the inability for the models to capture the seasonality of photosynthesis in moist Amazon forests may lead to an improper prediction of how such photosynthesis responds to pluvial and drought events, which could yield an errant quantification of the impact of changes in photosynthesis on atmospheric CO_2 concentration.

3.2 Methods

3.2.1 Study sites

Our study was conducted for each of the nine eddy flux tower locations that were part of the Large-Scale Biosphere Atmosphere Experiment in Amazonia (LBA) (Keller et al. 2004), and for the Amazon Tall Tower Observatory (ATTO) (Fig. S3.1) (Andreae et al. 2015). Unless otherwise noted, we carried out data analysis at the spatial resolutions of 0.5° and 1.0° (latitude and longitude) to match the spatial resolutions of GOME-2 and OCO-2 SIF data, respectively. Two of the towers were in the same gridcell, giving us a total of nine gridcells for analysis (Fig. S3.2). The percentage of forest cover area within these gridcells ranged from 15% to 99% as of 2017 (Table S3.1).

3.2.2 Solar-induced chlorophyll fluorescence

We used SIF retrievals from GOME-2 and OCO-2, which were available for 2007 – 2017 and September 2014 – October 2017, respectively. All SIF data analyses were conducted using the data as provided, without removing outliers or negative values. The GOME-2 and OCO-2 SIF

datasets have been rigorously validated with eddy flux tower GPP and gridded GPP datasets (Li et al. 2018; Sun et al. 2018; Zhang et al. 2016; Zhang et al. 2018b). We used daily average SIF values (SIF_{daily}) provided in the Level 3 (monthly) GOME-2 SIF v27 product from the MetOp-A satellite (Joiner et al. 2013; Joiner et al. 2016) because SIF_{daily} has been shown to have a more consistent relationship with daily GPP than instantaneous SIF (SIF_{inst}) (Zhang et al. 2018c). The sensor onboard GOME-2's MetOp-A satellite has degraded significantly, thus it is not advisable to conduct long-term trend analyses (Zhang et al. 2018a). The GOME-2 SIF products are noisy due to sensor degradation and the inherently low-energy signal of SIF (Joiner et al. 2013). The seasonality of GOME-2 SIF for each tower site is illustrated in Figure S3.3.

The OCO-2 v8 SIF Lite data product (B8100) was provided in daily files (Frankenberg et al. 2014). Each file provided SIF retrievals at 757 nm (SIF_{757}) and 771 nm (SIF_{771}). We averaged the two bands together by first applying a wavelength correction factor of 1.5 to SIF_{771} (Sun et al. 2018). To match the temporal resolution of the GOME-2 data, we averaged the SIF retrievals for each month. The OCO-2 data was provided pre-filtered to exclude poor quality data (Frankenberg 2015). GOME-2 and OCO-2 SIF values in our study should not be directly compared due to several differences, including spatial resolution, overpass time, viewing zenith angle, and the wavelengths used to retrieve SIF.

3.2.3 Vegetation Photosynthesis Model

To estimate monthly GPP for the entirety of the study period (2007-2017), we used the 8-day 500-m Vegetation Photosynthesis Model (GPP_{VPM}) light-use efficiency model (LUE) (Xiao et al. 2004; Xiao et al. 2005; Zhang et al. 2017b). In this model, the fraction of absorbed photosynthetically active radiation (*f*PAR) by vegetation was partitioned into PAR absorbed by

chlorophyll (fPAR$_{chl}$) and non-photosynthetic vegetation (fPAR$_{NPV}$) to estimate GPP. Thus, GPP$_{VPM}$ was a product of $fPAR_{chl}$, PAR, and light-use efficiency (ε_g):

$$GPP_{VPM} = PAR \times fPAR_{chl} \times \varepsilon_g \quad (1)$$

where $fPAR_{chl}$ was estimated as a function of the Enhanced Vegetation Index (EVI), which was calculated using MODIS MOD09A1 V006 data product (Zhang et al. 2017b). Maximum LUE (ε_0) is higher for C4 plants than C3 plants (Ehleringer et al. 1997; Epstein et al. 1997), so VPM incorporated global C4 vegetation percentage maps (Zhang et al. 2017b). The maximum light-use efficiencies used in the model were 0.035 mol CO_2 mol^{-1} PAR for C3 and 0.0525 mol CO_2 mol^{-1} PAR for C4. Thus, GPP$_{VPM}$ for each gridcell was calculated using the area fraction and light-use efficiency for C3 and C4 vegetation. ε_g is regulated by temperature and water stress (Haxeltine and Prentice 1996). To account for these stresses, VPM used temperature (T_{scalar}) and water scalars (W_{scalar}) to downregulate ε_0.

We calculated monthly daily average GPP$_{VPM}$ by first determining the monthly total and dividing it by the number of days in that month. In Figures 4-7, and for the statistical analyses that accompany these figures, we aggregated the original 500-m GPP$_{VPM}$ product to 0.05 degree to match the spatial resolution of the MAIAC data. Previous studies have validated VPM in biomes around the world using data from the eddy flux tower sites (Doughty et al. 2018; Xiao et al. 2005; Xin et al. 2017; Zhang et al. 2016; Zhang et al. 2017b) and SIF (Cui et al. 2017; Ma et al. 2018) data. The seasonality of GPP for each tower site is illustrated in Figure S3.4.

3.2.4 Vegetation indices

The Normalized Difference Vegetation Index (NDVI) and Enhanced Vegetation Index (EVI) (Huete et al. 2002) was obtained from the MODIS MOD13C2 V006 monthly data product (Didan 2015), which had a spatial resolution of 0.05°. Prior to aggregating NDVI and EVI to 0.5°,

we removed all poor and marginal quality grid cells using the quality reliability flag (0 = good quality). We further filtered NDVI and EVI by using a minimum threshold of 0.6 and 0.3, respectively. Land Surface Water Index (LSWI) (Xiao et al. 2002) was calculated using the MOD09A1 V006 500 m 8-day land surface reflectance product (Vermote 2015). Missing LSWI values in 2000 and 2001 were gap-filled with the same day of year (DOY) values from the subsequent years, and gaps in 2016 were filled with values from the same DOY in 2015 (Zhang et al. 2017b). Boxplots of these EVI, NDVI, and LSWI data were provided in Figures S5-7.

Previous studies have suggested that the bidirectional reflectance effect caused by sun-sensor geometry was the source of seasonality in MODIS-derived NDVI and EVI (Morton et al. 2014), and that surface reflectance data that is not corrected with the bidirectional reflectance distribution function (BRDF) is questionable (Hilker et al. 2015). However, several studies have shown that there is a dry-season increase in EVI and NDVI regardless of the MODIS surface reflectance product used, including MOD09, MOD13, MCD43, and MAIAC, although the frequency of good-quality data and the seasonal magnitudes of change vary among these products (Guan et al. 2015; Hilker et al. 2015; Maeda et al. 2014; Maeda et al. 2016; Saleska et al. 2016). Thus, we also incorporated BRDF-corrected EVI (EVIn) and NDVI (NDVIn) into our analysis, which was derived from the Multi-Angle Implementation of Atmospheric Correction (MAIAC) Version 6 MODIS product MCD19A1.006. The BRDF-corrected vegetation indices, EVIn and NDVIn, were provided as an 8-day, 0.05-degree product with global coverage in the Climate Model Grid (CMG) format and was accessed at https://portal.nccs.nasa.gov/datashare/maiac/DataRelease/. For Fig. 3.1, we aggregated the MAIAC data to 0.5-degree spatial resolution to match the spatial resolution of the other datasets used in the figure; 8-day values are shown. For Fig. 3.3, we aggregated the MAIAC data to monthly

values at 0.5-degree spatial resolution for consistency with the other datasets. For Figures 4-7, and all statistical analysis, we used the MAIAC data as provided in its original spatial and temporal resolution.

3.2.5 Climate data

We used air temperature (Fig. S3.8) and PAR (Fig. S3.9) data from the National Centers for Environmental Prediction (NCEP) Reanalysis 2 dataset, accessed at https://www.esrl.noaa.gov/psd/. These data were downscaled to 0.5° × 0.5° using a non-linear, distance-weighted spatial interpolation technique (Zhang et al. 2016; Zhao et al. 2005). Monthly precipitation data (Fig. S3.10) was obtained from the Tropical Rainfall Measuring Mission's (TRMM) Multi-Satellite Precipitation Analysis (TMPA) (Huffman et al. 2007). We aggregated the 3B43 v7 data product (Huffman et al. 2014, updated 2019b) to 0.5° × 0.5° from its original spatial resolution of 0.25° × 0.25°. Monthly ENSO indices in Figures 2 and S11 were provided by the Multivariant El-Niño Southern Oscillation Index Version 2 (MEI.v2) available at https://www.esrl.noaa.gov/psd/enso/mei/ (Wolter and Timlin 2011).

3.2.8 Forest cover

To determine changes in forest cover area during the study period (2007-2017), we mapped annual forest cover with a spatial resolution of 500-m using our previously published methods (Qin et al. 2016; Qin et al. 2019; Xiao et al. 2009). Only gridcells that were consistently forest and non-forest were used in our study, and moist forest were defined as those pixels that were consistent forest and had a mean annual precipitation (MAP) of more than 2000 mm as calculated using TRMM data for our study period of 2007-2017.

3.2.9 Statistical analyses

We conducted ordinary least squares regressions to determine the relationship between monthly GPP and GOME-2 SIF at each site. Regressions were through the origin (intercepts were forced to zero) as predicted GPP was expected to be nil when observed SIF was zero. We used one-sample t-tests for SIF, GPP, EVIn, and NDVIn (Figures 4-7) to determine if the difference between normal September or dry-season SIF and September or dry-season SIF during the La Niñas and El Niños was significantly different than zero (Tables S3.2-5).

3.3 Results

3.3.1 Seasonality of Amazon forests

GOME-2 and OCO-2 monthly SIF at the gridcells with forest eddy flux tower sites exhibited increases in the dry season and decreases during the wet season (Figs. S3.12-13). SIF data from both sources were highly correlated (Fig. S3.14) and exhibited remarkably similar seasonal dynamics over the life of OCO-2 (beginning Sept. 2014) at each site. GPP estimates were well correlated with SIF observations from GOME-2 and OCO-2 (Figs S3.15-16). Furthermore, the seasonality of the Enhanced Vegetation Index (EVI) and Land Surface Water Index (LSWI), which respectively provide information on canopy chlorophyll and water content, were also similar to the seasonality of SIF and GPP (Fig. 3.1, Figs. S3.17-19). For the five gridcells dominated by forests (ATTO, K34, K77/K83, CAX, and RJA), SIF, GPP, EVI, and PAR increased during the dry season (July-December) and decreased during the wet season (January-June) (Fig. S3.20).

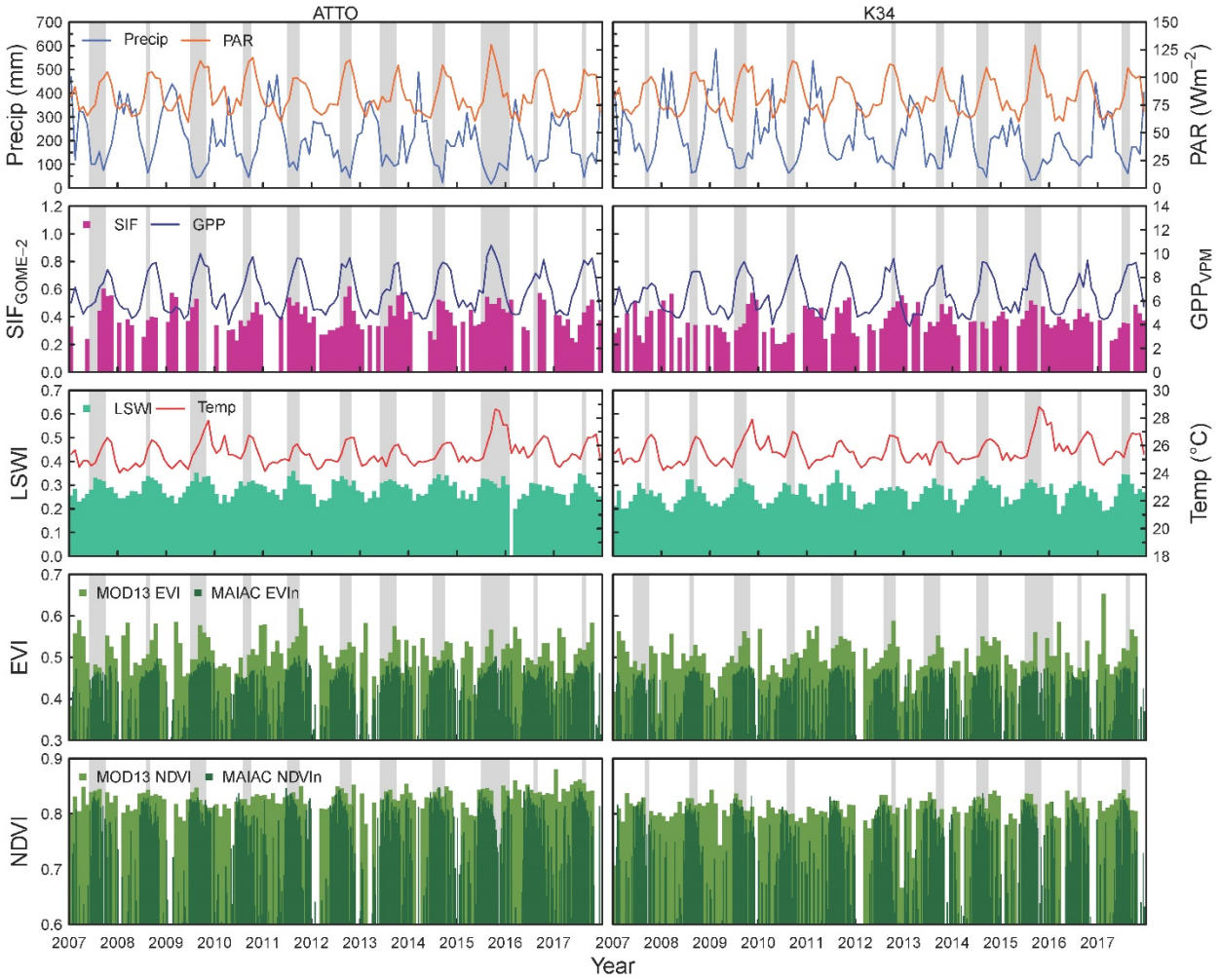

Figure 3.1 | Monthly dynamics of climate, SIF, photosynthesis, and greenness at the ATTO and K34 sites. Continuous data shown as lines. Shaded areas are months in which monthly total precipitation was less than 100mm. Shown are monthly total precipitation, photosynthetically active radiation (PAR), solar induced chlorophyll fluorescence (SIF; mw^{-2} m^{-2} nm^{-1} sr^{-1}), gross primary production (GPP; gC m^{-2} day^{-1}), land surface water index (LSWI), temperature, and enhanced vegetation index (EVI) and normalized vegetation difference index (NDVI) from MODIS and BRDF-corrected MAIAC (EVIn; NDVIn) products.

At the basin scale, we found that SIF and GPP were most often higher during September (typically the driest month) than during March (typically the wettest month) for gridcells that had at least 80% forest cover and 2000 mm mean annual precipitation (Fig. 3.2; Fig. S3.21). For gridcells that had <80% forest cover, SIF and GPP were often higher in March. This phenomenon was also observed by a previous analysis that found that increases in dry-season EVI and SIF for

tropical forests was largely determined by whether the forest had a mean annual precipitation (MAP) threshold of 2000 mm a year (Guan et al. 2015).

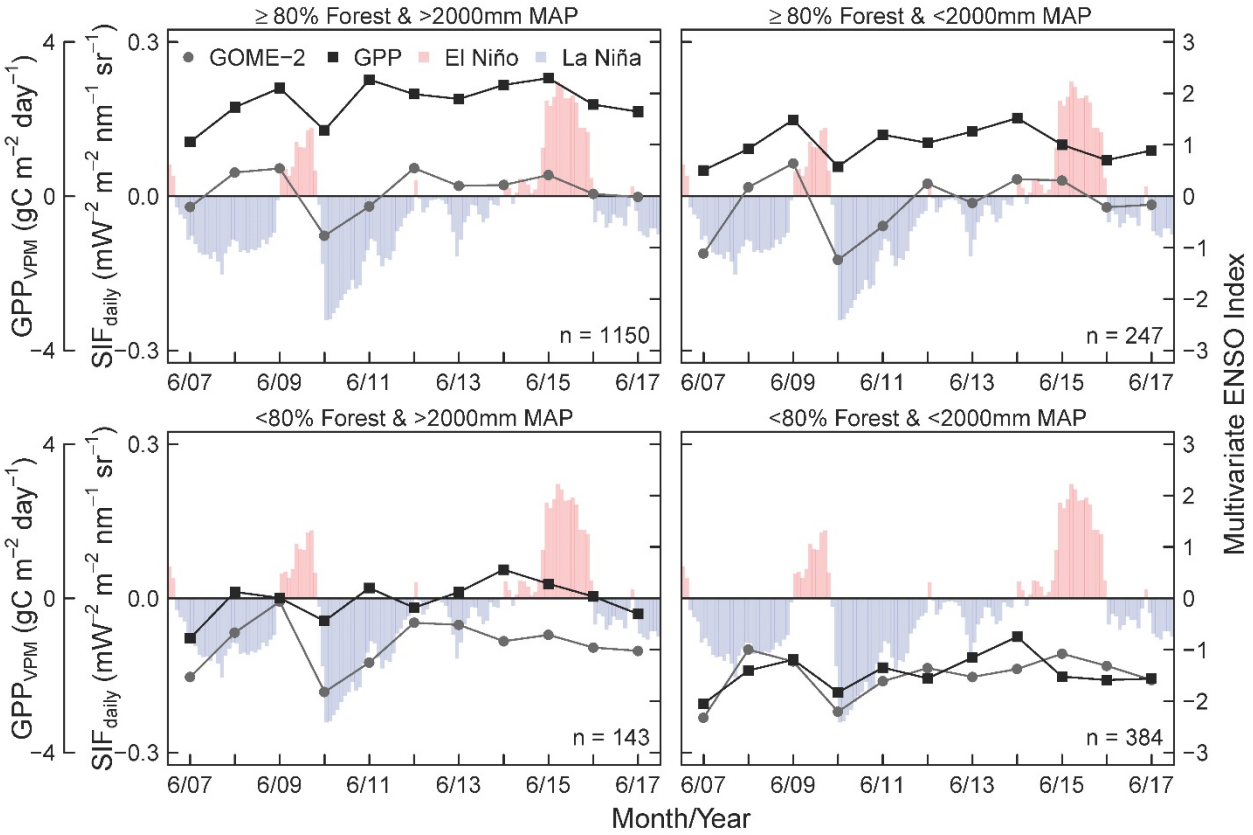

Figure 3.2 | The difference between mean September SIF or GPP and mean March SIF or GPP for each calendar year 2007-2017. Positive values indicate that GOME-2 SIF or GPP was higher during September, and negative values indicate that SIF or GPP was higher during March. Points were placed at the midpoint of each year, when ENSO typically oscillates. Bars are the Multivariate ENSO Index Version 2 (MEI.V2) values; red and blue bars indicate warm and cool periods, respectively. GOME-2 and GPP data in each panel represents the mean of gridcells with a percentage of forest cover ≥ or <80% and mean annual precipitation (MAP) ≥ or <2000 mm, as indicated by title above each panel.

3.3.2 Greenness, SIF, and GPP during La Niña and El Niño

To our surprise, at the two gridcells with the most forest cover (99% in ATTO and 96% in K34), dry-season greenness, SIF, and GPP during the 2009-2010 and 2015-2016 El Niño events were often higher than the multi-year mean and the preceding La Niña events (Fig. 3.3). At the gridcells containing eddy flux tower sites, there were no distinct changes in dry-season greenness,

SIF, or GPP because the gridcells were a mix of forests and other vegetation types or there was a substantial change in vegetative cover over time. However, dry-season GPP during the 2009-2010 El Niño was higher than the multi-year mean and preceding 2007-2008 La Niña at all five forested gridcells (Fig. S3.22). Dry-season GPP during the 2015-2016 El Niño exhibited a similar increase at the forested gridcells relative to the multi-year mean and the preceding 2010-2011 La Niña (Fig. S3.23), except at K77/K83 where substantial deforestation has occurred.

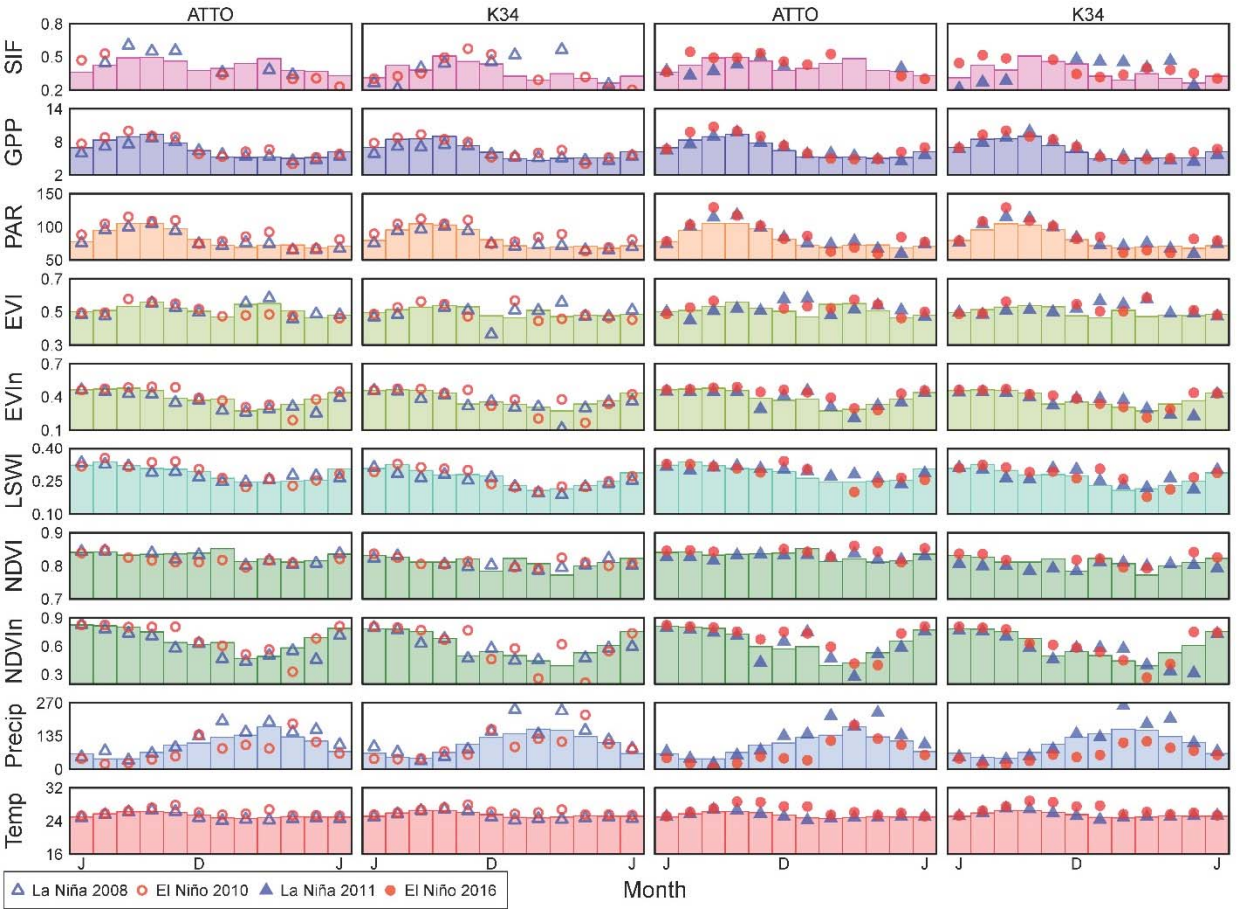

Figure 3.3 | ENSO year (July – June) seasonal dynamics of monthly mean SIF, photosynthesis, greenness, and climate at ATTO and K34. Symbols are monthly observations during La Niña (blue triangles) and El Niño (red circles) and bars are monthly means from 2007-2017 (excluding the La Niña and El Niño events). The left two panels show the 2007-2008 La Nina and 2009-2010 El Nino. The right two panels show the 2010-2011 La Nina and 2015-2016 El Nino. Illustrated are monthly mean SIF (mw^{-2} m^{-2} nm^{-1} sr^{-1}), GPP (gC m^{-2} day^{-1}), PAR (Wm^{-2}), EVI, EVIn, LSWI, NDVI, NDVIn, total precipitation (mm), and temperature (°C).

We further investigated our hypothesis that September and dry-season greenness, SIF, and GPP were higher than normal during the two El Niños and higher than normal during the two La Niñas at the basin scale and for moist forests using BRDF-corrected vegetation indices, SIF observations, and GPP estimates. We found that September SIF, GPP, EVIn, and NDVIn during the 2009-2010 El Niño were significantly higher than normal, and lower than normal during the preceding La Niñas of 2007-2008 for both the basin and moist forests (Fig. 3.4; Table S3.2). For the basin, September SIF, GPP, EVIn, and NDVIn were about 12%, 4.1%, 2.8%, and 1.9% higher than normal during the 2009-2010 El Niño, and were about 11%, 3.7%, 3.9%, and 1.9% lower than normal during the 2007-2008 La Niña, respectively. For moist forests, September SIF, GPP, EVIn, and NDVIn were about 8.8%, 5.8%, 1.9%, and 0.7% higher than normal during the 2009-2010 El Niño, and were about 6.7%, 6.3%, 3.9%, and 1.5% lower than normal during the 2007-2008 La Niña, respectively.

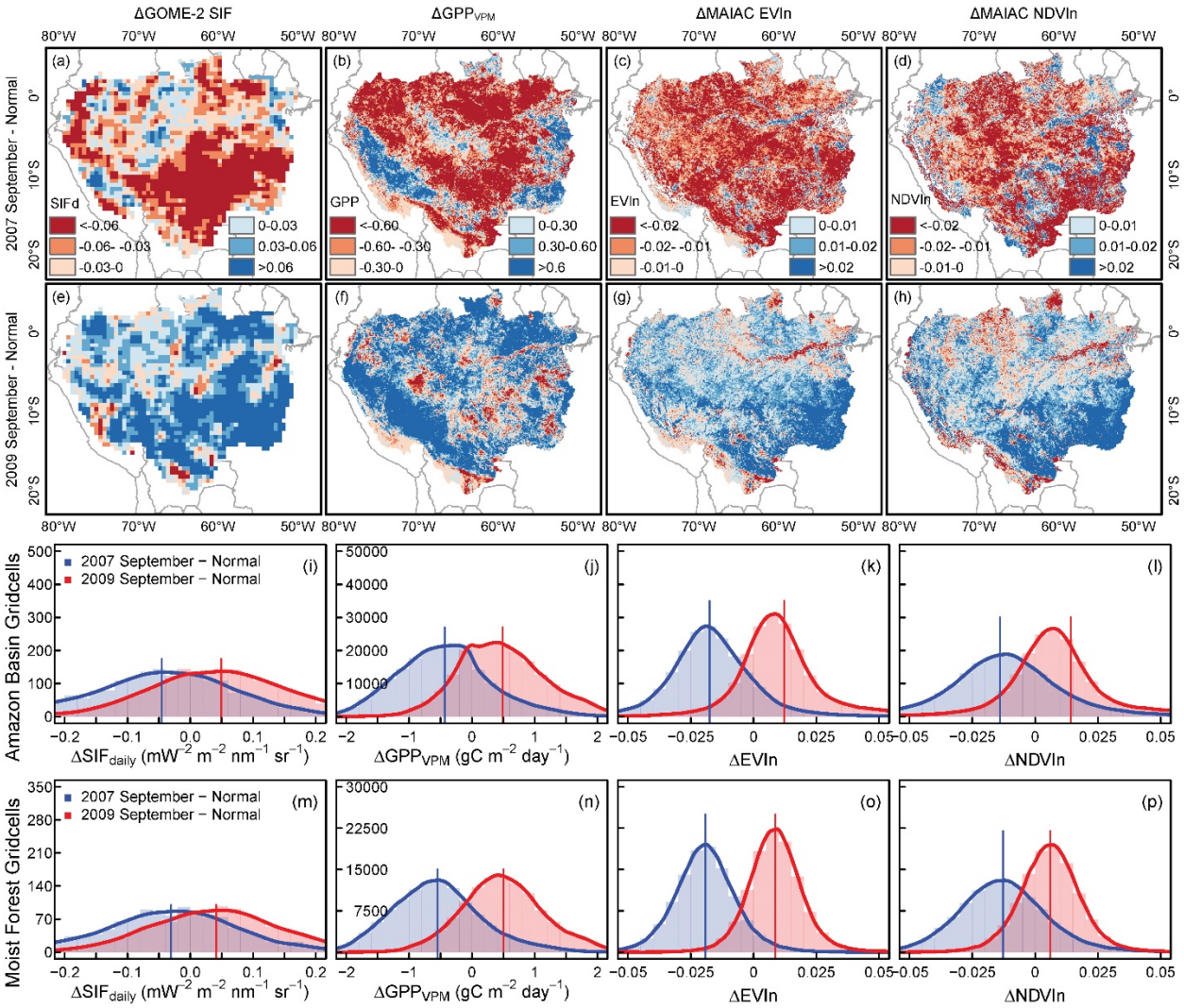

Figure 3.4 | Difference between September SIF, GPP, EVIn, and NDVIn during the 2007-2008 La Niña and 2009-2010 El Niño and the mean of normal years in the Amazon. Differences calculated as the La Niña or El Niño September minus the mean of the normal years, thus negative values indicate lower than normal and positive values indicate higher than normal. Frequency histograms in each column (i-p) correspond to the maps (a-h) above them. We used a one-sample t-test at the 95% level of confidence to test if the differences were significantly different from zero (Table S3.2). Moist forest gridcells were those with >80% forest cover and >2000 mm mean annual precipitation.

For the 2010-2011 La Niña and 2015-2016 El Niño, September SIF, GPP, EVIn, and NDVIn were significantly higher during each El Niño than the La Niña that preceded for both the Amazon Basin and moist forests (Fig. 3.5; Table S3.3). At the basin scale, September SIF, GPP, EVIn, and NDVIn were lower than normal during the La Nina and higher than normal during the El Nino. Results

were similar for moist forests, except that September GPP during the La Nina was higher than normal during the La Nina and EVIn was lower than normal during the El Nino.

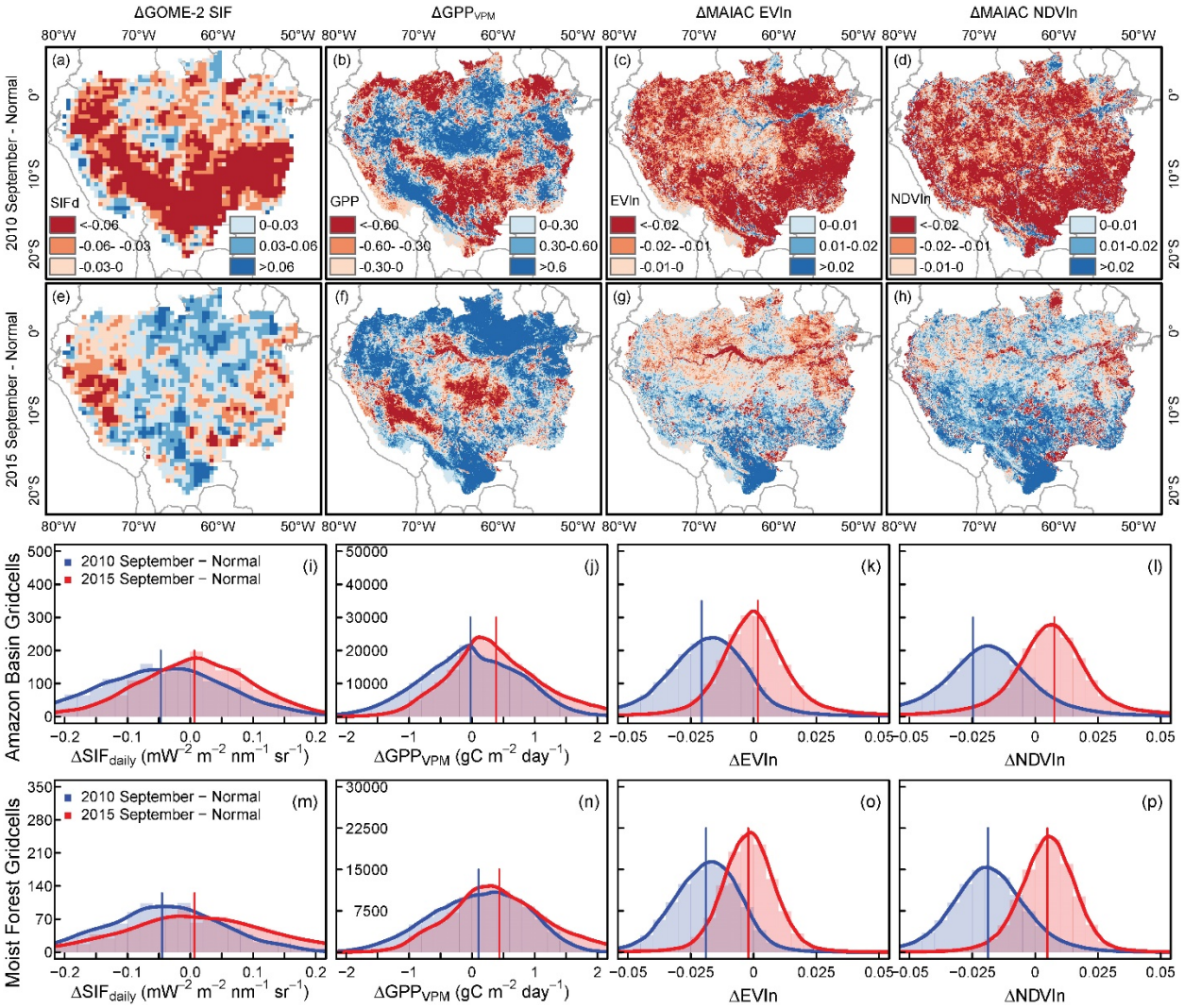

Figure 3.5 | Difference between September SIF, GPP, EVIn, and NDVIn during the 2010-2011 La Niña and 2015-2016 El Niño and the mean of normal years in the Amazon. Differences calculated as the La Niña or El Niño September minus the mean of the normal years, thus negative values indicate lower than normal and positive values indicate higher than normal. Frequency histograms in each column (i-p) correspond to the maps (a-h) above them. We used a one-sample t-test at the 95% level of confidence to test if the differences were significantly different from zero (Table S3.3). Moist forest gridcells were those with >80% forest cover and >2000 mm mean annual precipitation.

As for the dry season, the differences between SIF, GPP, EVIn, and NDVIn during the ENSO events and normal were much more subtle than the differences observed when we looked

at only September. At the basin scale, dry-season SIF, GPP, EVIn, and NDVIn were about 6.7%, 2.8%, 1.1%, and 0.8% higher than normal during the 2009-2010 El Niño, and were about 0.5%, 3.4%, 2.5%, and 0.8% lower than normal during the 2007-2008 La Niña (Fig. 3.6; Table S3.4). Results for these two ENSO events were similar for moist forest except for dry-season SIF during the 2007-2008 La Niña, which was 0.7% higher than normal.

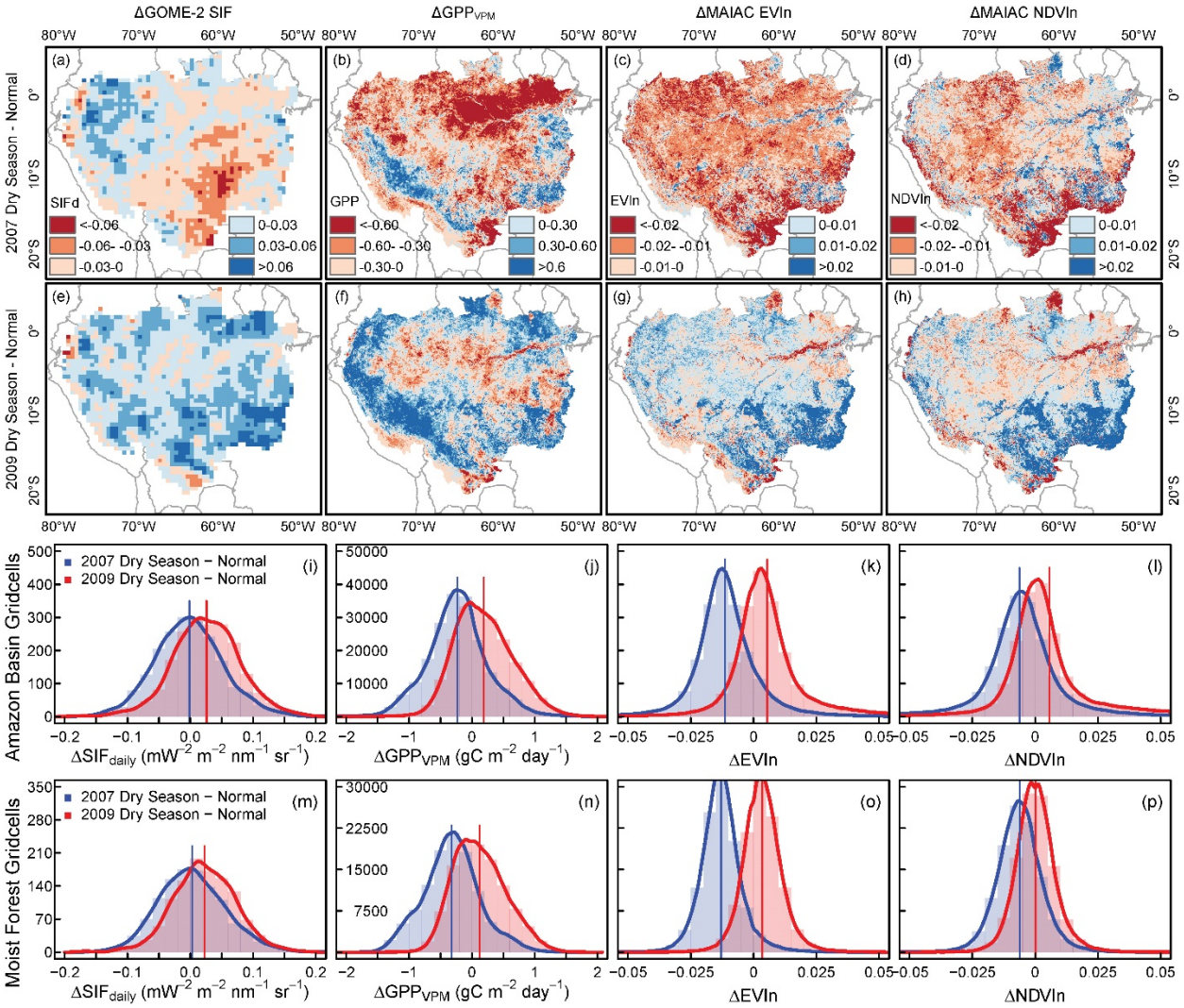

Figure 3.6 | Difference between dry-season SIF, GPP, EVIn, and NDVIn during the 2007-2008 La Niña and 2009-2010 El Niño and the mean of normal years in the Amazon. Differences calculated as the La Niña or El Niño dry-season (Jun-Oct) minus the mean of the normal years, thus negative values indicate lower than normal and positive values indicate higher than normal. Frequency histograms in each column (i-p) correspond to the maps (a-h) above them. We used a one-sample t-test at the 95% level of confidence to test if the differences were significantly different from zero (Table S3.4). Moist forest gridcells were those with >80% forest cover and >2000 mm mean annual precipitation.

However, the results were inconsistent on whether dry-season SIF, GPP, EVIn, or NDVIn were higher or lower than normal, particularly for the 2015-2016 El Niño. Dry-season SIF, GPP, EVIn, and NDVIn at the basin scale during the 2010-2011 La Niña were slightly lower than normal by about 2.3%, 0.1%, 2.5%, and 1.9%, respectively (Fig. 3.7; Table S3.5). The moist forest had similar lower than normal values, except for GPP which had a marginal increase of < 0.1%. Dry-season results were split for the 2015-2016 El Niño at the basin scale and for moist forest, with lower than normal SIF (3.6% and 4.4%) and EVIn (0.5% and 0.8%) and higher than normal GPP (2.2% and 2.7%) and NDVIn (0.3% and 0.1%).

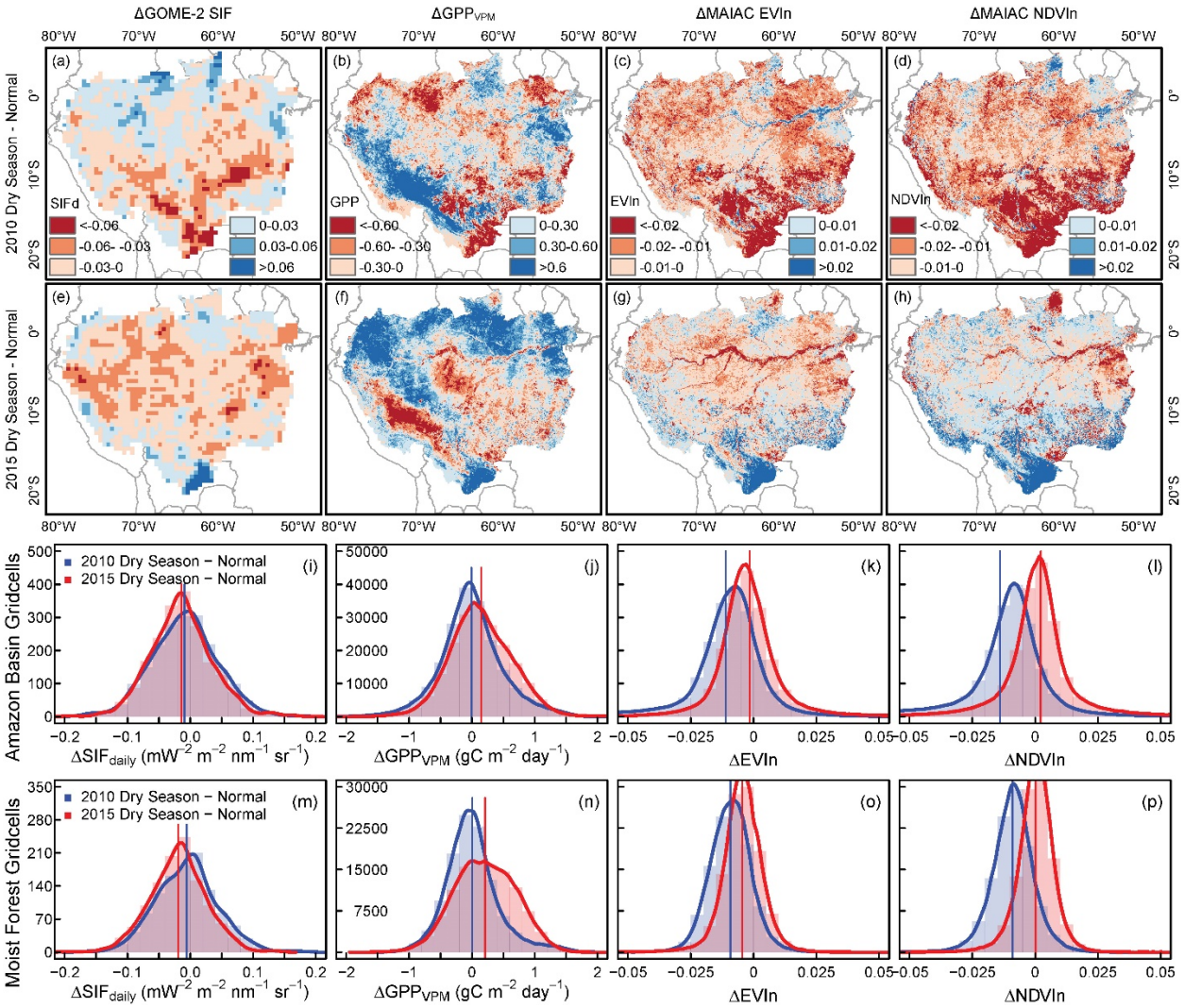

Figure 3.7 | Difference between dry-season SIF, GPP, EVIn, and NDVIn during the 2010-2011 La Niña and 2015-2016 El Niño and the mean of normal years in the Amazon. Differences calculated as the La Niña or El Niño dry-season (Jun-Oct) minus the mean of the normal years, thus negative values indicate lower than normal and positive values indicate higher than normal. Frequency histograms in each column (i-p) correspond to the maps (a-h) above them. We used a one-sample t-test at the 95% level of confidence to test if the differences were significantly different from zero (Table S3.5). Moist forest gridcells were those with >80% forest cover and >2000 mm mean annual precipitation.

3.4 Discussion

Our findings on the dry-season increase of greenness, SIF, and GPP for forested sites in the Amazon are also consistent with the results reported for the LBA eddy flux towers (Restrepo-Coupe et al. 2013), *in situ* observations of leaf flush, litterfall, and photosynthesis (Doughty et al.

2015; Rice et al. 2004; Saleska et al. 2003), prior satellite observations (Huete et al. 2006; Saleska et al. 2007; Xiao et al. 2005), and more recent *in situ* studies that observed greening and leaf flush using tower based cameras (Lopes et al. 2016; Wu et al. 2016). Importantly, the Vegetation Photosynthesis Model (VPM) was able to capture well the observed seasonality of photosynthesis, which has been poorly captured by several DGVMs (IBIS, ED2, JULES, and CLM3.5) that have simulated dry-season declines in GPP (Restrepo‐Coupe et al. 2017).

The increase of SIF, GPP, EVIn, and NDVIn during the dry season can be explained by the shedding of lianas and old leaves (4 to 5 years old) in the forest canopy, the exposure of younger leaves, and new leaf flush (Brando et al. 2010; Xiao et al. 2005). The amount of litterfall during the dry seasons are more than compensated for by new leaf production (Wu et al. 2016). During severe drought (El Niño) years, the amount of litterfall during the season increased, and the canopy has more young and mid-age leaves to be exposed to sun lights and observed by satellites, which may lead to higher dry-season SIF, GPP, EVIn, and NDVIn than the normal. In addition, bud development is queued by the length of day (Rivera et al. 2002), but leaf flushing and development coincides with increased radiation (Wright and Van Schaik 1994) and water availability (Brando et al. 2010). For moist Amazon forest with relatively little water limitation due to high mean annual precipitation and deep root systems (Nepstad et al. 1994), it is likely that leaf flush and development are accelerated in drier years when PAR is higher and cloud cover is lower than normal (Saleska et al. 2007). Thus, trees will utilize their water and light resources to their full potential to maximize leaf development and photosynthetic capacity until they become resource limited. Our analysis supports this theory in that September greenness, SIF, and GPP are higher than normal during El Niño, but overall there is relatively little difference between dry-season greenness, SIF, and GPP during normal, dry, and wet years. It is likely that in dry years, the forest

reaches water limitation more quickly, offsetting increased productivity that occurred earlier. Similarly, a wetter dry season may suppress the fall of old leaves (litterfall) and new leaf development, which would cause photosynthesis to peak later in the dry season. Thus, our observation that the difference between September greenness, SIF, and GPP during an ENSO event and normal is larger than the dry-season difference provides additional evidence that the observed changes are driven by changes in the forest canopy and not sun-sensor geometry.

Like the differences between September SIF, GPP, EVIn, and NDVIn during the El Niños and their preceding La Niñas, dry-season SIF, GPP, EVIn, and NDVIn was also higher during the El Niños that their preceding La Niñas except for SIF during the 2015-2016 El Niño (a comparison of which is perhaps inconsequential due to the sensor degradation that occurred between these two ENSO events). In each case, our results indicated that the differences between September or dry-season SIF, GPP, EVIn, and NDVIn during the four ENSO events and normal did not support our hypotheses that dry-season SIF, GPP, EVIn, and NDVIn was higher than normal during the El Niño years and lower than normal during the La Niña years. It is worth noting that changes in aboveground biomass (AGB) or net primary productivity (NPP) during a drought is a poor indicator of how drought affects GPP because both AGB and NPP often do not include the amount of litterfall. It has been suggested that during drought, trees may reduce plant respiration (Doughty et al. 2015). It has also been suggested that AGB may decrease despite increased GPP due to the allocation of carbon to belowground processes (Brando et al. 2010).

3.5 Conclusions

Our findings on the seasonality of greenness, SIF, and GPP of moist tropical forests in the Amazon during normal years and ENSO years could have profound implications on future studies of terrestrial carbon and water cycles and climate. The tropical forests play the largest role in the

seasonal dynamics and interannual variability of atmospheric carbon dioxide concentrations (Schimel et al. 2001). It has been estimated that about 22% of Amazonian rainfall is transpired by the forests within the basin (Staal et al. 2018). An inversion in the seasonality and reduction in transpiration is expected to increase the amplitude of droughts (Bagley et al. 2014) and affect the forest-rainfall cascades that are vital to Amazonian forests, particularly in the southwest where forests are more dependent on transpired water (Staal et al. 2018). Therefore, earth system models need to include variables that better track the canopy dynamics and phenology of evergreen tropical forests, which affects the seasonal dynamics of plant photosynthesis, transpiration, and their responses to changes in climate (Restrepo‐Coupe et al. 2017).

Our study has shown the complexity of assessing the dry-season greenness, SIF, and GPP of tropical forests at coarse spatial resolutions (0.5 and 1.0 degree), which is to a large degree due to varying proportions of forests and other land cover types within individual gridcells (Fig. S3.21). Non-forest vegetation types have different seasonal dynamics of greenness, SIF, and GPP due to diverse human management practices, such as haying, grazing livestock, and the planting and harvesting of crops. Therefore, earth system models need to include accurate annual maps of land cover types in their simulations to better predict the seasonal dynamics of carbon and water fluxes in the Amazon Basin. The use of such maps has become a more urgently needed by the modeling community, as the Amazonian landscape is rapidly changing due to deforestation and agricultural expansion and intensification (Nepstad et al. 2014; Qin et al. 2019; Tyukavina et al. 2017). Thus, the remote sensing community must work together and produce accurate and updated annual maps of Amazonian land cover types (Richards et al. 2017).

We also illustrated the potential of spaceborne GOME-2 and OCO-2 SIF data to provide new insight on the canopy structure and function of tropical forests, particularly during ENSO years.

Frequent cloud cover and aerosols in the Amazon have limited the number of good-quality SIF observations, which significantly hinder our progress in better understanding the seasonal dynamics of SIF. High-frequency *in situ* SIF observations have found that the relationship between SIF and GPP can change with environmental conditions and growth stage (Yang et al. 2018b). For example, it has been shown that SIF for taller and older Amazonian forests is less sensitive to precipitation variability than shorter and younger stands (Giardina et al. 2018). Therefore, it is important for us to integrate SIF data from other newly launched platforms (TROPOMI, OCO-3) and to-be-launched platforms such as FLEX and GeoCarb (Drusch et al. 2016; Polonsky et al. 2014).

3.6 Supplementary material

The original, unfiltered GOME-2 SIF data (including negative values) were used in all data analysis and figures (other than Figures S1 and S12) as instructed in the GOME-2 Read Me file at:

https://avdc.gsfc.nasa.gov/pub/data/satellite/MetOp/GOME_F/README_GOME-F_v27.pdf.

For better visualization of the GOME-2 SIF data in Figs. S1 and S12, we used three thresholds to exclude outliers most likely affected by noise: SIF must 1) not be less than 0.2 ($0.2 \leq SIF$); 2) not be less than 50% of the previous and subsequent SIF value ($SIF_{t-1} \times 0.5 \leq SIF_t \geq SIF_{t+1} \times 0.5$); and 3) not be more than 150% of the previous and subsequent SIF value ($SIF_{t-1} \times 1.5 \geq SIF_t \leq SIF_{t+1} \times 1.5$). If SIF_t could not be determined because SIF_{t-1} and/or SIF_{t+1} observations were poor quality or missing, then the nearest good observation was used in the threshold (e.g., SIF_{t-2} and/or SIF_{t+2}).

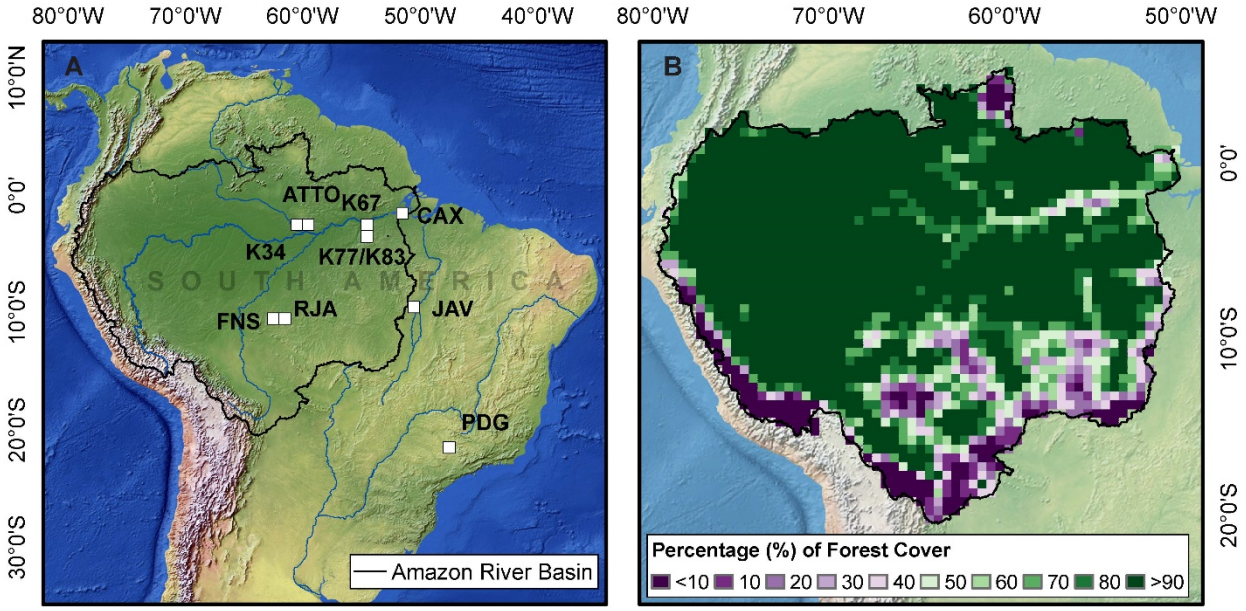

Figure S3.1 | Study site locations and forest area percentage. (A) Eddy tower locations in South America used in this study. The white boxes are the 1° x 1° OCO-2 pixels used in the study (drawn to scale). Aerial imagery for each site is further depicted in Fig. S2. (B) Percentage of forest cover in each 0.5° GOME-2 pixel.

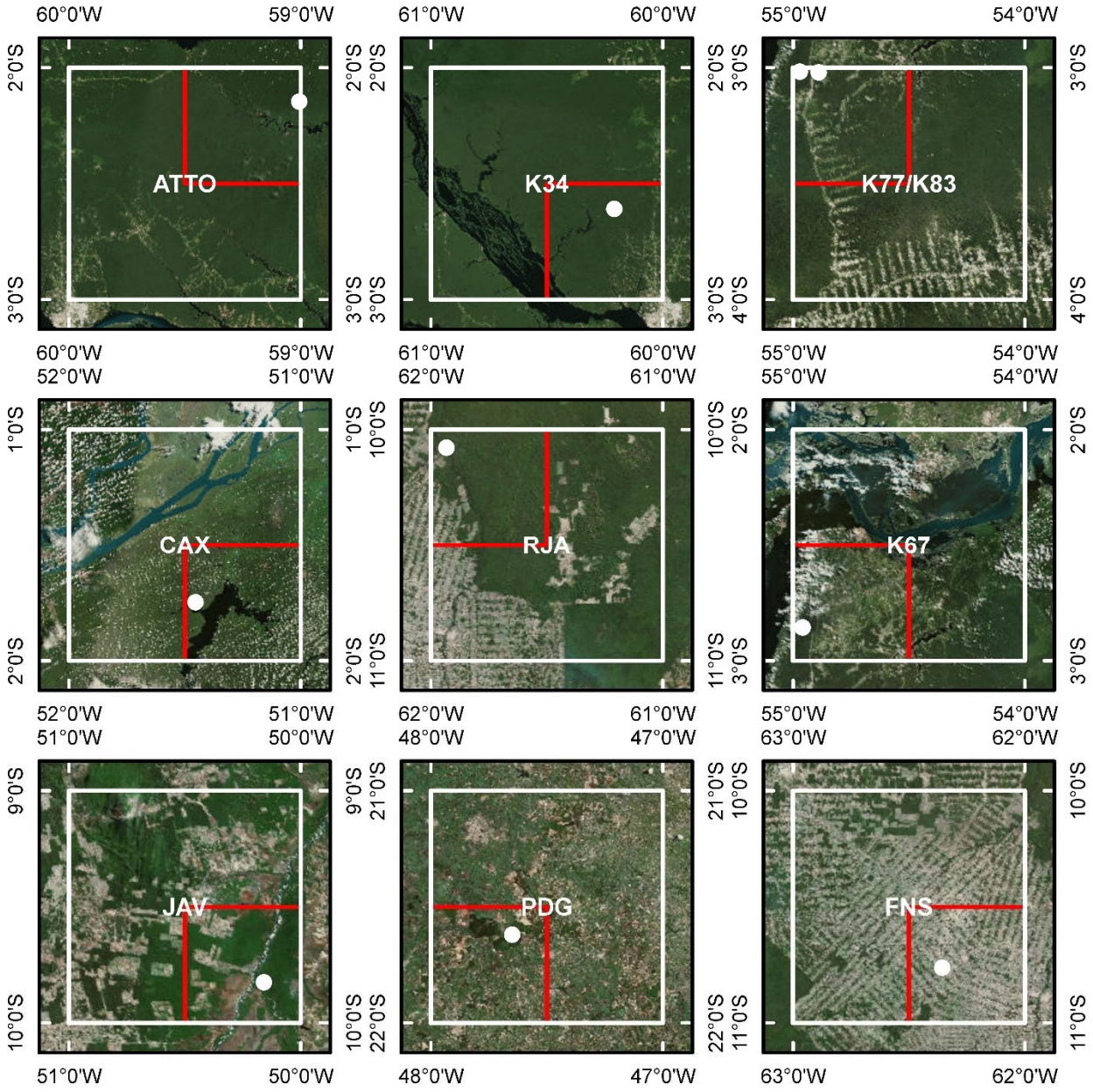

Figure S3.2 | Satellite imagery of the study sites. White boxes are 1° OCO-2 pixels, red boxes are 0.5° GOME-2 pixels, and white dots are the approximate reported location the eddy covariance tower. The percentage of forest cover in each 0.5° pixel is reported in Table S3.1. Note: K77/K83 exhibits a fishbone pattern of deforestation and CAX shows cloud streets (patterns like strings of pearls).

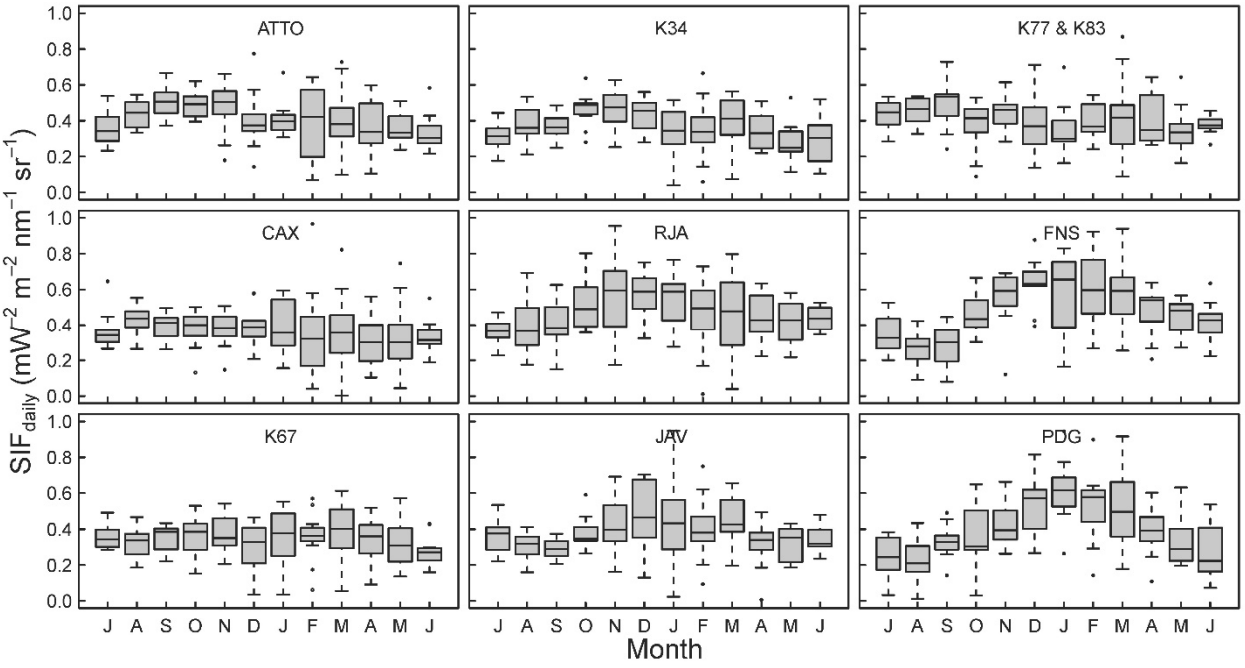

Figure S3.3 | Seasonality (July-June) of GOME-2 solar-induced chlorophyll fluorescence data for 2007-2017.

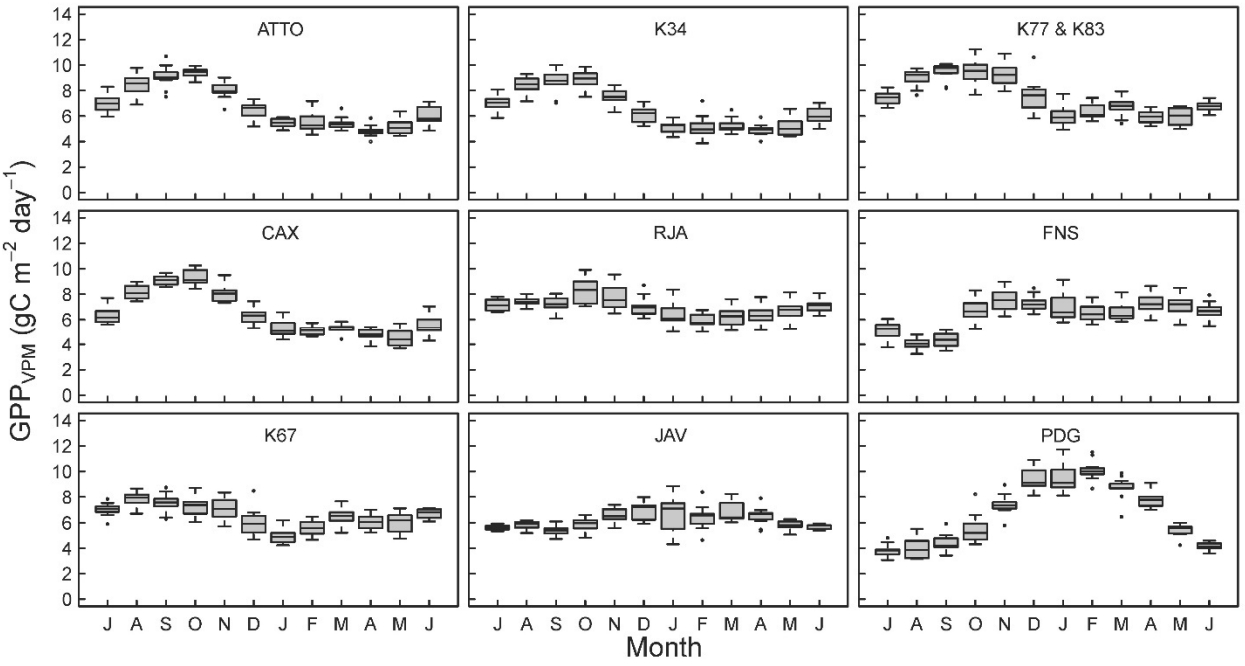

Figure S3.4 | Seasonality (July-June) of gross primary production estimated by the Vegetation Photosynthesis Model for 2007-2017.

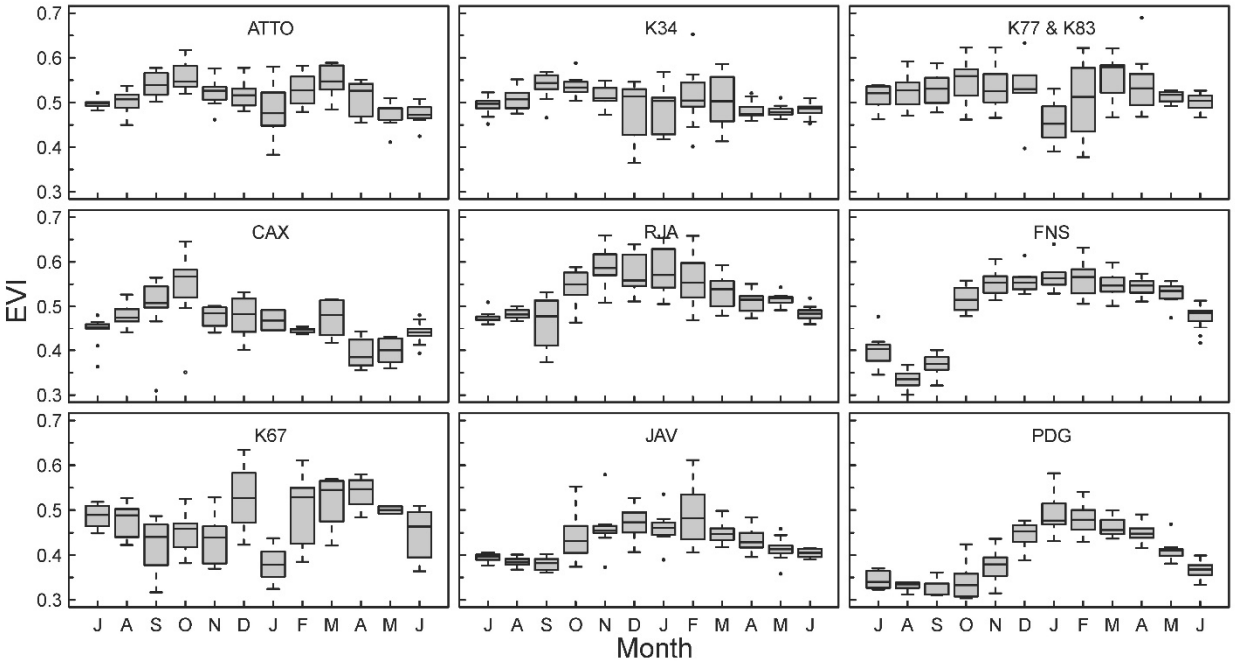

Figure S3.5 | Seasonality (July-June) of the enhanced vegetation index for 2007-2017.

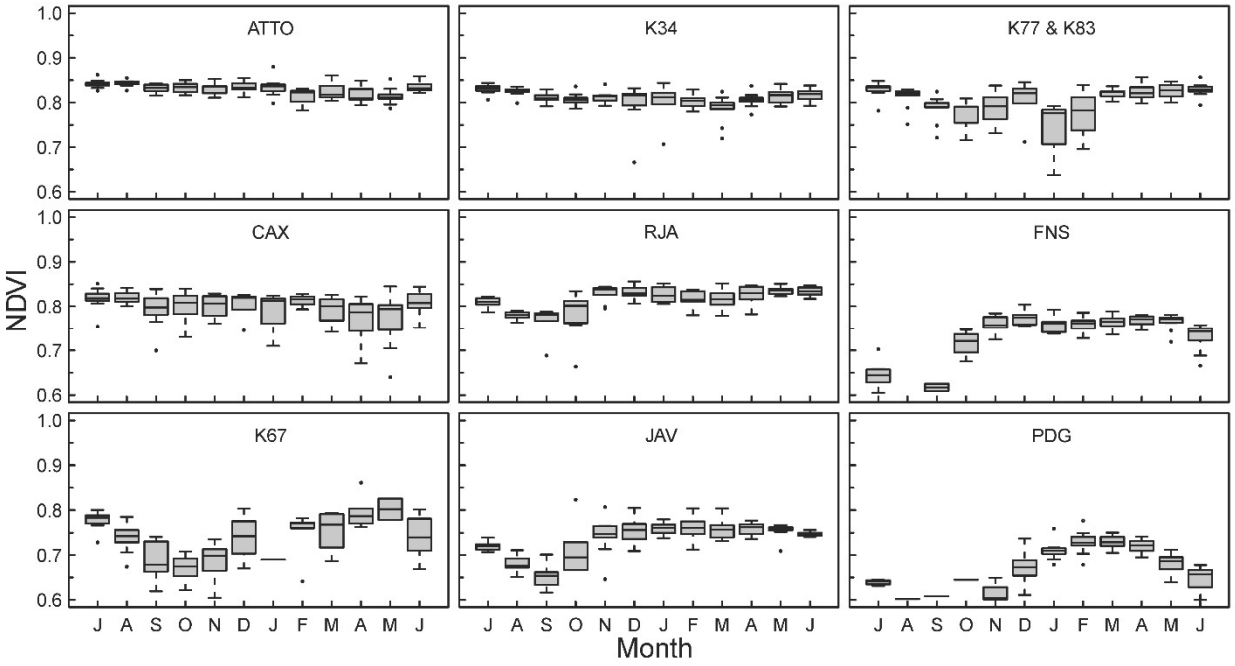

Figure S3.6 | Seasonality (July-June) of the normalized difference vegetation index for 2007-2017.

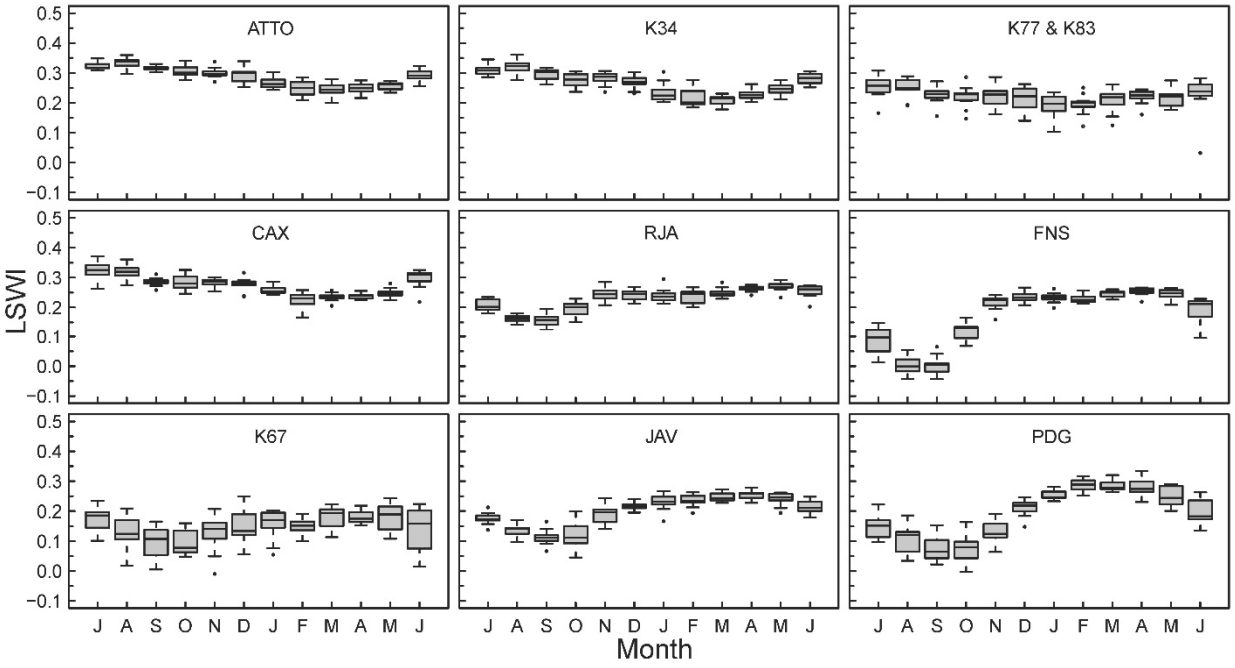

Figure S3.7 | Seasonality (July-June) of the land surface water index from 2007-2017.

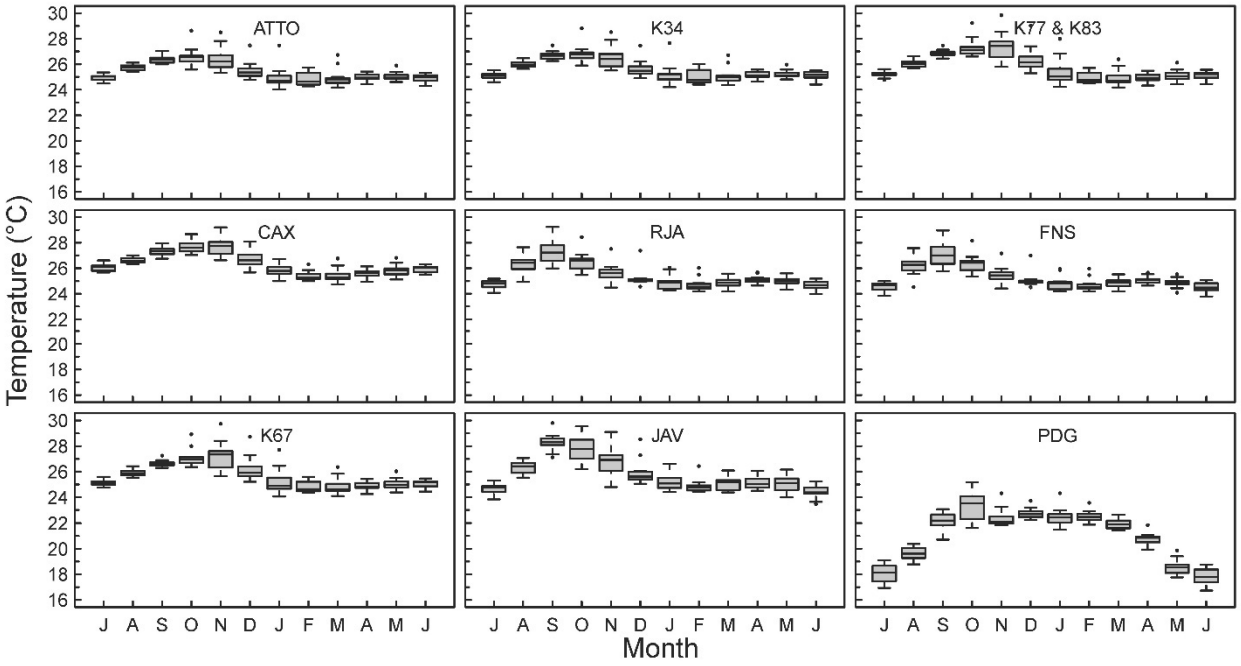

Figure S3.8 | Seasonality (July-June) of temperature for 2007-2017.

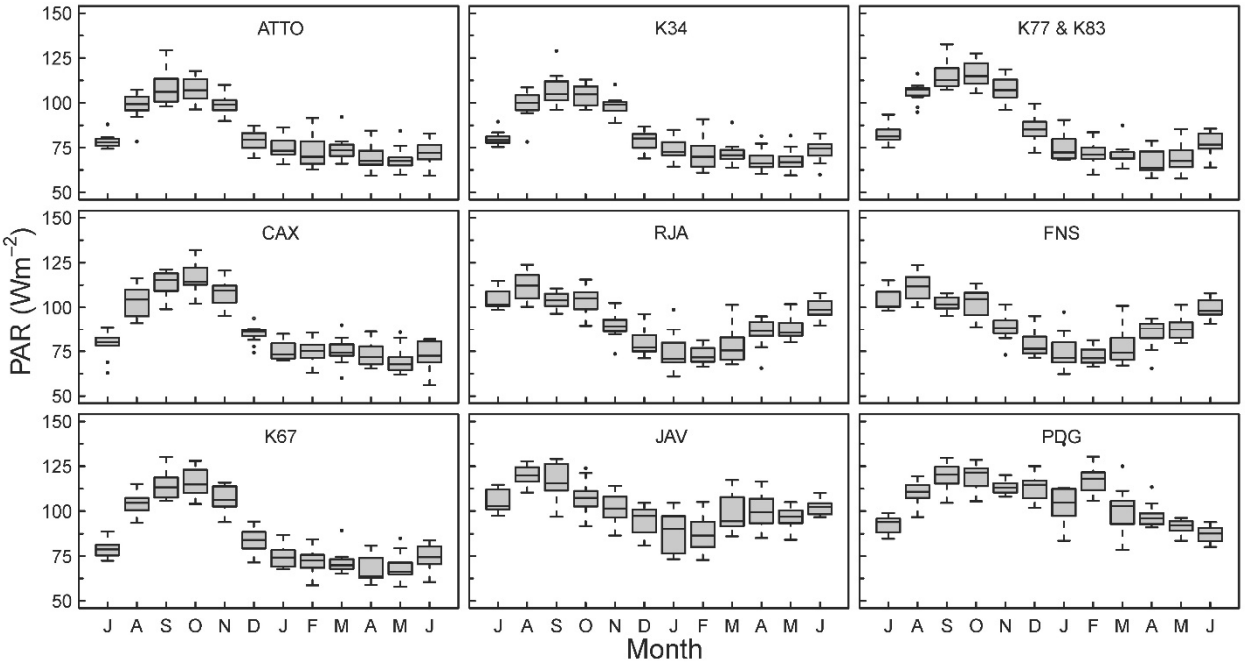

Figure S3.9 | Seasonality (July-June) of photosynthetically active radiation for 2007-2017.

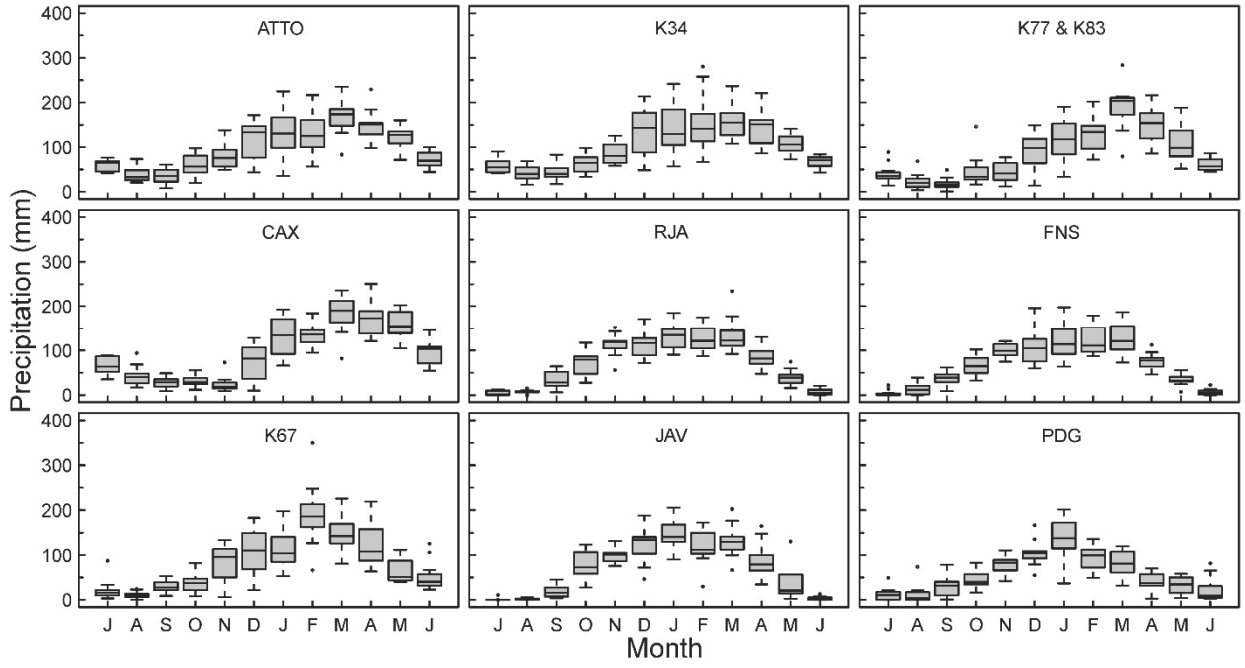

Figure S3.10 | Seasonality (July-June) of precipitation for 2007-2017.

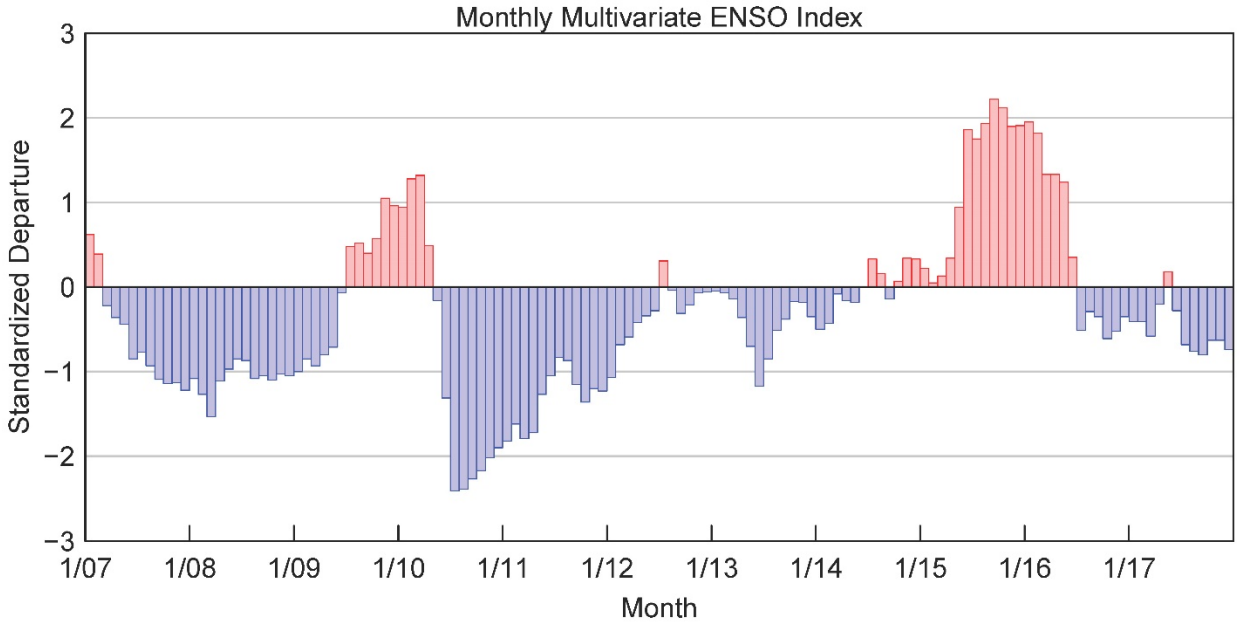

Figure S3.11 | Monthly Multivariate El Niño-Southern Oscillation Index for 2007-2017.

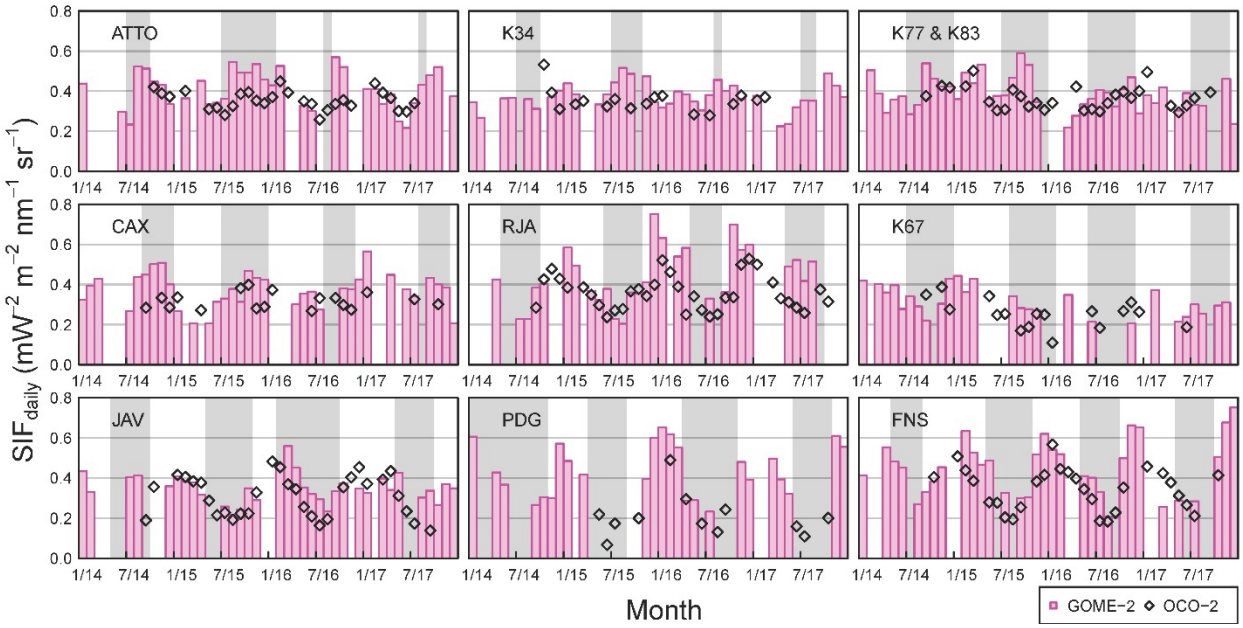

Figure S3.12 | Monthly solar-induced chlorophyll fluorescence from GOME-2 and OCO-2 for nine gridcells in South America 2014-2017. Shaded areas are months in which total precipitation was 100mm or less. SIF values are not comparable between the two platforms, but the seasonality of the data can be compared. Data for OCO-2 was available beginning in September 2014.

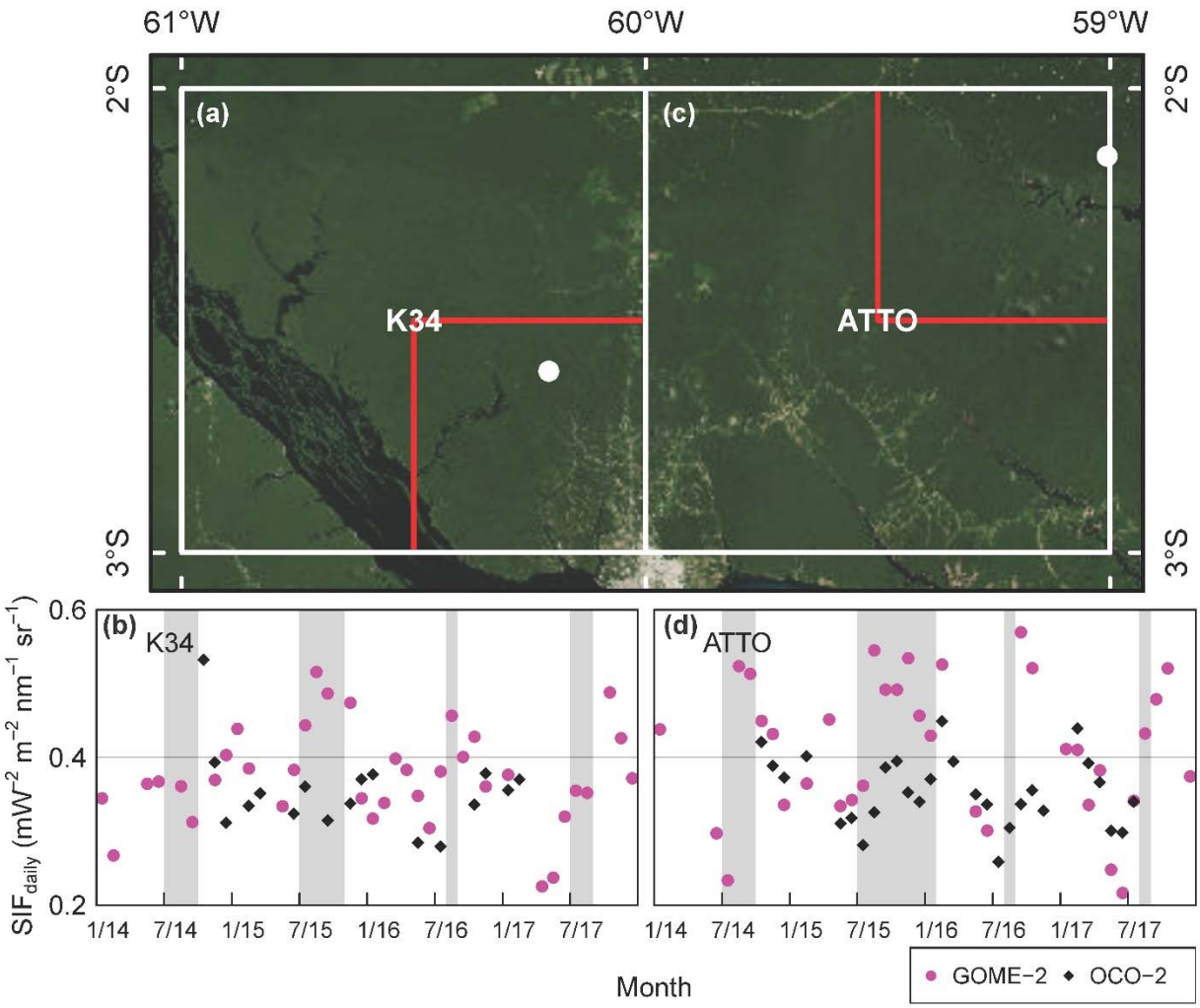

Figure S3.13 | Satellite imagery and observations of SIF for two Amazon forest gridcells during 2014-2017. In (a) and (c), the white boxes are 1° OCO-2 gridcells, the red boxes are 0.5° GOME-2 gridcells, and the white dots are the approximate locations of the eddy covariance towers. Shaded areas in (b) and (d) are dry months with <100 mm of precipitation. GOME-2 SIF data in the charts (b, d) were aggregated to 1° to match the footprint of OCO-2.

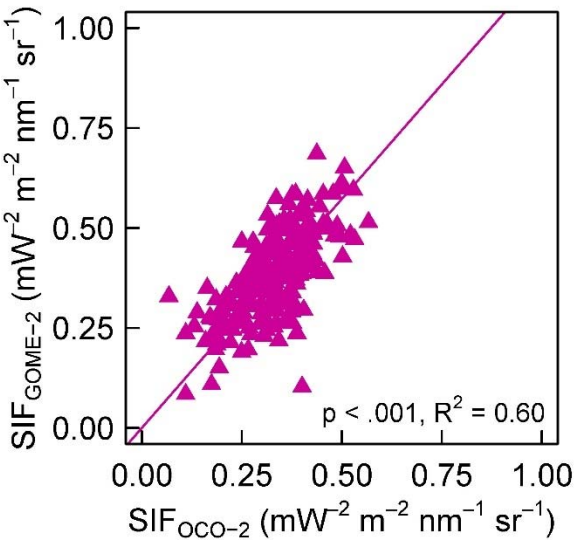

Figure S3.14 | Linear regression between monthly SIFGOME-2 and SIFOCO-2 for each site September 2014 – October 2017. SIF_{GOME-2} data was aggregated to one-degree spatial resolution to match that of SIF_{OCO-2}.

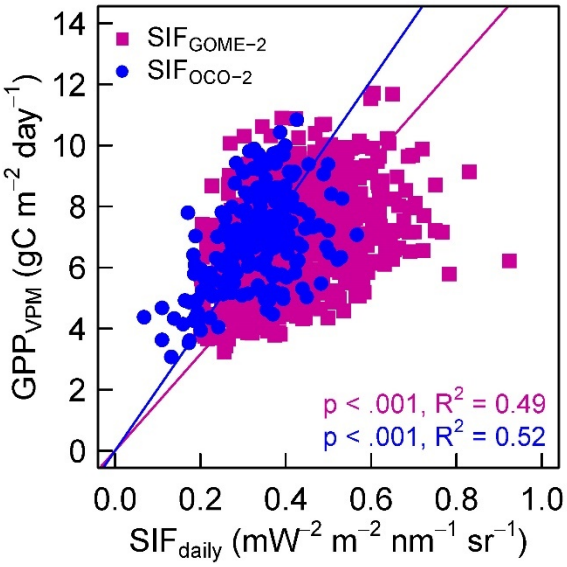

Figure S3.15 | Linear regressions between monthly GPPVPM, SIFGOME-2, and SIFOCO-2 for all sites and years. For the GPP_{VPM} and SIF_{GOME-2} regression analysis, half-degree spatial resolution data were used for 2007-2017. For the GPP_{VPM} and SIF_{OCO-2} regression analysis, one-degree spatial resolution data were used for September 2014 – October 2017.

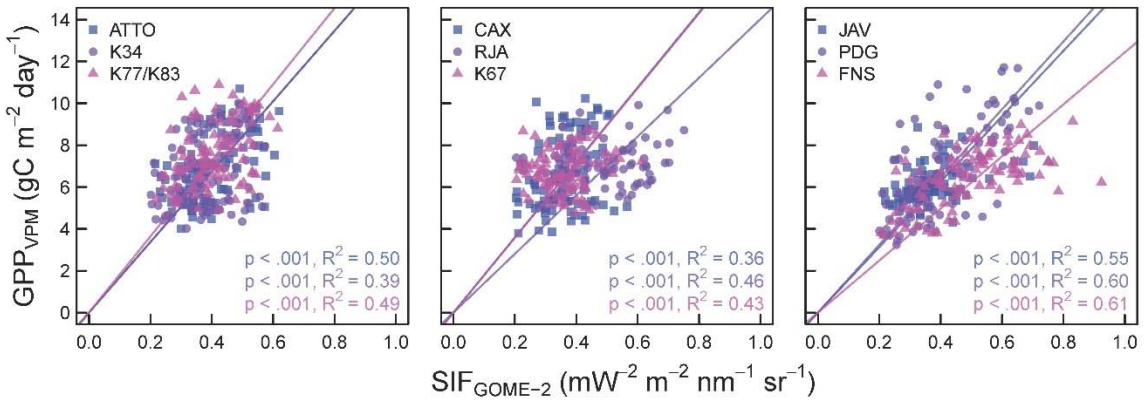

Figure S3.16 | Linear regressions between monthly GPPVPM and SIFGOME-2 for each site 2007-2017. GPP_{VPM} was aggregated to half-degree spatial resolution to match SIF_{GOME-2}.

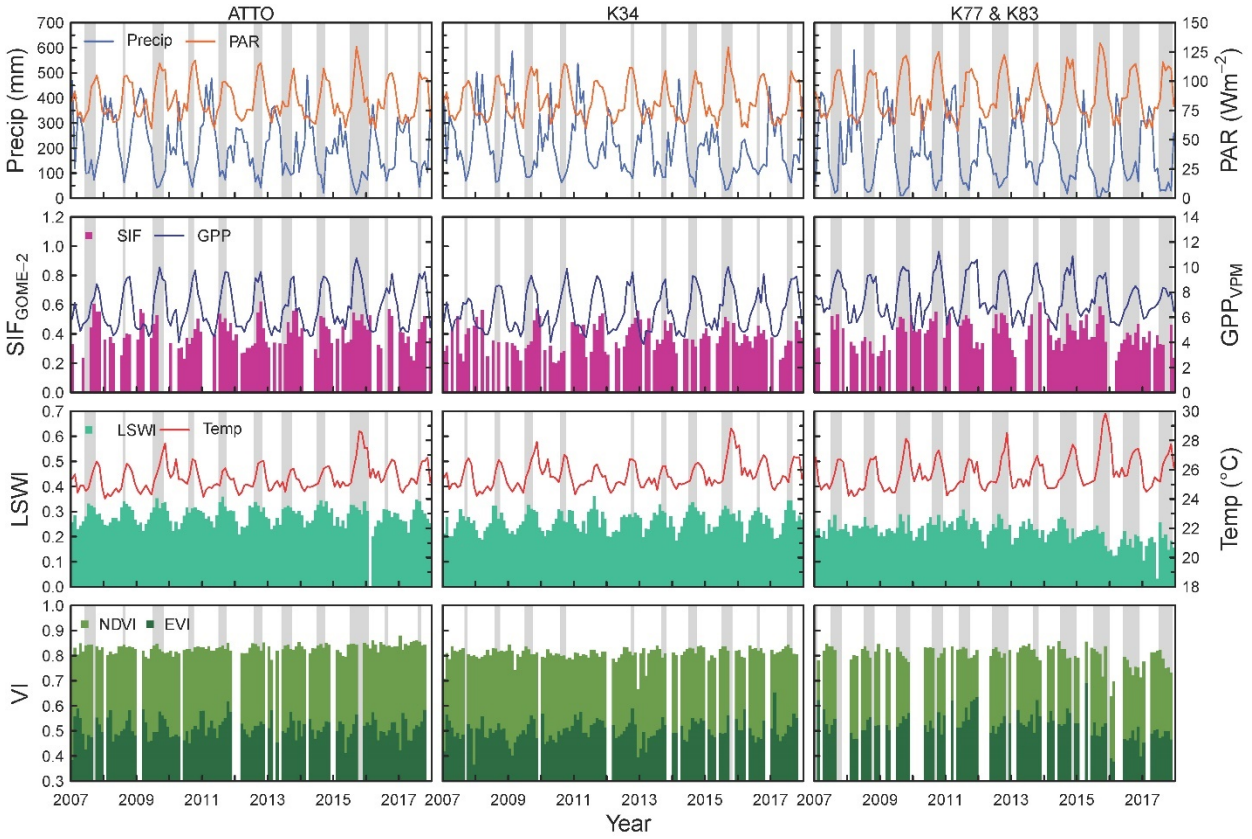

Figure S3.17 | Monthly dynamics of climate, SIF, productivity, and greenness for ATTO, K34, and K77/K83 for 2007-2017. Continuous data shown as lines. All data was aggregated or resampled to 0.5° degree to match the GOME-2 SIF data. Shown are monthly precipitation (mm), photosynthetically active radiation (PAR; Wm^{-2}), solar induced chlorophyll fluorescence (SIF; mw^{-2} m^{-2} nm^{-1} sr^{-1}), gross primary production (GPP; gC m^{-2} day^{-1}), land surface water index (LSWI), temperature (°C), and MOD13 enhanced vegetation index (EVI) and normalized vegetation difference index (NDVI).

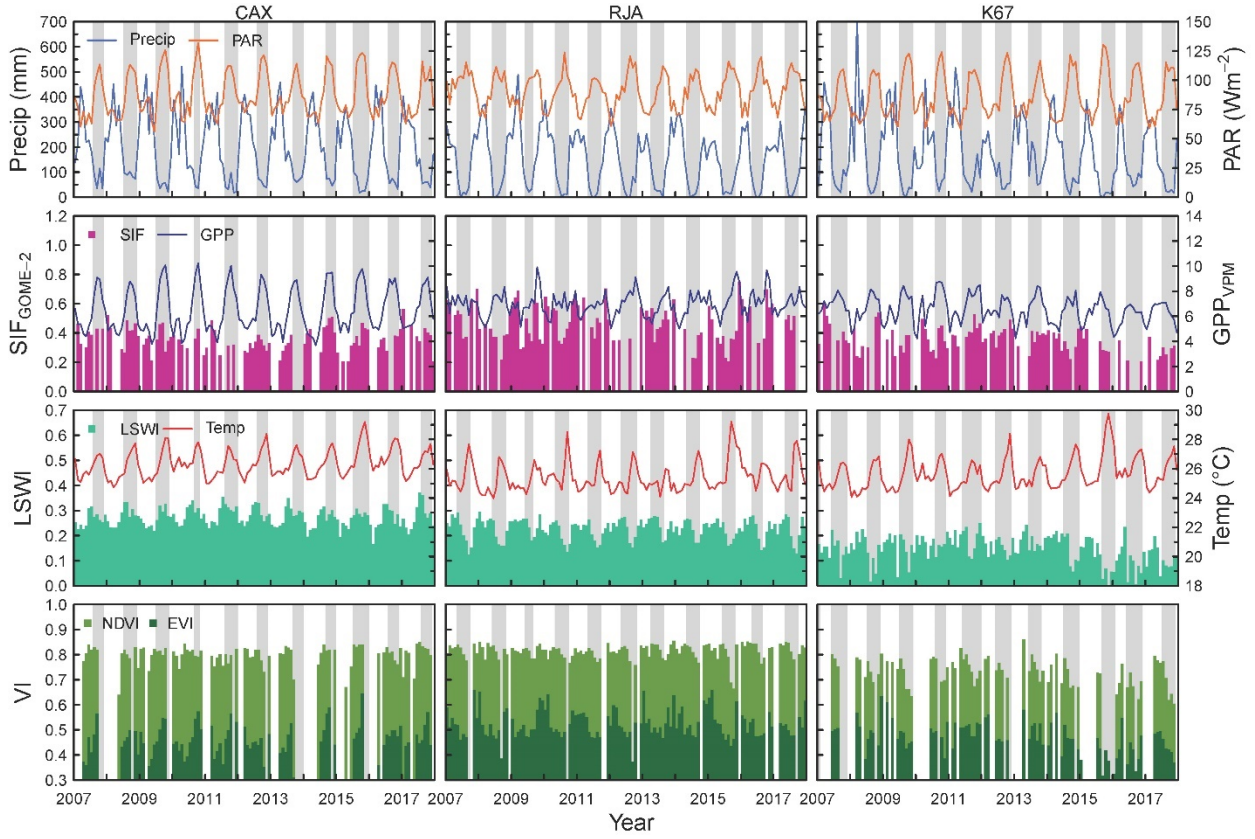

Figure S3.18 | Monthly dynamics of climate, SIF, productivity, and greenness for CAX, RJA, and K67 for 2007-2017. Continuous data shown as lines. All data was aggregated or resampled to 0.5° to match the GOME-2 SIF data. Shown are monthly precipitation (mm), photosynthetically active radiation (PAR; Wm^{-2}), solar induced chlorophyll fluorescence (SIF; mw^{-2} m^{-2} nm^{-1} sr^{-1}), gross primary production (GPP; gC m^{-2} day^{-1}), land surface water index (LSWI), temperature (°C), and MOD13 enhanced vegetation index (EVI) and normalized vegetation difference index (NDVI).

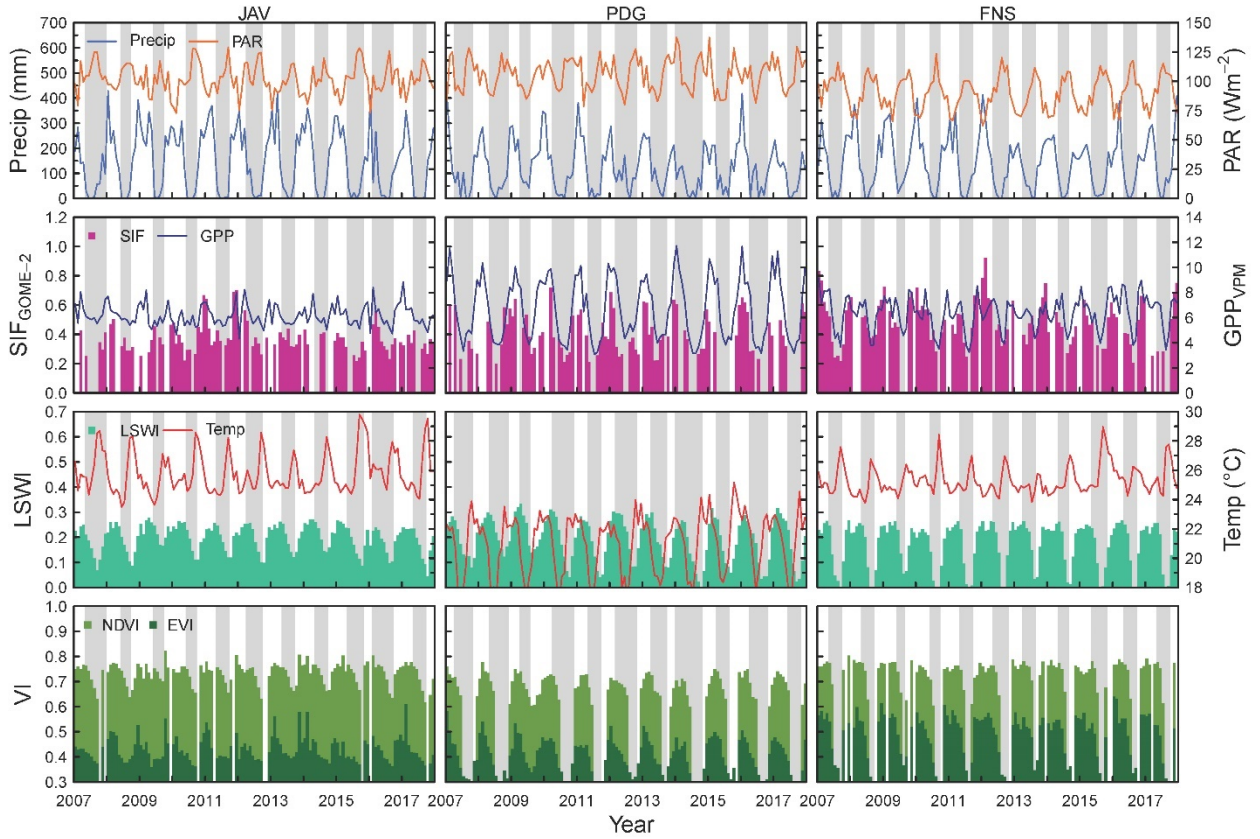

Figure S3.19 | Monthly dynamics of climate, SIF, productivity, and greenness for JAV, PDG, and FNS for 2007-2017. Continuous data shown as lines. All data was aggregated or resampled to 0.5° to match the GOME-2 SIF data. Shown are monthly precipitation (mm), photosynthetically active radiation (PAR; Wm^{-2}), solar induced chlorophyll fluorescence (SIF; mw^{-2} m^{-2} nm^{-1} sr^{-1}), gross primary production (GPP; gC m^{-2} day^{-1}), land surface water index (LSWI), temperature (°C), and MOD13 enhanced vegetation index (EVI) and normalized vegetation difference index (NDVI).

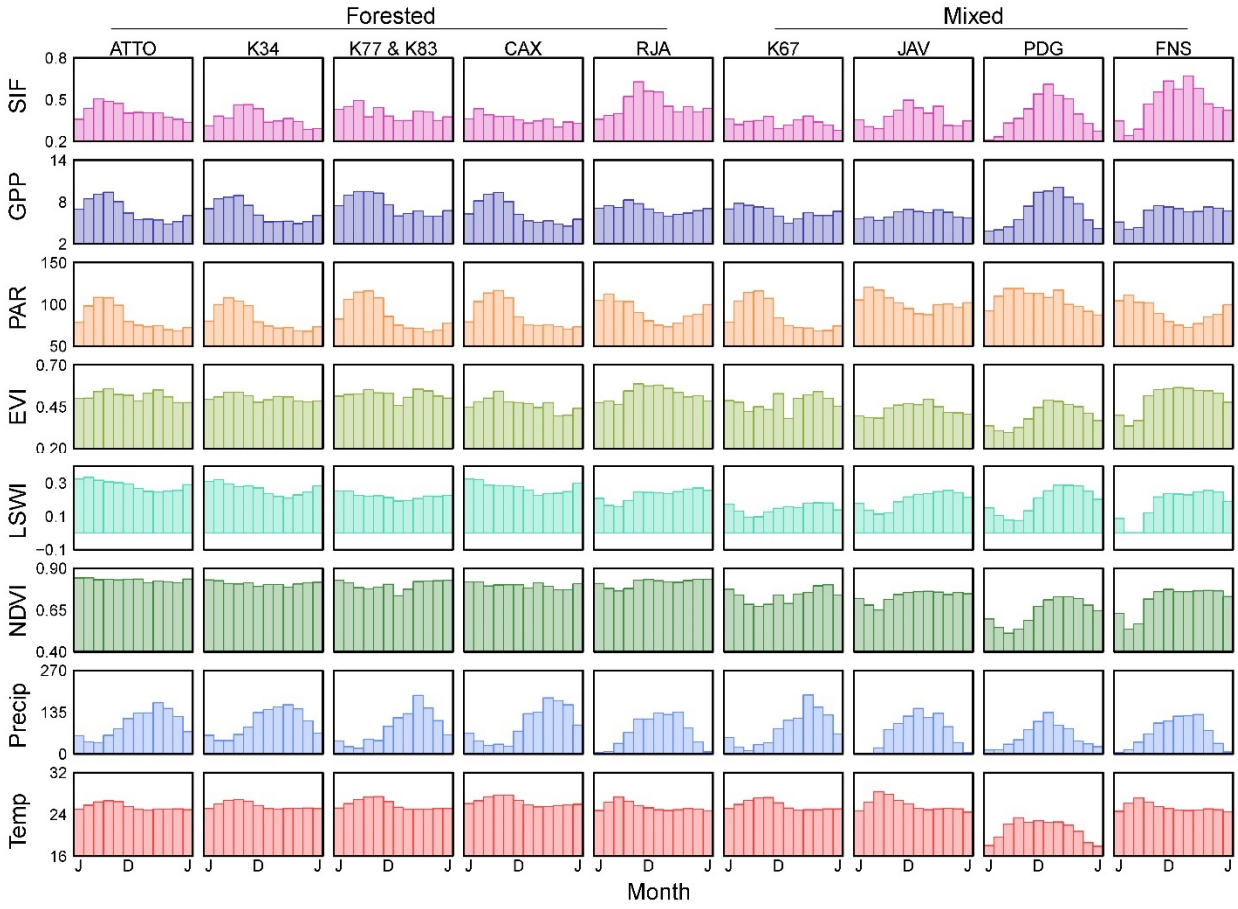

Figure S3.20 | Seasonality (July – June) of SIF, photosynthesis, greenness, and climate for 2007-2017 at nine 0.5° gridcells with 10 eddy flux tower sites. Bars are monthly means for the entire study period 2007-2017. Illustrated top to bottom are mean solar induced chlorophyll fluorescence (SIF; mw^{-2} m^{-2} nm^{-1} sr^{-1}), gross primary production (GPP; gC m^{-2} day^{-1}), photosynthetically active radiation (PAR; Wm^{-2}), MOD13 enhanced vegetation index (EVI), land surface water index (LSWI), MOD13 normalized vegetation difference index (NDVI), precipitation (mm), and temperature (°C).

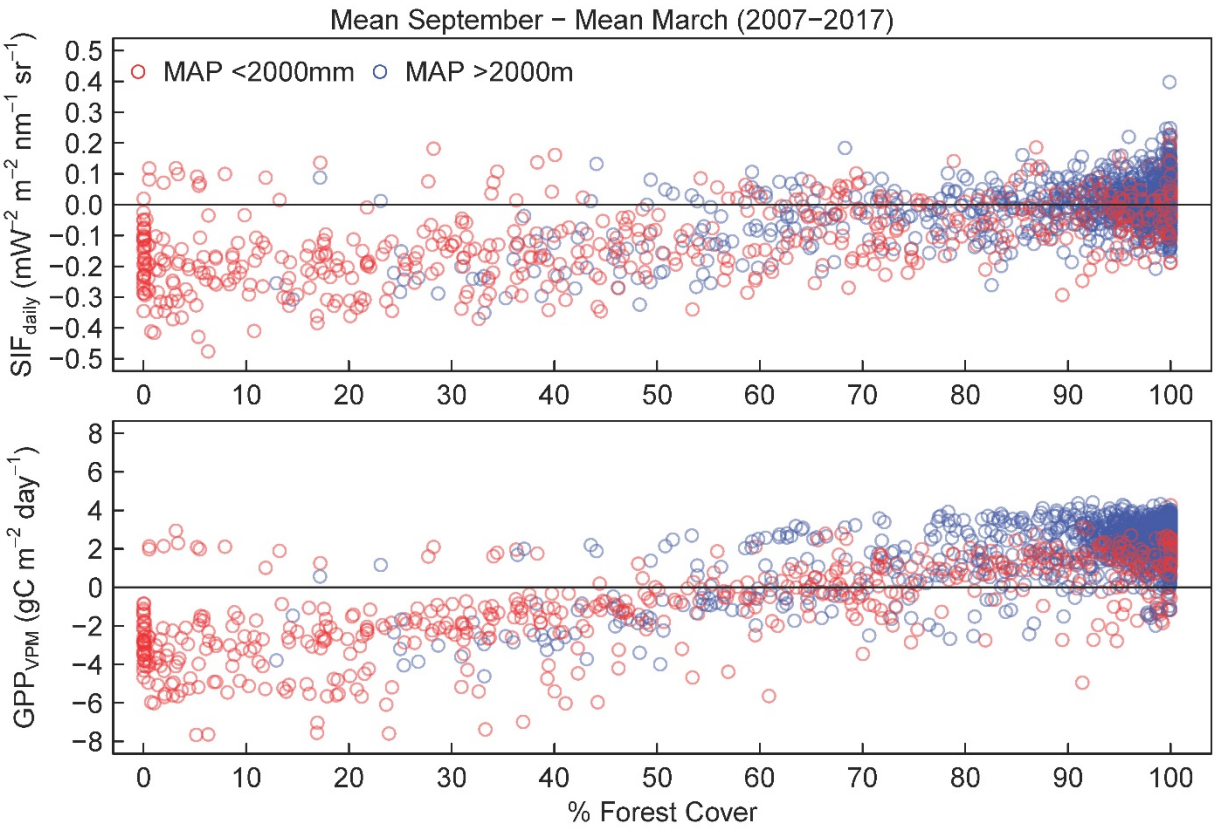

Figure S3.21 | The difference between mean September SIF and GPP and mean March SIF and GPP 2007-2017 for all gridcells in the Amazon Basin. Positive values indicate that SIF or GPP was higher on average in September. Negative values indicate that SIF or GPP was higher on average in March. Only gridcells that were consistently >80% or <80% were used.

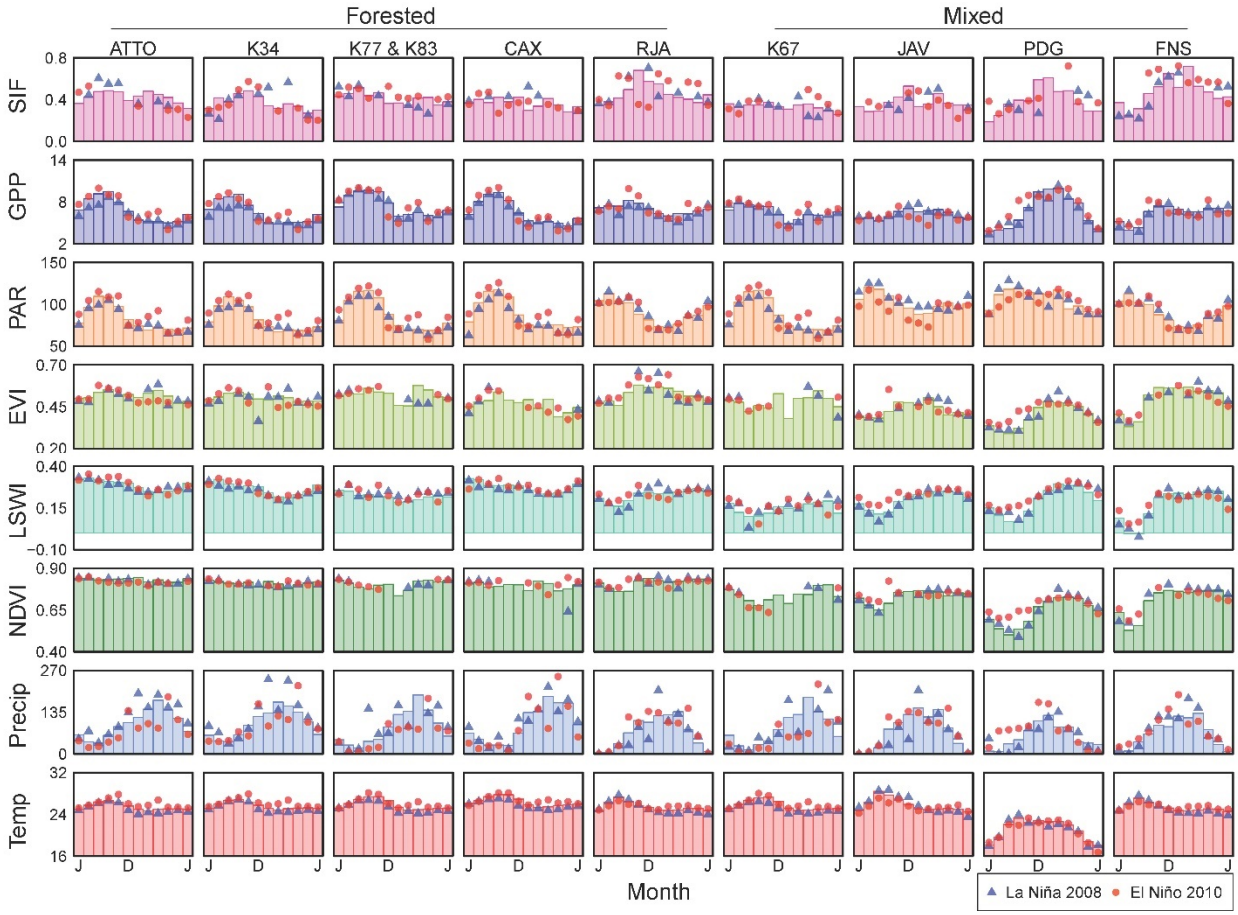

Figure S3.22 | Seasonality (July – June) of SIF, photosynthesis, greenness, and climate for 2007-2017, La Niña 2008, and El Niño 2010 at nine 0.5° gridcells with 10 eddy flux tower sites. Illustrated top to bottom are mean solar induced chlorophyll fluorescence (SIF; mw^{-2} m^{-2} nm^{-1} sr^{-1}), gross primary production (GPP; gC m^{-2} day^{-1}), photosynthetically active radiation (PAR; Wm^{-2}), MOD13 enhanced vegetation index (EVI), land surface water index (LSWI), MOD13 normalized vegetation difference index (NDVI), precipitation (mm), and temperature (°C).

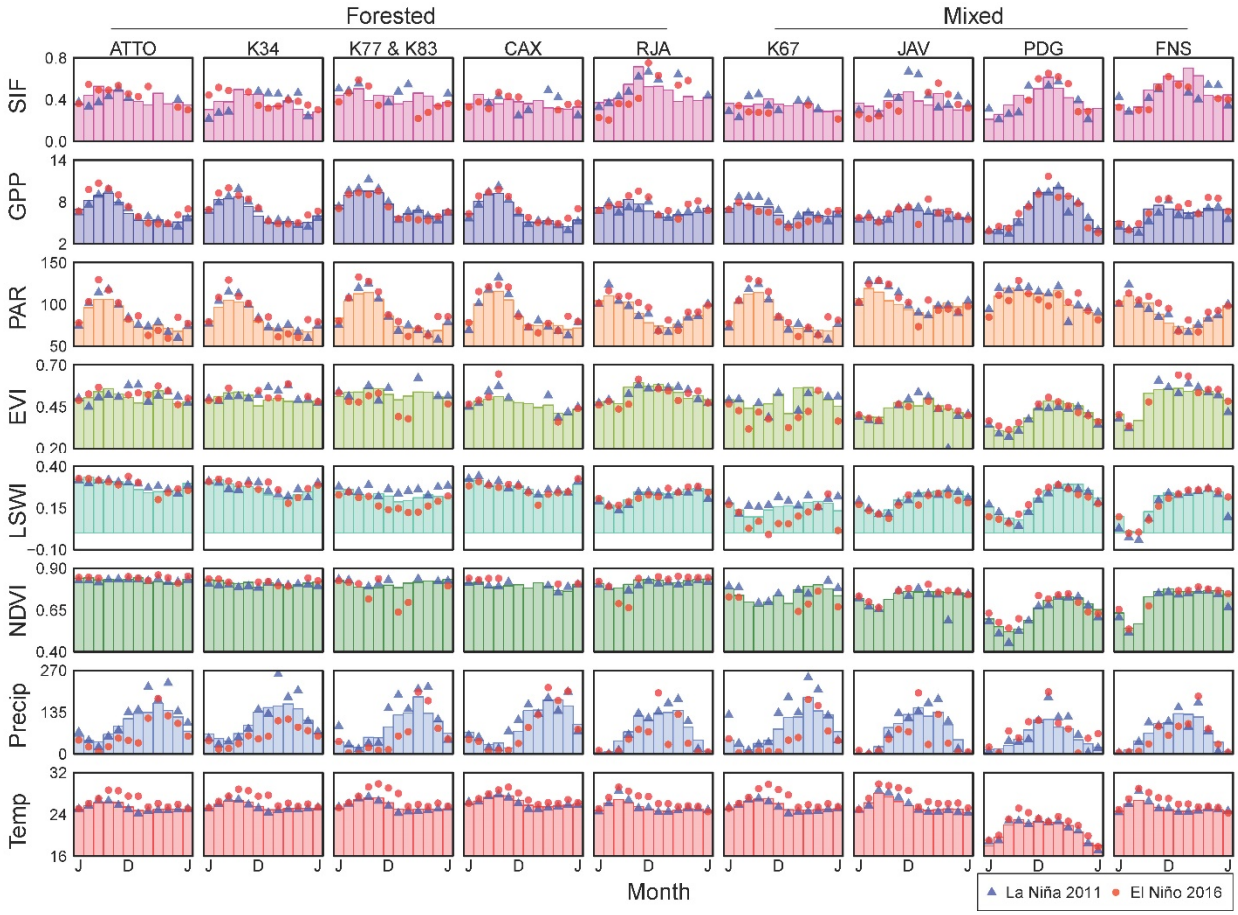

Figure S3.23 | Seasonality (July – June) of SIF, photosynthesis, greenness, and climate for 2007-2017, La Niña 2011, and El Niño 2016 at nine 0.5° gridcells with 10 eddy flux tower sites. Illustrated top to bottom are mean solar induced chlorophyll fluorescence (SIF; mw-2 m-2 nm-1 sr-1), gross primary production (GPP; gC m-2 day-1), photosynthetically active radiation (PAR; Wm-2), MOD13 enhanced vegetation index (EVI), land surface water index (LSWI), MOD13 normalized vegetation difference index (NDVI), precipitation (mm), and temperature (°C).

Table S3.1. Summary of nine study sites. The site name, latitude, and longitude of each eddy tower. The percentage of forest cover within each 0.5° (GOME-2) and 1.0° (OCO-2) pixel, and the net change in forest cover over the study period (2007-2017).

Site	Latitude	Longitude	2017 Forest Cover 0.5° (% Δ 2007-17)	2017 Forest Cover 1° (% Δ 2007-17)
ATTO	-2.1458	-59.006	99.3% (+0.1%)	99.2% (-0.2%)
K34	-2.609	-60.209	96.2% (-0.1%)	88.4% (-0.3%)
K77; K83	-3.0202; -3.01700	-54.8885; -54.97070	91.3% (-6.3%)	90.3% (-8.0%)
CAX	-1.7483	-51.454	83.1% (-0.7%)	85.9% (-1.2%)
RJA	-10.078	-61.933	82.8% (-2.7%)	73.47% (+0.2%)
K67	-2.857	-54.959	56.3% (-29.1%)	49.8% (-12.6%)
JAV	-9.8244	-50.159	52.3% (-5.6%)	32.0% (-19.6%)
PDG	-21.619	-47.65	19.8% (-9.7%)	14.4% (-30.2%)
FNS	-10.762	-62.357	14.3% (-31.8%)	21.1% (-26.9%)

Table S3.2. One-sample t-test results for September in the 2008 La Niña and 2010 El Niño and the percentage difference between normal and ENSO event for SIF, GPP, EVIn, and NDVIn. One-sample t-tests were conducted to determine if the difference between September SIF, GPP, EVIn, and NDVIn during the ENSO phases and the mean for all remaining Septembers was significantly different from zero. The distributions were illustrated in Fig. 4.

Amazon Basin								
September	ENSO	Gridcells (n)	Δ	95% CI	t-value	p-value	Norm	% Δ
2007 SIF	2007-2008 La Niña	1960	-0.045	-0.05, -0.04	-15.70	<0.001	0.41	-10.98%
2007 GPP		195434	-0.434	-0.44, -0.43	-250.57	<0.001	11.84	-3.67%
2007 EVIn		188637	-0.017	-0.018, -0.017	-395.13	<0.001	0.437	-3.89%
2007 NDVIn		188639	-0.014	-0.014, -0.014	-202.4	<0.001	0.737	-1.90%
2009 SIF	2009-2010 El Niño	1967	0.049	0.04, 0.05	18.81	<0.001	0.41	11.95%
2009 GPP		195436	0.49	0.49, 0.49	304.89	<0.001	11.84	4.14%
2009 EVIn		193787	0.012	0.012, 0.012	250.07	<0.001	0.437	2.75%
2009 NDVIn		193777	0.014	0.14, 0.14	195.16	<0.001	0.737	1.90%
Gridcells >80% Forest and >2000mm MAP								
2007 SIF	2007-2008 La Niña	1169	-0.031	-0.04, -0.02	-9.20	<0.001	0.466	-6.65%
2007 GPP		109376	-0.548	-0.55, -0.54	-253.94	<0.001	8.68	-6.31%

2007 EVIn		108004	-0.019	-0.19, -0.19	-501.46	<0.001	0.487	-3.90%
2007 NDVIn		108004	-0.012	-0.013, -0.013	-229.79	<0.001	0.818	-1.47%
2009 SIF	2009-2010 El Niño	1166	0.041	0.04, 0.05	13.24	<0.001	0.466	8.80%
2009 GPP		109379	0.502	0.50, 0.51	252.05	<0.001	8.68	5.78%
2009 EVIn		109120	0.009	0.009, 0.009	260.59	<0.001	0.487	1.85%
2009 NDVIn		109120	0.006	0.006, 0.006	158.82	<0.001	0.818	0.73%

Table S3.3. One-sample t-test results for September in the 2011 La Niña and 2016 El Niño and the percentage difference between normal and ENSO event for SIF, GPP, EVIn, and NDVIn. One-sample t-tests were conducted to determine if the difference between September SIF, GPP, EVIn, and NDVIn during the ENSO phases and the mean for all remaining Septembers was significantly different from zero. The distributions were illustrated in Fig. 5.

Amazon Basin								
September	ENSO	Gridcells (n)	Δ	95% CI	t-value	p-value	Norm	% Δ
2010 SIF	2010-2011 La Niña	1966	-0.047	-0.05, -0.04	-18.89	<0.001	0.41	-11.46%
2010 GPP		195434	-0.025	-0.029, -0.022	-13.90	<0.001	11.84	-0.21%
2010 EVIn		193009	-0.021	-0.021, -0.021	-395.20	<0.001	0.437	-4.81%
2010 NDVIn		193012	-0.025	-0.025, -0.025	-325.26	<0.001	0.737	-3.39%
2015 SIF	2015-2016 El Niño	1967	0.006	0.01, 0.01	3.01	<0.01	0.41	1.46%
2015 GPP		195431	0.389	0.39, 0.39	218.16	<0.001	11.84	3.29%
2015 EVIn		193639	0.002	0.002, 0.002	37.02	<0.001	0.437	0.46%
2015 NDVIn		193633	0.008	0.007, 0.008	122.82	<0.001	0.737	1.09%
Gridcells >80% Forest and >2000mm MAP								
2010 SIF	2010-2011 La Niña	1164	-0.045	-0.05, -0.04	-15.38	<0.001	0.466	-9.66%
2010 GPP		109378	0.107	0.102, 0.111	46.53	<0.001	8.68	1.23%
2010 EVIn		108643	-0.019	-0.019, -0.019	-441.16	<0.001	0.487	-3.90%
2010 NDVIn		108643	-0.019	-0.019, -0.019	-373.66	<0.001	0.818	-2.32%
2015 SIF	2015-2016 El Niño	1156	0.007	0.001, 0.01	2.74	<0.01	0.466	1.50%
2015 GPP		109377	0.434	0.429, 0.439	183.64	<0.001	8.68	5.00%
2015 EVIn		109092	-0.002	-0.002, -0.002	-60.80	<0.001	0.487	-0.41%

2015 NDVIn		109092	0.005	0.005, 0.005	136.17	<0.001	0.818	0.61%

Table S3.4. One-sample t-test results for dry season during the 2008 La Niña and 2010 El Niño and the percentage difference between normal and ENSO event for SIF, GPP, EVIn, and NDVIn. One-sample t-tests were conducted to determine if the difference between dry-season (June through October) SIF, GPP, EVIn, and NDVIn during the ENSO phases and the mean for all remaining dry seasons was significantly different from zero. The distributions were illustrated in Fig. 6.

Amazon Basin								
Dry Season	ENSO	Gridcells (n)	Δ	95% CI	t-value	p-value	Norm	% Δ
2007 SIF	2007-2008 La Niña	1967	-0.002	-0.004, 0.001	-1.28	0.202	0.388	-0.52%
2007 GPP		195436	-0.231	-0.23, -0.23	-209.02	<0.001	6.824	-3.39%
2007 EVIn		194285	-0.011	-0.011, -0.011	-339.39	<0.001	0.445	-2.47%
2007 NDVIn		194012	-0.006	-0.006, -0.006	-129.65	<0.001	0.758	-0.79%
2009 SIF	2009-2010 El Niño	1967	0.026	0.02, 0.03	21.61	<0.001	0.388	6.70%
2009 GPP		195437	0.189	0.19, 0.19	178.75	<0.001	6.824	2.77%
2009 EVIn		194279	0.005	0.005, 0.005	155.23	<0.001	0.445	1.12%
2009 NDVIn		194226	0.006	0.006, 0.006	111.99	<0.001	0.758	0.79%
Gridcells with >80% Forest and >2000mm MAP								
2007 SIF	2007-2008 La Niña	1148	0.003	0.001, 0.006	-2.02	0.043	0.43	0.70%
2007 GPP		109378	-0.321	-0.32, -0.32	-235.23	<0.001	7.777	-4.13%
2007 EVIn		109213	-0.013	-0.013,-0.013	-515.31	<0.001	0.487	-2.67%
2007 NDVIn		108946	-0.006	-0.006, -0.006	-221.46	<0.001	0.829	-0.72%
2009 SIF	2009-2010 El Niño	1148	0.023	0.02, 0.03	15.50	<0.001	0.43	5.35%
2009 GPP		109379	0.127	0.12, 0.13	100.58	<0.001	7.777	1.63%
2009 EVIn		108808	0.004	0.003,0.004	146.21	<0.001	0.487	0.82%
2009 NDVIn		108731	<0.001	<0.001, <0.001	9.27	<0.001	0.829	0.12%

Table S3.5. One-sample t-test results for dry season during the 2011 La Niña and 2016 El Niño and the percentage difference between normal and ENSO event for SIF, GPP, EVIn, and NDVIn. One-sample t-tests were conducted to determine if the difference between dry-season (June through October) SIF, GPP, EVIn, and NDVIn during the ENSO phases and the mean for all

remaining dry seasons was significantly different from zero. The distributions were illustrated in Fig. 7.

Amazon Basin								
Dry Season	ENSO	Gridcells (n)	Δ	95% CI	t-value	p-value	Norm	% Δ
2010 SIF	2010-2011 La Niña	1967	-0.009	-0.01, -0.01	-7.70	<0.001	0.388	-2.32%
2010 GPP		195436	-0.005	-0.01, -0.01	-3.98	<0.001	6.824	-0.07%
2010 EVIn		194706	-0.011	-0.011, -0.011	-286.27	<0.001	0.445	-2.47%
2010 NDVIn		194767	-0.014	-0.014, -0.013	-255.42	<0.001	0.758	-1.85%
2015 SIF	2015-2016 El Niño	1967	-0.014	-0.01, -0.01	-12.89	<0.01	0.388	-3.61%
2015 GPP		195432	0.151	0.15, 0.15	132.74	<0.001	6.824	2.21%
2015 EVIn		193862	-0.002	-0.002, 0.001	-41.80	<0.001	0.445	-0.45%
2015 NDVIn		193764	0.002	0.002, 0.002	45.9	<0.001	0.758	0.26%
Gridcells with >80% Forest and >2000mm MAP								
2010 SIF	2010-2011 La Niña	1148	-0.006	-0.01, -0.01	-3.90	<0.001	0.43	-1.40%
2010 GPP		109379	0.006	0.003, 0.008	4.53	<0.001	7.777	0.08%
2010 EVIn		109100	-0.009	-0.009, -0.009	-361.62	<0.001	0.487	-1.85%
2010 NDVIn		109087	-0.009	-0.009, -0.009	-335.81	<0.001	0.829	-1.09%
2015 SIF	2015-2016 El Niño	1148	-0.019	-0.02, 0.02	-14.46	<0.001	0.43	-4.42%
2015 GPP		109379	0.211	0.21, 0.21	143.67	<0.001	7.777	2.71%
2015 EVIn		108804	-0.004	-0.005, -0.004	-185.03	<0.001	0.487	-0.82%
2015 NDVIn		108618	<0.001	<0.001, <0.001	7.05	<0.001	0.829	0.12%

Chapter 4: TROPOMI reveals dry-season increase of solar-induced chlorophyll fluorescence in the Amazon forest

Abstract

Photosynthesis of the Amazon rainforest plays an important role in the regional and global carbon cycles, but despite considerable *in situ* and space-based observations it has been intensely debated whether there is a dry-season increase in greenness and photosynthesis of the moist tropical Amazonian forests. Solar-induced chlorophyll fluorescence (SIF), which is emitted by chlorophyll, has a strong positive linear relationship with photosynthesis at the canopy scale. Recent advancements have allowed us to observe SIF globally with Earth observation satellites. Here we show that forest SIF did not decrease in the early dry season and increased substantially in the late dry season and early part of wet season using SIF data from the TROPOspheric Monitoring Instrument (TROPOMI), which has unprecedented spatial resolution and near-daily global coverage. Using *in situ* CO_2 eddy flux data, we also show that cloud cover rarely affects photosynthesis at TROPOMI's midday overpass, a time when the forest canopy is most often light-saturated. The observed dry-season increases of forest SIF are not strongly affected by sun-sensor geometry, which was attributed as creating a pseudo dry-season green-up in the surface reflectance data. Our results provide strong evidence that greenness, SIF, and photosynthesis of the tropical Amazonian forest increases during the dry season.

4.1 Main

It has been heavily debated whether there is a dry-season green-up and increase in photosynthesis of the moist tropical Amazon forest (Huete et al. 2006; Morton et al. 2014; Myneni et al. 2007; Saleska et al. 2016; Xiao et al. 2006) among the remote sensing and ecological research communities. The answer to this question has important implications for understanding Earth's

carbon fluxes and the impact of climate variability and climate change on those fluxes. However, a resolution to this debate has been delayed due to arguments that the geometry between the satellite sensors and the sun causes a pseudo-seasonality in the reflectance data (Galvão et al. 2011; Morton et al. 2014).

Traditionally, spaceborne earth surface reflectance data over the terrestrial biosphere have been used to calculate vegetation indices, which are useful for observing changes in canopy "greenness" and estimating chlorophyll content at large spatial scales (Xiao et al. 2006; Xiao et al. 2005). However, vegetation indices do not provide direct information on the fate of sunlight absorbed by chlorophyll (absorbed photosynthetically active radiation; $APAR_{chl}$), whose individual photons take one of three pathways: photosynthesis, heat dissipation, and chlorophyll fluorescence (Genty et al. 1989). Under favorable conditions, most $APAR_{chl}$ is used for photosynthesis and a small amount ($\leq$ ~2%) is emitted by chlorophyll as fluorescence in the red and far-red portion of the electromagnetic spectrum (~650 – 800 nm), which is created by the de-excitation of absorbed photons in all living plants (Baker 2008).

Recently, quantification of the emission of solar-induced chlorophyll fluorescence (SIF) has become feasible from space, providing ample new opportunities to investigate the functioning of the photosynthetic machinery from remote sensing platforms (Frankenberg et al. 2011; Frankenberg et al. 2014; Joiner et al. 2011). SIF retrievals require high spectral resolution and signal-to-noise ratio, and the only satellite instruments that have met these requirements were designed for atmospheric remote sensing, such as the Greenhouse Gases Observing Satellite (GOSAT), Global Ozone Monitoring Experiment 2 (GOME-2), and Orbiting Carbon Observatory 2 (OCO-2) (Guanter et al. 2012; Joiner et al. 2016; Lee et al. 2013; Sun et al. 2018). Although the global SIF data sets developed from these satellite observations have provided valuable insight

into vegetation dynamics on Earth's surface, their coarse spatial and temporal resolutions have not sufficiently resolved some important questions about the spatial distribution and temporal variability of SIF and photosynthesis on Earth. SIF is not a direct measure of photosynthesis, but satellite- and *in situ*-observed SIF has been shown to have a strong positive linear relationship with photosynthesis at the canopy scale (Guanter et al. 2012; Sun et al. 2018; Yang et al. 2018b), implying that changes in canopy SIF indicate changes in photosynthesis in the same direction (Porcar-Castell et al. 2014; Verma et al. 2017). The TROPOspheric Monitoring Instrument (TROPOMI), a spectrometer onboard the Sentinel-5 Precursor satellite launched in October 2017 by the European Space Agency, enables a step-change in SIF research, providing unprecedented high spatial and temporal resolution SIF observations that can address many of these important questions (Zuromski et al. 2018).

Here we report and analyze TROPOMI SIF data from March 2018 to June 2019 over the Amazon. TROPOMI's high spatial and temporal resolution reveals previously unknown details on the spatial distribution of SIF in the Amazon (Fig. 4.1A-C) and enables us to track SIF for forests and non-forests over time (Fig. 4.2A, SI Appendix, Fig. 4.S1-4). We show new evidence that there is an overall dry-season increase in photosynthesis by Amazonian forests (Fig. 4.2A), where there was relatively little change in SIF in the early dry season (June – July), but a substantial increase in SIF in the late dry season (September – October) (Fig. 4.1A-C, Fig. 4.2A). Middle dry-season TROPOMI SIF in Fig. 4.1B, a point in time when the difference between forest and non-forest SIF is greatest, mimics the percentage of forest cover in each TROPOMI gridcell shown in Fig. 4.1F. The Amazon River and its tributaries in the northern part of the basin are also evident in Fig. 4.1A-C where surface water induces low SIF values. Wet-season SIF for seasonally moist forests (<2000 mm mean annual precipitation (MAP)) was higher than SIF for moist forests (<2000 mm MAP),

which indicated that perhaps the productivity of seasonally moist forests was water limited (Fig. 4.2). The ~2000 mm MAP threshold has previously been found to determine whether water is a factor limiting photosynthesis in tropical forests (Guan et al. 2015).

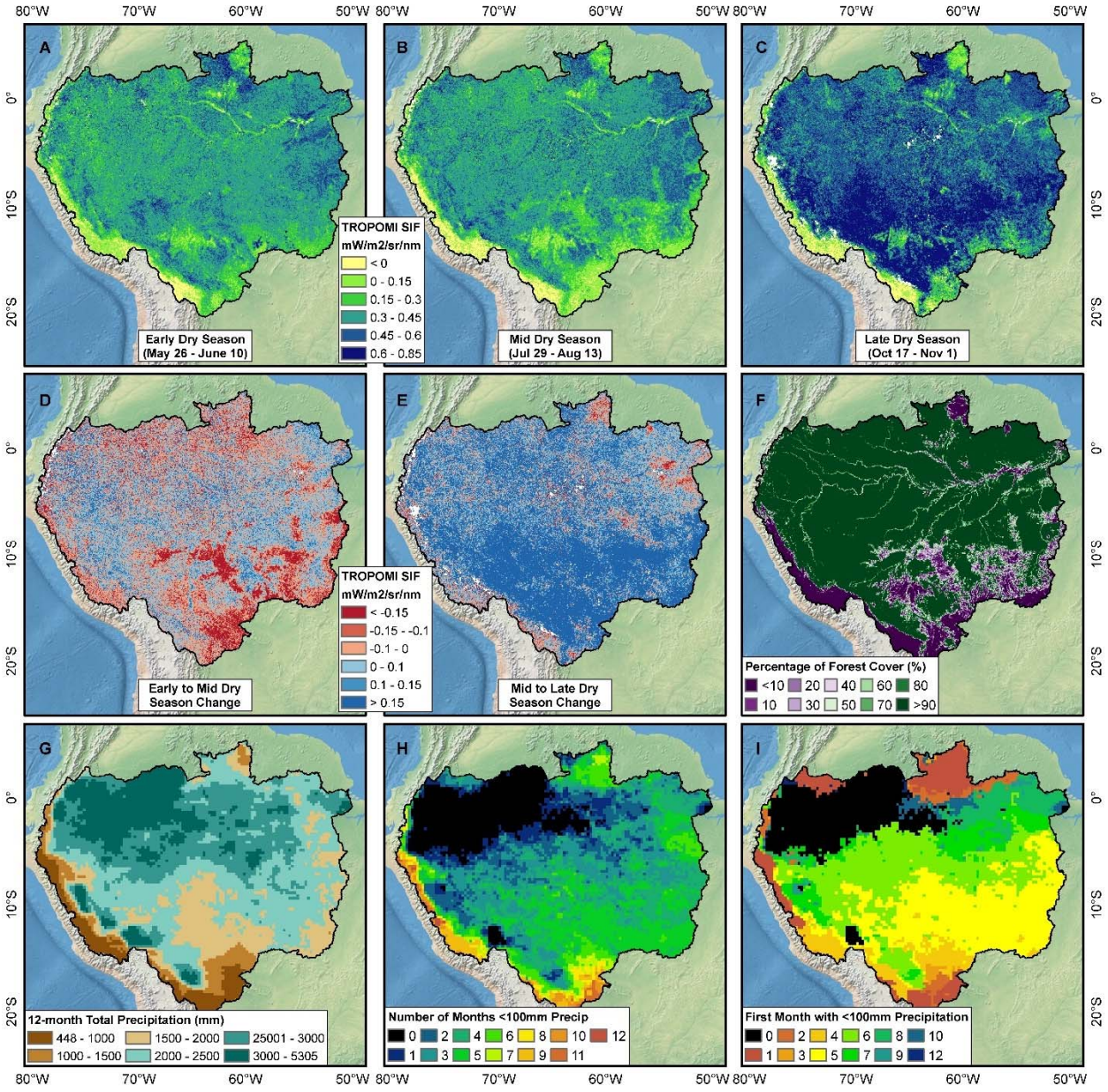

Figure 4.1 | Solar-induced chlorophyll fluorescence, forest cover, and precipitation in the Amazon Basin. SIF during the early (A), mid (B), and late (C) dry season. (D) Mid minus early dry-season SIF. (E) Late minus mid dry-season SIF. (F) Percentage forest cover in each TROPOMI 0.05° pixel. (G) Total precipitation March 2018 – February 2019. (H) Number of months with <100mm of precipitation. (I) First month with <100mm precipitation. (I) First month with <100mm precipitation.

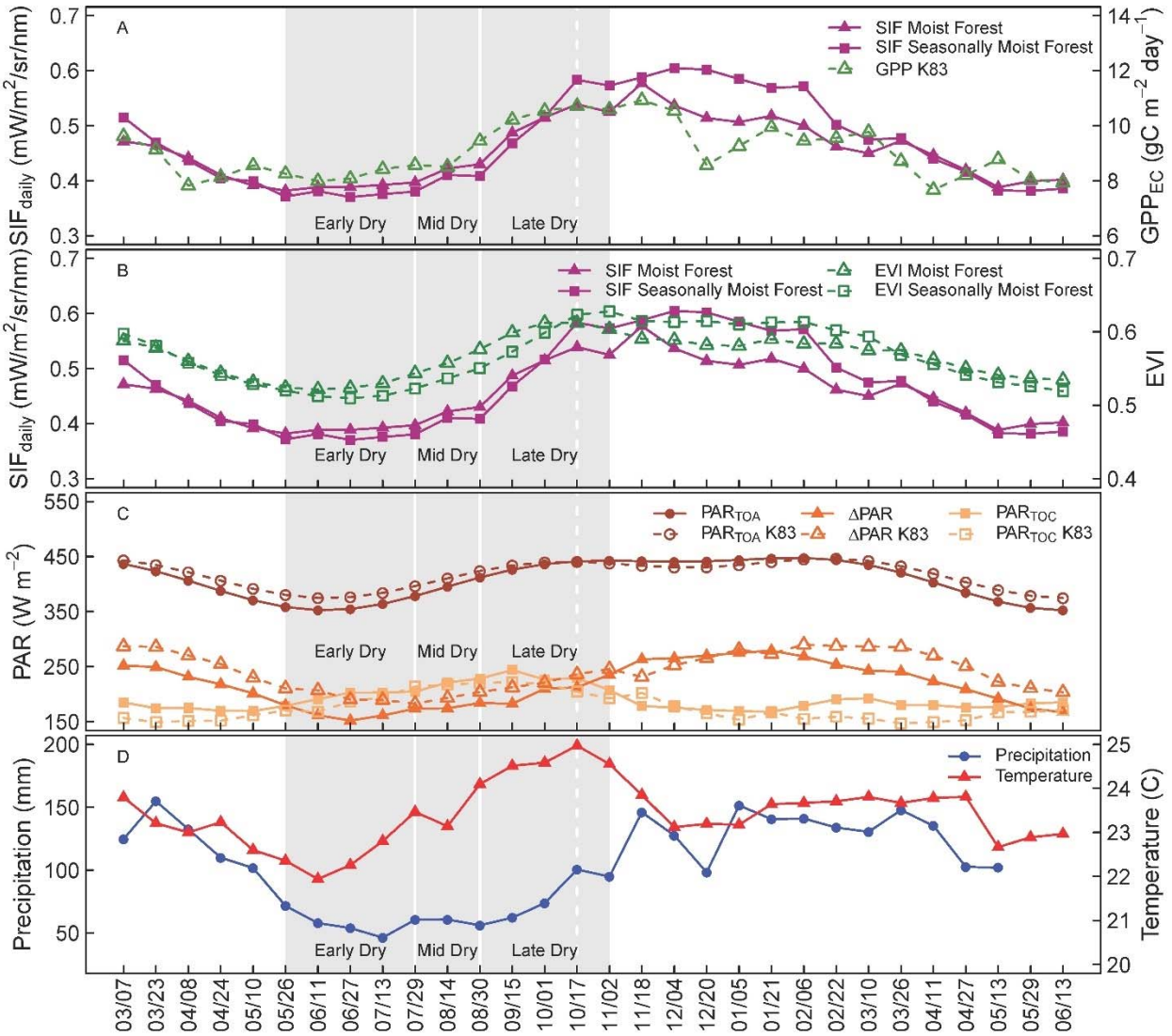

Figure 4.2 | Amazon forest SIF, photosynthesis, PAR, precipitation, and temperature. (A) TROPOMI SIF for moist and seasonally moist forest (>2000 mm and <2000 mm mean annual precipitation), and five-year mean GPP at the K83 moist forest flux tower site. (B) TROPOMI SIF for moist and seasonally moist forest, and BRDF-corrected EVI from MCD43A4 for moist and seasonally moist forest. (C) Basin-wide PAR at the top of the atmosphere (TOA), top of the canopy (TOC), the difference between the two (ΔPAR), and 5-year means of TOA, TOC, and ΔPAR from the K83 flux tower site. (D) Basin-wide mean precipitation and temperature. Points are 16-day means. Shaded areas represent the early, middle, and late dry season. The dashed line approximates when TROPOMI's phase angles are lowest.

For non-forest in the Amazon, SIF declined considerably in the early dry season (SI Appendix, Fig. S4.1, S4.4), especially in the cropland region of central Bolivia and in the arc of deforestation in the Brazilian states of Acre, Rondônia, and Mato Grosso (Fig. 4.1D). In the late dry season, non-forest SIF continually increased. There were some hotspots where SIF decreased during the late dry season, notably in the Serra do Cachimbo Mountain region, the plains of the Brazilian state of Roraima, and the deforested areas in the vicinity of Santarém and Altamira (Fig. 4.1E).

In forests, the dry-season increase in SIF can be attributed to the loss of old leaves, the flushing of new leaves, and an increase in canopy chlorophyll content, which has been observed using *in situ* litterfall traps, tower-based time lapse photography, and satellite-based vegetation indices (Lopes et al. 2016; Restrepo-Coupe et al. 2013; Xiao et al. 2006). For non-forest lands in the arc of deforestation, the decrease in SIF can be attributed to the harvest of crops and senescence of pasture, and the late dry-season increase in SIF is likely due to the early growth of pastures and crops such as maize, rice, sorghum, and soybean (Food and Agriculture Organization of the United Nations 2018). At the basin scale, late dry-season SIF for forest and non-forest increased through October despite decreased solar radiation in the canopy (PAR_{TOC}) (Fig. 4.2B) (Wright et al. 2017), which indicated that increased canopy chlorophyll content and photosynthesis drove dry-season increases in SIF and not PAR_{TOC}. TROPOMI SIF in the Amazon forest was remarkably consistent with *in situ* observations of increased dry-season photosynthesis in the moist tropical Amazon forest from the K83 CO_2 eddy flux tower (Fig. 4.1A), which is representative of dry-season observations of photosynthesis from the other moist tropical forest eddy flux tower sites in the Amazon (Restrepo-Coupe et al. 2013).

Two previous studies claimed that the geometry between the satellite sensors and the sun affects the surface reflectance data and thus the green-up during the dry season as shown by vegetation indices is a data artifact inducing false seasonality (Galvão et al. 2011; Morton et al. 2014). Is it possible that the seasonality of TROPOMI SIF in the Amazon is an artifact of sun-sensor geometry? TROPOMI has a wide swath of 2600 km with daily, near-global coverage and the satellite has a 17-day repeat cycle, meaning that every 17 days the satellite's nadir and swath footprint are nearly identical. The phase angle of each sounding, which is the angle between the axes from the sounding to the sun and to TROPOMI's sensor, varies along the swath. Each sounding along the swath also has a different footprint size, with the smallest footprint at nadir (3.5 x 7 km) and the largest at the edges of the swath (14 x 7 km).

SIF retrievals are sensitive to the phase angle, with higher SIF values at low phase angles when TROPOMI observes more directly illuminated parts of the canopy (Fig. 4.3) (Zuromski et al. 2018). TROPOMI's viewing angle for any location is most comparable every 17 days when the footprint of the satellite track and local solar overpass time are nearly identical because of their vicinity to the equator. Thus, we investigated if TROPOMI SIF has seasonality when viewing angle is held relatively constant by evaluating SIF for each satellite track and found that each track has the same seasonal pattern (SI Appendix, Figs. S1-4). Although we are not able to account for changes in solar illumination with this strategy, we can assume that the viewing geometry alone does not alter the observed seasonality. One possible explanation for the observed seasonality in TROPOMI SIF is that the decreasing zenith angle of the sun in the dry season causes TROPOMI phase angles to likewise decrease (SI Appendix, Fig. S4.5). However, we found that SIF increased during the dry season across all phase angles and that the increase was larger than what could be explained by phase angle alone (Fig. 4.4, SI Appendix, S6-8). Furthermore, if phase angle was

driving the observed seasonality in SIF, then we would expect SIF to decrease after the phase angles of the TROPOMI soundings reached their minimum. However, SIF increased for several weeks after TROPOMI phase angles began increasing and despite increased cloud cover (Fig. 4.2). We also found a significant and strong relationship between TROPOMI SIF and BRDF-corrected enhanced vegetation index (EVI) from MODIS MCD43A4 for moist and seasonally moist forest (R^2 = 0.82 and 0.93, respectively), and between TROPOMI SIF for moist forest and the K83 tower site (R^2 = 0.66) (SI Appendix, Fig. S4.9).

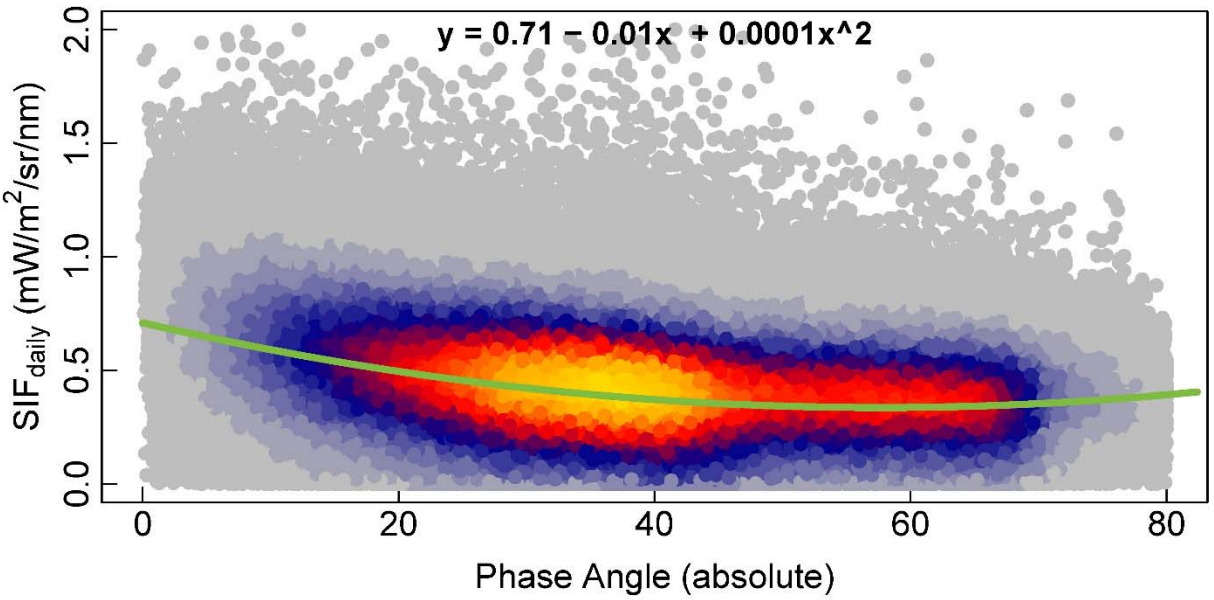

Figure 4.3 | Relationship between phase angle and TROPOMI SIFdaily. Points are 1,000,000 random samples from all soundings (n = 22,876,383) in the Amazon Basin during March 7, 2018 – June 29, 2019.

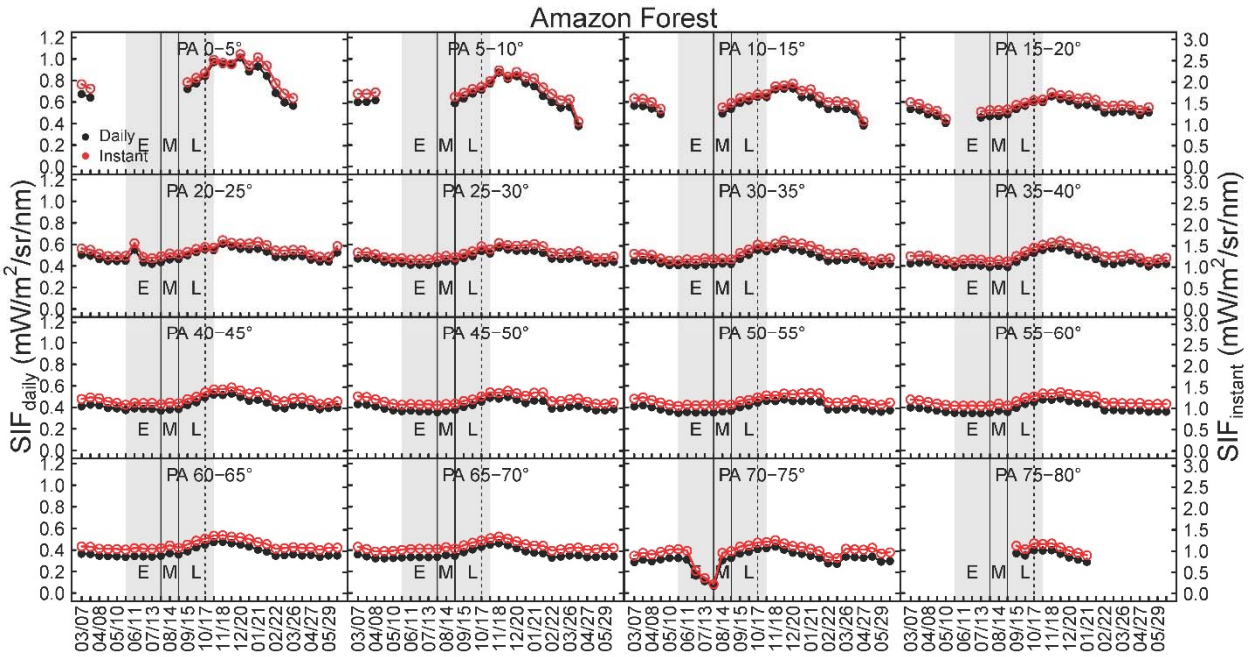

Figure 4.4 | TROPOMI SIFdaily and SIFinstant at different phase angles for the Amazon forest. Areas shaded in gray represent the early (E), mid (M), and late (L) dry seasons. The dashed line approximates when TROPOMI's phase angles are lowest. These trends were also illustrated for moist and seasonally moist forest with greater than and less than 2000 mm mean annual precipitation and for non-forest in the Supplementary Information (Figs. S6-8). Dates represent the first day of TROPOMI's 16-day revisit cycle. Tick marks are every 16 days and labels are every 32 days. The complete date range represented is March 7, 2018 – June 29, 2019.

The seasonality of TROPOMI SIF agrees with *in situ* seasonality of photosynthesis and MODIS EVI (Fig. 4.2A, B), but to what extent do incoming solar radiation and cloud cover affect canopy photosynthesis and space-borne observations of SIF in the Amazon? The amount of photosynthetically active radiation reaching the top of the canopy (PAR_{TOC}) is determined by the difference between the amount of incoming PAR at the top of the atmosphere (PAR_{TOA}) from the sun and the amount of PAR reflected into space and absorbed by clouds, trace gases, aerosols, and particulate matter (ΔPAR). Thus, seasonality in PAR_{TOA} (length of day and solar angle) and ΔPAR (mostly cloud cover/thickness) determine the amount and timing of instantaneous and daily PAR_{TOC} ($PAR_{TOC} = PAR_{TOA} - \Delta PAR$), which drives photosynthesis and serves as a phenological queue for tropical tree species (Wright and Van Schaik 1994).

Diurnally, there is a tight relationship between PAR_{TOC} and photosynthesis in the morning and evening as they rise and fall in tandem (Malhi et al. 1998). At midday, the relationship between PAR_{TOC} and photosynthesis decouples as the canopy becomes light saturated (SI Appendix, Fig. S4.10). Using *in situ* data, we found that during TROPOMI's early afternoon overpass time of 12:45-2:30 local solar time (LST) over the Amazon (SI Appendix, Fig. S4.11), photosynthesis is nearly always light saturated (Fig. 4.5A-C) and that ΔPAR rarely impacts photosynthesis (Fig. 4.5D-F). Dense clouds can block the emission of SIF into space, and TROPOMI soundings are prefiltered to remove soundings that are affected by high radiance levels due to cloud albedo and that have >80% cloud fraction. However, *in situ* data indicates that clouds cover rarely blocks enough solar irradiance at TROPOMI's overpass time to induce light limitation of photosynthesis (Fig. 4.5). We cannot completely rule out that seasonal changes in cloud cover and optical thickness may affect SIF dynamics in the Amazon, but we did observe that the strongest increase in SIF occurred during the mid to late dry season despite reduced PAR_{TOC} and increased ΔPAR and cloud fraction (SI Appendix, Fig. S4.12), which suggested that changes in cloud properties during the dry season had an insignificant effect on SIF retrievals. The seasonality of forest SIF was most similar to PAR_{TOA}, indicating that perhaps the timing of leaf flush in the forest is photosensitive to the length of the day and/or responsive to herbivory, which are not necessarily mutually exclusive (Coley and Barone 1996; van Schaik et al. 1993; Xiao et al. 2006).

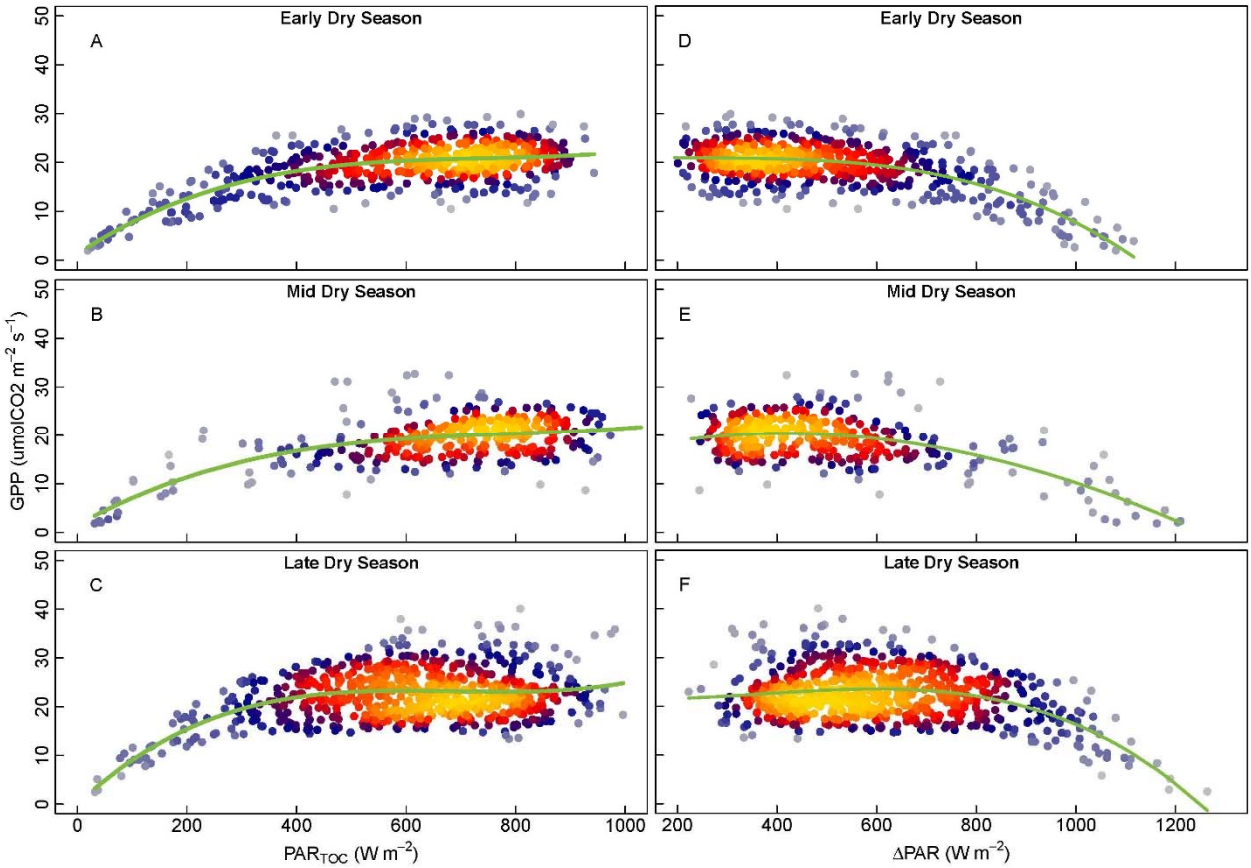

Figure 4.5 | Dry-season light and shade response of photosynthesis in the Amazon at TROPOMI overpass times (~12:45-2:30 LST) at K83 eddy tower. Light-response curves of photosynthesis and photosynthetically active radiation at the top of the canopy (PAR_{TOC}) in (A) early dry season, (B) mid dry season, and (C) late dry season. Shade-response curves of photosynthesis and the absorption and reflection of photosynthetically active radiation incoming from the top of the atmosphere (ΔPAR) before reaching the canopy in (D) early dry season, (E) mid dry season, and (F) late dry season.

In summary, the dry-season increase of TROPOMI SIF in the Amazon mimics the dry-season increase of photosynthesis as estimated from eddy flux data (Restrepo-Coupe et al. 2013), *in situ* observations by phenological cameras of seasonal canopy senescence and leaf flush (Lopes et al. 2016; Wu et al. 2016), and BRDF-corrected, reflectance-based satellite observations (Guan et al. 2015; Joiner et al. 2011; Saleska et al. 2007; Saleska et al. 2016). Our results not only help resolve the debate over whether there is a dry-season increase in photosynthesis in moist tropical

Amazon forest, but also indicate that changes in photosynthesis during the dry season is largely driven by land cover type and changes in the forest canopy.

4.2 Methods

4.2.1 TROPOMI observations

We used daily-corrected ungridded TROPOMI SIF data for all data analysis (Figs. 1, S1-4) and daily-corrected gridded TROPOMI SIF data in 0.05° spatial resolution for visualization in Fig. 4.1 (Zuromski et al. 2018). Gridded (0.20°) and ungridded data is available at ftp://fluo.gps.caltech.edu/data/tropomi/. It is also important to note that aerosols and clouds have different effects on SIF and reflected radiance at top-of-atmosphere (decreasing SIF, increasing reflectance), and cloud shadows reduce reflectance but not necessarily photosynthesis (Fig. 4.5), so any reflectance-based correction may introduce an artificial seasonality in the framework of our study (Zuromski et al. 2018). The data fields contain for each sounding the cloud fraction, daily correction factor, latitude and longitude of the center of the sounding, the latitude and longitude for each corner of the sounding footprint, viewing zenith angle, solar zenith angle, phase angle, instantaneous SIF and error, daily corrected SIF, and local solar time. Cloud fraction is calculated using the data from the Visible Infrared Imaging Radiometer Suite (VIIRS) satellite, which is an indicator of cloud cover but not cloud optical thickness. Daily mean SIF is estimated using a function that accounts for the measurement's solar zenith angle, time of measurement, and length of day (Frankenberg et al. 2011; Zuromski et al. 2018). Error estimate methods and additional data processing details have been previously published (Zuromski et al. 2018).

4.2.2 *In situ* eddy flux observations and MODIS data

In our analysis, we used Tier 1 FLUXNET2015 eddy flux data from the tower site K83 (BR-Sa3; Santarem Km83), located in seasonally moist tropical Amazon forest near -3.0180, -54.9714

(latitude/longitude), for the years 2000-2004 (Saleska et al. 2003) (http://dx.doi.org/10.18140/FLX/1440033). The seasonality in GPP, PAR_{TOA}, PAR_{TOC}, and PAR_{Δ} at K83 (Fig. 4.2A,B) was used in this manuscript as an example of observations from other eddy flux towers in the seasonally moist tropical Amazon forests (K34, K67, and CAX), which are in agreement and have been previously reported (Restrepo-Coupe et al. 2013). Prior to plotting the light- and shade-response curves (Fig. 4.5), which is half-hourly data, we filtered the data to include only the highest quality measured PAR (shortwave radiation incoming at the surface), thereby excluding gap-filled and ERA-Interim estimates. We also converted the local time of the eddy flux observations to local solar time (LST). TROPOMI overpass times in the Amazon ranged from about 12:45 to 2:30 LST (SI Appendix, Fig. S4.11), so we plotted EC data whose 30-minute timestamp range had midpoints between 1:00 and 2:15 LST.

We used bidirectional reflectance distribution function (BRDF) corrected surface reflectance from the MODIS MCD43A4 data product (Schaaf and Wang 2015) to calculate EVI. We calculated 16-day means of EVI from the daily data, which was available at 500-m spatial resolution, where EVI was calculated using bands 1 through 3:

$$\mathrm{EVI} = 2.5 * \frac{b2 - b1}{b2 - 6 * b1 + 7.5 * b3 + 1}$$

where b1 is the red band, b2 is the near infrared band, and b3 is the blue band (Huete et al. 1997a; Justice et al. 1998).

4.2.3 Land cover, precipitation, and PAR datasets

To determine forest and non-forest land cover, we used annual forest cover maps for 2008-2017 for the Amazon Basin with a spatial resolution of 500 m (Qin et al. 2019; Qin et al. 2017). Only TROPOMI soundings that were in land cover map pixels that were consistently forest or non-forest were used in the data analysis. To prevent the inclusion of mixed water/land TROPOMI

soundings from our analysis, we masked water from the TROPOMI data using the MOD44W Version 6 (Carroll et al. 2017) water mask with a 7km buffer. Implementing a similar buffer for forests to exclude TROPOMI mixed forest/non-forest soundings resulted in a near elimination of non-forest soundings due to the heterogeneity of non-forest area, thus we applied only a water mask to the TROPOMI data. Total annual and monthly precipitation (Fig. 4.1G-I) was derived using the monthly, 0.25° Version 7 Tropical Rainfall Measuring Mission (TRMM) Multi-Satellite Precipitation Analysis (3B43) (Huffman et al. 2014, updated 2019b). For 16-day precipitation means (Fig. 4.2C), we used the TRMM Research Derived Daily Product (3B42) (Huffman et al. 2014, updated 2019a). We calculated mean 16-day temperature (Fig. 4.2C) and 16-day PAR values (Fig. 4.2B) using daily mean downward shortwave radiation at the surface (PAR_{TOC}) and the top of the atmosphere (PAR_{TOA}) from the NCEP-DOE Reanalysis II data set (Kanamitsu et al. 2002). ΔPAR was calculated as the difference between PAR_{TOA} and PAR_{TOC}.

4.3 Supplementary material

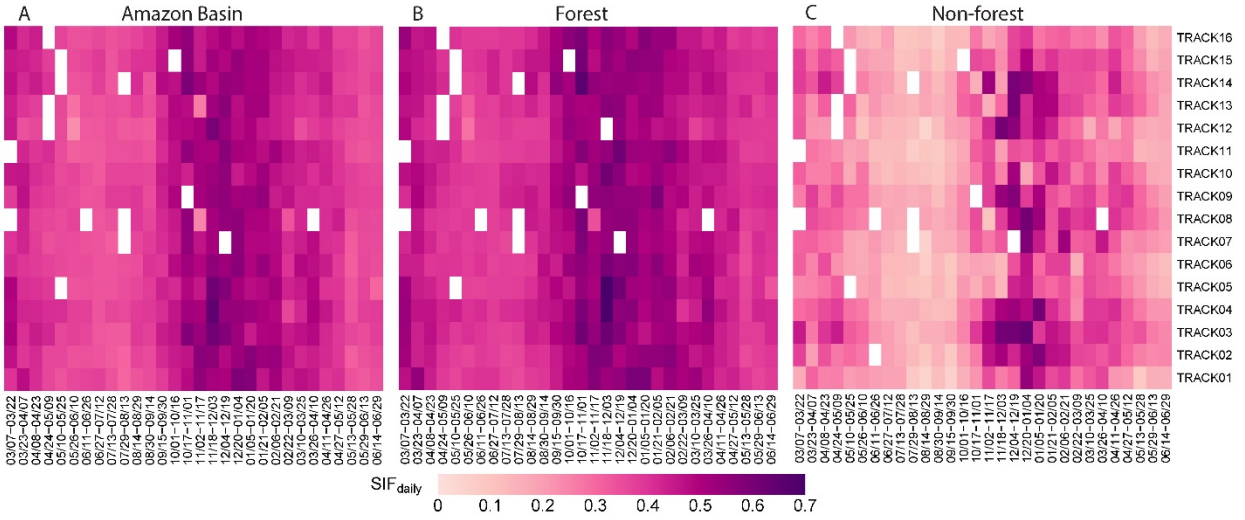

Figure S4.1 | Basin-wide mean daily SIF from TROPOMI March 2018 – June 2019. (A) The entire Amazon Basin. (B) All soundings in forests. (C) All soundings in non-forest. Soundings with footprints in water were masked out. Changes in mean daily and instantaneous SIF for the Amazon Basin, forest, and non-forest are further illustrated in figs. S2-4, and the standard errors of the means of the observations are listed in tables S4.1-S3.

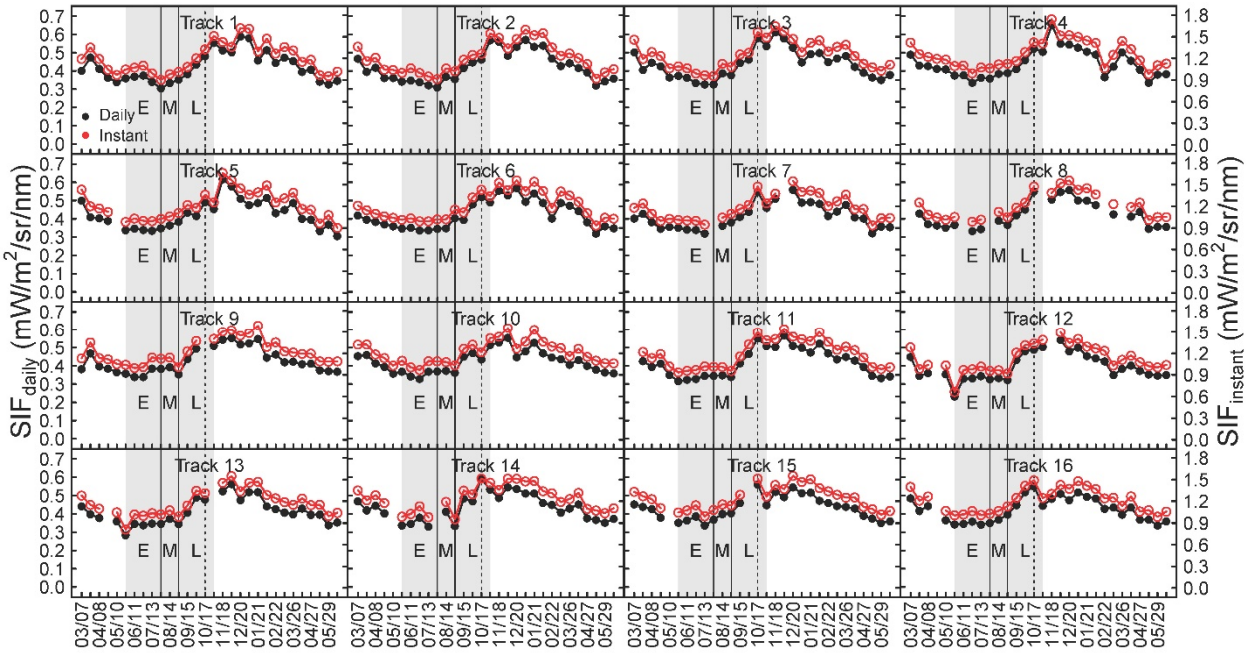

Figure S4.2 | Amazon Basin mean daily and instantaneous SIF for each of TROPOMI's tracks. Areas shaded in gray represent the early (E), mid (M), and late (L) dry seasons. The dashed line approximates when TROPOMI's phase angles are lowest. Dates represent the first day of TROPOMI's 16-day revisit cycle. Tick marks are every 16 days and labels are every 32 days. The complete date range represented is March 7, 2018 – June 29, 2019.

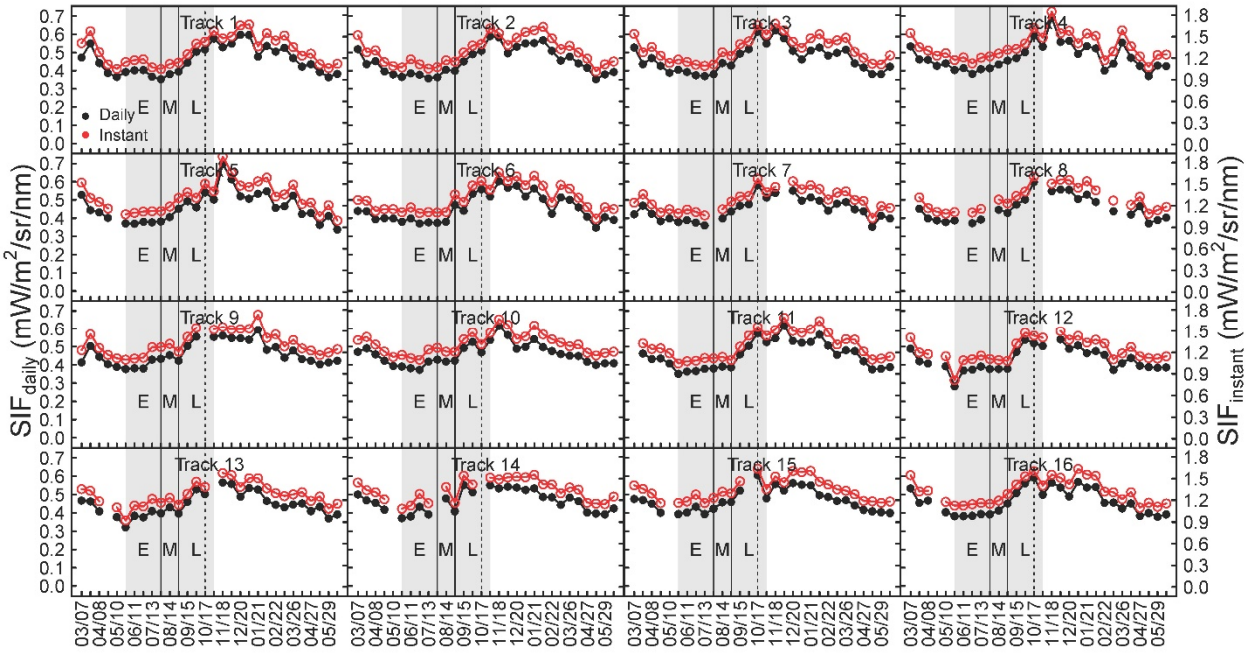

Figure S4.3 | Forest mean daily and instantaneous SIF for each of TROPOMI's tracks. Areas shaded in gray represent the early (E), mid (M), and late (L) dry seasons. The dashed line approximates when TROPOMI's phase angles are lowest. Dates represent the first day of

TROPOMI's 16-day revisit cycle. Tick marks are every 16 days and labels are every 32 days. The complete date range represented is March 7, 2018 – June 29, 2019.

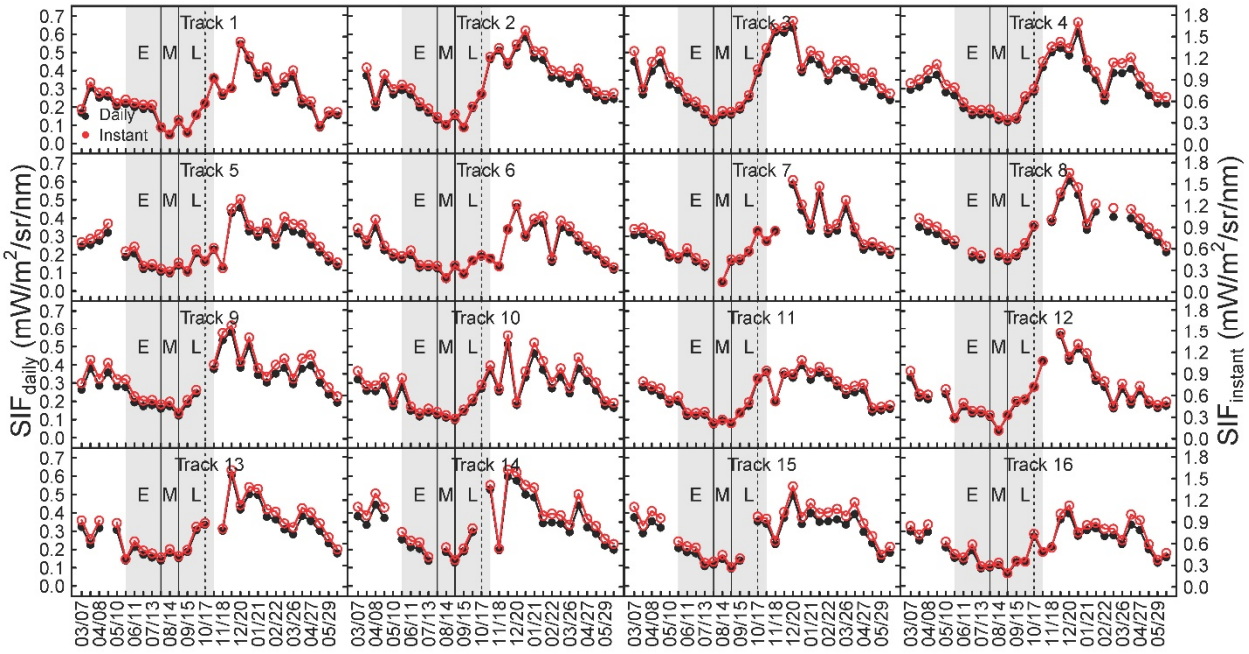

Figure S4.4 | Non-forest mean daily and instantaneous SIF for each of TROPOMI's tracks. Areas shaded in gray represent the early (E), mid (M), and late (L) dry seasons. The dashed line approximates when TROPOMI's phase angles are lowest. Dates represent the first day of TROPOMI's 16-day revisit cycle. Tick marks are every 16 days and labels are every 32 days. The complete date range represented is March 7, 2018 – June 29, 2019.

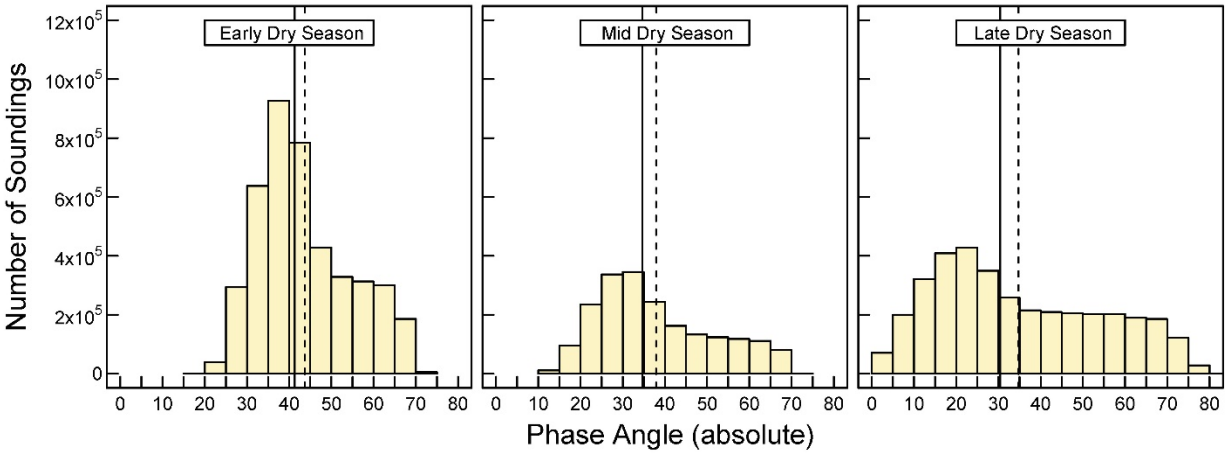

Figure S4.5 | The distribution of the phase angle of TROPOMI soundings in early, mid, and late dry season. Dashed line is the mean.

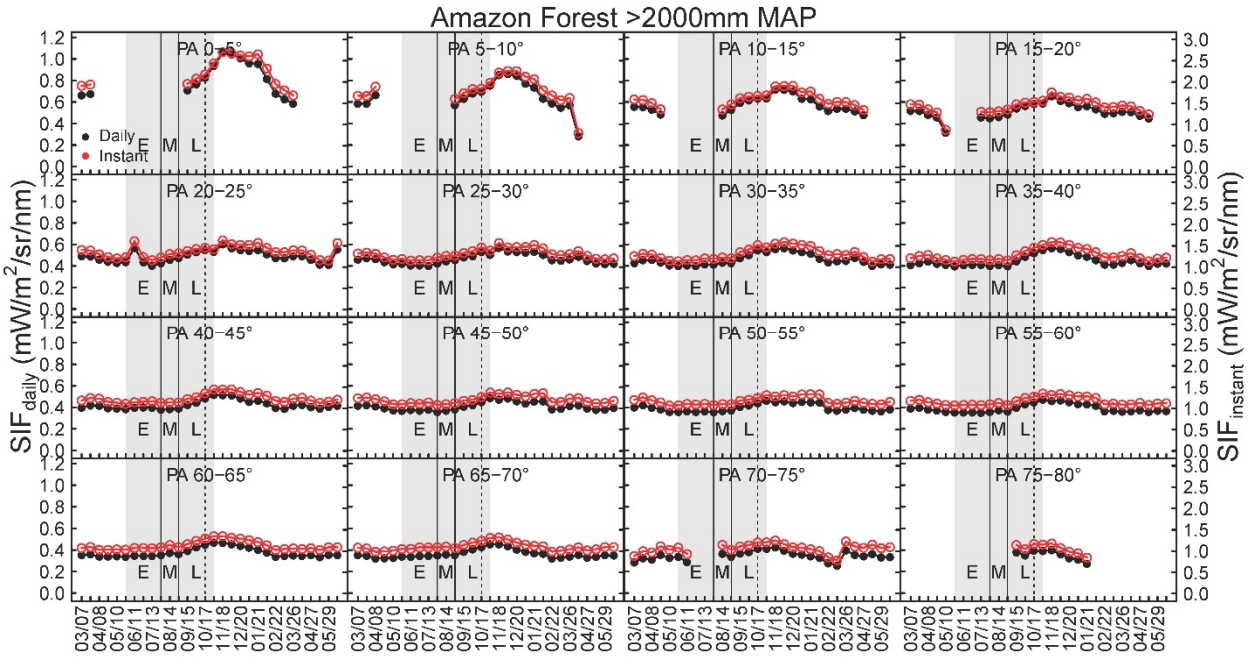

Figure S4.6 | SIF_{daily} and $SIF_{instant}$ at different phase angles (PA) for Amazon forest with mean annual precipitation (MAP) > 2000 mm. Areas shaded in gray represent the early (E), mid (M), and late (L) dry seasons. The dashed line approximates when TROPOMI's phase angles are lowest. Dates represent the first day of TROPOMI's 16-day revisit cycle. Tick marks are every 16 days and labels are every 32 days. The complete date range represented is March 7, 2018 – June 29, 2019.

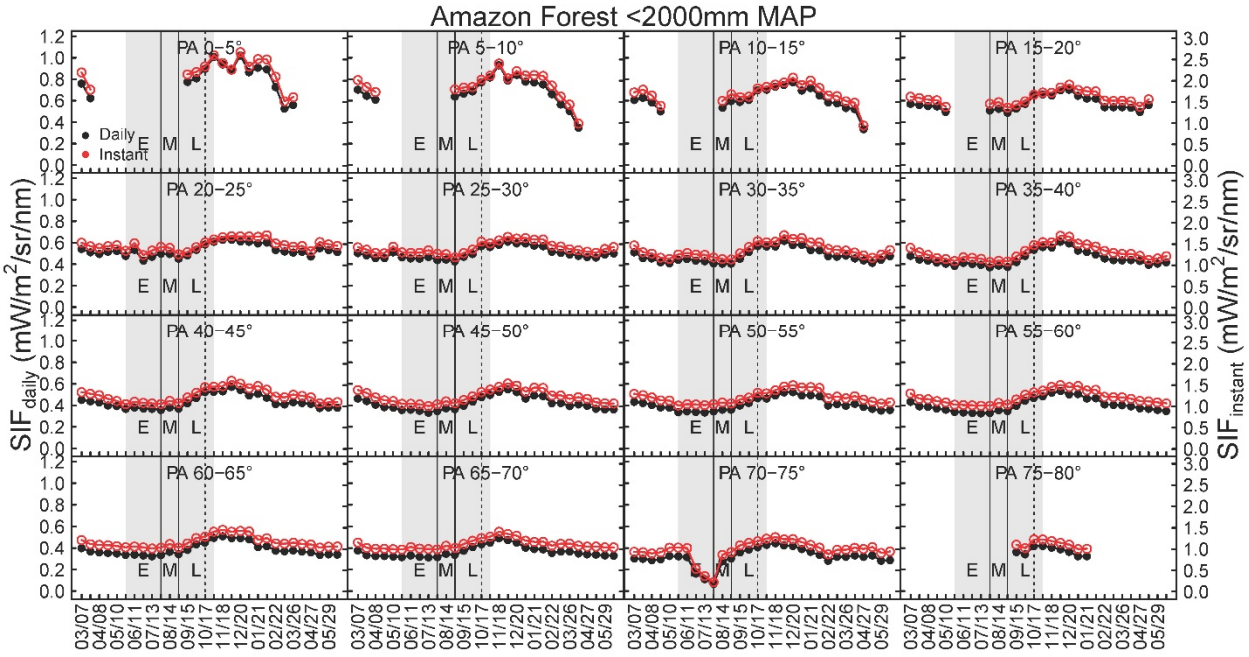

Figure S4.7 | SIF_{daily} and $SIF_{instant}$ at different phase angles (PA) for Amazon forest with mean annual precipitation (MAP) < 2000 mm. Areas shaded in gray represent the early (E), mid (M),

and late (L) dry seasons. The dashed line approximates when TROPOMI's phase angles are lowest. Dates represent the first day of TROPOMI's 16-day revisit cycle. Tick marks are every 16 days and labels are every 32 days. The complete date range represented is March 7, 2018 – June 29, 2019.

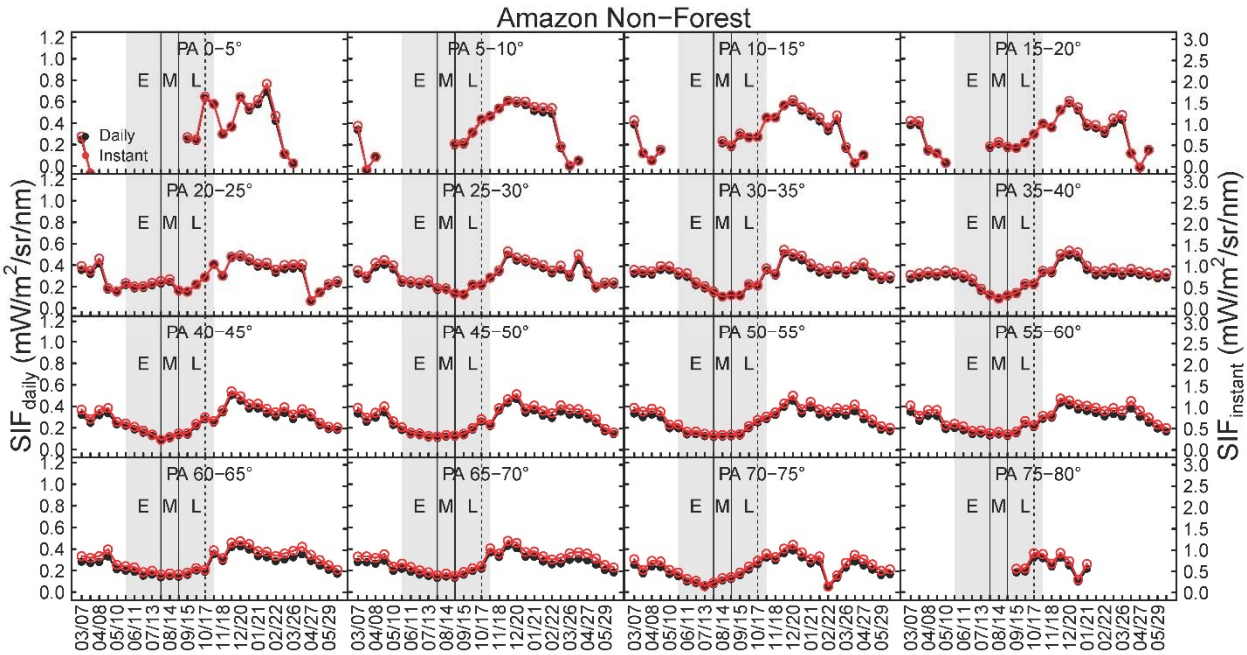

Figure S4.8 | SIF_{daily} and $SIF_{instant}$ at different phase angles (PA) for TROPOMI soundings of non-forest, non-water land cover in the Amazon. Areas shaded in gray represent the early (E), mid (M), and late (L) dry seasons. The dashed line approximates when TROPOMI's phase angles are lowest. Dates represent the first day of TROPOMI's 16-day revisit cycle. Tick marks are every 16 days and labels are every 32 days. The complete date range represented is March 7, 2018 – June 29, 2019.

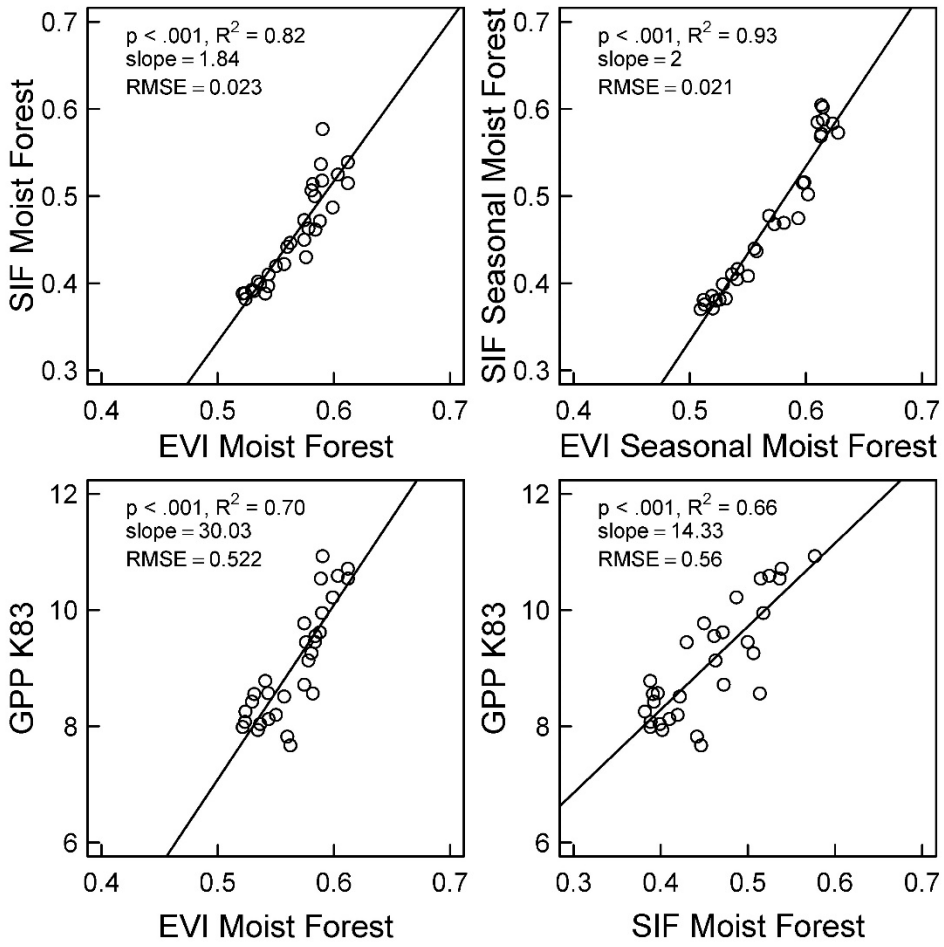

Figure S4.9 | Relationships between MODIS EVI, TROPOMI SIF, and GPP from the K83 eddy tower site.

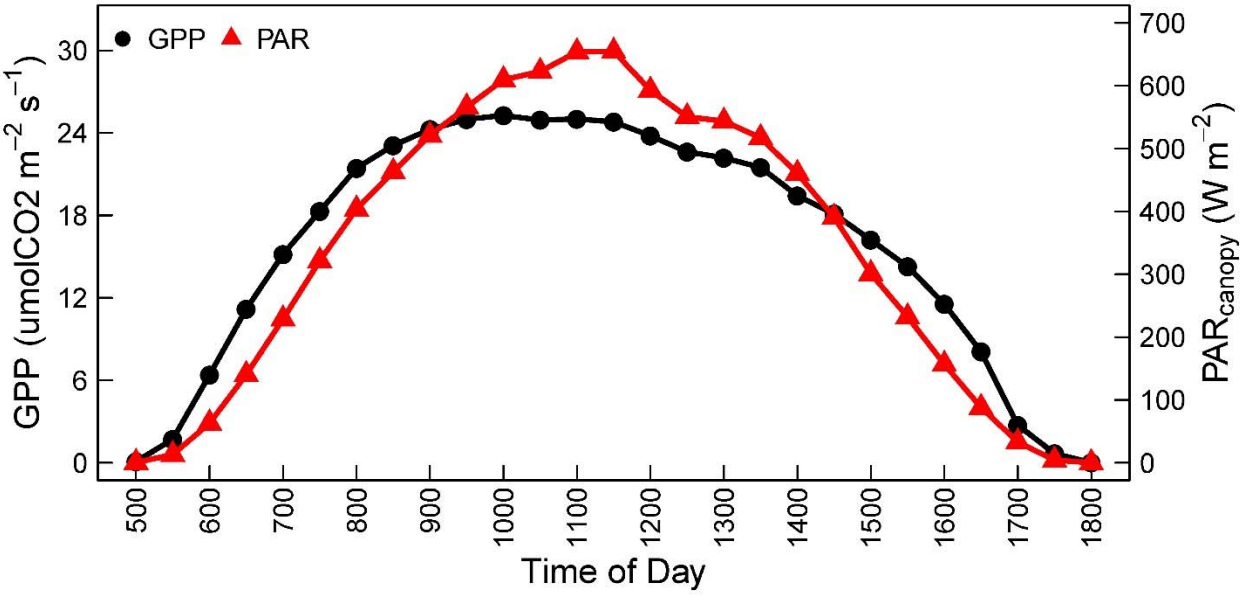

Figure S4.10 | Diurnal GPP and PAR at K83. Mean half-hourly GPP and PAR from K83 eddy flux tower 2000-2004.

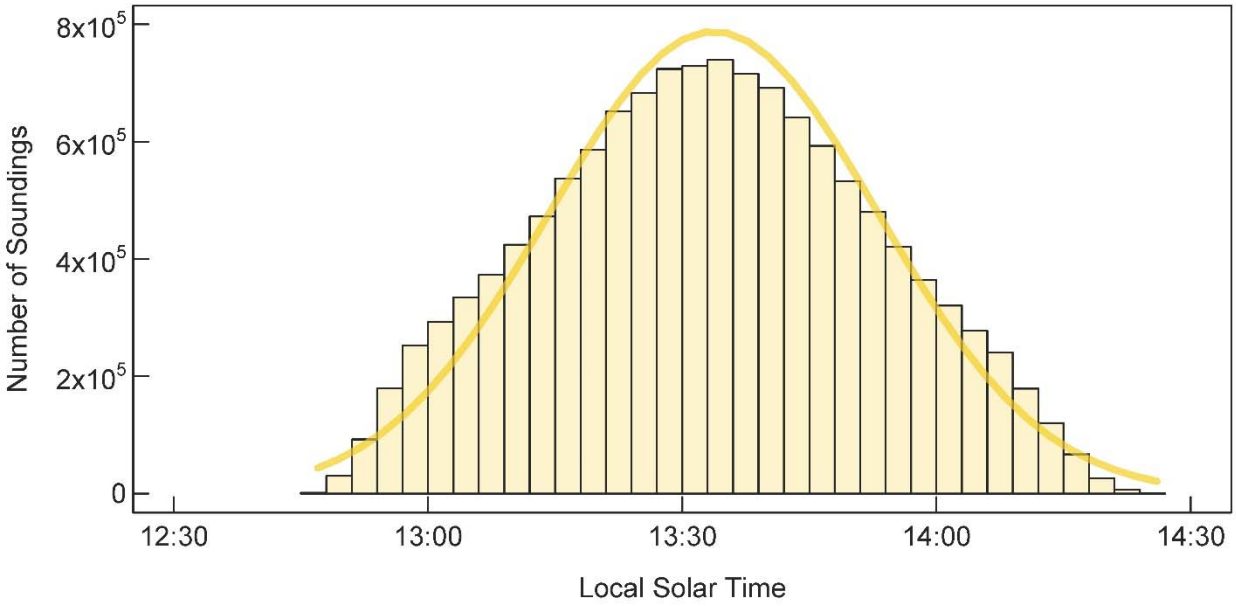

Figure S4.11 | Frequency of the local solar time of TROPOMI soundings in the Amazon.

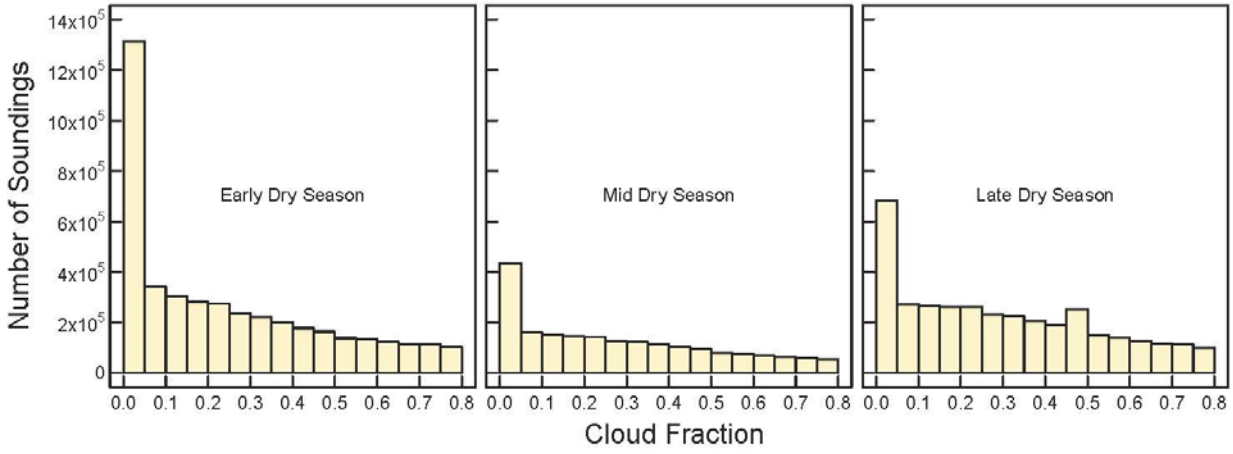

Figure S4.12 | Frequency histograms of early, mid, and late dry season cloud fraction of TROPOMI SIF soundings.

Table S4.1. Standard error of the mean of $SIF_{instant}$ observations in the Amazon Basin (Fig. S4.1A). Column header is the track number.

	1	2	3	4	5	6	7	8	9	10	11	12	13	14	15	16
03/07	0.004	0.002	0.001	0.001	0.001	0.001	0.001	NA	0.001	0.002	NA	0.001	0.001	0.001	0.001	0.001

03/23	0.002	0.001	0.002	0.001	0.001	0.001	0.001	0.001	0.001	0.001	0.001	0.002	0.001	0.002	0.002	0.001
04/08	0.001	0.001	0.001	0.001	0.001	0.001	0.001	0.001	0.001	0.001	0.001	0.001	0.001	0.001	0.001	0.001
04/24	0.001	0.001	0.001	0.001	0.001	0.001	0.001	0.001	0.001	0.001	0.001	NA	NA	0.001	0.001	NA
05/10	0.001	0.001	0.001	0.001	NA	0.001	0.001	0.001	0.001	0.001	0.001	0.001	0.001	NA	NA	0.001
05/26	0.001	0.001	0.001	0.001	0.001	0.001	0.001	0.001	0.001	0.001	0.001	0.001	0.001	0.001	0.001	0.001
06/11	0.001	0.02	0.001	0.001	0.001	0.001	0.001	NA	0.001	0.001	0.001	0.001	0.001	0.001	0.001	0.001
06/27	0.001	0.001	0.001	0.001	0.001	0.001	0.001	0.001	0.001	0.001	0.001	0.001	0.001	0.001	0.001	0.001
07/13	0.001	0.001	0.001	0.001	0.001	0.001	0.001	0.001	0.001	0.001	0.001	0.001	0.001	0.001	0.001	0.001
07/29	0.001	0.001	0.001	0.001	0.001	0.001	NA	NA	0.001	0.001	0.001	0.001	0.001	NA	0.001	0.001
08/14	0.001	0.001	0.001	0.001	0.001	0.001	0.001	0.001	0.001	0.001	0.001	0.001	0.001	0.001	0.001	0.001
08/30	0.001	0.001	0.001	0.001	0.001	0.001	0.001	0.001	0.001	0.001	0.001	0.001	0.001	0.001	0.001	0.001
09/15	0.001	0.001	0.001	0.001	0.001	0.001	0.001	0.001	0.001	0.001	0.001	0.001	0.001	0.001	0.001	0.001
10/01	0.001	0.001	0.001	0.001	0.001	0.001	0.001	0.001	0.001	0.001	0.001	0.002	0.001	0.001	NA	0.001
10/17	0.001	0.001	0.002	0.002	0.001	0.001	0.001	0.001	NA	0.001	0.001	0.001	0.001	0.006	0.001	0.001
11/02	0.001	0.001	0.001	0.001	0.002	0.001	0.002	0.015	0.001	0.001	0.001	0.001	0.046	0.002	0.002	0.001
11/18	0.001	0.002	0.002	0.002	0.002	0.001	0.002	0.001	0.002	0.002	0.002	0.049	0.002	0.002	0.002	0.002
12/04	0.001	0.001	0.002	0.002	0.002	0.001	NA	0.001	0.002	0.001	0.001	0.001	0.001	0.001	0.001	0.001
12/20	0.001	0.002	0.001	0.001	0.001	0.002	0.001	0.001	0.001	0.002	0.001	0.001	0.001	0.001	0.001	0.001
01/05	0.001	0.002	0.002	0.002	0.001	0.001	0.001	0.001	0.001	0.001	0.001	0.001	0.001	0.001	0.002	0.001
01/21	0.001	0.001	0.001	0.001	0.002	0.001	0.001	0.001	0.002	0.001	0.002	0.002	0.002	0.001	0.001	0.001
02/06	0.001	0.001	0.001	0.002	0.001	0.001	0.002	0.002	0.002	0.002	0.002	0.001	0.001	0.002	0.002	0.002
02/22	0.001	0.001	0.001	0.001	0.001	0.001	0.001	0.045	0.001	0.001	0.001	0.001	0.001	0.001	0.001	0.001
03/10	0.002	0.002	0.001	0.001	0.001	0.001	0.001	0.001	0.001	0.001	0.002	0.001	0.001	0.001	0.001	0.001
03/26	0.001	0.001	0.001	0.002	0.002	0.001	0.001	NA	0.002	0.001	0.001	0.001	0.001	0.002	0.001	0.001
04/11	0.001	0.001	0.001	0.001	0.001	0.001	0.001	0.001	0.001	0.001	0.001	0.001	0.001	0.001	0.001	0.001
04/27	0.001	0.001	0.001	0.001	0.001	0.001	0.001	0.001	0.001	0.001	0.001	0.001	0.001	0.001	0.001	0.001
05/13	0.002	0.001	0.001	0.001	0.001	0.001	0.001	0.001	0.001	0.001	0.001	0.001	0.001	0.001	0.001	0.001
05/29	0.001	0.001	0.001	0.001	0.001	0.001	0.001	0.001	0.001	0.001	0.001	0.001	0.001	0.001	0.001	0.001
06/14	0.001	0.001	0.001	0.001	0.001	0.001	0.001	0.001	0.001	0.001	0.001	0.001	0.001	0.001	0.001	0.001

Table S4.2. Standard error of the mean of $SIF_{instant}$ observations in the Amazon forest (Fig. S4.1B). Column header is the track number.

	1	2	3	4	5	6	7	8	9	10	11	12	13	14	15	16
03/07	0.011	0.004	0.003	0.004	0.005	0.004	0.004	NA	0.004	0.006	NA	0.003	0.004	0.003	0.003	0.004
03/23	0.004	0.004	0.007	0.005	0.004	0.003	0.003	0.004	0.004	0.004	0.003	0.003	0.004	0.004	0.005	0.004
04/08	0.004	0.003	0.003	0.003	0.004	0.005	0.003	0.004	0.003	0.003	0.003	0.003	0.003	0.003	0.003	0.003
04/24	0.004	0.003	0.003	0.002	0.003	0.003	0.003	0.003	0.002	0.003	0.004	NA	NA	0.002	0.002	NA
05/10	0.003	0.003	0.003	0.002	NA	0.002	0.003	0.002	0.002	0.003	0.002	0.002	0.002	NA	NA	0.002
05/26	0.002	0.002	0.002	0.002	0.002	0.003	0.003	0.003	0.002	0.002	0.003	0.003	0.003	0.002	0.002	0.003
06/11	0.003	NA	0.002	0.002	0.003	0.003	0.002	NA	0.002	0.002	0.002	0.002	0.002	0.002	0.002	0.002
06/27	0.002	0.002	0.002	0.002	0.002	0.002	0.002	0.002	0.002	0.002	0.002	0.002	0.002	0.002	0.002	0.002
07/13	0.003	0.002	0.002	0.002	0.002	0.002	0.002	0.002	0.002	0.002	0.002	0.002	0.002	0.002	0.002	0.002
07/29	0.002	0.002	0.002	0.002	0.003	0.003	NA	NA	0.002	0.002	0.003	0.002	0.002	NA	0.002	0.002

08/14	0.003	0.003	0.002	0.002	0.002	0.003	0.004	0.002	0.002	0.002	0.002	0.003	0.002	0.002	0.002	0.002
08/30	0.002	0.002	0.002	0.002	0.002	0.002	0.003	0.002	0.002	0.002	0.002	0.002	0.002	0.002	0.003	0.003
09/15	0.004	0.004	0.003	0.002	0.003	0.003	0.002	0.002	0.002	0.003	0.003	0.003	0.003	0.003	0.003	0.003
10/01	0.003	0.003	0.003	0.003	0.003	0.004	0.003	0.003	0.003	0.004	0.005	0.005	0.003	0.003	NA	0.004
10/17	0.004	0.004	0.008	0.005	0.005	0.005	0.007	0.006	NA	0.003	0.006	0.005	0.005	0.012	0.004	0.005
11/02	0.005	0.005	0.006	0.004	0.005	0.008	0.005	0.022	0.004	0.004	0.005	0.006	0.053	0.007	0.006	0.005
11/18	0.008	0.009	0.006	0.006	0.007	0.006	0.007	0.005	0.006	0.005	0.007	0.063	0.007	0.005	0.006	0.005
12/04	0.004	0.005	0.007	0.009	0.006	0.005	NA	0.005	0.005	0.006	0.004	0.008	0.004	0.005	0.005	0.006
12/20	0.006	0.007	0.005	0.005	0.007	0.006	0.006	0.006	0.007	0.005	0.006	0.007	0.006	0.005	0.005	0.006
01/05	0.005	0.006	0.008	0.006	0.004	0.007	0.011	0.005	0.004	0.006	0.005	0.005	0.003	0.005	0.005	0.004
01/21	0.004	0.005	0.003	0.004	0.005	0.005	0.006	0.005	0.007	0.005	0.005	0.009	0.007	0.004	0.004	0.004
02/06	0.005	0.004	0.004	0.005	0.005	0.005	0.009	0.008	0.006	0.005	0.006	0.005	0.004	0.006	0.006	0.004
02/22	0.004	0.003	0.004	0.005	0.006	0.006	0.006	0.059	0.004	0.004	0.004	0.005	0.004	0.003	0.003	0.005
03/10	0.005	0.004	0.004	0.003	0.004	0.005	0.004	0.004	0.003	0.004	0.007	0.006	0.005	0.004	0.004	0.004
03/26	0.005	0.005	0.005	0.005	0.005	0.003	0.005	NA	0.006	0.003	0.004	0.003	0.003	0.004	0.003	0.003
04/11	0.003	0.003	0.004	0.003	0.003	0.006	0.005	0.003	0.003	0.003	0.003	0.003	0.005	0.003	0.003	0.003
04/27	0.004	0.003	0.003	0.003	0.004	0.003	0.003	0.003	0.003	0.003	0.003	0.003	0.002	0.002	0.002	0.006
05/13	0.005	0.003	0.002	0.002	0.002	0.002	0.002	0.002	0.002	0.003	0.003	0.003	0.002	0.002	0.002	0.002
05/29	0.003	0.002	0.002	0.002	0.002	0.003	0.002	0.002	0.002	0.002	0.002	0.003	0.002	0.002	0.002	0.002
06/14	0.003	0.002	0.002	0.002	0.002	0.003	0.002	0.002	0.002	0.002	0.002	0.002	0.002	0.002	0.002	0.002

Table S4.3. Standard error of the mean of $SIF_{instant}$ observations in Amazon non-forest (Fig. S4.1C). Column header is the track number.

	1	2	3	4	5	6	7	8	9	10	11	12	13	14	15	16
03/07	0.004	0.002	0.002	0.002	0.001	0.001	0.001	NA	0.001	0.002	NA	0.001	0.001	0.001	0.001	0.002
03/23	0.002	0.001	0.002	0.001	0.001	0.001	0.001	0.001	0.001	0.001	0.001	0.002	0.002	0.002	0.002	0.001
04/08	0.001	0.001	0.001	0.001	0.001	0.001	0.001	0.002	0.002	0.001	0.001	0.001	0.001	0.001	0.001	0.001
04/24	0.001	0.001	0.001	0.001	0.001	0.001	0.001	0.001	0.001	0.001	0.001	NA	NA	0.001	0.001	NA
05/10	0.001	0.001	0.002	0.001	NA	0.001	0.001	0.001	0.001	0.001	0.001	0.001	0.001	NA	NA	0.001
05/26	0.001	0.001	0.001	0.001	0.001	0.001	0.001	0.001	0.001	0.001	0.001	0.002	0.001	0.001	0.001	0.001
06/11	0.001	0.02	0.001	0.001	0.001	0.002	0.001	NA	0.001	0.001	0.001	0.001	0.001	0.001	0.001	0.001
06/27	0.001	0.001	0.001	0.001	0.001	0.001	0.001	0.001	0.001	0.001	0.001	0.001	0.001	0.001	0.001	0.001
07/13	0.001	0.001	0.001	0.001	0.001	0.001	0.001	0.001	0.001	0.001	0.001	0.001	0.001	0.001	0.001	0.001
07/29	0.001	0.001	0.001	0.001	0.001	0.001	NA	NA	0.001	0.001	0.001	0.001	0.001	NA	0.001	0.001
08/14	0.001	0.001	0.001	0.001	0.001	0.001	0.001	0.001	0.001	0.001	0.001	0.001	0.001	0.001	0.001	0.001
08/30	0.001	0.001	0.001	0.001	0.001	0.001	0.001	0.001	0.001	0.001	0.001	0.001	0.001	0.001	0.001	0.001
09/15	0.001	0.001	0.001	0.001	0.001	0.001	0.001	0.001	0.001	0.001	0.001	0.001	0.001	0.001	0.001	0.001
10/01	0.001	0.001	0.001	0.001	0.001	0.001	0.001	0.001	0.001	0.001	0.002	0.002	0.001	0.001	NA	0.001
10/17	0.001	0.002	0.002	0.002	0.001	0.001	0.002	0.001	NA	0.001	0.001	0.001	0.001	0.006	0.001	0.001
11/02	0.001	0.002	0.002	0.002	0.002	0.001	0.002	0.02	0.001	0.001	0.001	0.001	0.081	0.002	0.002	0.001
11/18	0.001	0.002	0.002	0.002	0.003	0.001	0.002	0.002	0.002	0.002	0.002	NA	0.002	0.002	0.002	0.002
12/04	0.001	0.001	0.002	0.002	0.002	0.001	NA	0.001	0.002	0.001	0.001	0.001	0.001	0.001	0.001	0.002
12/20	0.002	0.002	0.001	0.001	0.002	0.002	0.001	0.001	0.002	0.002	0.001	0.001	0.001	0.001	0.001	0.001
01/05	0.002	0.002	0.002	0.002	0.001	0.001	0.001	0.001	0.002	0.001	0.002	0.002	0.001	0.001	0.002	0.002
01/21	0.001	0.002	0.001	0.002	0.002	0.001	0.001	0.001	0.002	0.001	0.002	0.002	0.003	0.002	0.001	0.002
02/06	0.001	0.001	0.002	0.002	0.002	0.002	0.002	0.003	0.002	0.002	0.003	0.001	0.001	0.002	0.002	0.002
02/22	0.002	0.001	0.002	0.002	0.001	0.001	0.002	0.067	0.001	0.001	0.002	0.002	0.001	0.001	0.001	0.002
03/10	0.002	0.002	0.002	0.001	0.001	0.001	0.001	0.001	0.001	0.001	0.002	0.002	0.001	0.001	0.001	0.001
03/26	0.001	0.001	0.002	0.002	0.002	0.001	0.001	NA	0.003	0.001	0.001	0.001	0.002	0.002	0.001	0.001
04/11	0.001	0.001	0.001	0.001	0.001	0.001	0.002	0.001	0.001	0.001	0.001	0.001	0.001	0.001	0.001	0.001
04/27	0.001	0.001	0.001	0.001	0.001	0.001	0.001	0.001	0.001	0.001	0.001	0.001	0.001	0.001	0.001	0.001
05/13	0.002	0.002	0.001	0.001	0.001	0.001	0.001	0.001	0.001	0.001	0.001	0.001	0.001	0.001	0.001	0.001
05/29	0.001	0.001	0.001	0.001	0.001	0.001	0.001	0.001	0.001	0.001	0.001	0.001	0.001	0.001	0.001	0.001
06/14	0.001	0.001	0.001	0.001	0.001	0.001	0.001	0.001	0.001	0.001	0.001	0.001	0.001	0.001	0.001	0.001

Table S4.4. Area of the Amazon Basin and land cover types used in our study.

Region	Area (km^2)
Amazon	5,974,715
Forest	3,787,974
Forest >2000mm MAP	2,815,460
Forest <2000mm MAP	952,526
Non-forest	698,303

Chapter 5: Inconsistencies between TROPOMI solar-induced chlorophyll fluorescence, gross primary production, and vegetation indices

Abstract

The newly launched TROPOspheric Monitoring Instrument (TROPOMI) provides near-daily global solar-induced chlorophyll fluorescence (SIF) retrievals at unprecedented spatial resolution. SIF and gross primary production (GPP) are linearly related at coarse spatiotemporal resolutions, but currently the spatiotemporal consistency between TROPOMI SIF, GPP estimates, and vegetation indices (VIs), which are often used to derive GPP estimates, is unknown. Here we report for all non-water landcover types on Earth the consistency in space and time between TROPOMI SIF, GPP from the Vegetation Photosynthesis Model (GPP_{VPM}), GPP derived from the Moderate Resolution Imaging Spectroradiometer (MODIS; GPP_{MOD17}), and bidirectional reflectance distribution function (BRDF) adjusted (MCD43) and standard, non-adjusted MODIS VIs (MOD09). We find that 1) SIF is highly consistent with GPP and VIs, except in evergreen broadleaf forest; 2) NIRv is not clearly more consistent with SIF than EVI; and 3) there is no notable difference in the consistency of BRDF-adjusted and non-adjusted with SIF, except in the evergreen broadleaf forest where non-adjusted VIs are substantially more consistent with SIF. Our results highlight the utility of TROPOMI SIF in areas of the world where modeled GPP and VIs have a relatively poor ability to capture vegetation dynamics, and have important implications on the application of SIF and VIs in modeling global GPP.

Significance Statement

Models of gross primary production (GPP) and space-borne vegetation indices (VIs) have provided insight into the seasonal dynamics of vegetation productivity and the response of vegetation to climate variability for decades, but such changes are difficult to validate at the

global scale with ground-based measurements. Retrievals from the newly launched TROPOspheric Monitoring Instrument (TROPOMI) of solar-induced chlorophyll fluorescence, which is emitted by plants during photosynthesis, gives us a better understanding of where and when GPP models and VIs are able and unable to capture changes in productivity.

1. Introduction

For decades, the monitoring of vegetation productivity, mapping of vegetation cover, and tracking land use change at the global scale have relied upon satellite observations of sunlight reflected by surfaces on Earth's terrain. Vegetation indices (VIs), such as the Normalized Difference Vegetation Index (NDVI) (Rouse Jr et al. 1974) and Enhanced Vegetation Index (EVI) (Huete et al. 1997a), have been used to track the 'greenness' of vegetation by observing the high absorption of visible sunlight by chlorophyll and the high reflectance of near infrared energy by leaves. Other vegetation indices, such as the Normalized Difference Water Index (NDWI) (Gao 1996a) and Land Surface Water Index (LSWI) (Xiao et al. 2004), have been used to remotely sense vegetation water content by considering the high absorption of energy by liquid water in the shortwave infrared region of the electromagnetic spectrum. These VIs have been successfully used to not only map vegetation and determine vegetation cover types but also in models to estimate the gross primary productivity (GPP) of vegetation, or photosynthesis, and its responses to changes in human management and climate variability. Although VIs are invaluable tools and are the backbone of observing vegetation dynamics from space, they only provide auxiliary information on vegetation structure, such as chlorophyll content, water content, and leaf area.

Recent scientific advancements now enable us to extract more direct information on photosynthesis, a vegetation function, from surface reflectance data by looking at parts of the far

red and near infrared spectrum where solar-induced chlorophyll fluorescence (SIF), which is emitted by plants during photosynthesis, is infilling an otherwise normal reflectance curve. SIF retrieval requires a high spectral resolution spectrometer to detect the infilling of fluorescence, which has only been satisfied by spaceborne platforms that target trace gases in the atmosphere. The first retrievals of SIF from spaceborne platforms were described in a series of papers in 2011 and 2012 and were conducted using the Greenhouse gases Observing SATellite (GOSAT) (Frankenberg et al. 2012; Guanter et al. 2012; Joiner et al. 2011) and SCanning Imaging Absorption SpectroMeter for Atmospheric CHartographY (SCIAMACHY) (Joiner et al. 2012). More recently, the Global Ozone Monitoring Experiment–2 (GOME-2) (Joiner et al. 2013) and Orbiting Carbon Observatory-2 (OCO-2) (Frankenberg et al. 2014) have been used to retrieve SIF.

These early platforms have been valuable test beds for different SIF retrieval methods (Joiner et al. 2016; Köhler et al. 2015) and early investigations into the dynamics of photosynthesis (Guan et al. 2015; Porcar-Castell et al. 2014; Sun et al. 2017), but the inherent noisiness of the data and coarse spatiotemporal resolution of the SIF data products (monthly, 4 to 0.5 degree) has limited finer-scale scientific inquiry. Excitingly, the newly launched TROPOspheric Monitoring Instrument (TROPOMI) onboard the Sentinel-5 Precursor satellite is providing SIF data with near-daily global coverage at much finer spatial resolutions than older platforms (3.5 x 7 km at nadir) (Köhler et al. 2018). The new TROPOMI SIF data has begun to provide valuable contributions to debates over the seasonality of terrestrial photosynthesis, which has important implications for understanding the inter- and intra-annual variability of Earth's atmospheric carbon dioxide concentration (Doughty et al. 2019).

Currently, there are three pressing scientific questions in the field of remote sensing that TROPOMI SIF can help us answer. First, in what regions are modeled GPP, NDVI, and EVI inconsistent with SIF? Previous studies have shown that traditional VIs have a poor consistency with SIF and/or GPP in evergreen needleleaf forest (Magney et al. 2019; Walther et al. 2016), evergreen broadleaf forest (Morton et al. 2014), and wetlands (Taddeo et al. 2019) and have suggested that GPP models that use these vegetation indices are likely not accurately estimating observed seasonal changes in productivity. We suspect that modeled GPP and VIs are relatively inconsistent in these three landcover types because spaceborne SIF can better capture vegetation dynamics in evergreen ecosystems where chlorophyll content remains constant, in cloudy regions, and in regions where inundation is consistent or frequent because 1) spaceborne SIF is less affected by radiances from non-vegetation, such as soil characteristics (Huete et al. 1985; Wang et al. 2019a), standing water (Taddeo et al. 2019), and snow (Delbart et al. 2005; Jönsson et al. 2010; Walther et al. 2016); 2) spaceborne SIF is less affected by cloud cover than VIs (Frankenberg et al. 2012; Guanter et al. 2015); and 3) canopy SIF is highly responsive to short and long term environmental conditions whereas canopy vegetation indices are not.

Second, does the near-infrared reflectance of terrestrial vegetation (NIRv), a new VI, have advantages over the traditionally used EVI and NDVI? Recently, a study has found that NIRv has a better relationship with modeled GPP (FluxCom) than SIF (GOME-2) and that NIRv could be a superior VI when used to model global GPP (Badgley et al. 2017). However, the relationship between NIRv and GPP and TROPOMI SIF has not been explored at the global scale. Furthermore, although Badgley et al. (2017) compared the differences between GPP vs. NDVI and GPP vs NIRv, no analysis was conducted with EVI. We anticipate that NIRv and EVI

have a similar consistency with TROPOMI SIF and modeled GPP, and that both have a better relationship with SIF than NDVI.

Third, is there a disagreement between BRDF-adjusted and non-adjusted vegetation indices when compared to SIF? It has been strongly argued that BRDF-adjusted VIs should be used when monitoring changes in vegetation or estimating GPP, especially in the tropics, because the adjustment can help account for differences in viewing and illumination geometry between surface reflectance observations (Morton et al. 2014). Others have pointed out that BRDF-adjustment can have disadvantages (Huete et al. 2002) and that a BRDF-adjustment decreases the magnitude of change, but that the changes remain significant (Guan et al. 2015; Maeda et al. 2014; Saleska et al. 2016). We suspect that BRDF-adjusted NIRv and EVI have a better relationship with SIF in the tropics than non-adjusted VIs, but that the difference will be relatively negligible for vegetation cover at mid and high latitudes.

Given these three questions and our hypotheses, our primary aims are to evaluate the spatial and temporal consistency between TROPOMI SIF, GPP, and VIs to 1) identify areas where the GPP models and VIs are inconsistent with SIF; 2) determine which VI is more consistent with SIF and GPP; and 3) ascertain the difference between BRDF-adjusted and non-adjusted VIs when compared to SIF. In our analysis we use GPP from two models, the Vegetation Photosynthesis Model (GPP_{VPM}) (Zhang et al. 2017b) and MOD17 (GPP_{MOD17}) from the Moderate Resolution Imaging Spectroradiometer (MODIS) product (Running and Zhao 2015). We compare the three VIs, NIRv, EVI, and NDVI, to SIF as calculated using two different MODIS surface reflectance data products: the standard MOD09 and the MCD43 bidirectional reflectance distribution function (BRDF) adjusted products. Our results have strong implications on future applications of SIF and VIs by highlighting the advantages of using SIF

for tracking vegetation dynamics and addressing some long-standing concerns over the effect of adjusting surface reflectance data for viewing and illumination geometry.

2. Methods

2.1 TROPOMI SIF retrievals

We calculated daily-corrected SIF by multiplying the daily correction factor and instantaneous SIF as provided in the ungridded (vector) SIF data at ftp://fluo.gps.caltech.edu/data/tropomi. TROPOMI has a 16-day revisit cycle, meaning that the satellite's overpass is slightly offset from the previous day and the footprint of any day's swath will repeat after 16 days. Thus, the angle between TROPOMI's sensor and any given point on Earth varies day-to-day. The angle at which SIF emission is observed from the vegetation canopy can affect the retrieved SIF value, so it is important to consider the viewing geometry when working with satellite-retrieved SIF data (Köhler et al. 2018). Currently, the relationship between viewing angle and observed SIF is not fully understood, so correcting the SIF data is not advisable and has not been performed for any of the SIF retrievals from previously launched satellites.

In our previous study, we calculated 16-day mean SIF to account for the potential effect of viewing geometry on observed SIF, with the logic being that the viewing geometry over a 16-day period is comparable to the subsequent 16-day periods (Doughty et al. 2019). Likewise, in this study we found that the viewing geometry over an 8-day period is comparable to the viewing geometry over the subsequent 8 days, as demonstrated in Fig. 5.1. This figure is an ideal scenario, but what is important is not that the viewing angles of each 8-day span are identical but that the distribution of the viewing angles in each 8-day span are relatively uniform across the range of viewing angles. We have demonstrated these distributions for two gridcells in Fig. 5.2.

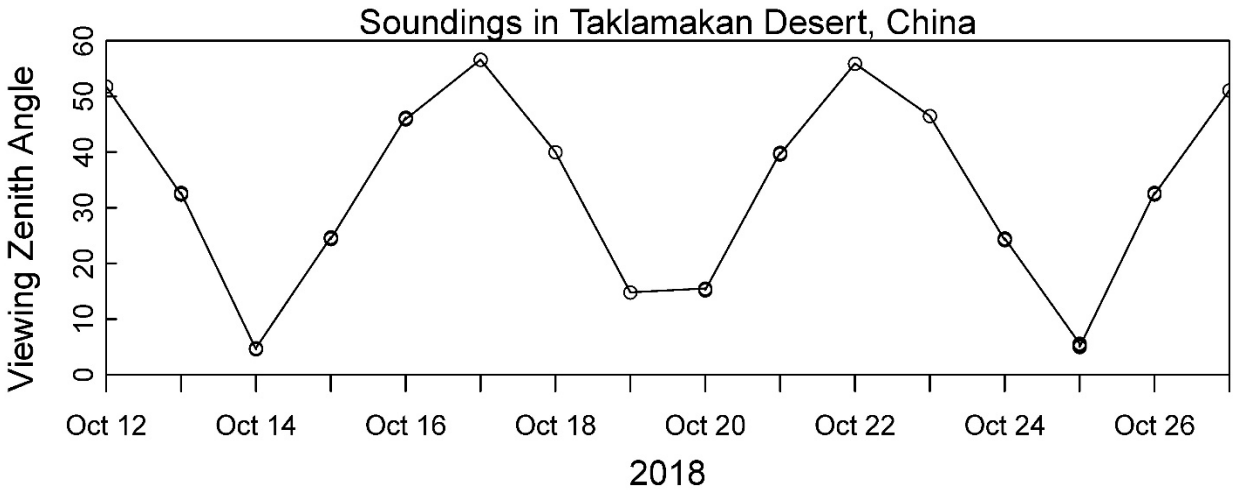

Figure 5.1 | Viewing zenith angles of all TROPOMI soundings within a 0.05-degree gridcell in the Taklamakan Desert, China. The VZAs in the first 8 overpasses are opposite of those in the second 8 days, indicating that the VZAs from which SIF retrievals are made in each 8-day group are comparable.

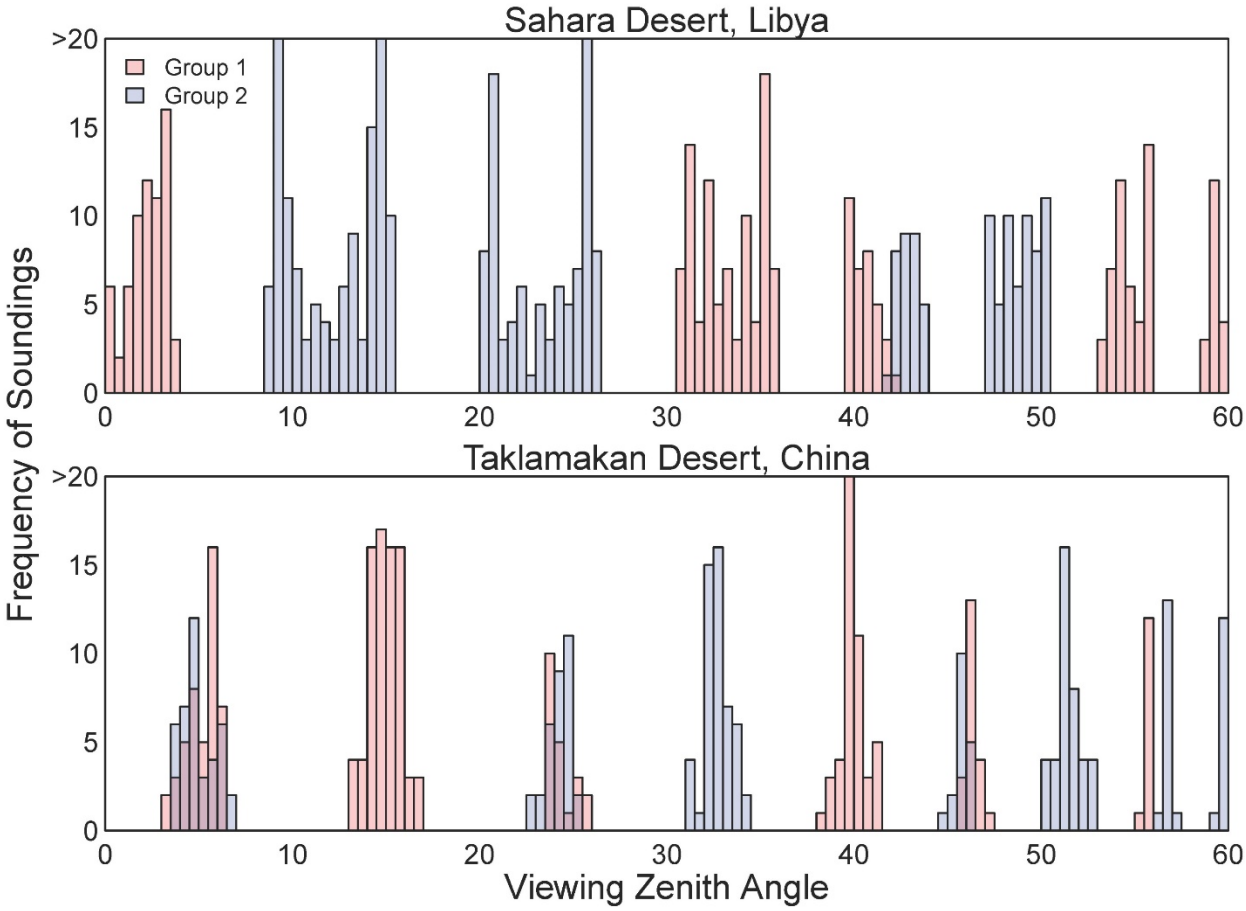

Figure 5.2 | Frequency distribution of TROPOMI viewing zenith angles for a 0.05-degree gridcell in each the Sahara and Taklamakan Deserts. The distributions of all viewing zenith angles are shaded red for the first 8 overpasses and blue for the second 8 overpasses from all 16-day spans during March 8th – December 20th, 2018. Each group has VZAs distributed complimentary to the other across the span of all VZAs.

Coincidentally, 8-day mean SIF also affords us the opportunity to compare TROPOMI SIF to MODIS vegetation indices (VIs). Thus, we gridded TROPOMI SIF vector data into 8-day means starting on March 6th, 2018, which corresponds to the temporal resolution of the 8-day MODIS-based products. Each SIF gridcell value was the area-weighted mean of all soundings within the gridcell over an 8-day period. We filtered the soundings with thresholds of 60° for viewing zenith angle, 0.8 for cloud fraction, 70° for solar zenith angles, and 120° for phase angles as described by Köhler et al. (2018). We gridded the SIF data to 0.05 and 0.20 degrees for comparison to GPP and VIs at the same resolution and found that GPP and VIs were generally

consistent with SIF at 0.05 degree where the SIF data had not been heavily filtered due to zenith angles and clouds (Fig. S5.1). In short, a coarser spatial resolution of 0.20 degrees was needed to establish whether there was a good relationship between SIF, GPP, and VIs outside of the mid to high latitude regions due to a lack of TROPOMI data after filtering, gaps in TROPOMI's coverage in the tropics, and the need to average soundings to reduce precision error and account for viewing geometry (Doughty et al. 2019; Frankenberg et al. 2014; Köhler et al. 2018). All results and analysis presented in this paper were produced using the 0.20-degree data.

2.2 Gross primary production

We compared two MODIS-derived GPP datasets to TROPOMI SIF, the Vegetation Photosynthesis Model (VPM) V02 and the MODIS MOD17A2H V006 products. Both datasets estimate GPP using the light use efficiency model (LUE) and are offered with a spatial and temporal resolution of 500 m and 8 days. We aggregated both datasets to 0.20-degree spatial resolution before we compared them with TROPOMI SIF. The VPM model uses EVI calculated from MOD09 surface reflectance as a proxy of the fraction of absorbed photosynthetically active radiation (PAR) by chlorophyll ($fPAR_{chl}$) and biome-specific light-use efficiency (ε_g) values to compute GPP as:

$$GPP_{VPM} = fPAR_{chl} \times \text{PAR} \times \varepsilon_g$$

GPP_{MOD17} differs primarily from GPP_{VPM} in that GPP_{MOD17} uses the fraction of PAR absorbed by the canopy ($fPAR_{canopy}$) rather than chlorophyll. Other global GPP datasets, such as FLUXCOM and the Breathing Earth System Simulator (BESS), were considered for use in this study but were not available for 2018.

2.3 Vegetation indices

We calculated the near-infrared reflectance of terrestrial vegetation (NIRv) (Badgley et al. 2017), Enhanced Vegetation Index (EVI) (Huete et al. 1997a), and Normalized Difference Vegetation Index (NDVI) (Rouse Jr et al. 1974) from two commonly used MODIS products, MOD09A1 V006 (Vermote 2015) and MCD43C4 V006 (Schaaf and Wang 2015). The MOD09 dataset is the standard MODIS surface reflectance product and the MCD43 surface reflectance dataset is adjusted for viewing geometry using the bidirectional reflectance distribution function (BRDF). The equations for MODIS NIRv, EVI, and NDVI are:

$$\mathrm{NIRv} = \frac{b2 - b1}{b2 - b1} \times b2$$

$$\mathrm{EVI} = 2.5 \times \frac{b2 - b1}{b2 - 6 * b1 + 7.5 * b3 + 1}$$

$$\mathrm{NDVI} = \frac{b2 - b1}{b2 - b1}$$

where $b1$ is the red band, $b2$ is the near infrared band, and $b3$ is the blue band.

The MOD09 EVI data that we used in this study was the same EVI data that was prepared for input into VPM. We derived MOD09 NIRv and NDVI using the same methods that were used to derive the MOD09 EVI data. More specifically, poor quality data were identified, gaps were filled, and the data was smoothed using the Best Index Slope Extraction algorithm, linear interpolation, and the Savitzky-Golay filter as detailed by Zhang et al. (2017b). The native spatial and temporal resolution of these MOD09 VIs are 500 m and 8 day, so we aggregated these VIs to 0.05- and 0.20-degree spatial resolution using the mean of the 500-m gridcells that comprise each 0.05- and 0.20-degree gridcell.

The MCD43C4 data we used to calculate VIs is a daily product, which we aggregated temporally to 8-day means. This dataset, which is provided in 0.05-degree spatial resolution, is

produced using 16 days of Terra and Aqua MODIS data, and is weighted to the ninth day of the retrieval period (Schaaf and Wang 2015). After calculating the VIs using the original MCD43C4 data, we aggregated the VIs to 0.20 degree by calculating the mean of the 0.05-degree gridcells in each 0.20-degree gridcell. The methods used to derive the MCD43 dataset are intended to remove the effects of viewing angle and directional reflectances, so the surface reflectance in this dataset approximates what the reflectance would be if it were observed at nadir during the local solar noon (Schaaf and Wang 2015). The Multi-Angle Implementation of Atmospheric Correction (MAIAC) (MCD19) vegetation indices were considered for use in this study but were not available for 2018.

2.4 Land cover

The land cover classes for 2018 used in our study were determined using the MCD12C1 V006 dataset. This MODIS product is provided annually at 0.05-degree spatial resolution and used the majority method when aggregating to 0.20-degrees. We used the corrected version published on or about August 12, 2019, which was revised to correct land cover classification errors that occurred when the data were originally produced. We used the International Geosphere-Biosphere Programme (IGBP) classifications from the first layer of the MCD12C1 data file, which attributes land cover classification based on the majority of land cover in each gridcell.

3. Results

3.1 Spatial inconsistencies between SIF, GPP and VIs

Latitudinally, we found annual mean GPP and VIs to be most inconsistent with TROPOMI SIF in the equatorial region where high quality satellite observations are plagued by frequent cloud cover (Fig. 5.3). GPP_{MOD17} had dramatically lower estimates of GPP than GPP_{VPM}, which seemed to underestimate GPP in the Amazon, Southeast Asia, and Western Europe, and

overestimated GPP in tropical Africa when compared to SIF. NDVI was relatively inconsistent with SIF across the latitudinal gradient, with NIRv and EVI being comparable and more consistent with SIF, especially in the equatorial region. At the global scale, GPP_{VPM} was more consistent with SIF ($R^2 = 0.85$) than GPP_{MOD17} ($R^2 = 0.77$) (Fig. 5.4). We also found no notable difference between BRDF-adjusted and non-adjusted NIRv and EVI when compared to SIF, but BRDF-adjusted NDVI was more consistent with SIF ($R^2 = 0.68$) than non-adjusted NDVI ($R^2 = 0.60$).

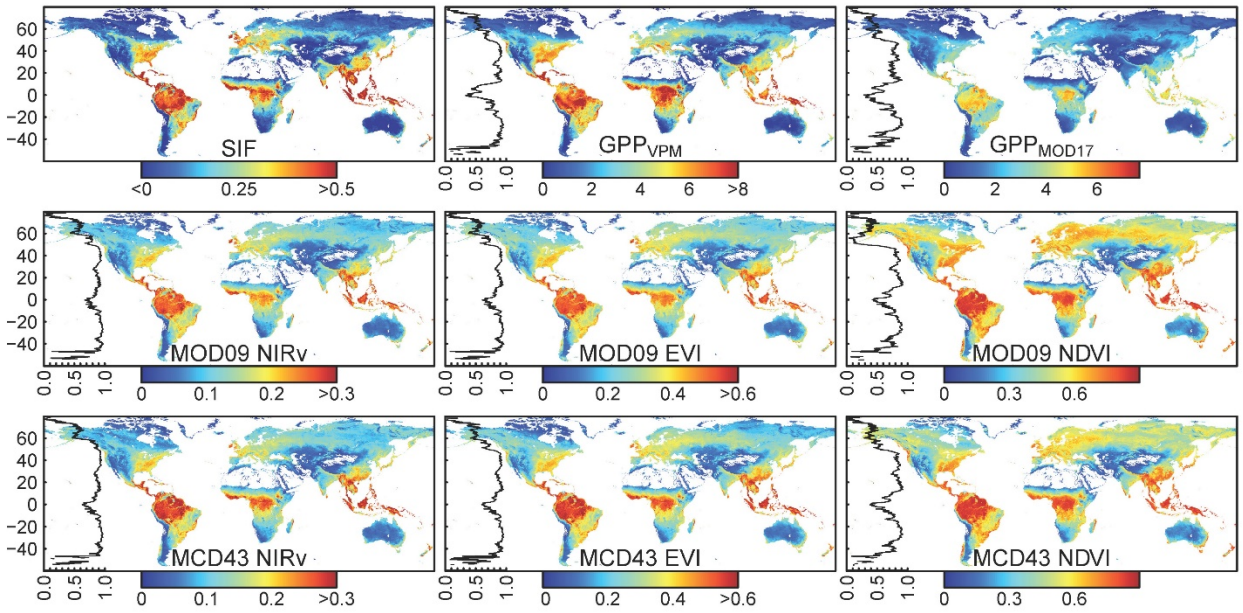

Figure 5.3 | Global comparison of mean 2018 TROPOMI SIF with GPP, NIRv, EVI, and NDVI. Inset graphs are significant ($p<0.05$) R^2 values (x axis) from linear regressions by latitude (y axis) with TROPOMI SIF. Spatial resolution is 0.20 degrees.

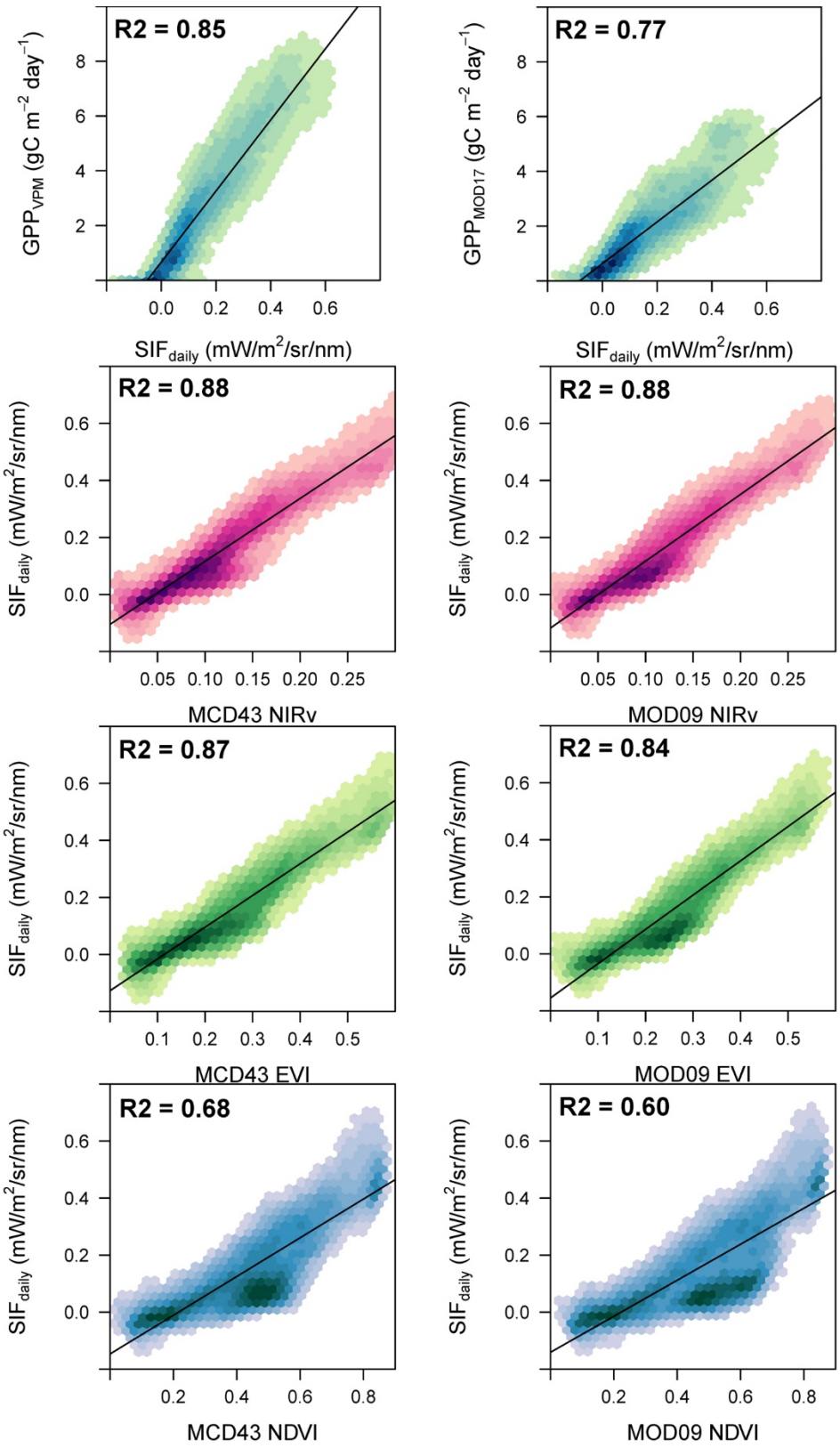

Figure 5.4 | Linear regression of mean 2018 TROPOMI SIF with GPP, EVI, and NDVI at 0.05 degree.

For each land cover type, we found GPP_{VPM} to be substantially more consistent with SIF than GPP_{MOD17}, especially in evergreen broadleaf, deciduous needleleaf, and deciduous broadleaf forests, wetlands, urban areas, and cropland/natural vegetation mosaics (Fig. 5.5). Relative to NIRv and EVI, which had very similar consistencies with SIF, NDVI was highly inconsistent with SIF for each land cover type and the inconsistencies were most notable across all forest types. BRDF-adjusted and non-adjusted VIs were comparable for each land cover type, except in deciduous needleleaf forest where non-adjusted VIs were slightly more consistent with SIF and in wetlands where BRDF-adjusted VIs were slightly more consistent.

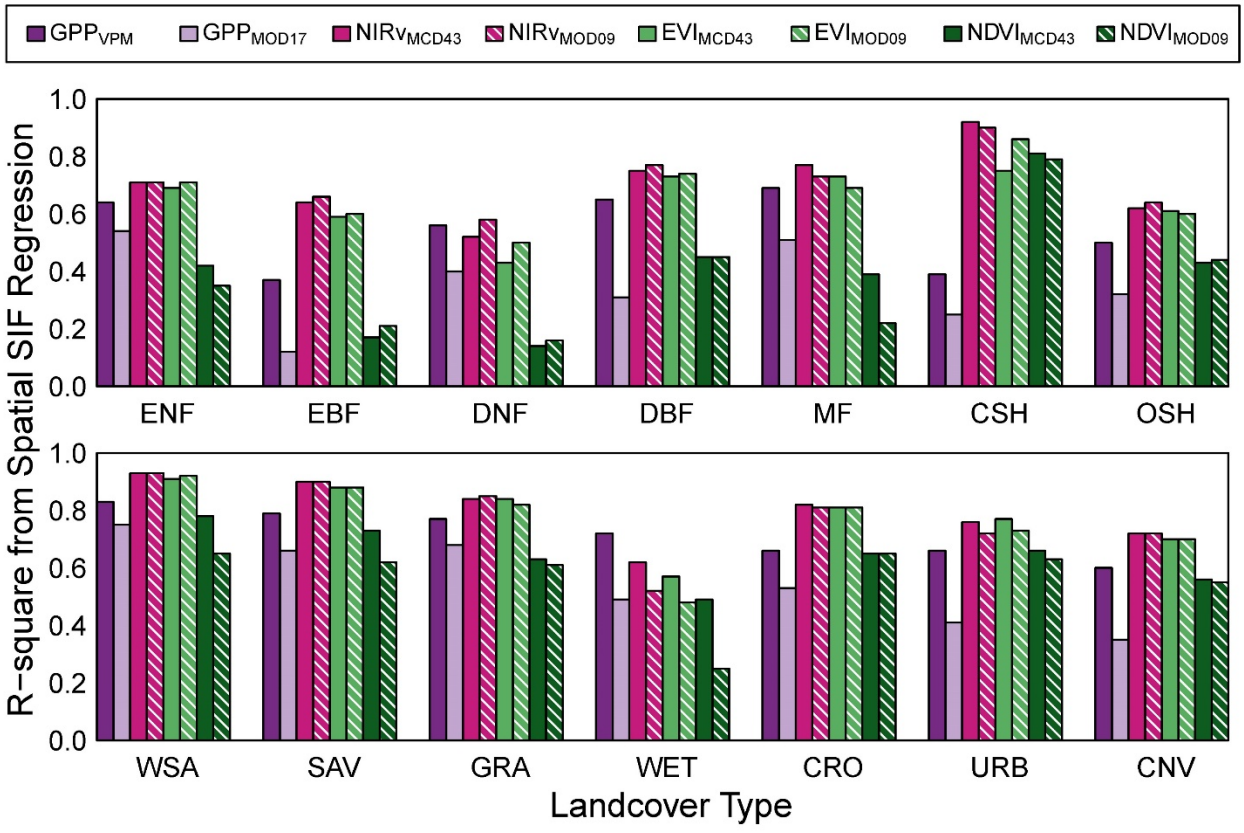

Figure 5.5 | R^2 values from spatial linear regression of TROPOMI SIF with GPP, NIRv, EVI, and NDVI by land cover type in 2018. All linear regressions had a significant relationship ($p<0.05$). ENF=Evergreen Needleleaf Forests; EBF=Evergreen Broadleaf Forests; DNF=Deciduous Needleleaf Forests; DBF=Deciduous Broadleaf Forests; MF=Mixed Forests; CSH=Closed Shrublands; OSH=Open Shrublands; WSA=Woody Savannas; SAV=Savannas;

GRA=Grasslands; WET=Permanent Wetlands; CRO=Croplands; URB=Urban and Built-up Lands; CNV=Cropland/Natural Vegetation Mosaics.

3.2 Temporal inconsistencies between SIF, GPP and VIs

Temporally, we generally found GPP_{MOD17} to be less consistent with SIF than GPP_{VPM}, especially in evergreen broadleaf forest, savannas, and cropland/natural vegetation mosaics (Fig. 5.6). Both GPP models performed relatively poorly in the evergreen broadleaf forest and in wetlands, with GPP_{MOD17} having no significant relationship with SIF in evergreen broadleaf forest. NDVI was not as consistent with SIF as NIRv and EVI and had especially low or no significant consistency in evergreen forests and wetlands. The consistencies of NIRv and EVI with SIF were largely comparable across land cover types, except in closed and open shrublands where BRDF-adjusted EVI was less consistent. The consistency of BRDF-adjusted NIRv and EVI with SIF was substantially lower than non-adjusted NIRv and EVI in the evergreen broadleaf forest. Overall, both GPP models and all adjusted and non-adjusted VIs had poor consistency with SIF in wetlands.

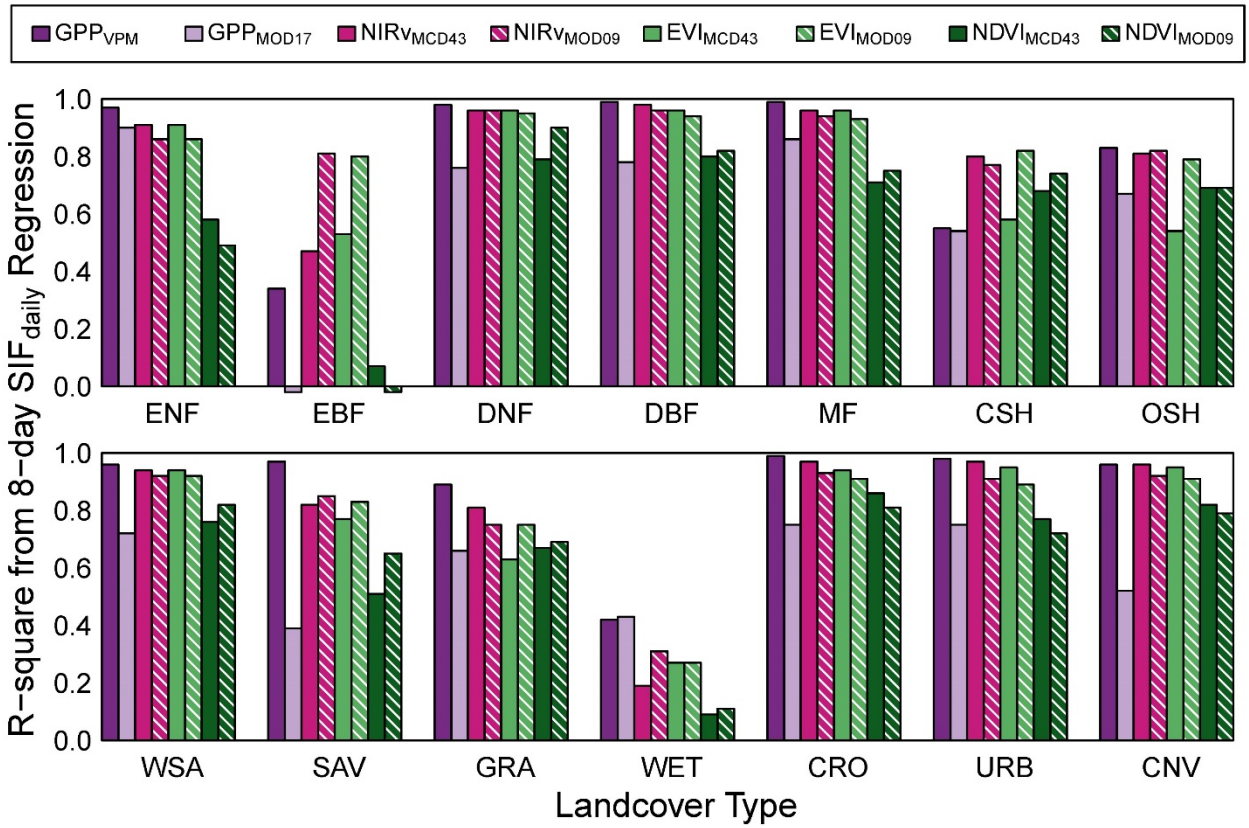

Figure 5.6 | R^2 values from linear regression of 8-day TROPOMI SIF with GPP, NIRv, EVI, and NDVI at 0.05 degree by land cover type in 2018. High R^2 values indicate a strong correlation in the seasonality of the variable and SIF for the respective land cover type. All linear regressions had a significant relationship ($p<0.05$) except for GPP_{MOD} and both NDVIs in evergreen broadleaf forest and $NDVI_{MCD43}$ in wetlands.

When looking at the distribution of R^2 values from gridcell-level (0.20 degree) regressions (Fig. 5.7), we found NDVI to be the most inconsistent with SIF and that both BRDF-adjusted and non-adjusted NIRv and EVI were highly consistent and comparable. Overall, GPP_{VPM} had higher consistency than GPP_{MOD17} and all VIs, but the R^2 maps show that GPP_{VPM} was less consistent with SIF in the equatorial region and Southeast Asia than the VIs but was more consistent at mid and high latitudes. GPP_{MOD17} was also highly inconsistent with SIF in the equatorial region and Southeast Asia, but also had relatively poor consistency in eastern and southern South America and South Africa. Both GPP models and all VIs had little to no significant relationship with SIF in Southeast Asia.

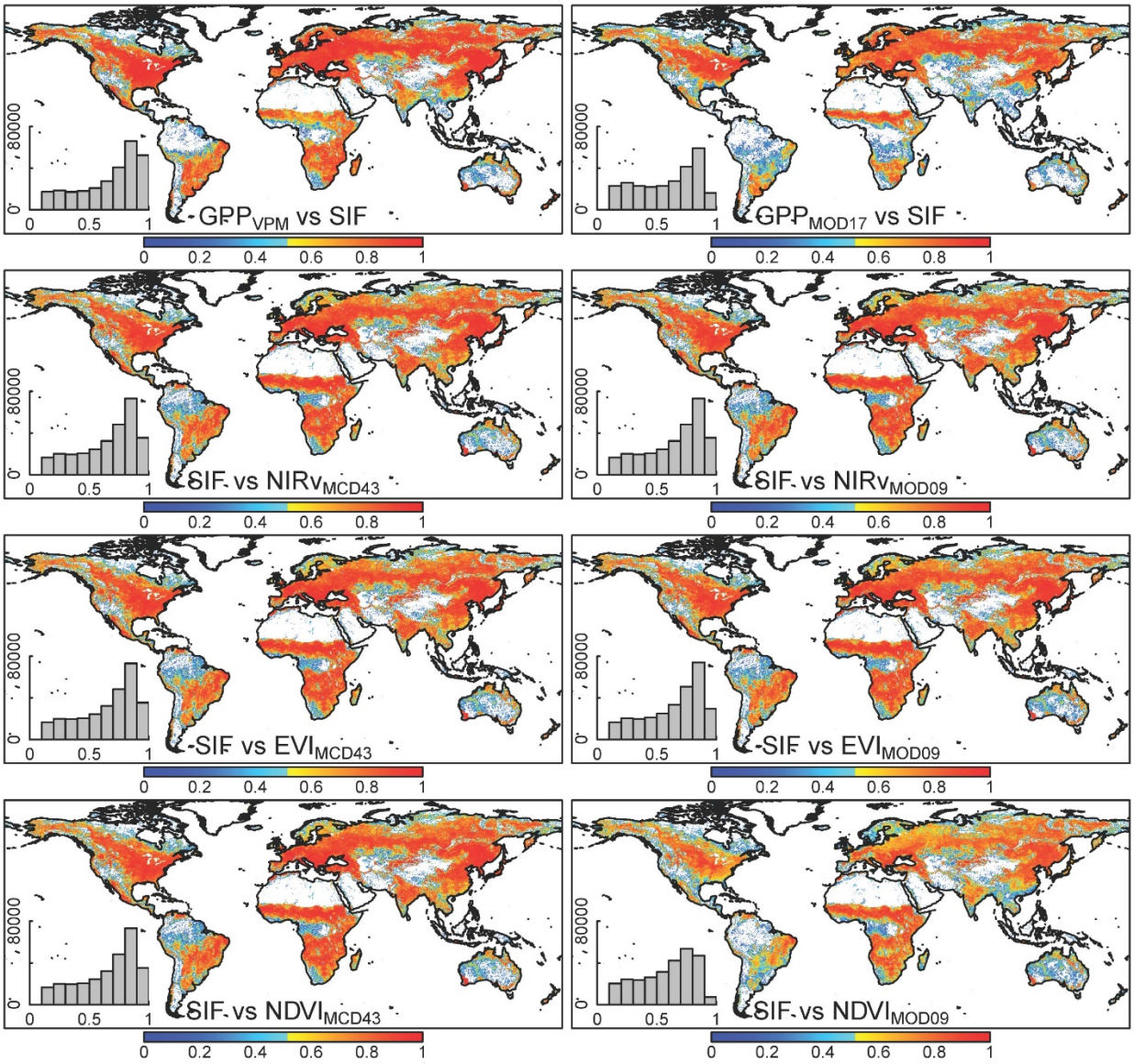

Figure 5.7 | R^2 values from pixel-based, time-series regression results for GPP versus SIF and SIF versus vegetation indices in 2018. High R^2 values signal a strong correlation with 8-day SIF from March through December 2018. Shown are only R^2 values from linear regression results with a significant p-value of <0.05. Spatial resolution is 0.20 degrees.

4. Discussion

4.1 Potential advantages and disadvantages of SIF

Before we discuss the results of our study, it is important to note that there are some trade-offs when using SIF and VIs when tracking vegetation dynamics and understanding these trade-offs will help us interpret our results. Spaceborne SIF is considered to have may

advantages over vegetation indices. SIF is sensitive to changes in leaf physiology, leaf function, and canopy structure. For instance, SIF is sensitive to xanthophylls and carotenes, which are pigments that help protect photosystems from degradation by dissipating energy away from chlorophyll and into heat (non-photochemical quenching). Carotenoids are produced by the leaves of evergreen needleleaf species in the winter, a time when photosynthesis is limited by freezing temperatures. Thus, the rapid creation or destruction of these pigments during the transition into and out of winter, which directly impact the amount of energy entering the photosystems for photosynthesis, affect retrieved SIF values whereas changes in carotenoids may not have a notable impact on vegetation indices (Magney et al. 2019; Nakaji et al. 2007; Stylinski et al. 2002).

SIF is also not as affected as traditional VIs by non-vegetation radiances, such as soil characteristics (Huete et al. 1985), open water (Taddeo et al. 2019), snow (Delbart et al. 2005; Jönsson et al. 2010; Walther et al. 2016), cloud cover (Frankenberg et al. 2014; Guanter et al. 2015), and where the land surface is heterogenous, such as urban areas (Wang et al. 2019b). SIF does not saturate when leaf area is high, unlike NDVI. TROPOMI SIF compares very well to tower based GPP estimates at Niwot Ridge, CO. SIF/GPP relationship remains strong under clear and diffuse sky conditions (Magney et al. 2019).

The performance of vegetation indices varies widely within and among ecosystem types. For example, EVI-based start of the growing season (SOS) was found to be late for boreal evergreen needleleaf forest (Walther et al. 2016), but was early in Alaskan tundra (Luus et al. 2017). A synthesis of six vegetation indices found a wide performance across and within vegetation indices for several wetland ecosystem types (Taddeo et al. 2019). In short, a host of environmental and physiological factors that determine canopy photosynthesis affect retrieved

SIF but may not substantially affect VIs. SIF is more immediately responsive to any factor that may inhibit or amplify photosynthesis.

However, the use of spaceborne SIF to track changes in photosynthesis is currently limited in three ways. For these reasons, it is advantageous to develop methods and analyses that utilize both SIF and VIs. First, SIF is a very low amount of energy emitted by plants and the retrieved SIF values tend to be inherently noisy due to detector noise. Thus, it is generally advised not to use single SIF values for analysis. Rather, to properly exploit the data one should average several soundings over space and/or time to reduce the precision errors in the mean of n samples by $1/\sqrt{n}$ (Frankenberg et al. 2014; Köhler et al. 2018).

Second, viewing and illumination geometry must be considered when working with spaceborne SIF data (Köhler et al. 2018). Day-to-day changes in cloud-free SIF are largely driven by noise, as previously discussed, and the viewing angle of the satellite – not actual changes in SIF (Porcar-Castell et al. 2014). Thus, it is advisable to average SIF values across space and/or time to not only reduce the precision error but also to account for the effect of different viewing geometries on retrieved SIF (Doughty et al. 2019). Ideally, any given number of SIF values that comprise a mean would be uniformly distributed among TROPOMI's viewing angles. It is also important to note that low phase angles, which is the angle between the satellite and the sun, can effect retrieved SIF values by altering the ratio of sunlit to shaded leaves observed by the satellite (Doughty et al. 2019; Köhler et al. 2018; Porcar-Castell et al. 2014). Thus, even if one accounts for viewing geometry, there is the potential that the seasonal variation in the solar zenith angle may influence the seasonality of SIF values.

Finally, although the spatial and temporal resolution of TROPOMI SIF soundings are a substantial improvement over preceding spaceborne platforms from which SIF has been

retrieved, the spatial resolution remains much coarser than the spatial resolution of platforms that have traditionally been used for deriving vegetation indices, such as MODIS (500 m) and Landsat (30 m). Also, TROPOMI has daily coverage at high and low latitudes, but in the equatorial region the revisit frequency is 13 out of 16 days. Unfortunately, these gaps in TROPOMI's coverage occur in Earth's cloudiest region where a high observation frequency is most needed, and data is most lacking. However, a new geostationary spaceborne platform, GeoCarb, is planned to launch as early as mid-2022 and will have the ability to provide daily and potentially sub-daily scans of most of North, Central, and South America (Polonsky et al. 2014).

4.2 Evergreen needleleaf forest

Evergreen needleleaf forest (ENF) is the largest forest type on Earth and plays an important role in the global water and carbon cycles (Myneni et al. 2001). This forest type is mainly restricted to high latitude and/or high elevation regions that experience prolonged, cold winters and snow fall. Thus, seasonal changes in VIs in these regions are largely driven by changes in snow cover (Delbart et al. 2005; Jönsson et al. 2010; Walther et al. 2016) and not changes in leaf-level chlorophyll content, which hasn't been found to vary significantly (Magney et al. 2019). The relatively small change in canopy chlorophyll and snow cover have been cited as possible reasons why EVI and NDVI have been found to perform poorly when deriving the start and end of the growing seasons as estimated using eddy flux towers (Karkauskaite et al. 2017) and GOME-2 SIF (Walther et al. 2016).

Although we found the seasonality of EVI and NIRv to be highly consistent with SIF at the landscape scale (R^2 = 0.86-0.91) and at the gridcell level (Fig. 5.7), there was a delay in the start of the season (SOS) EVI relative to SIF (Fig. 5.8). We noted a rapid increase in SIF beginning on April 7th, but non-adjusted EVI and NIRv did not have a notable increase until the

next 8-day period (Fig. 5.8) and surprisingly BRDF-adjusted EVI decreased from April 7th to April 15th (Fig. 5.9). Conversely, BRDF-adjusted NIRv had a notable increase beginning on April 7th and was most consistent with SOS SIF. As expected, NDVI had poor seasonal consistency with SIF, as also observed in situ by (Magney et al. 2019) at an evergreen needleleaf forest site at Niwot Ridge, Colorado, because of NDVI's long-known tendency to saturate when leaf area index is high (Huete et al. 1997b; Lüdeke et al. 1991). However, the SOS inconsistencies between the VIs and SIF did not carry over to the GPP_{VPM} and GPP_{MOD17} estimates (R^2 = 0.97 and 0.90, respectively), which indicated that the models' climate parameters and structure were able to accurately model photosynthesis despite a late increase in VIs relative to SIF (Fig. 5.10).

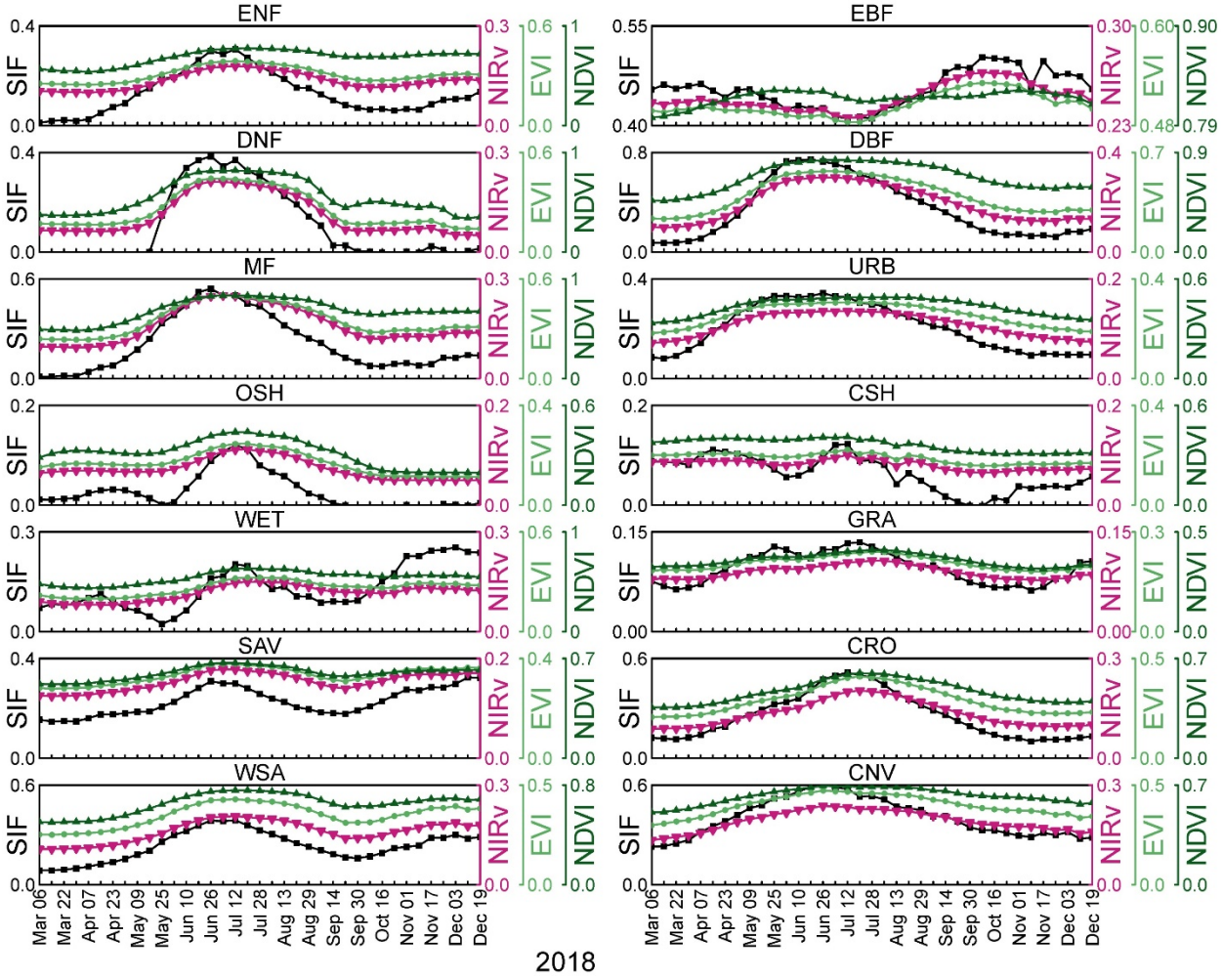

Figure 5.8 | Seasonality of 8-day TROPOMI SIF, and non-adjusted NIRv, EVI, and NDVI from MOD09 by land cover type in 2018.

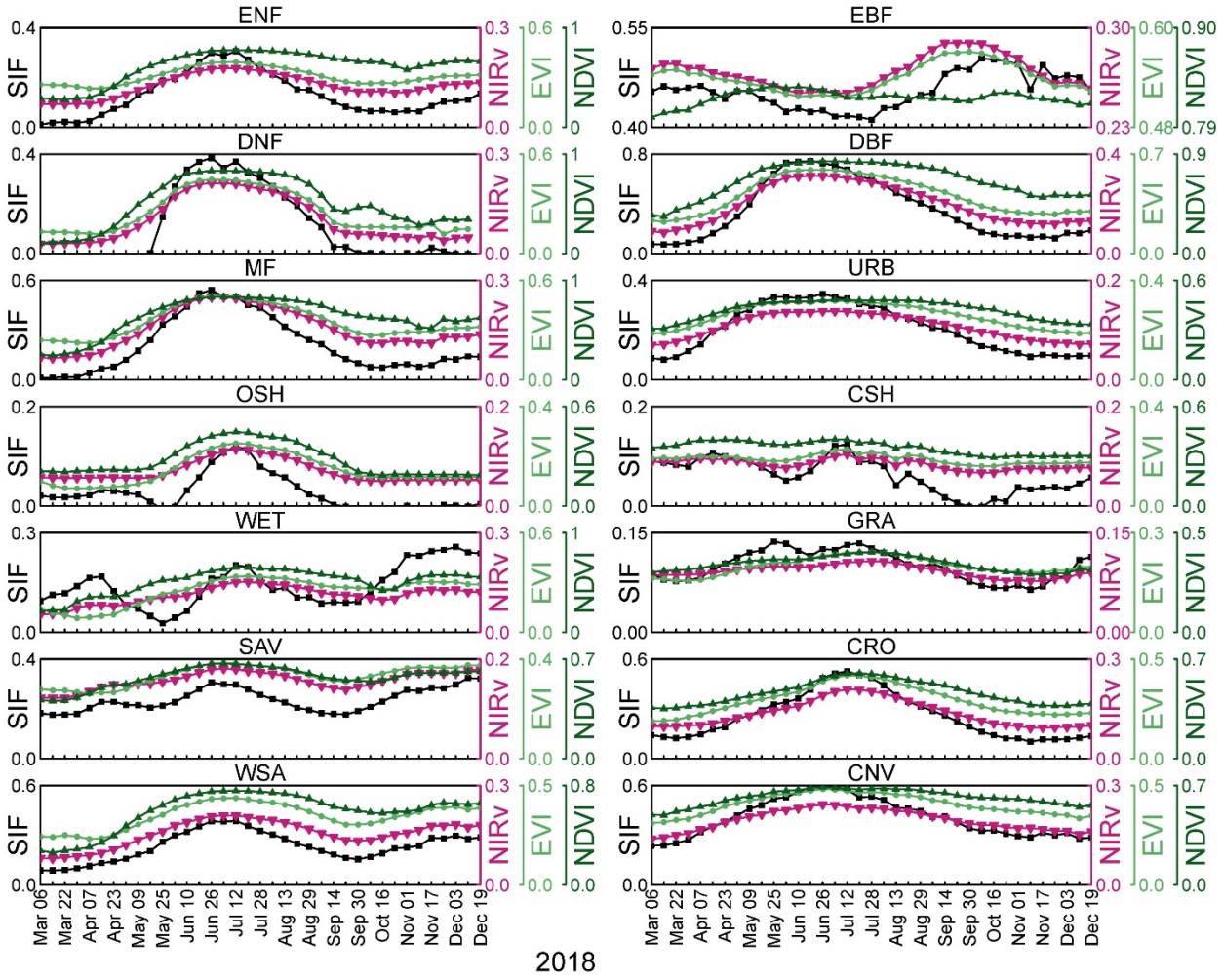

Figure 5.9 | Seasonality of 8-day TROPOMI SIF, and BRDF-adjusted NIRv, EVI, and NDVI from MCD43 by land cover type in 2018.

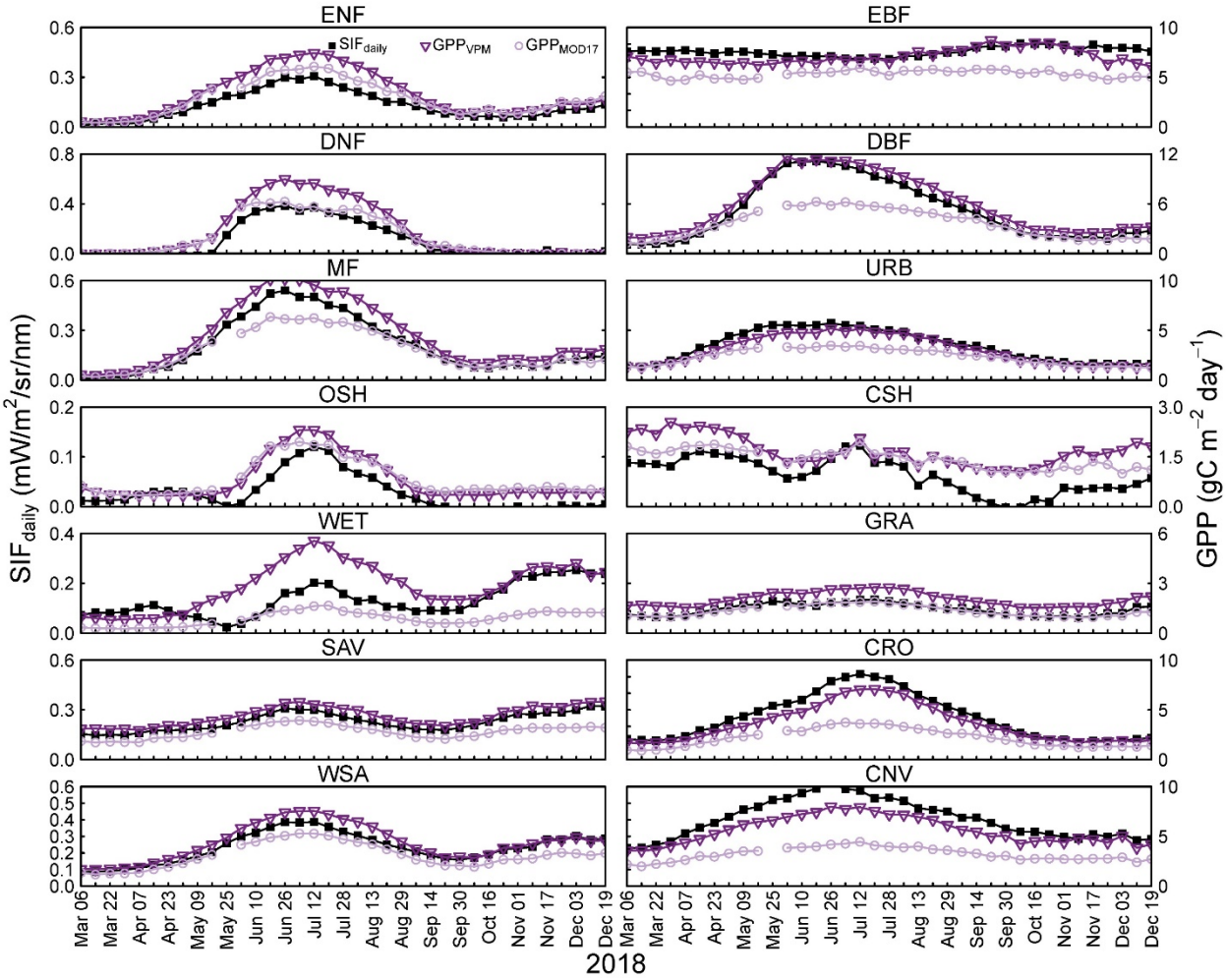

Figure 5.10 | Seasonality of 8-day TROPOMI SIF, GPP_{VPM}, and GPP_{MOD17} by land cover type in 2018.

Our findings on EVI agree with Walther et al. (2016) who found that start of the season (SOS) EVI occurred later than SIF, albeit the delay of SOS EVI we noted was not as long. Also, we did not observe a mismatch between end of season (EOS) SIF and EVI (or NIRv) as Walther et al. (2016) noted. Our findings likely differ because we looked at one year rather than several, and also because the GOME-2 data used by Walther et al. (2016) had a coarser spatial resolution and thus the gridcells were more likely to be mixed. Our findings indicate that although the overall consistency of EVI and NIRv with SIF (R^2 = 0.91 and 0.86 for BRDF-adjusted and non-

adjusted, respectfully) are statistically comparable, BRDF-adjusted NIRv best mimicked SOS SIF.

The start and end of the growing season is of particular interest in high latitude and high elevation forests because increasing global temperatures are expected to lengthen the growing season (Jarvis and Linder 2000) and their enormous spatial coverage on Earth's surface means that small increases in the duration of the growing season can have sizable impact on atmospheric carbon dioxide and methane concentrations (Kasischke and Stocks 2012; Ma et al. 2017). Thus, the ability to accurately monitor the start and end of the growing season for ENF is of extreme importance for informing models that project how these dates will change in the future under warming scenarios, and how longer growing seasons impact the carbon and water cycles, fire frequency, climate feedbacks, forest health, and forest community and ecosystem succession (Flannigan et al. 2000; Randerson et al. 2006; Soja et al. 2007).

4.3 Evergreen broadleaf forest

At the landscape level, we found that the seasonality of NIRv and EVI were both significantly consistent with SIF (R^2 = 0.47 to 0.81) in evergreen broadleaf forest (EBF), but NDVI and GPP_{MOD17} were not significantly consistent due to the tendency of NDVI tendency to saturate when leaf area index is high and the reliance of the GPP_{MOD17} model on NDVI as a proxy of the fraction of photosynthetically active radiation absorbed by the canopy ($fPAR_{canopy}$) (Huete et al. 2010; Propastin et al. 2012). GPP_{VPM} was moderately consistent with SIF in EBF (R^2 = 0.34) and increased with SIF in the during the dry season (~June-October). At the gridcell level, there was a lack consistency between VIs and GPP in the wettest and most cloudy regions of the Amazon and tropical Africa, and a near complete lack of consistency in Southeast Asia (Fig. 5.7). Although the GPP models were more consistent with SIF at mid to higher latitudes,

we noticed that they were less consistent with SIF than VIs in the tropics and subtropics. The inconsistencies of GPP and VIs with SIF in the tropics is driven by two main factors: 1) frequent cloud cover, which reduces the quantity and quality of surface reflectance observations and SIF retrievals and makes it highly likely that cloud conditions are different between the differing TROPOMI and MODIS overpass times; 2) the stronger effect of clouds on VIs than SIF; and 3) gaps in TROPOMI's coverage in the tropics. In Southeast Asia, the apparent underestimation of GPP and unexpectedly low VI values relative to the high values of SIF indicates that cloud cover is likely strongly affecting VIs in this region, and the heterogenous mixture of forest, croplands, other land cover types, and complex topography likely further complicate the relationship between spaceborne SIF and VIs.

Surprisingly, we found that the seasonality of non-adjusted NIRv and EVI in EBF were substantially more consistent with SIF (R^2 = 0.81 and 0.80) than their BRDF-adjusted counterparts (R^2 = 0.47 and 0.53) at the landscape scale. We suspect that the difference is likely driven by the BRDF algorithm used to correct the surface reflectance data for the seasonality of illumination geometry (lower phase angles during the fall equinox), which coincides with leaf flush and an increase in photosynthesis in the tropics (Lopes et al. 2016; Myneni et al. 2007; Restrepo-Coupe et al. 2013; Wu et al. 2016). This difference suggests the question of whether SIF needs to be adjusted for illumination geometry or if non-adjusted VIs should be preferable to those that are BRDF-adjusted.

There are some hurdles to adjusting SIF data and skepticism about whether it should be done, and if so how. First, SIF is emitted energy, not reflected, so traditional BRDF-adjustment algorithms are not directly applicable to SIF. Second, there is a lack of knowledge on the scattering of SIF within the canopy and its escape, which is highly dependent on vegetation type,

density, and structure, and retrieved SIF depends on sun-sensor geometry (Porcar-Castell et al. 2014). The most recent proposed method for adjusting SIF suggests the use of NIRv to estimate the fraction the SIF escape ratio (Zeng et al. 2019). However, the application of this method to spaceborne SIF retrievals appears impractical because: 1) the use of NDVI in the calculation of NIRv, which is much more sensitive to cloud cover than SIF, would negate the benefit that SIF provides in cloudy regions (Frankenberg et al. 2014; Guanter et al. 2015); 2) background radiance from non-vegetation surfaces, such as soil, may affect NIRv (Wang et al. 2019a) which would otherwise be absent from retrieved SIF values; and 3) NDVI, and hence NIRv, can't be computed from spaceborne platforms that provide SIF retrievals. Thus, one would have to rely on estimating the escape fraction of spaceborne SIF using a sensor on a different platform that has different sun-sensor geometry, overpass time, atmospheric conditions, detector error, and spatiotemporal resolution than the SIF retrievals.

Third, a past study has shown that BRDF-adjustment of the surface reflectance data does not change the seasonality of vegetation indices in the tropics and only reduces the magnitude of seasonal change (Guan et al. 2015). Likewise, it is likely that an adjustment of the SIF data would be relatively inconsequential, particularly since it has been shown that vegetation dynamics are driving seasonal changes in GPP (Lopes et al. 2016; Restrepo-Coupe et al. 2013; Wu et al. 2016; Wu et al. 2018) in Amazonian forests and that BRDF-adjusted EVI was found to be highly consistent with TROPOMI SIF for moist and seasonally moist forests in the Amazon (R^2 = 0.83 and 0.91, respectively) (Doughty et al. 2019).

4.4 NIRv

Recent studies have reported a strong correlation between NIRv and GPP, and that perhaps this relationship is stronger than the relationship between SIF and GPP, and thus NIRv

might be the preferred VI in modeling global GPP (Badgley et al. 2017; Dechant et al. 2019). However, an analysis of GPP at six eddy covariance sites (GPP_{EC}) in Australia by Wang et al. (2019a) found that OCO-2 SIF better captured the SOS and EOS GPP_{EC} than EVI or NIRv because SIF values are not contaminated by background soil and different plant species contribute to the SIF signal additively. Similarly, Li et al. (2018) found that OCO-2 SIF had a stronger relationship with GPP_{EC} than EVI and NIRv using 64 eddy flux sites across the globe, and that the EVI and NIRv performed very similarly. A study in the circumpolar region indicated a closer agreement between SIF and GPP estimates than NIRv, EVI, and NDVI (Walther et al. 2018), and another study found NIRv, NDVI, and two-band EVI to perform relatively poorly in estimating the SOS and EOS for tundra and grassland ecosystems (Yang et al. 2019).

In our analysis, we found the consistency of NIRv and EVI with SIF to be relatively indistinguishable, spatially and temporally, across all land cover types. Our results, and the few studies that compare NIRv, EVI, SIF, and GPP, suggest that NIRv does not have a clear advantage over EVI. As discussed, we found that BRDF-corrected NIRv may better capture the SOS SIF in evergreen needleleaf forests at the global scale, but further analysis at a finer spatiotemporal resolution needed to determine if there is a clear advantage. At the very least, we did not find any evidence which suggests that NIRv is more consistent with GPP than SIF.

4.5 BRDF-adjusted and non-adjusted VIs

Apart from the evergreen broadleaf forest as discussed, we did not find either BRDF-adjusted or non-adjusted NIRv or EVI to be clearly more consistent with SIF. BRDF-corrected NIRv and EVI were slightly more consistent with SIF in evergreen needleleaf forest, deciduous broadleaf forest, woody savannas, cropland, urban, and cropland/natural mosaics, but non-adjusted NIRv and EVI were more consistent with SIF in evergreen broadleaf forest, open

shrublands, savannas, and wetlands. The remaining landcover types, deciduous needleleaf forest, closed shrublands, and grasslands, exhibited mixed results. Our results suggest that the use of BRDF-adjusted or non-adjusted NIRv or EVI in modeling global GPP would only have notable differences for evergreen broadleaf forest. Nevertheless, BRDF-adjustment would not change the seasonality of tropical GPP estimates, only the magnitude (Guan et al. 2015; Saleska et al. 2016) of the seasonality.

5. Conclusion

Here we compared GPP_{VPM}, GPP_{MOD17}, and BRDF-adjusted and non-adjusted NIRv, EVI, and NDVI to global TROPOMI SIF observations for 2018. We found GPP_{VPM} to be substantially more consistent with TROPOMI SIF than GPP_{MOD17}, most notably in evergreen broadleaf forest, savannas, and cropland/natural vegetation mosaics. Both GPP models performed poorly in the tropics relative to NIRv and EVI when compared to SIF, but GPP_{VPM} had an overall better consistency with SIF than VIs due to its strong relationship at mid and high latitudes. NDVI was found to be most inconsistent with SIF, which was true across all land cover types. SOS BRDF-adjusted NIRv was more consistent with SOS SIF than the other vegetation indices, and non-adjusted NIRv and EVI were much more consistent with SIF than their BRDF-adjusted counterparts. We did not find a notable difference between NIRv and EVI compared to SIF, and apart from evergreen broadleaf forest there was not a substantial difference between BRDF-adjusted and non-adjusted NIRv and EVI. The inconsistencies of GPP and VIs relative to SIF indicate where GPP models may be improved, where more observations are needed, and highlight the advantages of using SIF to track vegetation dynamics.

Supplementary material

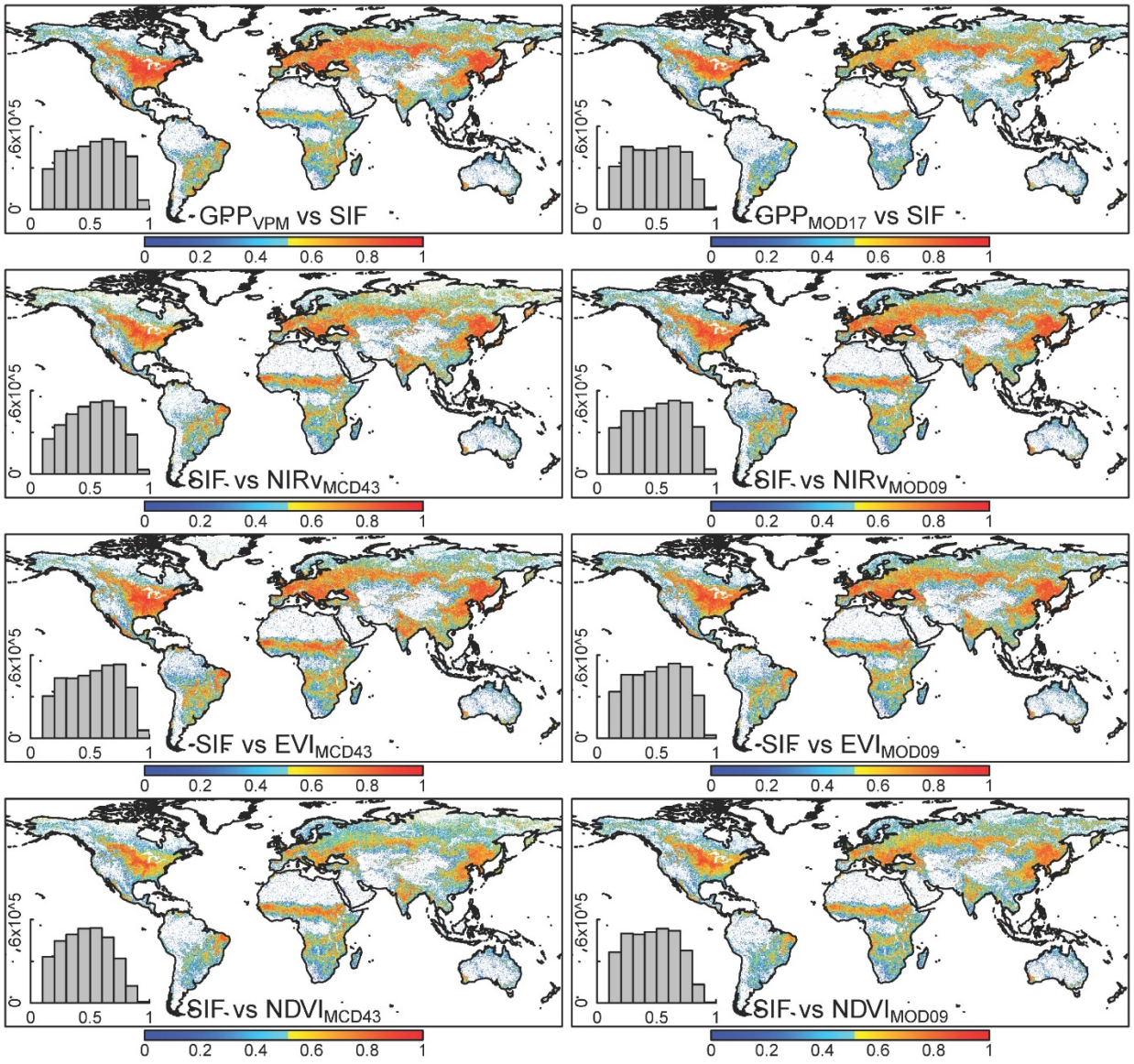

Figure S5.1 | R^2 values from pixel-based, time-series regression results at 0.05 degrees for GPP versus SIF and SIF versus vegetation indices in 2018. High R^2 values signal a strong correlation with 8-day SIF from March through December 2018. Shown are only R^2 values from linear regression results with a significant p-value of <0.05. Spatial resolution is 0.05 degrees.

Chapter 6: Conclusions and perspectives

Advancement of knowledge

My research has advanced our knowledge in the field of remote sensing of vegetation in two main ways. First, we demonstrated the ability to track the seasonality and magnitude of C3 and C4 cropland productivity in Oklahoma over many years using satellite-based data and the Vegetation Photosynthesis Model (VPM). Further, we analyzed the impact of pluvial and drought periods on the productivity of irrigation-permitted and non-permitted croplands. This ability to measure the impact of irrigation and pluvial and drought events on the productivity of croplands at regional scales is not only important for understanding annual changes in carbon cycle fluxes, but has important implications for monitoring food production and understanding how anthropogenic activity may help mitigate or enhance the impacts of pluvial and drought events.

Second, we have made a considerable contribution to the debate on whether there is a dry-season increase in the productivity of Amazon forests. We show that all indicators of productivity, such as the Enhanced Vegetation Index (EVI), solar-induced chlorophyll fluorescence (SIF), and gross primary productivity (GPP), agree that there is a dry-season increase. Furthermore, we refuted the argument head-on that sun-sensor geometry was driving the changes in EVI, SIF, and GPP using BRDF-adjusted vegetation indices (MCD43 and MAIAC), non-adjusted vegetation indices (MOD09 and MCD13), and several satellite platforms (GOME-2, TROPOMI, and MODIS). We further extended our analyses to show how greenness, SIF, and GPP greenness deviated from normal during two La Nina and El Nino periods.

The remote sensing community has been energized by the discovery that solar-induced chlorophyll fluorescence (SIF) can be detected using the high spectral resolution surface

reflectance data from satellites that are intended to measure trace gasses in Earth's atmosphere. In the last few years, site-level SIF experiments have been established in a variety of land cover types, including grasslands, forests, and croplands, and more sites are planned. Until the launch of TROPOMI, scientific inquiry into global SIF retrievals was limited by the coarse spatial and/or temporal resolution SIF data. The new data from TROPOMI is now helping answer some long-standing debates over the seasonality of photosynthesis in the tropics, as demonstrated in Chapter 4.

In the future, we expect TROPOMI to provide detailed insight into the regional and global impacts of El Niño, La Niña, and flash drought, which are currently rather limited by the coarse spatiotemporal resolution of GOME-2 SIF data and GOME-2 sensor degradation (Chapter 3). The new, relatively high resolution TROPOMI data has not yet been used to evaluate the impacts of drought and climate variability on vegetation, but the consistency between the global TROPOMI SIF dataset, GPP models, and vegetation indices (Chapter 5) indicates that SIF will be a useful tool in the future for monitoring croplands and forest health because SIF is less affected by cloud cover and background radiances than vegetation indices and SIF is directly related to the partitioning of energy within the leaf.

Spaceborne SIF data, especially at high spatiotemporal resolution, also provides a form of validation for global GPP products that have previously been limited to validation via eddy flux towers, most of which are part of the FLUXNET network. The traditional method used to validate GPP products was to compare site-level (gridcell) GPP estimates to eddy flux tower GPP measurements. Although the global network of eddy flux towers has been an invaluable tool for understanding global carbon fluxes and validating models, most of these towers are at mid northern latitudes and are a rough sample of the carbon dynamics of Earth's ecosystems

over space and time. The only way to investigate phenological changes and carbon fluxes in remote areas, such as the Amazon, is with satellite observations. Now, high resolution and high frequency spaceborne SIF data is giving us information in every pixel on the function (light absorption and emission) of vegetation, which can be compared with model estimates.

SIF: Current limitations and opportunities for future research

Although TROPOMI has unprecedented spatial and temporal resolution, there are gaps in TROPOMI's coverage in the equatorial region which bar us from observing as many as 3 days in each of TROPOMI's 16-day revisit cycle. These gaps in the data occur in the tropical region where cloud cover most often prohibits good observations and where more frequent observations are most desperately needed. The upcoming launch of the geostationary GeoCarb platform, a joint project between NASA and the University of Oklahoma, will fill these voids by providing daily scans of North, Central, and South America.

Traditional, space-based light-use efficiency models (LUE) estimate gross primary production (GPP) using a known quantity of sunlight, a vegetation index as a proxy of the fraction of sunlight absorbed by chlorophyll or the canopy, and a maximum LUE value that is downregulated by factors limiting photosynthesis, such as temperature and water. These models perform extremely well, especially GPP_{VPM}, in most parts of the globe when compared to eddy flux towers (Chapter 2) and TROPOMI SIF (Chapter 5). Future applications of SIF will undoubtedly involve the incorporation of SIF into GPP modeling, but SIF will never be a perfect solution because of the rather complex relationship between the fixation of carbon, which occurs during the dark reaction (Calvin Benison Cycle), and SIF, which is emitted from the leaf during the light reaction. In short, the relationship between the number of carbon molecules fixed in the dark reaction and the number of photons emitted as SIF is not linear under extreme

environmental conditions and the slope of their relationship is expected to differ over time for a single land cover type and across ecosystems. Also, the scattering, reabsorption, and emission (escape ratio) of SIF from a vegetation canopy is largely dependent on canopy structure, which is extremely heterogenous across space and time.

However, the benefit to SIF is not so much that it is a proxy of the amount of carbon fixed by photosynthesis, but that it is a better proxy for changes in photosynthesis than vegetation indices, a direct indicator of the fate of absorbed energy, and a better indicator of changes in plant function. Future avenues of research will focus on resolving some existing challenges in the application of SIF data. First, single SIF retrieval error can be sizable, so it is necessary to average soundings over space and/or time to reduce precision error, which reduces the spatial and temporal resolution of the dataset. Future technological advances in sensor design and SIF retrieval may help reduce precision error.

Second, differences in viewing and illumination geometry affect retrieved SIF values, and currently there is no accepted method for estimating the fraction of SIF that escapes the canopy (at different angles) that could be used to adjust retrieved SIF values, and it is somewhat debated whether adjustment should be done. Nevertheless, more knowledge is needed to understand the emission of SIF from canopies for Earth's different ecosystems, and how viewing and illumination geometry affect spaceborne SIF retrievals. In Chapters 4 and 5, I average TROPOMI soundings over 8- and 16-day windows to account for differences in viewing geometry. However, with GeoCarb we will not have the luxury to average soundings over a range of viewing angles because the platform will be geostationary. Thus, for a given location we will have a superb record of SIF retrievals that is not subject to daily changes in viewing angle, but it might be difficult to directly compare changes in SIF at one location to changes in

SIF at another location because the relative magnitude of change will be a function of sun-sensor geometry.

One potential way to gather the data needed to understand the angular characteristics of SIF emission would be to use the Orbiting Carbon Observatory-3 (OCO-3) on the international space station, and while in targeting mode make several overlapping scans of a small area, called Small Area Maps (SAMs). As the space station scans, the viewing geometry will change because the station is moving. The soundings with overlapping footprints should give insight into changes in retrieved SIF due to differences in viewing geometry while other factors are relatively constant, such as illumination geometry, atmospheric and environmental conditions, and photosynthesis. Although it may remain unwise to adjust retrieved SIF values for viewing and illumination geometry after such an analysis, the knowledge we gain could allow us to create quality flags for SIF data products according to viewing and illumination geometry or inform us on whether we should avoid retrievals from certain angles.

GPP: Current limitations and opportunities for future research

Eddy covariance GPP (GPP_{EC}) is used as the *in-situ* litmus test to determine if modeled GPP is performing well. However, such comparisons are not perfect because GPP_{EC} is itself not observed and is instead partitioned from net carbon exchange using one, several, or a combination of models. Eddy covariance systems can't account for the entire energy budget, can experience instrument error and downtime, and are high maintenance. Thus, we don't expect GPP_{EC} and modeled GPP to ever achieve a perfect correlation and is never the goal. Nevertheless, EC towers can give us an idea of where modeled GPP works well and where it does not.

The high correlation between GPP_{VPM} and GPP_{EC} at most sites indicates that the model performs very well, but the model results can be further improved with better input data. Namely, the VPM model uses a relatively course and static C3/C4 vegetation map for simulations, but the C3/C4 ratio is constantly changing in grassland ecosystems and in croplands. Also, VPM and many other GPP models use light-use efficiency values from the Biome Properties Lookup Table, which are biome-scale, static light-use efficiency values that may not capture the diversity and variability of light-use efficiency values within biomes. Better input temperature data would also be useful, as the current input temperature data has a very coarse resolution (~2 degrees). Currently, VPM does not account for the carbon fertilization effect, which would likely affect global interannual trends in GPP. Lastly, a linear function of EVI is used as a proxy of the fraction of the amount of photosynthetically active radiation absorbed by chlorophyll, but this relationship might be non-linear.

Conclusion

The ability to monitor changes in photosynthesis and vegetation cover on Earth's surface is vital to understanding how photosynthesis and vegetation respond over time to changes in the environment, climate, and human activity. These responses are fundamental in understanding the role of vegetation in atmospheric CO_2 and CH_4 concentrations, the water cycle, and nutrient cycling. Without this basic knowledge, our projections of future atmospheric carbon concentrations, climate, climate variability, and the feedback processes between them will be highly uncertain.

References

Al-Kaisi, M.M., & Shanahan, J.F. (1999). Irrigation of Winter Wheat. *Colorado State University Cooperative Extension*

Albert, L.P., Wu, J., Prohaska, N., Camargo, P.B., Huxman, T.E., Tribuzy, E.S., Ivanov, V.Y., Oliveira, R.S., Garcia, S., & Smith, M.N. (2018). Age-dependent leaf physiology and consequences for crown-scale carbon uptake during the dry season in an Amazon evergreen forest. *New phytologist*

Andreae, M., Acevedo, O., Araùjo, A., Artaxo, P., Barbosa, C., Barbosa, H., Brito, J., Carbone, S., Chi, X., & Cintra, B. (2015). The Amazon Tall Tower Observatory (ATTO): overview of pilot measurements on ecosystem ecology, meteorology, trace gases, and aerosols. *Atmospheric Chemistry and Physics, 15*, 10723-10776

Aragao, L.E.O., Malhi, Y., Barbier, N., Lima, A., Shimabukuro, Y., Anderson, L., & Saatchi, S. (2008). Interactions between rainfall, deforestation and fires during recent years in the Brazilian Amazonia. *Philosophical Transactions of the Royal Society of London B: Biological Sciences, 363*, 1779-1785

Aragao, L.E.O., Malhi, Y., Roman-Cuesta, R.M., Saatchi, S., Anderson, L.O., & Shimabukuro, Y.E. (2007). Spatial patterns and fire response of recent Amazonian droughts. *Geophysical Research Letters, 34*

Arbuckle, J.G., Prokopy, L.S., Haigh, T., Hobbs, J., Knoot, T., Knutson, C., Loy, A., Mase, A.S., McGuire, J., & Morton, L.W. (2013). Climate change beliefs, concerns, and attitudes toward adaptation and mitigation among farmers in the Midwestern United States. *Climatic Change, 117*, 943-950

Asner, G.P., & Alencar, A. (2010). Drought impacts on the Amazon forest: the remote sensing perspective. *New phytologist, 187*, 569-578

Badgley, G., Field, C.B., & Berry, J.A. (2017). Canopy near-infrared reflectance and terrestrial photosynthesis. *Science advances, 3*, e1602244

Bagley, J.E., Desai, A.R., Harding, K.J., Snyder, P.K., & Foley, J.A. (2014). Drought and deforestation: has land cover change influenced recent precipitation extremes in the amazon? *Journal of climate, 27*, 345-361

Bajgain, R., Xiao, X., Basara, J., Wagle, P., Zhou, Y., Zhang, Y., & Mahan, H. (2016). Assessing agricultural drought in summer over Oklahoma Mesonet sites using the water-related vegetation index from MODIS. *International Journal of Biometeorology*, 1-14

Bajgain, R., Xiao, X., Wagle, P., Basara, J., & Zhou, Y. (2015). Sensitivity analysis of vegetation indices to drought over two tallgrass prairie sites. *ISPRS Journal of Photogrammetry and Remote Sensing, 108*, 151-160

Baker, N.R. (2008). Chlorophyll fluorescence: a probe of photosynthesis in vivo. *Annu. Rev. Plant Biol., 59*, 89-113

Basara, J.B., Maybourn, J.N., Peirano, C.M., Tate, J.E., Brown, P.J., Hoey, J.D., & Smith, B.R. (2013). Drought and associated impacts in the Great Plains of the United States-a review. *International Journal of Geosciences, 4*, 72

Becker, M.F., & Runkle, D.L. (1998). Hydrogeology, water quality, and geochemistry of the Rush Springs aquifer, western Oklahoma. In: US Geological Survey, Water Resources Division; Branch of Information Services [distributor]

Bennett, F.G. (1984). Resistance to powdery mildew in wheat: a review of its use in agriculture and breeding programmes. *Plant pathology, 33*, 279-300

Blackburn, G.A. (1998). Quantifying chlorophylls and caroteniods at leaf and canopy scales: An evaluation of some hyperspectral approaches. *Remote Sensing of Environment, 66*, 273-285

Boegh, E., Soegaard, H., Broge, N., Hasager, C., Jensen, N., Schelde, K., & Thomsen, A. (2002). Airborne multispectral data for quantifying leaf area index, nitrogen concentration, and photosynthetic efficiency in agriculture. *Remote Sensing of Environment, 81*, 179-193

Bonal, D., Bosc, A., Ponton, S., GORET, J.Y., Burban, B., Gross, P., BONNEFOND, J.M., Elbers, J., Longdoz, B., & Epron, D. (2008). Impact of severe dry season on net ecosystem exchange in the Neotropical rainforest of French Guiana. *Global Change Biology, 14*, 1917-1933

Brando, P.M., Goetz, S.J., Baccini, A., Nepstad, D.C., Beck, P.S., & Christman, M.C. (2010). Seasonal and interannual variability of climate and vegetation indices across the Amazon. *Proceedings of the National Academy of Sciences*, 200908741

Brock, F.V., Crawford, K.C., Elliott, R.L., Cuperus, G.W., Stadler, S.J., Johnson, H.L., & Eilts, M.D. (1995). The Oklahoma Mesonet: a technical overview. *Journal of Atmospheric and Oceanic Technology, 12*, 5-19

Carroll, M., DiMiceli, C., Wooten, M., Hubbard, A., Sohlberg, R., & Townshend, J. (2017). MOD44W MODIS/Terra Land Water Mask Derived from MODIS and SRTM L3 Global 250m SIN Grid V006. *NASA EOSDIS Land Process DAAC: Sioux Falls, SD, USA*

Carter, B., & Gregory, M. (2008). Soil map of Oklahoma. *Norman (OK): Oklahoma Geological Survey*

Chandrasekar, K., Sesha Sai, M., Roy, P., & Dwevedi, R. (2010). Land Surface Water Index (LSWI) response to rainfall and NDVI using the MODIS Vegetation Index product. *International Journal of Remote Sensing, 31*, 3987-4005

Chaves, M.M., Maroco, J.P., & Pereira, J.S. (2003). Understanding plant responses to drought—from genes to the whole plant. *Functional plant biology, 30*, 239-264

Chen, T., van der Werf, G.R., Dolman, A., & Groenendijk, M. (2011). Evaluation of cropland maximum light use efficiency using eddy flux measurements in North America and Europe. *Geophysical Research Letters, 38*

Christian, J., Christian, K., & Basara, J.B. (2015). Drought and pluvial dipole events within the great plains of the United States. *Journal of Applied Meteorology and Climatology, 54*, 1886-1898

Coley, P.D., & Barone, J. (1996). Herbivory and plant defenses in tropical forests. *Annual Review of ecology and Systematics, 27*, 305-335

Condit, R., Aguilar, S., Hernandez, A., Perez, R., Lao, S., Angehr, G., Hubbell, S.P., & Foster, R.B. (2004). Tropical forest dynamics across a rainfall gradient and the impact of an El Nino dry season. *Journal of tropical Ecology, 20*, 51-72

Cui, Y., Xiao, X., Zhang, Y., Dong, J., Qin, Y., Doughty, R.B., Zhang, G., Wang, J., Wu, X., Qin, Y., Zhou, S., Joiner, J., & Moore, B. (2017). Temporal consistency between gross primary production and solar-induced chlorophyll fluorescence in the ten most populous megacity areas over years. *Scientific Reports, 7*

Dechant, B., Ryu, Y., Badgley, G., Zeng, Y., Berry, J.A., Zhang, Y., Goulas, Y., Li, Z., Zhang, Q., & Kang, M. (2019). Canopy structure explains the relationship between photosynthesis and sun-induced chlorophyll fluorescence in crops

Delacre, M., Lakens, D., & Leys, C. (2017). Why Psychologists Should by Default Use Welch's t-test Instead of Student's t-test. *International Review of Social Psychology, 30*

Delbart, N., Kergoat, L., Le Toan, T., Lhermitte, J., & Picard, G. (2005). Determination of phenological dates in boreal regions using normalized difference water index. *Remote Sensing of Environment, 97*, 26-38

Didan, K. (2015). MOD13C2 MODIS Terra Vegetation Indices Monthly L3 Global 0.05 Deg CMG V006. *NASA EOSDIS Land Processes DAAC*

Doraiswamy, P., Hatfield, J., Jackson, T., Akhmedov, B., Prueger, J., & Stern, A. (2004). Crop condition and yield simulations using Landsat and MODIS. *Remote Sensing of Environment, 92*, 548-559

Doughty, C.E., Metcalfe, D., Girardin, C., Amézquita, F.F., Cabrera, D.G., Huasco, W.H., Silva-Espejo, J., Araujo-Murakami, A., Da Costa, M., & Rocha, W. (2015). Drought impact on forest carbon dynamics and fluxes in Amazonia. *Nature, 519*, 78

Doughty, R., Köhler, P., Frankenberg, C., Magney, T.S., Xiao, X., Qin, Y., Wu, X., & Moore, B. (2019). TROPOMI reveals dry-season increase of solar-induced chlorophyll fluorescence in the Amazon forest. *Proceedings of the National Academy of Sciences*, 201908157

Doughty, R., Xiao, X., Wu, X., Zhang, Y., Bajgain, R., Zhou, Y., Qin, Y., Zou, Z., McCarthy, H., Friedman, J., Wagle, P., Basara, J., & Steiner, J. (2018). Responses of gross primary production of grasslands and croplands under drought, pluvial, and irrigation conditions during 2010–2016, Oklahoma, USA. *Agricultural Water Management, 204*, 47--59

Drusch, M., Moreno, J., Del Bello, U., Franco, R., Goulas, Y., Huth, A., Kraft, S., Middleton, E.M., Miglietta, F., & Mohammed, G. (2016). The fluorescence explorer mission concept—ESA's earth explorer 8. *IEEE Transactions on Geoscience and Remote Sensing, 55*, 1273-1284

Dunn, B.H., & Olson, H.M. (2009). Cow-calf beef production with irrigated forages

Eck, H.V. (1988). Winter wheat response to nitrogen and irrigation. *Agronomy journal, 80*, 902-908

Ehleringer, J.R., Cerling, T.E., & Helliker, B.R. (1997). C4 photosynthesis, atmospheric CO2, and climate. *Oecologia, 112*, 285-299

Epstein, H., Lauenroth, W., Burke, I., & Coffin, D. (1997). Productivity patterns of C3 and C4 functional types in the US Great Plains. *Ecology, 78*, 722-731

Ewing, A., & Engle, D. (1988). Effects of late summer fire on tallgrass prairie microclimate and community composition. *American Midland Naturalist*, 212-223

Fernando, D.N., Mo, K.C., Fu, R., Pu, B., Bowerman, A., Scanlon, B.R., Solis, R.S., Yin, L., Mace, R.E., & Mioduszewski, J.R. (2016). What caused the spring intensification and winter demise of the 2011 drought over Texas? *Climate dynamics, 47*, 3077-3090

Fischer, M.L., Torn, M.S., Billesbach, D.P., Doyle, G., Northup, B., & Biraud, S.C. (2012). Carbon, water, and heat flux responses to experimental burning and drought in a tallgrass prairie. *Agricultural and forest meteorology, 166*, 169-174

Flanagan, P.X., Basara, J.B., Illston, B.G., & Otkin, J.A. (2017a). The Effect of the Dry Line and Convective Initiation on Drought Evolution over Oklahoma during the 2011 Drought. *Advances in Meteorology, 2017*

Flanagan, P.X., Basara, J.B., & Xiao, X. (2017b). Long-term analysis of the asynchronicity between temperature and precipitation maxima in the United States Great Plains. *International Journal of Climatology*

Flannigan, M.D., Stocks, B.J., & Wotton, B.M. (2000). Climate change and forest fires. *Science of the Total Environment, 262*, 221-229

Food and Agriculture Organization of the United Nations (2018). GIEWS Country Brief Brazil

Frankenberg, C. (2015). Solar Induced Chlorophyll Fluorescence OCO-2 Lite Files (B7000) User Guide. *California Institute of Technology/Jet Propulsion Laboratory*

Frankenberg, C., Fisher, J.B., Worden, J., Badgley, G., Saatchi, S.S., Lee, J.E., Toon, G.C., Butz, A., Jung, M., & Kuze, A. (2011). New global observations of the terrestrial carbon cycle from GOSAT: Patterns of plant fluorescence with gross primary productivity. *Geophysical Research Letters, 38*

Frankenberg, C., O'Dell, C., Berry, J., Guanter, L., Joiner, J., Köhler, P., Pollock, R., & Taylor, T.E. (2014). Prospects for chlorophyll fluorescence remote sensing from the Orbiting Carbon Observatory-2. *Remote Sensing of Environment, 147*, 1-12

Frankenberg, C., O'Dell, C., Guanter, L., & McDuffie, J. (2012). Remote sensing of near-infrared chlorophyll fluorescence from space in scattering atmospheres: implications for its retrieval and interferences with atmospheric CO_2 retrievals. *Atmospheric Measurement Techniques, 5*, 2081-2094

Galvão, L.S., dos Santos, J.R., Roberts, D.A., Breunig, F.M., Toomey, M., & de Moura, Y.M. (2011). On intra-annual EVI variability in the dry season of tropical forest: A case study with MODIS and hyperspectral data. *Remote Sensing of Environment, 115*, 2350-2359

Gao, B.-C. (1996a). NDWI—A normalized difference water index for remote sensing of vegetation liquid water from space. *Remote Sensing of Environment, 58*, 257-266

Gao, B. (1996b). NDWI—A normalized difference water index for remote sensing of vegetation liquid water from space. *Remote Sensing of Environment, 58*, 257-266

Gatti, L., Gloor, M., Miller, J., Doughty, C., Malhi, Y., Domingues, L., Basso, L., Martinewski, A., Correia, C., & Borges, V. (2014). Drought sensitivity of Amazonian carbon balance revealed by atmospheric measurements. *Nature, 506*, 76

Genty, B., Briantais, J.-M., & Baker, N.R. (1989). The relationship between the quantum yield of photosynthetic electron transport and quenching of chlorophyll fluorescence. *Biochimica et Biophysica Acta (BBA)-General Subjects, 990*, 87-92

Gheysari, M., Mirlatifi, S.M., Homaee, M., Asadi, M.E., & Hoogenboom, G. (2009). Nitrate leaching in a silage maize field under different irrigation and nitrogen fertilizer rates. *Agricultural Water Management, 96*, 946-954

Giardina, F., Konings, A.G., Kennedy, D., Alemohammad, S.H., Oliveira, R.S., Uriarte, M., & Gentine, P. (2018). Tall Amazonian forests are less sensitive to precipitation variability. *Nature Geoscience, 11*, 405-409

Gitelson, A.A., Vina, A., Ciganda, V., Rundquist, D.C., & Arkebauer, T.J. (2005). Remote estimation of canopy chlorophyll content in crops. *Geophysical Research Letters, 32*

Graham, E.A., Mulkey, S.S., Kitajima, K., Phillips, N.G., & Wright, S.J. (2003). Cloud cover limits net CO2 uptake and growth of a rainforest tree during tropical rainy seasons. *Proceedings of the National Academy of Sciences, 100*, 572-576

Guan, K., Pan, M., Li, H., Wolf, A., Wu, J., Medvigy, D., Caylor, K.K., Sheffield, J., Wood, E.F., & Malhi, Y. (2015). Photosynthetic seasonality of global tropical forests constrained by hydroclimate. *Nature Geoscience, 8*, 284

Guanter, L., Aben, I., Tol, P., Krijger, J., Hollstein, A., Köhler, P., Damm, A., Joiner, J., Frankenberg, C., & Landgraf, J. (2015). Potential of the TROPOspheric Monitoring Instrument (TROPOMI) onboard the Sentinel-5 Precursor for the monitoring of terrestrial chlorophyll fluorescence. *Atmospheric Measurement Techniques, 8*, 1337-1352

Guanter, L., Frankenberg, C., Dudhia, A., Lewis, P.E., Gómez-Dans, J., Kuze, A., Suto, H., & Grainger, R.G. (2012). Retrieval and global assessment of terrestrial chlorophyll fluorescence from GOSAT space measurements. *Remote Sensing of Environment, 121*, 236-251

Haxeltine, A., & Prentice, I. (1996). A general model for the light-use efficiency of primary production. *Functional Ecology*, 551-561

He, M., Kimball, J.S., Maneta, M.P., Maxwell, B.D., Moreno, A., Beguería, S., & Wu, X. (2018). Regional Crop Gross Primary Productivity and Yield Estimation Using Fused Landsat-MODIS Data. *Remote Sensing, 10*, 372

Hilker, T., Lyapustin, A.I., Hall, F.G., Myneni, R., Knyazikhin, Y., Wang, Y., Tucker, C.J., & Sellers, P.J. (2015). On the measurability of change in Amazon vegetation from MODIS. *Remote Sensing of Environment, 166*, 233-242

Hoagland, B. (2000). The vegetation of Oklahoma: A classification for landscape mapping and conservation planning. *The Southwestern Naturalist*, 385-420

Hsiao, T.C., & Acevedo, E. (1974). Plant responses to water deficits, water-use efficiency, and drought resistance. *Agricultural meteorology, 14*, 59-84

Huete, A., Didan, K., Miura, T., Rodriguez, E.P., Gao, X., & Ferreira, L.G. (2002). Overview of the radiometric and biophysical performance of the MODIS vegetation indices. *Remote Sensing of Environment, 83*, 195-213

Huete, A., Didan, K., van Leeuwen, W., Miura, T., & Glenn, E. (2010). MODIS vegetation indices. *Land remote sensing and global environmental change* (pp. 579-602): Springer

Huete, A., Jackson, R., & Post, D. (1985). Spectral response of a plant canopy with different soil backgrounds. *Remote Sensing of Environment, 17*, 37-53

Huete, A., Liu, H., Batchily, K., & Van Leeuwen, W. (1997a). A comparison of vegetation indices over a global set of TM images for EOS-MODIS. *Remote Sensing of Environment, 59*, 440-451

Huete, A.R., Didan, K., Shimabukuro, Y.E., Ratana, P., Saleska, S.R., Hutyra, L.R., Yang, W., Nemani, R.R., & Myneni, R. (2006). Amazon rainforests green-up with sunlight in dry season. *Geophysical Research Letters, 33*

Huete, A.R., Liu, H., & van Leeuwen, W.J. (1997b). The use of vegetation indices in forested regions: issues of linearity and saturation. In, *IGARSS'97. 1997 IEEE International Geoscience and Remote Sensing Symposium Proceedings. Remote Sensing-A Scientific Vision for Sustainable Development* (pp. 1966-1968): IEEE

Huffman, G.J., Bolvin, D.T., Nelkin, E.J., Wolff, D.B., Adler, R.F., Gu, G., Hong, Y., Bowman, K.P., & Stocker, E.F. (2007). The TRMM multisatellite precipitation analysis (TMPA): Quasi-global, multiyear, combined-sensor precipitation estimates at fine scales. *Journal of hydrometeorology, 8*, 38-55

Huffman, G.J., Stocker, E.F., Bolvin, D.T., & Nelkin, E.J. (2014, updated 2019a). 3B42 Research Derived Daily Product. *NASA/GSFC, Greenbelt, MD, USA*

Huffman, G.J., Stocker, E.F., Bolvin, D.T., & Nelkin, E.J. (2014, updated 2019b). 3B43: Multisatellite Precipitation. *NASA/GSFC, Greenbelt, MD, USA*

Jarvis, P., & Linder, S. (2000). Botany: constraints to growth of boreal forests. *Nature, 405*, 904

Jiménez-Muñoz, J.C., Mattar, C., Barichivich, J., Santamaría-Artigas, A., Takahashi, K., Malhi, Y., Sobrino, J.A., & Van Der Schrier, G. (2016). Record-breaking warming and extreme drought in the Amazon rainforest during the course of El Niño 2015–2016. *Scientific Reports, 6*, 33130

Jin, C., Xiao, X., Wagle, P., Griffis, T., Dong, J., Wu, C., Qin, Y., & Cook, D.R. (2015). Effects of in-situ and reanalysis climate data on estimation of cropland gross primary production using the Vegetation Photosynthesis Model. *Agricultural and Forest Meteorology, 213*, 240-250

Johnson, K.S., & Luza, K.V. (2008). *Earth sciences and mineral resources of Oklahoma*. Oklahoma Geological Survey

Joiner, J., Guanter, L., Lindstrot, R., Voigt, M., Vasilkov, A., Middleton, E., Huemmrich, K., Yoshida, Y., & Frankenberg, C. (2013). Global monitoring of terrestrial chlorophyll fluorescence from moderate-spectral-resolution near-infrared satellite measurements: methodology, simulations, and application to GOME-2. *Atmospheric Measurement Techniques, 6*, 2803-2823

Joiner, J., Yoshida, Y., Guanter, L., & Middleton, E.M. (2016). New methods for the retrieval of chlorophyll red fluorescence from hyperspectral satellite instruments: simulations and application to GOME-2 and SCIAMACHY. *Atmos. Meas. Tech., 9*, 3939-3967

Joiner, J., Yoshida, Y., Vasilkov, A., & Middleton, E. (2011). First observations of global and seasonal terrestrial chlorophyll fluorescence from space. *Biogeosciences, 8*, 637-651

Joiner, J., Yoshida, Y., Vasilkov, A., Middleton, E., Campbell, P., & Kuze, A. (2012). Filling-in of near-infrared solar lines by terrestrial fluorescence and other geophysical effects: simulations and space-based observations from SCIAMACHY and GOSAT. *Atmospheric Measurement Techniques, 5*, 809-829

Jönsson, A.M., Eklundh, L., Hellström, M., Bärring, L., & Jönsson, P. (2010). Annual changes in MODIS vegetation indices of Swedish coniferous forests in relation to snow dynamics and tree phenology. *Remote Sensing of Environment, 114*, 2719-2730

Justice, C.O., Vermote, E., Townshend, J.R., Defries, R., Roy, D.P., Hall, D.K., Salomonson, V.V., Privette, J.L., Riggs, G., & Strahler, A. (1998). The Moderate Resolution Imaging Spectroradiometer (MODIS): Land remote sensing for global change research. *IEEE Transactions on Geoscience and Remote Sensing, 36*, 1228-1249

Kahan, D.M. (2015). Climate-Science Communication and the Measurement Problem. *Political Psychology, 36*, 1-43

Kahan, D.M. (2016). 'Ordinary science intelligence': a science-comprehension measure for study of risk and science communication, with notes on evolution and climate change. *Journal of Risk Research*, 1-22

Kahan, D.M., Peters, E., Wittlin, M., Slovic, P., Ouellette, L.L., Braman, D., & Mandel, G. (2012). The polarizing impact of science literacy and numeracy on perceived climate change risks. *Nature Climate Change, 2*, 732-735

Kanamitsu, M., Ebisuzaki, W., Woollen, J., Yang, S.-K., Hnilo, J., Fiorino, M., & Potter, G. (2002). NCEP-DOE AMIP-II Reanalysis (R-2). *Bulletin of the American Meteorological Society, 83*, 1631-1644

Karkauskaite, P., Tagesson, T., & Fensholt, R. (2017). Evaluation of the plant phenology index (PPI), NDVI and EVI for start-of-season trend analysis of the Northern Hemisphere boreal zone. *Remote Sensing, 9*, 485

Kasischke, E.S., & Stocks, B.J. (2012). *Fire, climate change, and carbon cycling in the boreal forest*. Springer Science & Business Media

Keller, M., Alencar, A., Asner, G.P., Braswell, B., Bustamante, M., Davidson, E., Feldpausch, T., Fernandes, E., Goulden, M., & Kabat, P. (2004). Ecological research in the large-scale biosphere–atmosphere experiment in Amazonia: early results. *Ecological Applications, 14*, 3-16

Kelting, R.W. (1954). Effects of Moderate Grazing on the Composition and Plant Production of a Native Tall-Grass Prairie in Central Oklahoma. *Ecology, 35*, 200-207

Khand, K., Taghvaeian, S., & Ajaz, A. (2017). Drought and its impact on agricultural water resources in Oklahoma. *Oklahoma Cooperative Extension Service*

Kim, S., Gitz, D.C., Sicher, R.C., Baker, J.T., Timlin, D.J., & Reddy, V.R. (2007). Temperature dependence of growth, development, and photosynthesis in maize under elevated CO2. *Environmental and Experimental Botany, 61*, 224-236

Köhler, P., Frankenberg, C., Magney, T.S., Guanter, L., Joiner, J., & Landgraf, J. (2018). Global retrievals of solar induced chlorophyll fluorescence with TROPOMI: first results and inter-sensor comparison to OCO-2. *Geophysical Research Letters*

Köhler, P., Guanter, L., & Joiner, J. (2015). A linear method for the retrieval of sun-induced chlorophyll fluorescence from GOME-2 and SCIAMACHY data. *Atmospheric Measurement Techniques, 8*, 2589

Koren, G., van Schaik, E., Araújo, A.C., Boersma, K.F., Gärtner, A., Killaars, L., Kooreman, M.L., Kruijt, B., van der Laan-Luijkx, I.T., & von Randow, C. (2018). Widespread reduction in sun-induced fluorescence from the Amazon during the 2015/2016 El Niño. *Philosophical Transactions of the Royal Society B: Biological Sciences, 373*, 20170408

Lal, R. (2004). Soil carbon sequestration impacts on global climate change and food security. *science, 304*, 1623-1627

Laurance, W.F., & Williamson, G.B. (2001). Positive feedbacks among forest fragmentation, drought, and climate change in the Amazon. *Conservation Biology, 15*, 1529-1535

Lee, J.-E., Frankenberg, C., van der Tol, C., Berry, J.A., Guanter, L., Boyce, C.K., Fisher, J.B., Morrow, E., Worden, J.R., & Asefi, S. (2013). Forest productivity and water stress in Amazonia: Observations from GOSAT chlorophyll fluorescence. *Proceedings of the Royal Society of London B: Biological Sciences, 280*, 20130171

Lewis, S.L., Brando, P.M., Phillips, O.L., van der Heijden, G.M., & Nepstad, D. (2011). The 2010 amazon drought. *science, 331*, 554-554

Li, X., Xiao, J., He, B., Arain, M.A., Beringer, J., Desai, A.R., Emmel, C., Hollinger, D.Y., Krasnova, A., & Mammarella, I. (2018). Solar-induced chlorophyll fluorescence is strongly correlated with terrestrial photosynthesis for a wide variety of biomes: First global analysis based on OCO-2 and flux tower observations. *Global Change Biology*

Liu, J., Bowman, K.W., Schimel, D.S., Parazoo, N.C., Jiang, Z., Lee, M., Bloom, A.A., Wunch, D., Frankenberg, C., & Sun, Y. (2017). Contrasting carbon cycle responses of the tropical continents to the 2015–2016 El Niño. *science, 358*, eaam5690

Lloyd, J., & Taylor, J. (1994). On the temperature dependence of soil respiration. *Functional Ecology*, 315-323

Lopes, A.P., Nelson, B.W., Wu, J., de Alencastro Graça, P.M.L., Tavares, J.V., Prohaska, N., Martins, G.A., & Saleska, S.R. (2016). Leaf flush drives dry season green-up of the Central Amazon. *Remote Sensing of Environment, 182*, 90-98

Lüdeke, M., Janecek, A., & Kohlmaier, G.H. (1991). Modelling the seasonal CO2 uptake by land vegetation using the global vegetation index. *Tellus B, 43*, 188-196

Luus, K., Commane, R., Parazoo, N., Benmergui, J., Euskirchen, E., Frankenberg, C., Joiner, J., Lindaas, J., Miller, C., & Oechel, W. (2017). Tundra photosynthesis captured by satellite-observed solar-induced chlorophyll fluorescence. *Geophysical Research Letters, 44*, 1564-1573

Ma, J., Xiao, X., Zhang, Y., Doughty, R., Chen, B., & Zhao, B. (2018). Spatial-temporal consistency between gross primary productivity and solar-induced chlorophyll fluorescence of vegetation in China during 2007–2014. *Science of the Total Environment, 639*, 1241-1253

Ma, S., Jiang, J., Huang, Y., Shi, Z., Wilson, R.M., Ricciuto, D., Sebestyen, S.D., Hanson, P.J., & Luo, Y. (2017). Data-constrained projections of methane fluxes in a northern Minnesota peatland in response to elevated CO2 and warming. *Journal of Geophysical Research: Biogeosciences, 122*, 2841-2861

MacKown, C.T., Heitholt, J.J., & Rao, S.C. (2007). Agronomic feasibility of a continuous double crop of winter wheat and soybean forage in the southern Great Plains. *Crop science, 47*, 1652-1660

Maeda, E.E., Heiskanen, J., Aragão, L.E., & Rinne, J. (2014). Can MODIS EVI monitor ecosystem productivity in the Amazon rainforest? *Geophysical Research Letters, 41*, 7176-7183

Maeda, E.E., Moura, Y.M., Wagner, F., Hilker, T., Lyapustin, A.I., Wang, Y., Chave, J., Mõttus, M., Aragão, L.E., & Shimabukuro, Y. (2016). Consistency of vegetation index seasonality across the Amazon rainforest. *International Journal of Applied Earth Observation and Geoinformation, 52*, 42-53

Magney, T.S., Bowling, D.R., Logan, B.A., Grossmann, K., Stutz, J., Blanken, P.D., Burns, S.P., Cheng, R., Garcia, M.A., & Köhler, P. (2019). Mechanistic evidence for tracking the seasonality of photosynthesis with solar-induced fluorescence. *Proceedings of the National Academy of Sciences, 116*, 11640-11645

Malhi, Y., Nobre, A.D., Grace, J., Kruijt, B., Pereira, M.G., Culf, A., & Scott, S. (1998). Carbon dioxide transfer over a Central Amazonian rain forest. *Journal of Geophysical Research: Atmospheres, 103*, 31593-31612

Marengo, J.A., Nobre, C.A., Tomasella, J., Oyama, M.D., Sampaio de Oliveira, G., De Oliveira, R., Camargo, H., Alves, L.M., & Brown, I.F. (2008). The drought of Amazonia in 2005. *Journal of climate, 21*, 495-516

Marengo, J.A., Tomasella, J., Alves, L.M., Soares, W.R., & Rodriguez, D.A. (2011). The drought of 2010 in the context of historical droughts in the Amazon region. *Geophysical Research Letters, 38*

Mase, A.S., Gramig, B.M., & Prokopy, L.S. (2017). Climate change beliefs, risk perceptions, and adaptation behavior among Midwestern US crop farmers. *Climate Risk Management, 15*, 8-17

Masoner, J.R., Mladinich, C., Konduris, A., & Smith, S.J. (2003). Comparison of irrigation water use estimates calculated from remotely sensed irrigated acres and state reported irrigated acres in the Lake Altus drainage basin, Oklahoma and Texas, 2000 growing season. In

McCorkle, T.A., Williams, S.S., Pfeiffer, T.A., & Basara, J.B. (2016). Atmospheric contributors to heavy rainfall events in the Arkansas-Red River Basin. *Advances in Meteorology, 2016*

McKee, T.B., Doesken, N.J., & Kleist, J. (1993). The relationship of drought frequency and duration to time scales. In, *Proceedings of the 8th Conference on Applied Climatology* (pp. 179-183): American Meteorological Society Boston, MA

McPherson, R.A., Fiebrich, C.A., Crawford, K.C., Kilby, J.R., Grimsley, D.L., Martinez, J.E., Basara, J.B., Illston, B.G., Morris, D.A., & Kloesel, K.A. (2007). Statewide monitoring of the mesoscale environment: A technical update on the Oklahoma Mesonet. *Journal of Atmospheric and Oceanic Technology, 24*, 301-321

Middleton, N.J., & Thomas, D.S. (1992). World atlas of desertification

Mitchell, R.B., Masters, R.A., Waller, S.S., Moore, K.J., & Young, L.J. (1996). Tallgrass prairie vegetation response to spring burning dates, fertilizer, and atrazine. *Journal of Range Management*, 131-136

Morton, D.C., Nagol, J., Carabajal, C.C., Rosette, J., Palace, M., Cook, B.D., Vermote, E.F., Harding, D.J., & North, P.R. (2014). Amazon forests maintain consistent canopy structure and greenness during the dry season. *Nature, 506*, 221

Muchow, R. (1990). Effect of high temperature on grain-growth in field-grown maize. *Field Crops Research, 23*, 145-158

Muchow, R., Sinclair, T., & Bennett, J.M. (1990). Temperature and solar radiation effects on potential maize yield across locations. *Agronomy journal, 82*, 338-343

Musick, J., & Lamm, F. (1990). Preplant irrigation in the central and southern High Plains-A review. *Transactions of the ASAE, 33*, 1835-1842

Myneni, R.B., Dong, J., Tucker, C.J., Kaufmann, R.K., Kauppi, P.E., Liski, J., Zhou, L., Alexeyev, V., & Hughes, M. (2001). A large carbon sink in the woody biomass of Northern forests. *Proceedings of the National Academy of Sciences, 98*, 14784-14789

Myneni, R.B., Yang, W., Nemani, R.R., Huete, A.R., Dickinson, R.E., Knyazikhin, Y., Didan, K., Fu, R., Juárez, R.I.N., & Saatchi, S.S. (2007). Large seasonal swings in leaf area of Amazon rainforests. *Proceedings of the National Academy of Sciences, 104*, 4820-4823

Nakaji, T., Ide, R., Oguma, H., Saigusa, N., & Fujinuma, Y. (2007). Utility of spectral vegetation index for estimation of gross CO2 flux under varied sky conditions. *Remote Sensing of Environment, 109*, 274-284

Nayyar, H., & Gupta, D. (2006). Differential sensitivity of C 3 and C 4 plants to water deficit stress: association with oxidative stress and antioxidants. *Environmental and Experimental Botany, 58*, 106-113

Nepstad, D., Lefebvre, P., Lopes da Silva, U., Tomasella, J., Schlesinger, P., Solórzano, L., Moutinho, P., Ray, D., & Guerreira Benito, J. (2004). Amazon drought and its implications for forest flammability and tree growth: A basin-wide analysis. *Global Change Biology, 10*, 704-717

Nepstad, D., McGrath, D., Stickler, C., Alencar, A., Azevedo, A., Swette, B., Bezerra, T., DiGiano, M., Shimada, J., & da Motta, R.S. (2014). Slowing Amazon deforestation through public policy and interventions in beef and soy supply chains. *science, 344*, 1118-1123

Nepstad, D.C., de Carvalho, C.R., Davidson, E.A., Jipp, P.H., Lefebvre, P.A., Negreiros, G.H., da Silva, E.D., Stone, T.A., Trumbore, S.E., & Vieira, S. (1994). The role of deep roots in the hydrological and carbon cycles of Amazonian forests and pastures. *Nature, 372*, 666

Nepstad, D.C., Tohver, I.M., Ray, D., Moutinho, P., & Cardinot, G. (2007). Mortality of large trees and lianas following experimental drought in an Amazon forest. *Ecology, 88*, 2259-2269

Niu, S., Sherry, R.A., Zhou, X., & Luo, Y. (2013). Ecosystem carbon fluxes in response to warming and clipping in a tallgrass prairie. *Ecosystems, 16*, 948-961

O'Leary, M.H. (1988). Carbon isotopes in photosynthesis. *Bioscience, 38*, 328-336

Oates, L.G., & Jackson, R.D. (2014). Livestock management strategy affects net ecosystem carbon balance of subhumid pasture. *Rangeland Ecology & Management, 67*, 19-29

Oklahoma Climatological Survey (2015). Oklahoma Monthly Climate Summary. *Oklahoma Climatological Survey, Norman, OK*

Oklahoma Climatological Survey (2017a). Caddo County Climate Summary. *Oklahoma Climatological Survey, Norman, OK*

Oklahoma Climatological Survey (2017b). The Climate of Caddo County

Oklahoma Water Resources Board (2012). Rush Springs Aquifer of Oklahoma. *Oklahoma Water Resources Board, Oklahoma City, Oklahoma*

Oklahoma Water Resources Board (2017). Permitted Groundwater Well Locations for Groundwater Use Permits. *Oklahoma Water Resources Board, Oklahoma City, Oklahoma*

Ozdogan, M., Yang, Y., Allez, G., & Cervantes, C. (2010). Remote sensing of irrigated agriculture: Opportunities and challenges. *Remote Sensing, 2*, 2274-2304

Palmer, W.C. (1965). *Meteorological drought*. US Department of Commerce, Weather Bureau Washington, DC

Palmer, W.C. (1968). Keeping track of crop moisture conditions, nationwide: The new crop moisture index

Parazoo, N.C., Bowman, K., Frankenberg, C., Lee, J.E., Fisher, J.B., Worden, J., Jones, D., Berry, J., Collatz, G.J., & Baker, I.T. (2013). Interpreting seasonal changes in the carbon balance of southern Amazonia using measurements of XCO2 and chlorophyll fluorescence from GOSAT. *Geophysical Research Letters, 40*, 2829-2833

Payero, J.O., Tarkalson, D.D., Irmak, S., Davison, D., & Petersen, J.L. (2008). Effect of irrigation amounts applied with subsurface drip irrigation on corn evapotranspiration, yield, water use efficiency, and dry matter production in a semiarid climate. *Agricultural Water Management, 95*, 895-908

Peck, R. (1979). Water relations and yield of winter wheat grown under three watering regimes in the High Plains. In, *Proceedings of the Oklahoma Academy of Science* (pp. 53-59)

Phillips, O.L., Aragão, L.E., Lewis, S.L., Fisher, J.B., Lloyd, J., López-González, G., Malhi, Y., Monteagudo, A., Peacock, J., & Quesada, C.A. (2009). Drought sensitivity of the Amazon rainforest. *science, 323*, 1344-1347

Polonsky, I., O'Brien, D., Kumer, J., & O'Dell, C. (2014). Performance of a geostationary mission, geoCARB, to measure CO 2, CH 4 and CO column-averaged concentrations. *Atmospheric Measurement Techniques, 7*, 959-981

Porcar-Castell, A., Tyystjärvi, E., Atherton, J., Van der Tol, C., Flexas, J., Pfündel, E.E., Moreno, J., Frankenberg, C., & Berry, J.A. (2014). Linking chlorophyll a fluorescence to photosynthesis for remote sensing applications: mechanisms and challenges. *Journal of Experimental Botany, 65*, 4065-4095

Propastin, P., Ibrom, A., Knohl, A., & Erasmi, S. (2012). Effects of canopy photosynthesis saturation on the estimation of gross primary productivity from MODIS data in a tropical forest. *Remote Sensing of Environment, 121*, 252-260

Qin, Y., Xiao, X., Dong, J., Zhang, G., Roy, P.S., Joshi, P.K., Gilani, H., Murthy, M.S.R., Jin, C., & Wang, J. (2016). Mapping forests in monsoon Asia with ALOS PALSAR 50-m mosaic images and MODIS imagery in 2010. *Scientific Reports, 6*, 20880

Qin, Y., Xiao, X., Dong, J., Zhang, Y., Wu, X., Shimabukuro, Y., Arai, E., Biradar, C., Wang, J., & Zou, Z. (2019). Improved estimates of forest cover and loss in the Brazilian Amazon in 2000–2017. *Nature Sustainability*, 1

Qin, Y., Xiao, X., Dong, J., Zhou, Y., Wang, J., Doughty, R.B., Chen, Y., Zou, Z., & Moore, B. (2017). Annual dynamics of forest areas in South America during 2007-2010 at 50-m spatial resolution. *Remote Sensing of Environment, 201*, 73-87

Randerson, J.T., Liu, H., Flanner, M.G., Chambers, S.D., Jin, Y., Hess, P.G., Pfister, G., Mack, M., Treseder, K., & Welp, L. (2006). The impact of boreal forest fire on climate warming. *science, 314*, 1130-1132

Reichstein, M., Falge, E., Baldocchi, D., Papale, D., Aubinet, M., Berbigier, P., Bernhofer, C., Buchmann, N., Gilmanov, T., & Granier, A. (2005). On the separation of net ecosystem exchange into assimilation and ecosystem respiration: review and improved algorithm. *Global Change Biology, 11*, 1424-1439

Rejesus, R.M., Mutuc-Hensley, M., Mitchell, P.D., Coble, K.H., & Knight, T.O. (2013). US agricultural producer perceptions of climate change. *Journal of agricultural and applied economics, 45*, 701-718

Restrepo-Coupe, N., da Rocha, H.R., Hutyra, L.R., da Araujo, A.C., Borma, L.S., Christoffersen, B., Cabral, O.M., de Camargo, P.B., Cardoso, F.L., & da Costa, A.C.L. (2013). What drives the seasonality of photosynthesis across the Amazon basin? A cross-site analysis of eddy flux tower measurements from the Brasil flux network. *Agricultural and forest meteorology, 182*, 128-144

Restrepo-Coupe, N., Levine, N.M., Christoffersen, B.O., Albert, L.P., Wu, J., Costa, M.H., Galbraith, D., Imbuzeiro, H., Martins, G., & da Araujo, A.C. (2017). Do dynamic global vegetation models capture the seasonality of carbon fluxes in the Amazon basin? A data-model intercomparison. *Global Change Biology, 23*, 191-208

Rice, A.H., Pyle, E.H., Saleska, S.R., Hutyra, L., Palace, M., Keller, M., De Camargo, P.B., Portilho, K., Marques, D.F., & Wofsy, S.C. (2004). Carbon balance and vegetation dynamics in an old-growth Amazonian forest. *Ecological Applications, 14*, 55-71

Richards, P., Arima, E., VanWey, L., Cohn, A., & Bhattarai, N. (2017). Are Brazil's deforesters avoiding detection? *Conservation letters, 10*, 470-476

Rivera, G., Elliott, S., Caldas, L.S., Nicolossi, G., Coradin, V.T., & Borchert, R. (2002). Increasing day-length induces spring flushing of tropical dry forest trees in the absence of rain. *Trees, 16*, 445-456

Roelfs, A.P. (1992). *Rust diseases of wheat: concepts and methods of disease management*. Cimmyt

Rogiers, N., Eugster, W., Furger, M., & Siegwolf, R. (2005). Effect of land management on ecosystem carbon fluxes at a subalpine grassland site in the Swiss Alps. *Theoretical and applied climatology, 80*, 187-203

Rosenzweig, C., Tubiello, F.N., Goldberg, R., Mills, E., & Bloomfield, J. (2002). Increased crop damage in the US from excess precipitation under climate change. *Global Environmental Change, 12*, 197-202

Rouse Jr, J.W., Haas, R., Schell, J., & Deering, D. (1974). Monitoring vegetation systems in the Great Plains with ERTS

Running, S., & Zhao, M. (2015). MOD17A2H MODIS/Terra Gross Primary Productivity 8-Day L4 Global 500m SIN Grid V006. *NASA EOSDIS Land Processes DAAC*

Running, S.W., Nemani, R.R., Heinsch, F.A., Zhao, M., Reeves, M., & Hashimoto, H. (2004). A continuous satellite-derived measure of global terrestrial primary production. *AIBS Bulletin, 54*, 547-560

Ruxton, G.D. (2006). The unequal variance t-test is an underused alternative to Student's t-test and the Mann–Whitney U test. *Behavioral Ecology, 17*, 688-690

Saatchi, S., Asefi-Najafabady, S., Malhi, Y., Aragão, L.E., Anderson, L.O., Myneni, R.B., & Nemani, R. (2013). Persistent effects of a severe drought on Amazonian forest canopy. *Proceedings of the National Academy of Sciences, 110*, 565-570

Saleska, S.R., Didan, K., Huete, A.R., & Da Rocha, H.R. (2007). Amazon forests green-up during 2005 drought. *science, 318*, 612-612

Saleska, S.R., Miller, S.D., Matross, D.M., Goulden, M.L., Wofsy, S.C., Da Rocha, H.R., De Camargo, P.B., Crill, P., Daube, B.C., & De Freitas, H.C. (2003). Carbon in Amazon forests: unexpected seasonal fluxes and disturbance-induced losses. *science, 302*, 1554-1557

Saleska, S.R., Wu, J., Guan, K., Araujo, A.C., Huete, A., Nobre, A.D., & Restrepo-Coupe, N. (2016). Dry-season greening of Amazon forests. *Nature, 531*, E4

Samanta, A., Ganguly, S., Hashimoto, H., Devadiga, S., Vermote, E., Knyazikhin, Y., Nemani, R.R., & Myneni, R.B. (2010). Amazon forests did not green-up during the 2005 drought. *Geophysical Research Letters, 37*

Schaaf, C., & Wang, Z. (2015). MCD43A4 MODIS/Terra+ Aqua BRDF/Albedo Nadir BRDF Adjusted RefDaily L3 Global-500m V006. *NASA EOSDIS Land Processes DAAC*

Schimel, D.S., House, J.I., Hibbard, K.A., Bousquet, P., Ciais, P., Peylin, P., Braswell, B.H., Apps, M.J., Baker, D., & Bondeau, A. (2001). Recent patterns and mechanisms of carbon exchange by terrestrial ecosystems. *Nature, 414*, 169

Senapati, N., Chabbi, A., Gastal, F., Smith, P., Mascher, N., Loubet, B., Cellier, P., & Naisse, C. (2014). Net carbon storage measured in a mowed and grazed temperate sown grassland shows potential for carbon sequestration under grazed system. *Carbon Management, 5*, 131-144

Sexton, B., Moncrief, J., Rosen, C., Gupta, S., & Cheng, H. (1996). Optimizing nitrogen and irrigation inputs for corn based on nitrate leaching and yield on a coarse-textured soil. *Journal of environmental quality, 25*, 982-992

Shapiro, B.I., Brorsen, B.W., & Doster, D.H. (1992). Adoption of double-cropping soybeans and wheat. *Journal of agricultural and applied economics, 24*, 33-40

Snyder, C., Bruulsema, T., Jensen, T., & Fixen, P. (2009). Review of greenhouse gas emissions from crop production systems and fertilizer management effects. *Agriculture, Ecosystems & Environment, 133*, 247-266

Soja, A.J., Tchebakova, N.M., French, N.H., Flannigan, M.D., Shugart, H.H., Stocks, B.J., Sukhinin, A.I., Parfenova, E., Chapin III, F.S., & Stackhouse Jr, P.W. (2007). Climate-induced boreal forest change: predictions versus current observations. *Global and Planetary Change, 56*, 274-296

Staal, A., Tuinenburg, O.A., Bosmans, J.H., Holmgren, M., van Nes, E.H., Scheffer, M., Zemp, D.C., & Dekker, S.C. (2018). Forest-rainfall cascades buffer against drought across the Amazon. *Nature Climate Change*, 1

Stylinski, C., Gamon, J., & Oechel, W. (2002). Seasonal patterns of reflectance indices, carotenoid pigments and photosynthesis of evergreen chaparral species. *Oecologia, 131*, 366-374

Sun, Y., Frankenberg, C., Jung, M., Joiner, J., Guanter, L., Köhler, P., & Magney, T. (2018). Overview of Solar-Induced chlorophyll Fluorescence (SIF) from the Orbiting Carbon Observatory-2: Retrieval, cross-mission comparison, and global monitoring for GPP. *Remote Sensing of Environment, 209*, 808-823

Sun, Y., Frankenberg, C., Wood, J.D., Schimel, D., Jung, M., Guanter, L., Drewry, D., Verma, M., Porcar-Castell, A., & Griffis, T.J. (2017). OCO-2 advances photosynthesis observation from space via solar-induced chlorophyll fluorescence. *science, 358*, eaam5747

Taddeo, S., Dronova, I., & Depsky, N. (2019). Spectral vegetation indices of wetland greenness: Responses to vegetation structure, composition, and spatial distribution. *Remote Sensing of Environment, 234*, 111467

Tilman, D., & Downing, J.A. (1994). Biodiversity and stability in grasslands. *Nature, 367*, 363-365

Trost, B., Prochnow, A., Drastig, K., Meyer-Aurich, A., Ellmer, F., & Baumecker, M. (2013). Irrigation, soil organic carbon and N2O emissions. A review. *Agronomy for sustainable development, 33*, 733-749

Tyukavina, A., Hansen, M.C., Potapov, P.V., Stehman, S.V., Smith-Rodriguez, K., Okpa, C., & Aguilar, R. (2017). Types and rates of forest disturbance in Brazilian Legal Amazon, 2000–2013. *Science advances, 3*, e1601047

United States Department of Agriculture National Agricultural Statistics Service (2017). Cropland Data Layer. *USDA-NASS, Washington, DC*

United States Department of Agriculture National Agricultural Statistics Service Oklahoma Field Office (2017). County estimates. *USDA-NASS, Washington DC*

United States Drought Monitor (2017). Time Series Data. *National Drought Mitigation Center (NDMC), the U.S. Department of Agriculture (USDA) and the National Oceanic and Atmospheric Administration (NOAA), Lincoln, Nebraska*

van Schaik, C.P., Terborgh, J.W., & Wright, S.J. (1993). The phenology of tropical forests: adaptive significance and consequences for primary consumers. *Annual Review of ecology and Systematics, 24*, 353-377

VanWinkle, T.N., & Friedman, J.R. (2017). What's good for the soil is good for the soul: scientific farming, environmental subjectivities, and the ethics of stewardship in southwestern Oklahoma. *Agriculture and Human Values, 34*, 607-618

Verma, M., Schimel, D., Evans, B., Frankenberg, C., Beringer, J., Drewry, D.T., Magney, T., Marang, I., Hutley, L., & Moore, C. (2017). Effect of environmental conditions on the relationship between solar-induced fluorescence and gross primary productivity at an OzFlux grassland site. *Journal of Geophysical Research: Biogeosciences, 122*, 716-733

Vermote, E. (2015). MOD09A1 MODIS/Terra Surface Reflectance 8-Day L3 Global 500m SIN Grid V006. *NASA EOSDIS Land Processes DAAC*

Volesky, J.D., & Clark, R.T. (2003). Use of irrigated pastures and economics of establishment and grazing. In, *Range Beef Cow Symposium* (p. 60)

Wada, Y., van Beek, L.P., van Kempen, C.M., Reckman, J.W., Vasak, S., & Bierkens, M.F. (2010). Global depletion of groundwater resources. *Geophysical Research Letters, 37*

Wagle, P., Xiao, X., & Suyker, A.E. (2015). Estimation and analysis of gross primary production of soybean under various management practices and drought conditions. *ISPRS Journal of Photogrammetry and Remote Sensing, 99*, 70-83

Wagle, P., Xiao, X., Torn, M.S., Cook, D.R., Matamala, R., Fischer, M.L., Jin, C., Dong, J., & Biradar, C. (2014). Sensitivity of vegetation indices and gross primary production of tallgrass prairie to severe drought. *Remote Sensing of Environment, 152*, 1-14

Walther, S., Guanter, L., Heim, B., Jung, M., Duveiller, G., Wolanin, A., & Sachs, T. (2018). Assessing the dynamics of vegetation productivity in circumpolar regions with different satellite indicators of greenness and photosynthesis. *Biogeosciences, 15*, 6221-6256

Walther, S., Voigt, M., Thum, T., Gonsamo, A., Zhang, Y., Köhler, P., Jung, M., Varlagin, A., & Guanter, L. (2016). Satellite chlorophyll fluorescence measurements reveal large-scale decoupling of photosynthesis and greenness dynamics in boreal evergreen forests. *Global Change Biology, 22*, 2979-2996

Wang, C., Beringer, J., Hutley, L.B., Cleverly, J., Li, J., Liu, Q., & Sun, Y. (2019a). Phenology Dynamics of Dryland Ecosystems Along the North Australian Tropical Transect Revealed by Satellite Solar-Induced Chlorophyll Fluorescence. *Geophysical Research Letters, 46*, 5294-5302

Wang, J., Lu, S., Wang, W., Tang, L., Ma, S., & Wang, Y. (2019b). Estimating vegetation productivity of urban regions using sun-induced chlorophyll fluorescence data derived from the OCO-2 satellite. *Physics and Chemistry of the Earth, Parts A/B/C*

Weaver, S.J., Baxter, S., & Harnos, K. (2016). Regional Changes in the Interannual Variability of US Warm Season Precipitation. *Journal of climate, 29*, 5157-5173

Wickham, J., Stehman, S.V., Gass, L., Dewitz, J.A., Sorenson, D.G., Granneman, B.J., Poss, R.V., & Baer, L.A. (2017). Thematic accuracy assessment of the 2011 National Land Cover Database (NLCD). *Remote Sensing of Environment, 191*, 328-341

Wickham, J.D., Stehman, S.V., Gass, L., Dewitz, J., Fry, J.A., & Wade, T.G. (2013). Accuracy assessment of NLCD 2006 land cover and impervious surface. *Remote Sensing of Environment, 130*, 294-304

Wolf, S., Keenan, T.F., Fisher, J.B., Baldocchi, D.D., Desai, A.R., Richardson, A.D., Scott, R.L., Law, B.E., Litvak, M.E., & Brunsell, N.A. (2016). Warm spring reduced carbon cycle impact of the 2012 US summer drought. *Proceedings of the National Academy of Sciences, 113*, 5880-5885

Wolter, K., & Timlin, M.S. (2011). El Niño/Southern Oscillation behaviour since 1871 as diagnosed in an extended multivariate ENSO index (MEI. ext). *International Journal of Climatology, 31*, 1074-1087

Wright, J.S., Fu, R., Worden, J.R., Chakraborty, S., Clinton, N.E., Risi, C., Sun, Y., & Yin, L. (2017). Rainforest-initiated wet season onset over the southern Amazon. *Proceedings of the National Academy of Sciences, 114*, 8481-8486

Wright, S.J., & Van Schaik, C.P. (1994). Light and the phenology of tropical trees. *The American Naturalist, 143*, 192-199

Wu, J., Albert, L.P., Lopes, A.P., Restrepo-Coupe, N., Hayek, M., Wiedemann, K.T., Guan, K., Stark, S.C., Christoffersen, B., & Prohaska, N. (2016). Leaf development and demography explain photosynthetic seasonality in Amazon evergreen forests. *science, 351*, 972-976

Wu, J., Kobayashi, H., Stark, S.C., Meng, R., Guan, K., Tran, N.N., Gao, S., Yang, W., Restrepo-Coupe, N., & Miura, T. (2018). Biological processes dominate seasonality of remotely sensed canopy greenness in an Amazon evergreen forest. *New phytologist, 217*, 1507-1520

Xiao, X. (2006). Light absorption by leaf chlorophyll and maximum light use efficiency. *IEEE Transactions on Geoscience and Remote Sensing, 44*, 1933-1935

Xiao, X., Biradar, C., Czarnecki, C., Alabi, T., & Keller, M. (2009). A simple algorithm for large-scale mapping of evergreen forests in tropical America, Africa and Asia. *Remote Sensing, 1*, 355-374

Xiao, X., Boles, S., Frolking, S., Salas, W., Moore Iii, B., Li, C., He, L., & Zhao, R. (2002). Observation of flooding and rice transplanting of paddy rice fields at the site to landscape scales in China using VEGETATION sensor data. *International Journal of Remote Sensing, 23*, 3009-3022

Xiao, X., Hagen, S., Zhang, Q., Keller, M., & Moore III, B. (2006). Detecting leaf phenology of seasonally moist tropical forests in South America with multi-temporal MODIS images. *Remote Sensing of Environment, 103*, 465-473

Xiao, X., Hollinger, D., Aber, J., Goltz, M., Davidson, E.A., Zhang, Q., & Moore, B. (2004). Satellite-based modeling of gross primary production in an evergreen needleleaf forest. *Remote Sensing of Environment, 89*, 519-534

Xiao, X., Zhang, Q., Saleska, S., Hutyra, L., De Camargo, P., Wofsy, S., Frolking, S., Boles, S., Keller, M., & Moore, B. (2005). Satellite-based modeling of gross primary production in a seasonally moist tropical evergreen forest. *Remote Sensing of Environment, 94*, 105-122

Xin, F., Xiao, X., Zhao, B., Miyata, A., Baldocchi, D., Knox, S., Kang, M., Shim, K.-m., Min, S., & Chen, B. (2017). Modeling gross primary production of paddy rice cropland through analyses of data from CO 2 eddy flux tower sites and MODIS images. *Remote Sensing of Environment, 190*, 42-55

Xin, Q., Gong, P., Yu, C., Yu, L., Broich, M., Suyker, A.E., & Myneni, R.B. (2013). A production efficiency model-based method for satellite estimates of corn and soybean yields in the Midwestern US. *Remote Sensing, 5*, 5926-5943

Xu, L., Samanta, A., Costa, M.H., Ganguly, S., Nemani, R.R., & Myneni, R.B. (2011). Widespread decline in greenness of Amazonian vegetation due to the 2010 drought. *Geophysical Research Letters, 38*

Yang, J., Tian, H., Pan, S., Chen, G., Zhang, B., & Dangal, S. (2018a). Amazon drought and forest response: Largely reduced forest photosynthesis but slightly increased canopy greenness during the extreme drought of 2015/2016. *Global Change Biology, 24*, 1919-1934

Yang, K., Ryu, Y., Dechant, B., Berry, J.A., Hwang, Y., Jiang, C., Kang, M., Kim, J., Kimm, H., & Kornfeld, A. (2018b). Sun-induced chlorophyll fluorescence is more strongly related to absorbed light than to photosynthesis at half-hourly resolution in a rice paddy. *Remote Sensing of Environment, 216*, 658-673

Yang, W., Kobayashi, H., Wang, C., Shen, M., Chen, J., Matsushita, B., Tang, Y., Kim, Y., Bret-Harte, M.S., & Zona, D. (2019). A semi-analytical snow-free vegetation index for improving estimation of plant phenology in tundra and grassland ecosystems. *Remote Sensing of Environment, 228*, 31-44

Yonts, C., Lyon, D., Baltensperger, D., Blumenthal, J., Harveson, R., Hein, G., & Smith, J. (2009). Producing Irrigated Winter Wheat. *NebGuide G1455. Lincoln, Ne.: UNL Institute of Agriculture and Natural Resources*

Yuan, W., Cai, W., Nguy-Robertson, A.L., Fang, H., Suyker, A.E., Chen, Y., Dong, W., Liu, S., & Zhang, H. (2015). Uncertainty in simulating gross primary production of cropland ecosystem from satellite-based models. *Agricultural and forest meteorology, 207*, 48-57

Zeng, Y., Badgley, G., Dechant, B., Ryu, Y., Chen, M., & Berry, J.A. (2019). A practical approach for estimating the escape ratio of near-infrared solar-induced chlorophyll fluorescence. *Remote Sensing of Environment, 232*, 111209

Zhang, T., Zhang, Y., Xu, M., Zhu, J., Wimberly, M.C., Yu, G., Niu, S., Xi, Y., Zhang, X., & Wang, J. (2015). Light-intensity grazing improves alpine meadow productivity and adaption to climate change on the Tibetan Plateau. *Scientific Reports, 5*, 15949

Zhang, Y., Joiner, J., Gentine, P., & Zhou, S. (2018a). Reduced solar-induced chlorophyll fluorescence from GOME-2 during Amazon drought caused by dataset artifacts. *Global Change Biology*

Zhang, Y., Xiao, X., Jin, C., Dong, J., Zhou, S., Wagle, P., Joiner, J., Guanter, L., Zhang, Y., & Zhang, G. (2016). Consistency between sun-induced chlorophyll fluorescence and gross primary production of vegetation in North America. *Remote Sensing of Environment, 183*, 154-169

Zhang, Y., Xiao, X., Wolf, S., Wu, J., Wu, X., Gioli, B., Wohlfahrt, G., Cescatti, A., van der Tol, C., & Zhou, S. (2018b). Spatio-temporal Convergence of Maximum Daily Light-Use Efficiency Based on Radiation Absorption by Canopy Chlorophyll. *Geophysical Research Letters*

Zhang, Y., Xiao, X., Wu, X., Zhou, S., Zhang, G., Qin, Y., & Dong, J. (2017a). Global gross primary production from vegetation photosynthesis model for 2000-2016. In, *Supplement to: Zhang, Y et al. (submitted): A global moderate resolution dataset of gross primary production of vegetation for 2000-2016. Scientific Data*: PANGAEA

Zhang, Y., Xiao, X., Wu, X., Zhou, S., Zhang, G., Qin, Y., & Dong, J. (2017b). A global moderate resolution dataset of gross primary production of vegetation for 2000–2016. *Scientific data, 4*, 170165

Zhang, Y., Xiao, X., Zhang, Y., Wolf, S., Zhou, S., Joiner, J., Guanter, L., Verma, M., Sun, Y., & Yang, X. (2018c). On the relationship between sub-daily instantaneous and daily total gross primary production: Implications for interpreting satellite-based SIF retrievals. *Remote Sensing of Environment, 205*, 276-289

Zhao, M., Heinsch, F.A., Nemani, R.R., & Running, S.W. (2005). Improvements of the MODIS terrestrial gross and net primary production global data set. *Remote Sensing of Environment, 95*, 164-176

Zhou, Y., Xiao, X., Wagle, P., Bajgain, R., Mahan, H., Basara, J.B., Dong, J., Qin, Y., Zhang, G., & Luo, Y. (2017a). Examining the short-term impacts of diverse management practices on plant phenology and carbon fluxes of Old World bluestems pasture. *Agricultural and forest meteorology, 237*, 60-70

Zhou, Y., Xiao, X., Zhang, G., Wagle, P., Bajgain, R., Dong, J., Jin, C., Basara, J.B., Anderson, M.C., & Hain, C. (2017b). Quantifying agricultural drought in tallgrass prairie region in the US Southern Great Plains through analysis of a water-related vegetation index from MODIS images. *Agricultural and forest meteorology, 246*, 111-122

Ziolkowska, J.R. (2016). Socio-Economic Implications of Drought in the Agricultural Sector and the State Economy. *Economies, 4*, 19

Zuromski, L.M., Bowling, D.R., Köhler, P., Frankenberg, C., Goulden, M.L., Blanken, P.D., & Lin, J.C. (2018). Solar-Induced Fluorescence Detects Interannual Variation in Gross Primary Production of Coniferous Forests in the Western United States. *Geophysical Research Letters, 45*, 7184-7193